The University of Nottingham

Division of Materials, Mechanics and Structures

Development of a Photocuring System for Cationic Epoxy Formulations Using Side Emitting Optical Fibres

by

Ammar Darwish Al-Obaidani

(BSc, MSc)

Thesis submitted to the University of Nottingham for the degree of Doctor of Philosophy

May 2009

Abstract

Photocuring of polymers and polymer composites, from epoxy resin based formulations, has been of growing interest over the past two decades. The photocuring occurs when an epoxy formulation is exposed to electromagnetic radiation, usually ultraviolet (UV) radiation. This process has been explored widely and it can be described as an open mould process by which the epoxy formulation is exposed directly to the radiation. However, for a closed mould process, thermal curing, rather than radiation curing, typically is employed. The potential of using photocuring for a closed mould process has not yet been investigated in detail. The challenge in photocuring of polymers and polymer composites in a closed mould is directing the radiation into the mould to activate the photocuring process, which is not possible using the conventional methods. Hence, for this reason the present work is focused on the development of a closed mould photocuring system using side emitting optical fibres.

This photocuring system using side emitting optical fibres relies upon the optimisation of epoxy based resins. As a result, an extensive characterisation of different types of UV curable cationic epoxy resins is carried out using two pre-formulated commercial resins, formulations from bisphenol A/F, and formulations from cycloaliphatic epoxy. The formulations showed different reactivity and hardness. An important result is that the cycloaliphatic epoxy resin formulations cured much faster than the other bisphenol A/F formulations, having a more uniform hardness distribution and UV radiation transparency during the curing.

Side emitting optical fibres are adopted to photocure epoxy in a closed mould. Different types of side emitting optical fibres are characterised to determine irradiation efficiency. The optical fibres had either a silica core or a PMMA core. The silica core fibres have a silicone cladding containing radiation scattering particles (either ZnO or Al_2O_3) and diffuser (either PA6 or ETFE). The PMMA core polymer optical fibres (PMMA POFs) have a

PVDF cladding with micro-perforations as a side emission mechanism. Silica core fibres with the Al_2O_3 scattering particles and the PMMA core fibre are more suitable for the closed mould application as they transmitted efficiently in the UV radiation band. The high side emission characteristics of the PMMA POF compared to the silica core fibre showed higher potential for use in the closed mould photocuring process.

As the polymerisation speed is influenced by the amount of flux density of the radiation source, a high flux lamp (Hg lamp, 40 W/cm^2) is coupled to the side emitting optical fibres. This lamp caused thermal degradation to the PMMA POF at the launch point when in use. A cooling device is made to minimise the thermal degradation generated by radiation absorption. After improving the optical transmission stability of the PMMA POF, its side emission is enhanced by various treatments, such as permanent modification of the fibre geometry with adjusted bend radii as well as by mechanically embedding silica scattering particles into the fibre and applying micro-cuts.

The developed, closed mould photocuring system consists of: enhanced side emitting PMMA POF, a cooling device, high emission Hg lamp, and a closed mould setup. 1.5 mm and 5 mm thick components, made from an optimised epoxy formulation (based on cycloaliphatic epoxy), are cured using the photocuring system. The 1.5 mm thick component (20 mm wide and 245 mm long) is cured in 45 minutes using a single PMMA POF treated with silica particles (side emission of ~81 % of the total launched emission). The 5 mm thick component (75 mm wide and 170 mm long) partly cured in 45 minutes by simultaneously using three PMMA POFs treated with silica particles and geometric modification (side emission of ~96 % of the total launched emission). This sample eventually cured with time (up to 36 hours) due to dark reaction. The efficiency of the developed closed mould photocuring system is validated by curing a 1.5 mm thick component made from a pre-formulated polyester resin formulation. This component cured in 7 minutes (30 mm wide and 245 mm long) using a single PMMA POF treated with silica particles.

Acknowledgements

Contents

Glossary

Attenuation	Gradual loss of power density through a medium.
Band	An electromagnetic spectral range.
Cationic polymerisation	A process in which the active end of the growing polymer chain molecule produces a positive ion. The generation of this positive ion progresses the polymer chain. In photoinitiated cationic polymerisation, the curing process is not inhibited by atmospheric oxygen and the chain reaction proceeds after UV exposure (dark reaction). The cationic polymerisation is so-called due to the cationic initiator used with the base resin.
Diluent	An additive that reduces the overall viscosity of a resin system.
Electromagnetic radiation	A form of photon energy in which electric and magnetic field components oscillate in a phase perpendicular to each other.
Irradiation or 'flux density'	Power incident on a surface. It is a way of measuring electromagnetic radiation. Irradiance E_λ is a measure of momentary exposure quantified in Watts/cm^2 (W/ cm^2).
Lamp intensity or 'power density'	The overall power of the lamp measured in Watts (W).

PMMA POF	Refers to a group of Polymethyl methacrylate core polymer optical fibres (POF) which could be of different diameters and also having different cladding materials. Each one is called an optical fibre.
POFs	Defines different groups of polymer optical fibres; i.e. fibres with different core material.
Polyols	Additives for resin formulations to enhance the polymerisation process and mechanical properties. Such additive improves the chain mobility and results in an enhanced polymerisation.
Radiant Exposure	Electromagnetic radiation energy on an area per unit time.
Radiant power or 'radiant flux'	Electromagnetic radiant energy per unit time in Watts (W).

Nomenclature

A - Absorbance (no unit)

Al_2O_3 – Aluminium oxide

BSE – Back scattered electrons

CA – Cylinder area

DGEBA – Diglycidyl ether of bisphenol A

DSC – Differential scanning calorimetry

E – Irradiation or 'flux density' (W/ cm^2)

E_{cons} – Consumed energy (kWh)

E_λ – Wavelength dependent irradiation or absolute spectral irradiance (W/ cm^2)

E_a – Activation energy for dissociation (J)

EB – Electron beam

EDX – Energy Dispersive X-ray spectroscopy

EM – Electromagnetic

ETFE – Ethylene tetrafluoroethylene

FTIR – Fourier Transform Infrared Spectroscopy

h – Hour

H – Radiant Exposure (J/cm^2)

Hg – Mercury

I – Intensity or 'power' of the incident light passing through a material in Watts (W)

I_0 – Initial intensity or 'power' of the incident light in Watts (W)

LAN – Local area network

LED – Light emitting diode

LD – Laser diode

mins – Minute

NA – Numerical aperture

n_1 – Refractive index of the optical fibre core

n_2 – Refractive index of the optical fibre cladding

n_{epoxy} – Refractive index of cycloaliphatic epoxy resin

OD – Optical density (OD)

P_{output} Power output (kW)

PA6 – Polyamide-6

PDMS – Polydimethylsiloxane

PHR – Parts per hundred resin

PMMA – Polymethyl methacrylate

POF –   A group of polymer optical fibres of similar material

POFs –   Multiple groups of polymer optical fibres. Not of similar material

PS –   Polystyrene

PVDF –   Polyvinylidene Fluoride

RS –   Resin system

Q –   Total energy in Joules/unit area (J/cm^2)

SE –   Side emission window of an optical fibre (mm^2)

SEM –   Scanning Electron Microscopy

SI –   Step index

S_G –   Scattering particles agglomerates size (µm)

S_H –   Micro-holes sizes (µm)

S_P –   Scattering particles size (µm)

t –   Time (second, minute and hour)

TIR –   Total internal reflection

T_g –   Glass transition temperature (°C)

UV –   Ultraviolet

VUV –   Vacuum ultraviolet

V_P –   Estimated particles volume fraction

ZnO – Zinc oxide

x – Longitudinal axis of an optical fibre (mm)

r – Radial axis from the side of an optical fibre or 'perpendicular to the x-axis along the length of the optical fibre' (mm)

$\Delta H_{absorption}$ – Enthalpy absorbed in Joules (J)

$\Delta H_{reaction}$ – Heat of photochemical reactions in Joules (J)

Greek Symbols

ψ_1 – Angle of incidence in degree (°)

ψ_2 – Angle of refraction in degree (°)

$\psi_{critical}$ – Critical angle in degree (°)

α – Nominal absorption coefficient (cm^{-1})

$\Delta\alpha$ – Relative change in the nominal absorption coefficient (cm^{-1})

c – Absorbing species (mol L^{-1})

c_i – Absorbing species caused by photo-degradation (mol L^{-1})

α_i – Absorption coefficient caused by photo-degradation (cm^{-1})

α_λ – Absorption coefficient at wavelength λ (cm^{-1})

λ – Wavelength (nm)

θ_{ac} – Cone of acceptance angle in degree (°)

e – Total rate of energy absorption (W/cm^2)

k_λ – Response spectrum (cm^{-1})

k – Attenuation coefficient of an optical fibre (cm^{-1})

Chapter 1

Introduction

1.1. Radiation Curing of Polymers

Photocuring of polymers by means of irradiation in the ultraviolet (UV) or visible bands of the electromagnetic spectrum shows several potential advantages compared to thermal curing. In photocuring processes, the chain polymerisation occurs through a photochemical event in which propagating active centres are generated, typically cations or radicals. One of the main advantages of radiation curing is lower shrinkage within the cured product. This permits tighter dimensional tolerances to be maintained. The cycle time is significantly reduced (minutes rather than hours) and, as no heating is required, the energy consumption in UV curing is typically lower, and the tool design is less complex. Since the curing process normally starts from the component surface, liquid resin is encapsulated below the surface, and the emission of volatile substances into the environment can be lowered significantly. Radiation curing is found to be an efficient, fast curing technique in curing varnishes, paints, printing inks, adhesives, and is employed in the production of printing plates, microcircuits, dental material and optical disks [1-2]. However, radiation curing of polymers has not been used commercially for closed mould processes unlike thermal curing processes.

1.2. UV Curing of Epoxy Using Side Emitting Optical Fibres

Conventional UV curing methods can only be applied if the component can be directly irradiated and, due to the absorption of radiation, the material thickness is limited. The motivation for investigating photocuring processes using side emitting optical fibres embedded within a component is the potential to achieve compatibility with economical closed mould processes. Thus, the objective is to photocure an epoxy used in a closed mould process, to allow curing of thick- and thin-sectioned components or to cure adhesives in bond lines between opaque material sheets (Figure 1-1).

1. **Side emitting optical fibre**

2. **Opaque surface**

3. **Epoxy resin surrounding the optical fibre**

4. **Radiation entering the optical fibre**

5. **Radiation scattered from the side of the optical fibre**
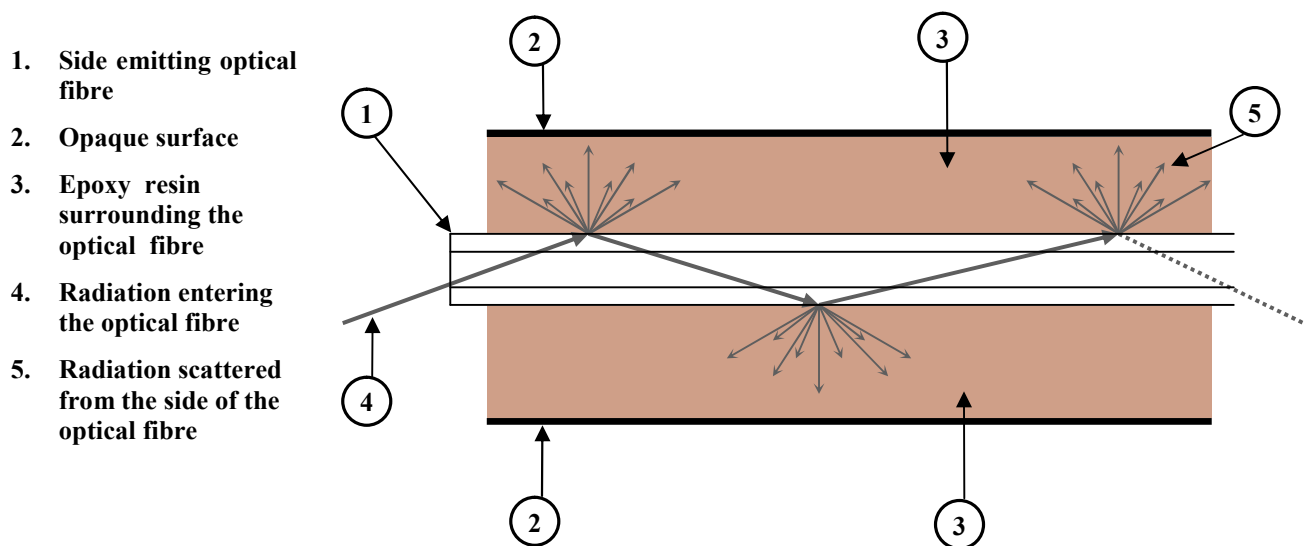
Figure 1-1. Schematic illustration of radiation curing of resin using a side emitting optical fibre.

In optical fibres for telecommunication and data transfer applications, radiation is transmitted with minimal loss and emitted only from the end face. Side emitting optical fibres, on the other hand, are typically designed as linear light sources frequently used for illumination and decoration purposes [3-10].

The challenge in the photocuring of epoxy using side emitting optical fibres is that UV radiation may undergo strong attenuation within the fibres and cause degradation of the fibres themselves while being transmitted through the optical fibres. On the other hand, the amount of energy emitted from the optical fibres is critical for initiation of the photoreactions within the epoxy to produce curing [11-13].

1.3. Area of Novelty in the Photoinitiated Resin Curing Field

 A significant amount of work has been published in the field of radiation curing processes. The curing process is similar for all of the work reviewed, and is accomplished by using a radiation source to irradiate different resin systems for curing films, such as coatings, inks or adhesives. None of the work reviewed described radiation curing for an adhesive in a bonded structure, whereby the adhesive is a thin film used to join two opaque substrates such as aluminium. This is due to the difficulty in exposing the reactive species of a photoinitiator in an adhesive to the radiation necessary for initiating polymerisation. One way of activating the reactive species would be to embed a side emitting optical fibre within the adhesive bond. The radiation would be launched from a source into the optical fibre, and then released along the length of the optical fibre in a radial pattern into the adhesive, activating the reactive species within it.

According to the knowledge of the author, photocuring of polymers and polymer composites using side emitting optical fibres has never been established and very few studies related to this curing method are available. Fawdington et al. [14] and Bilanin et al. [15] have patented methods for curing composites using side emitting optical fibres. Recently, during researching the presented work in this thesis, Yahathugoda et al. [16] reported an experimental study of UV curing for polyester resin using a side emitting glass

optical fibre within thick components. The work by Yahathugoda et al. [16] is from a joint project between Pera Innovation (UK) and the University of Nottingham. No work has been reported on the photocuring of epoxy resin systems using a side emitting optical fibre which suggests the novelty of researching this area.

The efficiency of photocuring varies for different types of epoxy resin systems, as the reactivity is highly dependent upon the mixing ratio of the base epoxy resin, photoinitiator and additives which will be discussed in Chapter 2 [2]. Equally, a side emitting optical fibre, which is available in many types, must be selected based upon its ability to transmit the required radiation for curing. Hence, photocuring of epoxy using a side emitting optical fibre relies upon optimising both: a highly reactive epoxy resin system and a side emitting optical fibre which emits efficiently the required radiation for the photocuring process.

For effective photocuring of polymeric resins, resin formulations need to be matched with the emission characteristics of the equipment used [11, 17-18]. The key factors for efficient photoinitiated curing with and without side emission optical fibres are summarised in Figure 1-2. The chart shows two main streams: resin and radiation equipment requirements. The resin system should consist of adjusted compositional ratios of the base resin, a photoinitiator and additives necessary for deep curing and sufficient mechanical properties. Deep efficient curing of resins can be achieved by using a high emission radiation source, as the photons emitted by the radiation source would propagate efficiently to deep resin mediums due to their high energy. The selection of the radiation source has to be based upon its compatibility with the optical fibre that it is connected to. In addition, the emitted spectral irradiance from a radiation source must match the absorption spectrum of the resin system for efficient photocuring. Finally, in the case of using a side emitting optical fibre, the material of the optical fibre must be highly transparent to the required absorption spectrum at which the resin system cures. Hence, by applying the above key matching factors, efficient photocuring of a resin system can be achieved.

Photoinitiated curing system using optical fibre

Critical key matching factors

Resin system

Radiation source

- Effective Irradiance E_λ (W/cm^2) with spectral emission matching or close to matching resin system absorption spectrum
- Compatible with optical fibre

or bypass for direct curing

Side emitting optical fibre

- Efficient optical transmission of the required spectral emission for the photocuring process

Base resin & additives

- Required mechanical properties
- Optical transmission to deep mediums
- Efficient curing rates

Photoinitiator

- Compatible with the base resin
- Absorption spectrum must match, or be close to, the radiation source spectral emission

Curing Process

Efficient product with reasonable mechanical properties and curing time

Figure 1-2. Matching factors methodology for an efficient photoinitiated curing system [11, 17-18].

1.4. Objective and Overview of the Thesis

The aim of this work is to develop a closed mould photocuring system to cure a photoinitiated cationic epoxy resin. The curing methodology of the system is aimed to cure the photoinitiated cationic epoxy resin by using an embedded side emitting optical fibre with radiation exposure ranging from ultraviolet to visible blue (350 nm to 450 nm). To accomplish the objective, different types of epoxy resins and commercial side emitting optical fibres are characterised to establish an optimised curing system for making thick and thin components. The experimental results of the optical fibre characterisation from Chapter 3 have already been published in a journal paper (Appendix 1.A). Appendix 1.A also lists conference papers regarding the optimisation techniques of different types of epoxy formulations and the curing of epoxy resin using an enhanced PMMA POF (polymer optical fibre) which are discussed in detail in Chapter 2 and Chapter 5, respectively.

 This thesis comprises six chapters, including the above introduction:

Chapter 2 contains a study in the optimisation of an epoxy resin from an extensive characterisation of different types of UV curable cationic epoxy resins. The characterisation carried out through experimentation includes: the time required for UV curing of resin systems with different compositional ratios, hardness of cured samples, viscosity and spectroscopic measurements of the radiation absorption of resin systems before and during curing.

Chapter 3 discusses an experimental characterisation of various types of side emitting optical fibres. The characterisation process is conducted for determining: the architecture of each fibre, the material of the fibre components, the side emission mechanism and the optical transmission of the side emitting optical fibres.

Chapter 4 presents an experimental study on the effect of polymer degradation on the transmission of a PMMA POF when exposed to high intensity UV-A and visible blue light.

Chapter 5 discusses the experimental techniques for measuring the attenuation of the PMMA POF and enhancing the side emission efficiency of the PMMA POF by introducing a number of fibre treatment techniques. These are used to cure thick- and thin-sectioned composite samples using the optimised epoxy resin system from Chapter 2.

Chapter 6 contains the overall discussion and conclusions of this thesis as well as recommendations for further work.

Chapter 2

Optimisation of Epoxy Resin Formulations

2.1. Introduction

Photoinitiated curing of polymers and polymer composites consists of two fields that make the curing process work. These fields are: the radiation source and the resin system formulation. In this type of curing, radiation energy is used to cause a chemical reaction within a polymer resin. The chemical reaction transforms a liquid resin to a solid polymer [11-12]. Resin formulation reactivity plays the main role in radiation curing. Efficient curing requires a radiation source to emit a radiation wavelength compatible with the photoinitiator absorption spectrum. For curing an epoxy resin in a closed mould using an embedded side emitting optical fibre, a radiation source is used to launch the radiation into one end of the optical fibre, and the radiation is then emitted from the side of the fibre to cause photocuring of the surrounding epoxy resin. The fibre delivers a low radiation intensity to the surrounding medium compared to the irradiation intensity directly emitted by a radiation source. Hence, the reactivity of an epoxy resin system should be optimised in order to improve its photocuring efficiency when a side emitting optical fibre is used. This chapter discusses the optimisation of different types of epoxy resin systems in terms of speed of photocuring, resin systems viscosity and the optical transmission of the optimised epoxy resin systems throughout the curing process.

2.2. Background

2.2.1. Radiation Sources

The radiation used in resin curing applications ranges from vacuum ultraviolet (VUV) to visible yellow (250 nm to 670 nm, respectively), as shown in the electromagnetic spectrum, Figure 2-1. The wavelength used in the resin curing process is dependent upon the resin system characteristics. Typical wavelength bands used in resin curing applications by radiation energy sources are summarised in Table 2-1.
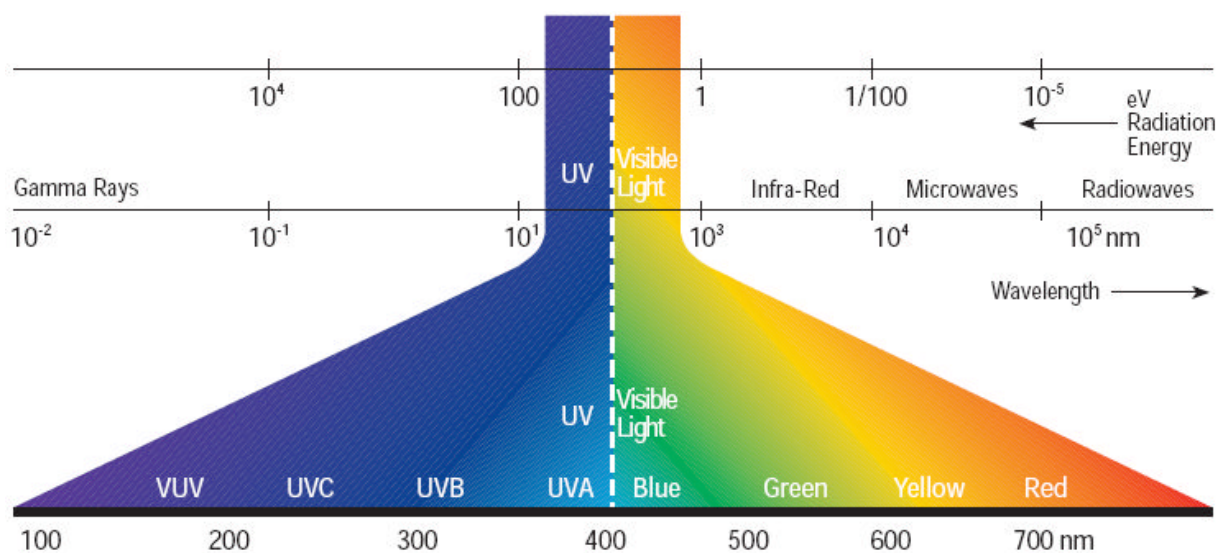
Figure 2-1. The electromagnetic spectrum [19].

Table 2-1. Radiation bands used in resin curing [1, 19-23], and the types of lamps emitting irradiation corresponding with the electromagnetic spectrum band type

Electromagnetic spectrum bands		Types of lamps with irradiation emission in various wavelengths , (λ/nm)					
Band Type	Wavelength, λ/nm	Blacklight lamps	Medium pressure mercury vapor lamps with electrodes	High pressure mercury vapor lamps	Electrodeless mercury vapor lamps	Metal halide lamps	Light emitting diode (LED) and Laser diode (LDs)
Visible green to Red	490-635	-	-	-	-	-	A selection with a variety of wavelengths
Visible Blue	400-490	-	-	400-425	A selection of bulbs each covering a certain band	400-450	
UVA	315-400	320-400	350-380	320-400		315-400	
UVB	280-315	-	-	-		-	
UVC	100-280	-	240-270	-		-	

As shown in Table 2-1, there are many types of commercial radiation sources that can be employed in the resin curing process depending upon the initiation wavelength at which a resin formulation polymerises. For instance, *Blacklight lamps* or 'fluorescent lamps' can be used for curing resin formulations in the UVA band [20]. Lamps are also available with irradiation emission at different bands of the electromagnetic spectrum. *Medium pressure mercury vapor lamps with electrodes* or 'mercury arc lamps' emit highly in both UVC and UVA bands (Table 2-1) where typical UV photoinitiators absorb [20]. For the curing applications in the UVA and visible blue electromagnetic spectrum bands, *high pressure mercury vapor* and *metal halide lamps* are used. *High pressure mercury vapor lamps*

irradiate intense emission in the UVA and visible blue bands (Table 2-1) [20]. *Metal halide lamps* are derived from medium pressure mercury arc lamps with a modified spectral output by the addition of metal halides to give intense emission in the UVA and visible blue bands (Table 2-1), Figure 2-2. Metal halide lamps are also used for spot light curing equipment provided with or without a mono-refractive index silica glass rod light guide [20, 22]. Other lamps like *electrodeless mercury vapor lamps* come with three bulb options; each bulb covers a certain band starting from UVC towards the visible light. The selection of the bulb is dependent upon the photoinitiator absorption spectrum peaks [20]. Furthermore, an arc lamp bulb consists of two electrodes which are separated by a gas, including neon, argon, xenon, sodium, metal halide and mercury. Other types of radiation sources such as *Light emitting diode* (LED) and *Laser diode* (LDs) are also used for photocuring applications. These have a variety of wavelengths and mainly are used for localized wavelength curing. They are also available with optical fibre connecters [23].
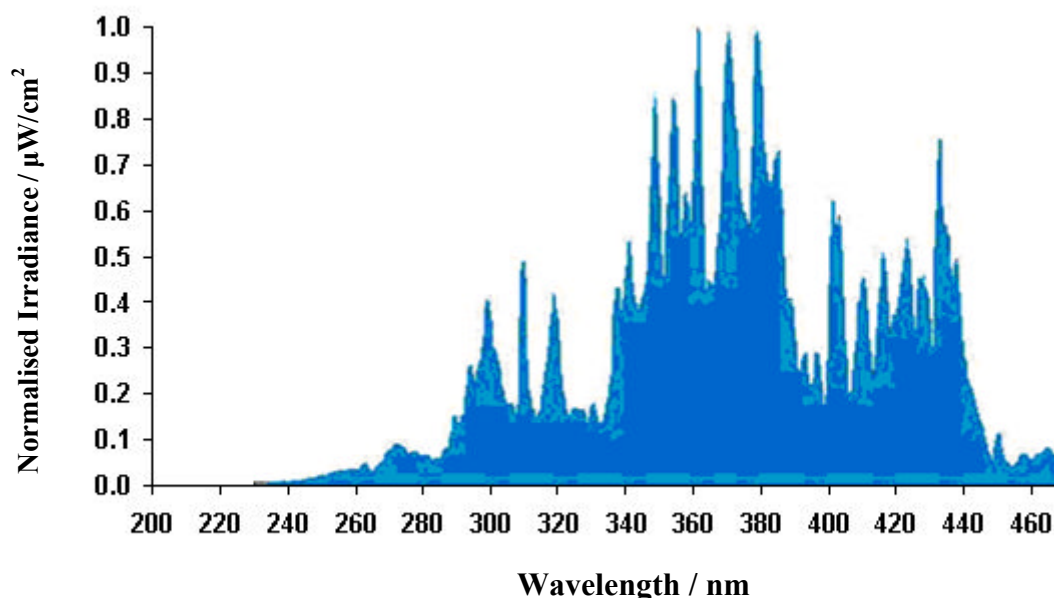
Figure 2-2. Spectral output of a flood lamp with a Metal Halide D-type iron doped bulb [22].

The appropriate selection of a lamp is based upon the match between the spectral output and the type of photoinitiator used in a particular resin system. Designing a conventional radiation curing application requires consideration of four major factors that lead to successful curing results of a three-dimensional object [1, 17-18, 24]; spectral output of the lamp, radiation intensity, resin system optical properties, and cure characteristics needed. The cure characteristics of a resin are properties the resin exhibits all through the photocuring process, such as depth of cure, curing speed, mechanical properties and overall shrinkage. More details and examples can be found in Appendix B-1 'B1'.

2.2.2. Photoinitiated Crosslinking Polymerisation

Photoinitiated curing of resins has been studied extensively for the last two decades. In this process the liquid resin is transformed from a liquid to a solid state using reactive species from photolysis of an initiator, which is decomposed by irradiation. The irradiation can be induced by photons (UV curing) or electrons (electron beam (EB) curing) [25-26]. Curing using photons ranges from the ultraviolet (UV) to the visible blue band. For efficient production of cations or radicals from a chemical compound (photoinitiators) mixed in a specific resin system, the selection of the radiant source is dependent upon its efficient photon emission. The source also must deliver sufficient energy for a photoinitiator mixed in a specific resin system to generate a reactive acid. The photoinitiated curing process effectively is instantaneous in coatings and printing applications. However, curing periods increase significantly when resin thickness is increased [11, 27].
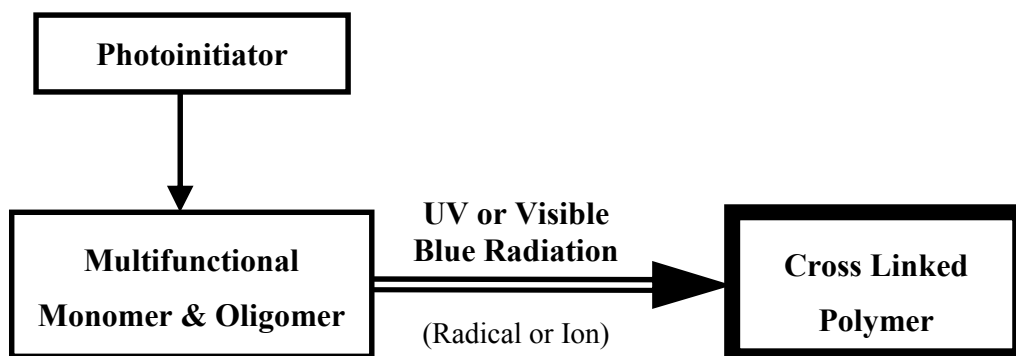
Figure 2-3. General scheme of the photoinitiated curing processes [11, 25-26].

The basic principle of the photoinitiated curing process is demonstrated in Figure 2-3. First, the photoinitiator is mixed with multifunctional monomers and oligomers to form a photoinitiated resin system in liquid form. Then, the resin is induced by a radiant source that initiates the photoinitiator species causing rapid crosslinking of the polymer chain until the liquid resin is transformed into a crosslinked polymer network (solid) [26]. The composition of the monomers and oligomers depends upon the type of cured resin application.

Photocuring resin systems are of two major classes [11]:

- Photoinitiated radical polymerisation of multifunctional monomers, such as acrylates or unsaturated polyesters

- Photoinitiated cationic polymerisation of multifunctional epoxides and vinyl ethers

Of the two, the photoinitiated radical polymerisation process has been used most extensively. However, cationic polymerisation is undergoing rapid growth [26]. Both polymerisation processes take place in three steps: initiation, propagation and termination [1]. However, each one of these classes has a different polymerisation mechanism due to the

photoinitiator functionality; see Appendix B-1 'B2 & B3', the photocuring reaction of cationic polymerisation of epoxide is also included in Appendix B-1 'B3'.

Studies showed that these two classes of polymerisation can be combined in order to make a resin system that gives superior properties after curing. Examples of these hybrid systems are: vinyl ether/epoxide, vinyl ether/unsaturated ester and epoxide/acrylate [11].

The photoinitiator composition ratio in both classes varies with the types of resin systems. Increasing the photoinitiator ratio in a resin system results in top surface degradation during irradiation and non uniformity of mechanical properties through the cured polymer [2].

2.2.3. Photoinitiated Cationic Polymerisation

Practical use of the photoinitiated cationic polymerisation process was developed in the late 1960s by employing aryldiazonium salts as photoinitiators. Subsequently, a series of practical, shelf stable and efficient onium salt photoinitiators were developed, and hence, the field of cationic UV curing was established [28].

The compositional mixture of a photoinitiated cationic polymerisation resin system consists of:

- Di-functional monomers

- Photoinitiator

- Additives to modify curing or mechanical properties, such as diluents, polyols or other monomers

The photoinitiated cationic polymerisation process is used increasingly due to its unique properties, such as: [1, 25, 29]

- Ring-opening polymerisation

- Immunity to atmospheric oxygen inhibition, unlike photoinitiated radical polymerisation

- Improved adhesion over free-radical, UV-cured coatings due to low shrinkage that varies between 4 % to 6 % of the total resin formulation volume [1].

The advantage of using cationic polymerisation is that the polymerisation process carries-on even after the UV radiation source is removed. This effect is known as shadow curing, post-polymerisation or dark reaction, as mentioned by others [1, 30-31]. Dark reaction leads to a progressive curing of the resin until it is fully cured. This reaction effect is often observed in the cationic ring-opening photo-polymerisation of epoxide and other cyclic ether monomers [32]. However, the curing time during dark reaction could be very long depending on the thickness of the part as well as on the chemical composition of the resin [1]. The dark reaction rate can be measured using a photo-differential scanning calorimetry (photo-DSC) technique. Photo-DSC studies the kinetics of the polymerisation reactions. These exothermic polymerisation reactions are determined by measuring the heat released during the process [32].

Contamination of the resin system in the case of adhesive bonding, by the substrate, can slow or stop the curing process and results in poor adhesion, micro-wrinkling or both. Proton donor contaminants such as organic amines, basic pigments or water tend to deactivate the cationic catalyst by neutralizing the protons generated from photolysis of the photoinitiator resulting in a poor curing response [33].

Although the cationic reaction is not affected by oxygen, cationic cure is affected by high ambient humidity that leads to a deactivation of the photoinitiator, especially when additives like polyol are used [21, 33]; an example is shown in Appendix B-1 'B3'. To overcome the humidity problem and for further improvement of the cationic curing process, a relative humidity no greater than 87 % with a dry air purge is suggested [21].

2.2.4. Cationic Photoinitiators

Cationic photoinitiators are salts that can be found in a range of classes. Onium salts are the most widely used photoinitiator, as shown in Table 2-2. However, only three of these salts have commercial applications (diaryliodonium, triarylsulfonium and ferrocenium) [28]. Most of the research into cationic photoinitiated polymerization is done with both aryl sulfonium or iodonium salts ($\Phi_3S^+PF_6^-$, $\Phi_2I^+SbF_6^-$) respectively [25-28, 34-36]. Each one of these salts is a group of cationic photointiators, as indicated by the capital **X** in the Structure column, Table 2-2. The Structure column represents the number of variable compositions to form the cationic photointiators.

Table 2-2. Structures of onium salt cationic photoinitiators [28]

Name	Structure
Diazonium salts	$ArN_2\ X^-$
Diarylionium salts	$\mathbf{Ar_2I^+\ X^-}$
Diarylbromonium salts	$Ar_2Br^+\ X^-$
Triarylsulfonium salts	$\mathbf{Ar_3S^+\ X^-}$
Triarylselenonium salts	$Ar_3Se^+\ X^-$
Dialkylphenacylsulfonium salts	$ArCOCH_2S^+R_2\ X^-$
Dialkl-4-hydroxyphenyl-sulfonium salts	$HOAr\ S^+R_2\ X^-$
Ferrocenium salts	$\mathbf{C_5H_5Fe^+\ Ar\ X^-}$

Diaryliodonium and triarylsulfonium salts are highly photosensitive and compatible with a variety of reactive monomers and oligomers. They have quantum yields ranging from 0.5 to 0.7; the quantum yield is a measure of the efficiency of a salt reactivity per absorbed photon. In addition, their photolyses are not affected by temperature, radical inhibitors or oxygen. Highly reactive multifunctional epoxy resins containing triarylsulfonium salts can polymerise even if heated to 150 °C [12]. These photoinitiators have excellent thermal stability in the absence of light, which enables them to be incorporated into highly reactive monomeric substrates that give short UV cure times. In addition, their structure can be modified in simple and straightforward ways to achieve specific UV absorption characteristics [25, 28].

The amount of cationic photoinitiator in a resin can influence the mechanical properties after curing. Martysz et al. [26] found that the higher the amount of triarylsulfonium salt photoinitiator in the epoxy, the harder the epoxy became. The authors also found that the hardness became constant beyond a concentration of approximately 5 % of the overall photoinitiator ratio in the epoxy resin system. Hence, the type and the percentage of cationic photoinitiator in a resin, control the mechanical properties of the final product.

Photoinitiated cationic polymerisation undergoes initiation, propagation, chain transfer, and eventual termination processes (see Appendix B-1 'B3' for more details). During the photocuring process, the radiation is only involved in the initiation step of the curing process to generate a catalytic quantity of acid. The strength of the acid produced for efficient curing rates is dependent on the cation structure of the photoinitiator, because it determines the rate of acid generation as well as the anion. The anion does not determine the photochemical behaviour of the photoinitiator, but it has a major influence on the rate and degree of polymerisable monomers produced. Photoinitiator salts with nucleophilic and intermediate nucleophilic anions did not polymerise cationic monomers, however, intermediate nucleophilic anions did polymerise highly reactive monomers like vinyl ethers. Cationic monomers can be polymerised by non-nucleophilic anions. Examples of these

monomers are epoxides, cyclic ethers, mono- and polyfunctional vinyl compounds, spiroesters, spirocarbonates, and cyclic siloxanes [12]. Types of anions for any particular photoinitiator have an influence on the mechanical properties with respect to the amount of photoinitiator used [26]. Martysz et al. [26] found that 2 % of triarylsulfanium salt with the PF_6^- anion gives comparable hardness values as 5 % of triarylsulfanium salt with the SbF_6^- anion when used with 1-propenyl ethers.

2.2.5. Photosensitisation of Cationic Photoinitiators

Photosensitizers are used to tune or shift the wavelength absorption of photoinitiators, so that they can react at higher wavelengths than what the photoinitiators are designed for. Many studies have been done to understand the mechanisms of photosensitization with different cationic photoinitiators [13, 29, 37-43]. Generally, photosensitizers are expensive compared to photoinitiators, however, Crivello et al. [26] derived cost effective and efficient photosensitizers.

The onium salts, such as diaryliodonium and triarylsulfonium salts do not absorb radiation above 350 nm, where mercury lamps emit high radiation. Using photosensitizers with these cationic photoinitiators broadens their spectral response to both long wavelength UVA and the visible radiation bands.

Diaryliodonium salts can be photosensitized with condensed ring aromatic hydrocarbons, diaryl ketones and dyes. Triarylsulfonium salts can only be photosensitized by condensed ring aromatic hydrocarbons [12, 29, 40]. Cho et al. [29] observed an increased absorption spectrum when testing a mixture of anthracene photosensitizer and triarylsulfonium hexafluorophosphate photoinitiator in similar ratios. However, other studies reported that the anthracene photosensitizer should be between 1 % to 10 % of the total weight of the photoinitiator for efficient curing results, as reported by Smith et al. [41-42]. Crivello et al. [43] suggested using an anthracene photosensitizer concentration ranging from 10 % to 50

% by weight, based on the weight of the photoinitiator, which is half of the weight used by Cho et al. [29].

2.2.6. Photopolymerisation of Epoxy Resin

Epoxy Background

Epoxy resins were developed late in the 1940s [44]. They are also known as epoxide resins and, occasionally, as ethoxyline resins [45-46].

Epoxy resins are used in structural and specialty composite applications, such as automotive and aerospace, due to their unique combination of properties that are unattainable with other thermoset resins [45]. For instance, diglycidyl ether epoxies have been used successfully in many industrial applications, such as adhesives, coatings, encapsulates, casting materials, potting compounds, binders and matrix material for fibre reinforced laminates [45-49]. Cycloaliphatic epoxies, which are another type of epoxy resin, have advantages such as: weathering resistance, arc resistance and track resistance, making them a good choice in applications like: tension insulators, rocket motor cases and transformer encapsulation [46].

Epoxies provide performance advantages compared to general purpose unsaturated polyester resins, such as higher strength, modulus and fracture toughness. Furthermore, one of the main advantages of epoxies is their good adhesion to many substrates, such as aluminium. Epoxies have lower residual micro-stresses when cured compared to polyesters, due to a lower shrinkage of approximately 3 % by volume, whereas shrinkage of 8 % is common for polyesters [45, 49] in the classical thermal curing process. In photocuring applications similar percentages of shrinkage were found for these resins [1].

However, epoxy resins are expensive compared to general purpose polyester and vinyl ester resins. They are four times more costly than general purpose polyester resins and twice the

price of the vinyl ester resins. Additionally, from the polymerisation point of view, epoxy resins take a longer time to cure compared to polyester resins [45, 49].

Cationic UV Curing of Epoxy

Photoinitiated cationic epoxy polymerisation offers a number of advantages compared to thermally cured epoxy, for the following reasons [50]:

- The reactions are solvent free

- There are no residual amines, and

- The reaction can be carried out at low temperatures

Most thermally activated epoxies use solvents, amines and a temperature source (usually an oven) for curing. Solvents are low molecular weight liquids used to lower the viscosity of epoxy formulations to control there flowability during processing [51].

Residual amines are only found in thermally cured epoxy. They are used as an initiator. Using amines in UV curing resins affects the polymerisation, because basic or alkaline materials, such as organic amines or basic pigments, can neutralize the photoinitiator, and consequently, the cure will be dramatically slowed or stopped [21].

Photoinitiated cationic epoxy cures at room temperature. However, heating the resin increases the mobility of the monomers that influences the reactivity and results in faster as well as more efficient polymerisation [1]. Heat during curing is generated when normal lamp sources are used, but in the case of spot radiation lamps or optical fibre a heat source could be used to enhance polymerisation.

Furthermore, the curing shrinkage of UV cured epoxy is lower than with traditional hardeners, providing enhanced adhesion property as well as being an attractive option for

parts requiring tight dimensional tolerances [45, 52]. The shrinkage rate for photo-curable resins is highly dependent on the resin system as well as on additives, such as polyol monomers [52].

Types of UV Curable Epoxy Resins

In photoinitiated curing of epoxy, two base epoxy resins are used; diglycidyl ether and cycloaliphatic epoxy resins. Cycloaliphatic epoxies have a much lower viscosity than standard diglycidyl ether resins. Generally, cycloaliphatic epoxy compounds show higher reactivity than glycidyl compounds (for more details, see Appendix B-1 'B4') in both thermal and photocured cationic polymerisation, and this is due to their compact structure (rings) [28, 46, 53]. The photopolymerisation of cycloaliphatic epoxy are also found less affected by moisture compared to diglycidyl ether epoxy, as reported by Hartwig et al. [33]. Most studies on epoxy photocuring have focused on cycloaliphatic epoxies due to their fast curing comparing to the other types of epoxy resins [34]. Crivello et al. [28, 54] cured cycloaliphatic epoxies with different carbon rings, Figure 2-4, and found that the curing periods varies from one type to another.
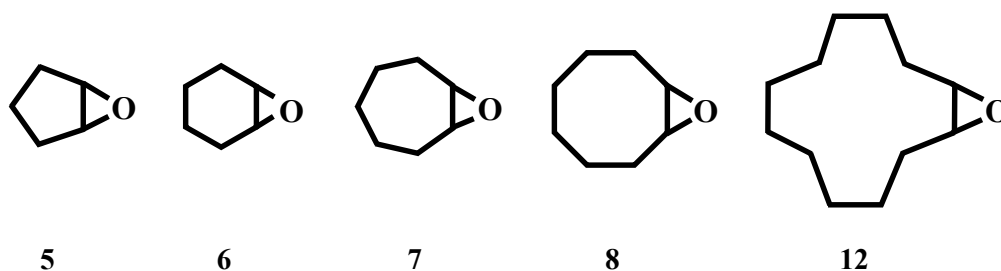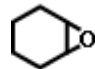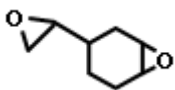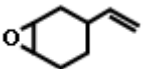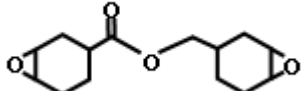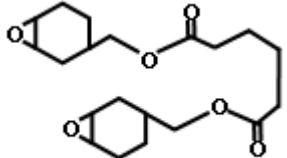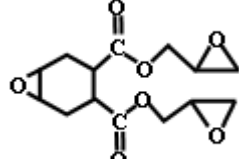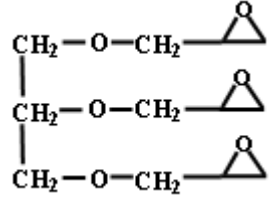
Figure 2-4. Cycloaliphatic epoxy monomers with ring sizes from 5 to 12 carbon atoms [28].

The finished product of cycloaliphatic epoxies is brittle compared to diglycidyl ethers due to the lack of flexibility of the molecules that causes more rigid segments between the crosslinks [46, 55]. This is improved by additives like polyols [21, 52, 55]. In addition, cycloaliphatic epoxies are more expensive than diglycidyl ether epoxies [46]. Table 2-3 shows typical cycloaliphatic epoxies used by different authors in photocuring studies.

Table 2-3. Types of cycloaliphatic epoxy resins used in photoinitiated curing applications

No.	Chemical name	Chemical structure
1	Cyclohexene oxide (CHO) [56, 57]	
2	4-vinylcyclohexene oxide (VCHO) [56]	
3	4-vinylcyclohexen dioxide (VCHDO) [56]	
4	**Difunctional cycloaliphatic epoxy** [21, 36-38, 58]**:** 3,4-Epoxycyclohexylmeth- 3',4'-epoxycyclohexane Carboxlate	
5	Bis-(3,4-epoxycyclohexylmethyl) Adipate [21]	
6	Di(2,3-epoxypropyl)3,4-epoxy-1,2-cyclohexanedioate [58]	
7	1,2,3-(2,3-epoxypropyl)-glycidylether [58]	

2.2.7. Additives in Epoxy Resin Systems

Additives (monomers) are used to lower the formulation viscosity and to enhance both the curing speed as well as the properties of the crosslinked polymer [11, 34]. There are two classes of additives reported in the literature. The first class of additives improves the curing rate as well as the mechanical properties of epoxy monomers. The second class shifts the absorption spectra of the photoinitiators used in the epoxy resin systems: known as photosensitizers, as discussed earlier in Section 2.2.5.

Polyols and alcohol are the two main additives reported by many authors for improving the behaviour of monomers during curing as well as the mechanical properties of the cured polymer. Alcohol and polyols co-react with epoxides by acting as chain transfer agents [11, 55, 59]. These additives are also known as diluents due to their effect in reducing the overall viscosity of a resin system.

Using polyols increases flexibility, adhesion and depth of cure for samples thicker than 1mm. However, high proportions of polyol results in poor mechanical properties and curing rate [55]. Examples of polyols used with epoxy resin systems are:

- Oxetane resin [53]

- ε-Caprolactone Triol [21]

- Poly(ε- Caprolactone) [55]

Sangermano et al. [57] reported that oxetane addition in cycloaliphatic epoxy resulted in an improved curing conversion, as oxetane accelerates the curing process and improves mechanical properties.

Further acceleration of the curing rate of cycloaliphatic epoxides can be achieved by using a temperature source to increase the chain mobility of the resin system [30] as well as by

adding alcohol monomers; which accelerate opening of the epoxide ring [20, 59]. Olsson et al. [59] conducted a study on temperature and hexanediol alcohol addition effects on the curing rate of 20 μm cycloaliphatic epoxy films (3,4-Epoxycyclohexylmeth-3',4'-epoxy-cyclohexane Carboxlate). It was found that at 60 °C with gradually increased percentages of alcohol mass from 10 % to 20 % resulted in faster curing rates compared to an epoxy without alcohol.

In epoxy curing applications, Decker et al. [27] reported that slow UV cure of epoxy monomers is caused by an inefficient initiation process and that the low absorbance of photoinitiator salt is considered to be one of the reasons for this. Hence, they proposed the use of a small amount of photosensitizer in the resin system in order to shift the absorption spectrum to the 350 nm - 400 nm range where the mercury lamp has its maximum emission. Adding 0.5 wt% of ITX (isopropylthioxanthone) improved the polymerisation of difunctional cycloaliphatic epoxy by a factor of 3 [27]. Curing epoxy resins at wavelengths greater than 400 nm (Visible light) is also possible. Spectra Group Limited Inc [60] offers a photoinitiator (H-Nu 470) that is capable of visible radiation cationic polymerisation. This photoinitiator is a mixture of photosensitizer and iodenum salt. The company suggests that the photosensitizer they provide with the photoinitiator will give a poor curing result if used with sulfonum salts, which are used extensively for epoxy curing [21, 27, 61]. However, in the presence of iodenum salt, sulfonum salt can be added to enhance the curing process if required [60].

2.2.8. Photocuring Monitoring Techniques

The photocuring behaviour of resins throughout the curing process can be studied by various methods which are usually based on either thermal or spectral output measurements. In photocuring kinetic studies, differential scanning calorimetry (DSC) has been commonly used [11, 17, 29, 32, 36, 62-63]. This technique operates by measuring the heat flow due to

the chemical reaction during polymerisation. The accuracy of the DSC technique becomes limited with curing reactions occurring in less than 10 seconds due to its long response time, which is about 2 seconds [17]. Hence, real-time Fourier transformation infrared spectroscopy (FTIR) having a response time in milliseconds is used instead, especially when curing resins with intense UV [17, 35, 63]. DSC and FTIR techniques are used extensively for obtaining resin conversion versus time profiles. However, these techniques do not give information about the change in the optical transmission at which the epoxy resins photocure, typically in the UV band. Furthermore, methods like DSC and FTIR are used for testing thin film samples (thickness $\leq$ 1 mm) which are more likely to be for coatings applications. The resin compositional ratio and speed of conversion varies when photocuring thick components compared to a thin film, as reported by Narayanan et al. [2]. As the polymerisation of resins progresses from the face exposed to the radiation source to the layers below, the optical properties of the cured epoxy layers [64-67], can result in higher absorption of radiation. Hence, the transmitted radiation through the sample will drop exponentially as the resin polymerises and may result in longer curing periods for deeper resin mediums.

Therefore, to study the photocuring of thick components using different epoxy resins formulations, spectral transmission of the radiation at which the resin formulations polymerise should be monitored. Desilles et al. [68] suggested a technique for monitoring the spectral change during resin conversion. Teramoto et al. [69] and Arun et al. [70] measured the rate of resin conversion using a spectrometer by which a number of spectral outputs were recorded at constant time intervals.

2.2.9. Depth of Cure

There are several types of photoinitiators used for different base resins in the photocuring process of polymers and polymer composites [2, 71-73]. The activation of these photoinitiators by UV irradiation varies according to the designed absorption of UV irradiation in the electromagnetic wavelength bands, typically UV or the visible bands of the spectrum. Due to the depth of cure, resin formulations for curing thick components require less photoinitiator compared to thin films [2, 21].

For electromagnetic field, high frequencies (shorter wavelength) radiation carries greater energy, as shown in Figure 2-5 [1]. Hence, irradiation in the UVC band produces higher energy than irradiation in the UVA band (Figure 2-1). This makes the photoinitiators designed for absorbing UVC irradiation more efficient [1, 21]. However, these short wavelength irradiations do not penetrate efficiently into thick resin mediums and they are also harmful to humans. Therefore, for efficient photocuring of thick components, photoinitiators designed for activation by irradiation at longer wavelength should be used.

frequency, energy

gamma rays — X-rays — ultraviolet — visible — infrared — microwave — radiofrequency

wavelength, depth of penetration
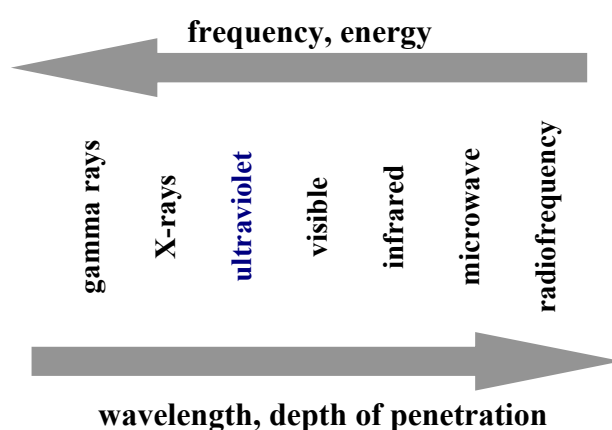
Figure 2-5. Electromagnetic spectrum, qualitatively [1].

2.2.10. Main Tasks to Optimise Epoxy Based Formulations

The main objective of this work is to cure a photoinitiated cationic epoxy resin using a side emitting optical fibre with radiation exposure ranging from ultraviolet to visible blue (315 nm to 450 nm). In order to accomplish this objective an experimental programme was undertaken to gain an understanding of epoxy curing behaviour by optimising different types of epoxy resin formulations. The optimisation process intended to develop an epoxy resin that is highly reactive and can be cured in thick sections (5 mm). The radiation delivered by side emitting optical fibres should provide deep photocuring with a minimum number of fibres, as shown schematically in Figure 2-6.

The experimental work to characterise cationic epoxy resin systems was carried out to determine:

1. Optimised formulations for different types of epoxy resin systems

2. The optical properties of the optimised resin systems before and during curing
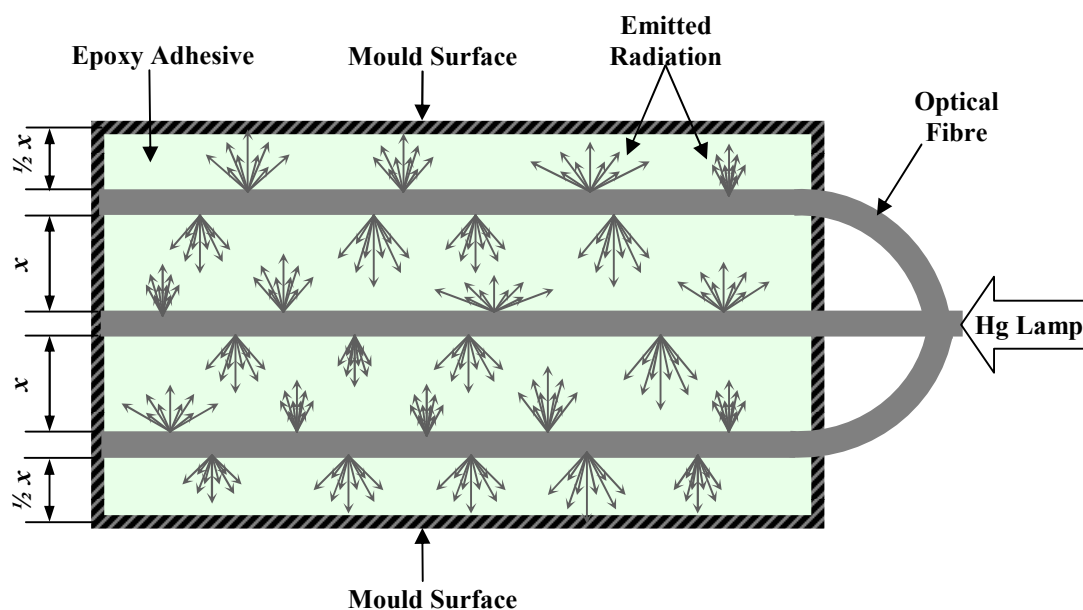
Figure 2-6. A plan view schematic illustration of an epoxy resin photocuring process in a closed mould using three embedded side emitting optical fibres spaced a distance x apart.

The characterisation of epoxy based resin formulations has been studied widely. Most of the literature found reported the photocuring of thin epoxy resin samples [11-12, 29], which differs from the photocuring of thick samples (5 mm) [2]. Thus, there is no hardness, viscosity or absorption data available for thick photopolymerised components from epoxy resins that can be directly compared with this work; however, references will be made to the literature at conditions found relevant.

Hardness of a polymer is determined initially by the structural parameters, such as chain flexibility and cross-link density. Generally, hardness will increase with the rigidity and cross-link density of the molecular network [26]. For this reason, hardness may also be involved in describing the curing behaviour during a photopolymerisation process of resin formulations, as has been reported by Decker et al. [74].

2.3. Optimisation of Epoxy Resin Formulations

2.3.1. Objective

This work is carried out to optimise different formulations of epoxy resin systems by studying the conversion rate efficiency of the resin systems, hardness, viscosity and the consumed energy for photocuring process.

As different epoxy resin formulations can produce varying curing speeds and final mechanical properties [11, 21, 28, 31, 34, 47, 52, 55], in this section, three different types of cationic epoxy resin systems were characterised. The first type was a pre-formulated epoxy resin, while the other two were formulated in-house. The formulations of the later two types of epoxy resins fall under two categories: resin systems made using epoxy bisphenol A/F and resin systems made using cycloaliphatic epoxy. The characterisation for all resin systems was carried out by casting thick samples (5 mm). An UVA and visible blue emitting flood lamp was used to produce all of the cured samples discussed within this section. The level of polymerisation was characterised by the hardness of samples.

The objective in using the flood lamp in the epoxy resin characterising process is that later in Chapter 5, the curing behaviour of epoxy resin will be investigated using optical fibres connected to another lamp (Hg lamp) which emits similar spectral output (UVA and visible blue) as the flood lamp.

2.3.2. Experimental Details

Materials

- **UV curable cationic epoxy resins commercially available, pre-formulated:** Two types of resins were purchased from the Dymax Corporation [22]; 4-20586 and 6-20353. These two resins were supplied as ready to use formulations with no details on the chemical composition ratios and they were used as supplied with no further modification.

- **Epoxy resins used for developing various resin systems:**

    o **Epoxy 1**: Bisphenol A/F, purchased from Dow Chemical Company [21]

    o **Epoxy 2**: Cycloaliphatic epoxy (UVR-6105), purchased from Univar Europe [75]

- **Photoinitiators:**

    o Triarylsulfonium hexafluorophosphate salts (UVI-6992), and

    o Triarylsulfonium hexafluoroantimonate salts (UVI-6976)

    Both were provided by the Dow Chemical Company [21]

- **Polyol additive:**

    o Oxetane OXT-101, provided by DKSH Great Britain Ltd [76],

- **Photosensitization additives:**

    o H-Nu 470 photoinitiator purchased from Spectra Group Ltd. [60], and

    o Anthracene photosensitizer purchased from Sigma-Aldrich Company Ltd. [77].

Experimental equipment and setup

1. A 400 Watt 2000-EC flood lamp (Dymax Corp. [22]) was used for the photocuring process. The lamp is equipped with a mercury arc metal halide D-type iron doped bulb that delivers 0.1 W/cm^2 output over the spectral range from 280 nm to 450 nm. Maximum efficiency occurs after seven minutes (warm-up). The generated temperature by irradiation on the top side of the casting mould was 73 °C (measured using a thermocouple after 7 mins).

2. Casting mould: Aluminium support and casting tool with top and bottom toughened glass covers to allow UV light penetration

3. Melinex polyester film (Made from polyester converters) [78]

4. Barcol Hardness tester for soft materials [79]

5. The viscosity measurements were conducted using a Brookfield digital viscometer from Brookfield Engineering Laboratories, INC (model: DV-II + Viscometer) [80].

Resin system preparation

The compositional ratio of epoxy and oxetane weight in a resin system is much greater than the photoinitiators, which causes a difficulty in using a single weighing scale to measure all compositions of a resin system as the resin system parts are added. Hence, the compositional ratios of the epoxy resin systems were weighed using two digital weighing scales. The compositional ratio of the photoinitiators was measured using the Sartorius scale (Sartorius HR60), which is designed for measuring light substances down to 0.0001 g resolution. The other weighing scale is designed for weighing heavier substances (AND EK-1200i), and thus, was used for measuring the compositional ratios of epoxy resins and

oxetane additive. It is designed to measure to 0.1 g resolution. All epoxy resin formulations made in house, were mixed using the pneumatic mixing device with an aluminium stirring tool. All of the resin formulations were mixed in a polypropylene cup. See Appendix C-1 'C1' for more details of the equipments used for preparing different epoxy formulations.

Mould preparation and experimental setup

The curing behaviour of epoxy resin was studied by curing thick samples. A casting mould consisting of an aluminium form with top and bottom toughened glass covers was designed. The toughened glass covers, with a thickness of 7 mm, allowed radiation penetration into the resin. The mould was used for casting 150 x 110 x 5 mm (long, wide and thick, respectively) samples for studying the curing behaviour of the different resin systems.

The mould was similarly prepared for all epoxy resins. First, the mould was cleaned with acetone in order to remove moisture or dirt inclusions which could affect the curing process. Next, all of the mould parts were coated with five layers of mould release agent (PMR-90 [81]) so that the cast epoxy did not stick to the mould. A Melinex polyester film (Mylar) was then placed on the surface of the bottom toughened glass cover and the casting tool was placed on top of it. The resin was poured into the tool and covered with another Melinex polyester film. Finally, the mould parts were assembled together using four clamps each at a corner. A schematic illustration of the mould is shown in Figure 2-7. Figure 2-8 shows the experimental setup of all equipment used for the curing process.
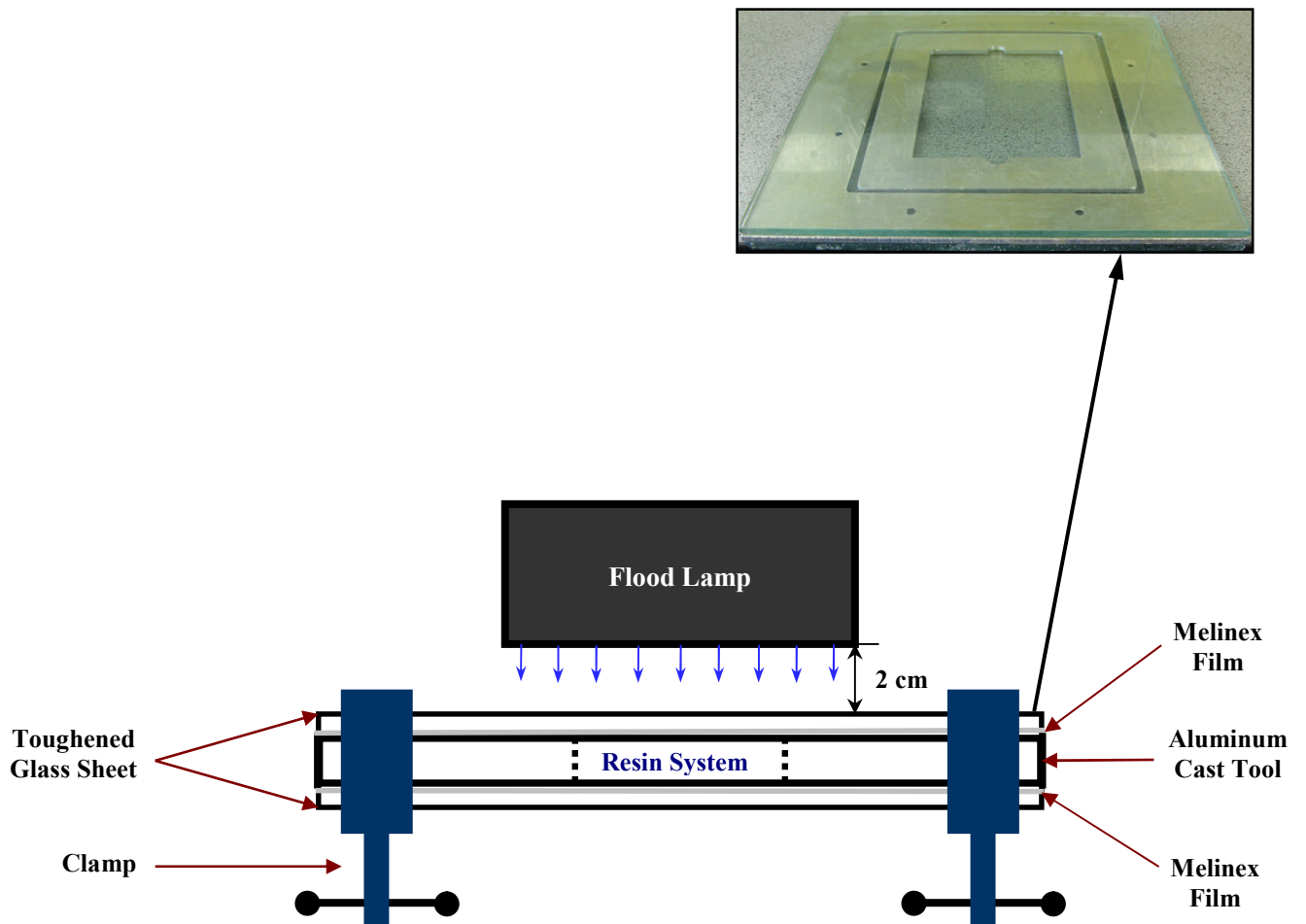
Figure 2-7. Schematic diagram showing the mould parts.
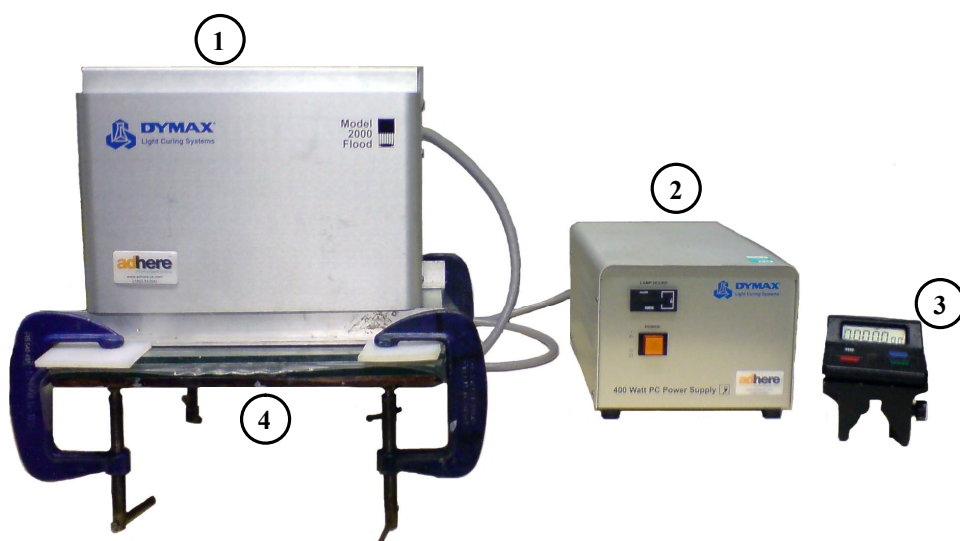
Figure 2-8. Equipment setup for epoxy resin systems characterisation:

1. Flood lamp bulb and reflector case

2. Flood lamp power supply

3. Stop watch for measuring curing duration

4. Casting mould

Resin curing test

Hardness testing was done to measure the relative degree of cure of the photocured samples [74, 82], as been described earlier in Section 2.2.10. The hardness distribution was measured across the top and bottom surfaces of the photocured samples. Hardness values of the top and bottom surfaces should be similar to avoid residual stresses that can cause problems such as part distortion or peeling of an adhesive. The hardness measurements were conducted according to BS 2782-10 [83] using the Barcol hardness tester, shown in Figure 2-9.

Figure 2-9. Barcol hardness tester.

Viscosity measurements of resin systems

Viscosity measurements were conducted for the optimised resin systems. The viscosities were measured using a Brookfield digital viscometer (Figure 2-10) from Brookfield Engineering Laboratories, INC (model: DV-II + Viscometer) [80]. This viscometer measures the viscosity using a rotating spindle (S61) immersed in the resin, as shown in Figure 2-10. The liquid resin was added to a beaker (Figure 2-10) until the body of the spindle was covered as required for accurate viscosity measurements.
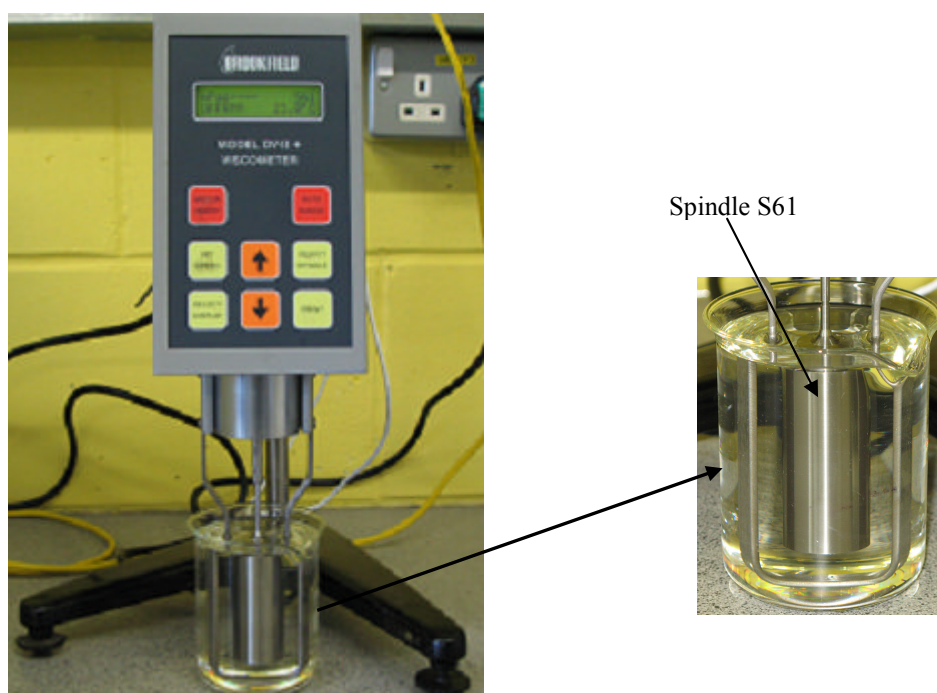
Figure 2-10. Brookfield digital viscometer with spindle S61 immersed in epoxy resin.

2.3.3. Results and Discussion

The cationic epoxy resins from Dymax were used as received with no addition of any other compound. The characterisation process of bisphenol A/F and cycloaliphatic epoxy (UVR-6105) consisted of two phases. Firstly, finding the most efficient compositional ratio of each photoinitiator (UVI-6992 & UVI-6976) with each epoxy resin by producing different mixed ratio samples using the casting tool (150 x 110 x 5 mm). Secondly, adding an oxetane (OXT-101) to the optimised resin system compositions to improve their reactivity.

Initially, curing epoxy samples within the mould was unsuccessful, especially from the lower side of the sample casting. Hence, Melinex polyester films were used within the casting mould, as described earlier in Figure 2-7. Epoxy samples were cured using two Melinex polyester films; one film on top of the bottom toughened glass sheet and another one beneath the top toughened glass sheet (Figure 2-7). The Melinex polyester films provided the samples with a good surface finish compared with the glass covered castings. In addition, using Melinex polyester films enhanced the curing period of all the resin systems used in this work, because all of the samples made without using the Melinex polyester films reacted with the mould release agent, slowing the curing process. Such behaviour of the curing process was reported by Dow Chemical Company [21], which suggested that the photoinitiator within the resin formulation was neutralized from the sides facing the mould release agent. Finally, the degree of cure of each resin system was tested with the Barcol hardness tester.

The degree of cure of all epoxy formulations was determined by measuring the hardness development within the castings as a result of radiation exposure at progressive exposures intervals. This process was repeated until the castings exhibited constant hardness values which indicated the end of the polymerisation. Hence, the cure time was established. For instance, the pre-formulated epoxy resin's degree of cure was found by irradiating for four intervals of 20 minutes. The hardness measurements were conducted after each interval. The hardness values of these formulations were found to be constant after the fourth irradiation

interval. Hence, the curing time at the fourth 20 minute interval was reduced to determine when the castings started exhibiting constant hardness by splitting this interval into another four intervals of 5 minutes. Thus, it was found that these formulations cured in 65 minutes. A similar process was also conducted for the in-house prepared formulations with different exposure periods due to the observed high conversion characteristics of these formulations, as will be discussed later in this Chapter.

Finally, for the purpose of studying the variability of the hardness of all the formulations used in this work, the measurements were conducted on three castings from each formulation; pre-formulated epoxy resins, in-house optimised formulations from bisphenol A/F and cycloaliphatic epoxides.

2.3.3.1. Dymax 4-20586 and 6-20353 Pre-formulated Epoxy Resins

Both epoxy resins were cured with the same curing conditions. Each was exposed to UV radiation for 65 mins and left for 90 mins so that the mould cooled. Cooling was necessary because taking the cured epoxy sample immediately out of the mould resulted in the sample bending. Both epoxies were found to be fully cured, and with a good surface finish on all edges, however, both epoxies had a slightly non uniform surface due to the resin shrinkage.

In order to study the curing rate of the samples, the hardness of the top and bottom surfaces were measured over the same areas, as shown in Figure 2-11. The hardness measurements of the top and bottom surfaces of three castings from formulations 4-20586 and 6-20353 did not exhibit repeatable hardness values when measured from the same location. The hardness values indicated fluctuation at each measured location (Figure 2-11). An example of that can be observed from the hardness values of the top and bottom surfaces of formulation 4-20586 in Figures 2-12 and 2-13. The figures also show that the bottom surfaces exhibit higher fluctuation in hardness than the top surfaces. Similar behaviour was also observed for the in-house prepared formulations based on bisphenol A/F.
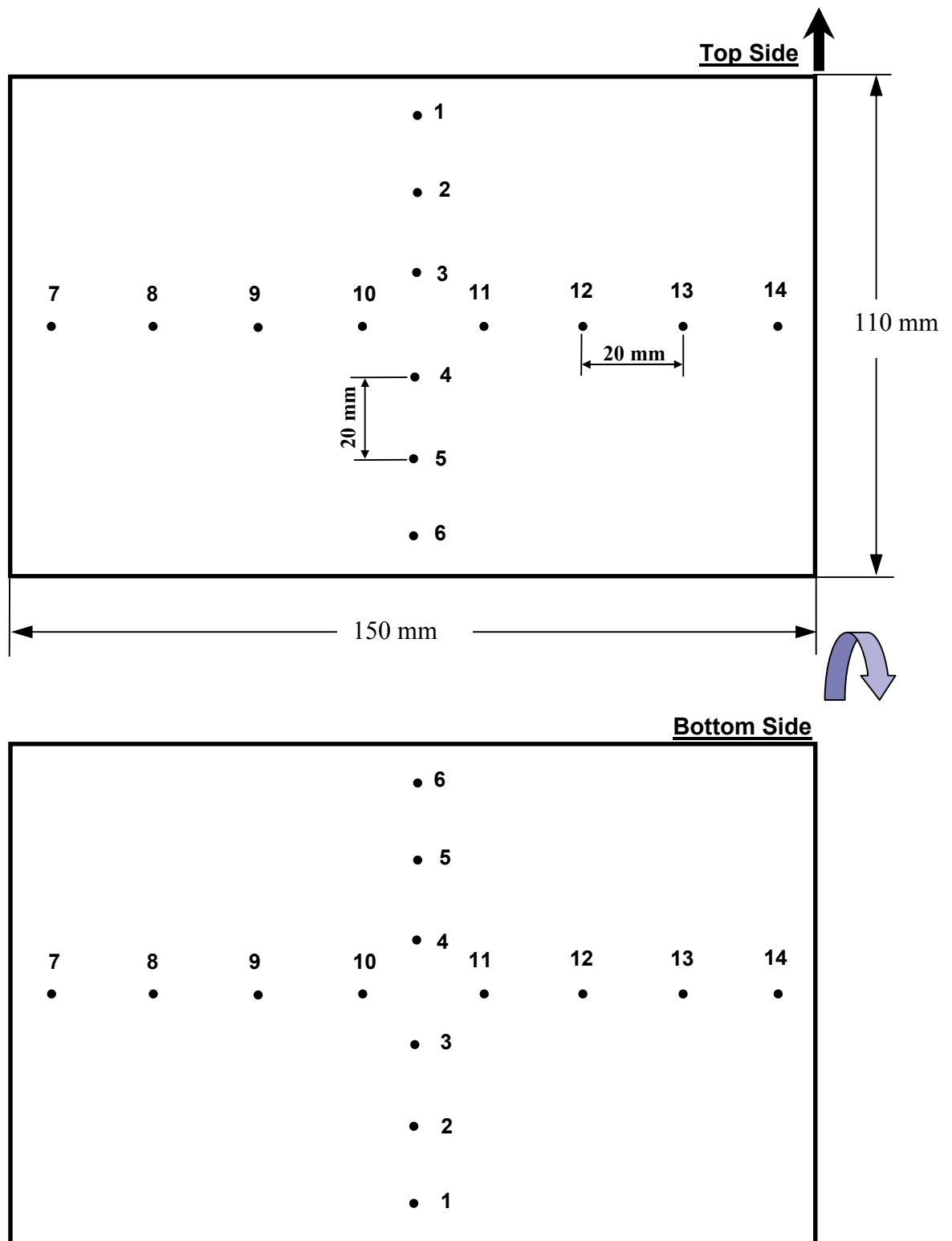
Figure 2-11. Schematic illustration of hardness measurements from both sides of each cured sample. The hardness was measured at the numbered locations and distances. All castings were of 5 mm thick, 150 mm long and 110 mm wide. An average of four measurements was taken from each measured location (BS 2782-10 [83]). Not to scale.

Top Surface: ◆ Casting 1, ■ Casting 2, ▲ Casting 3.
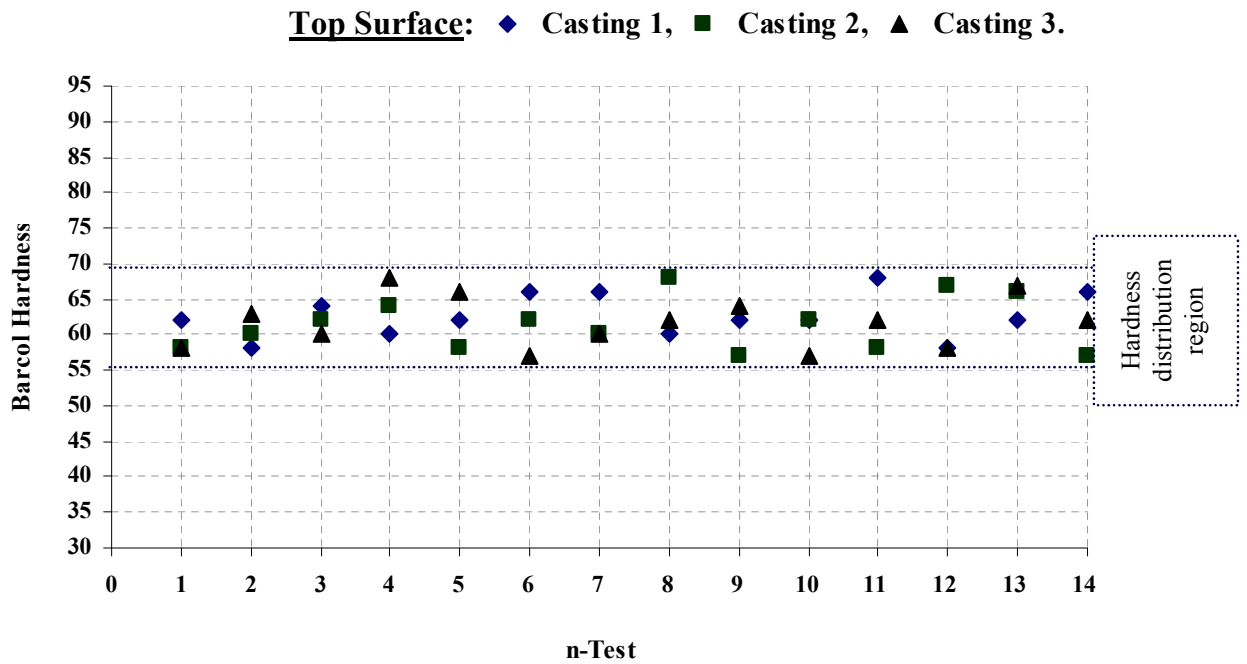
Figure 2-12. Graph of Barcol hardness versus number of test points from the top side of the three castings from resin system 4-20586. The specimens were cured in 65 mins using the flood lamp (0.1 W/cm^2).

Bottom Surface: ■ Casting 1, ● Casting 2, ◆ Casting 3.
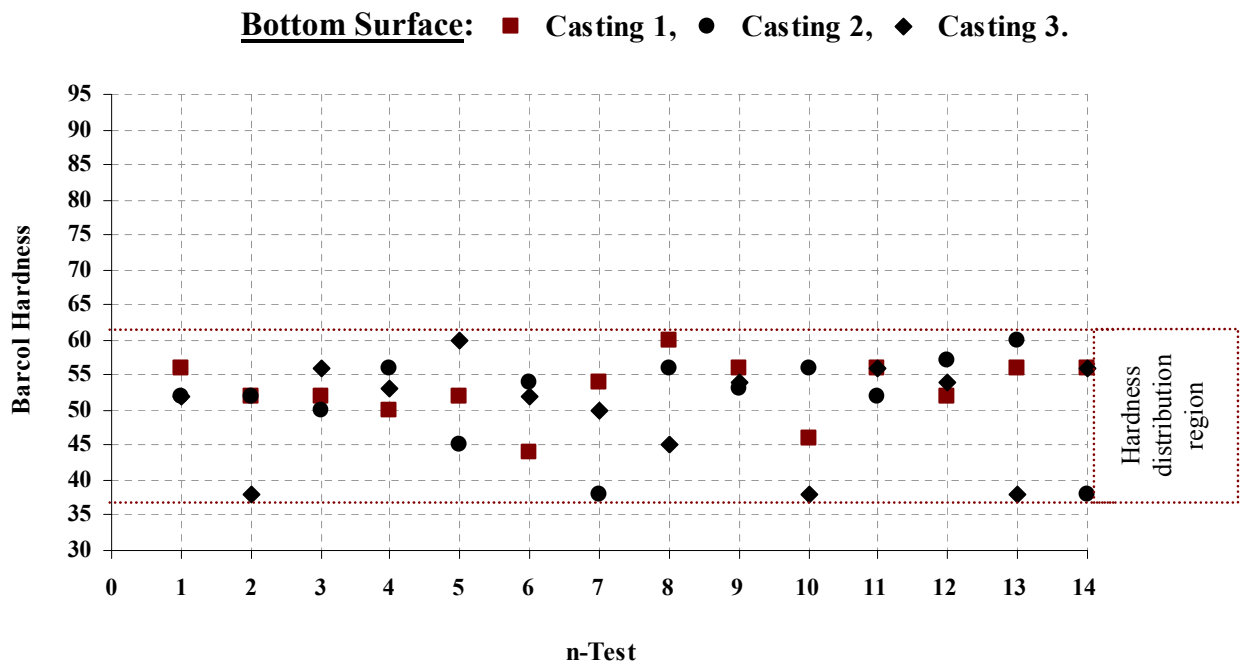
Figure 2-13. Graph of Barcol hardness versus number of test points from the bottom side of the three castings form resin system 4-20586. The specimens were cured in 65 mins using the flood lamp (0.1 W/cm^2).

The results of formulations 4-20586 and 6-20353 are plotted in Figures 2-14 and 2-15 and tabulated in Table 2-4. The sample made from 6-20353 epoxy showed higher hardness and less hardness variation across the casting (Figures 2-14 & 2-15) than the one made from 4-20586, which is expected to be due to its chemical formulation as the curing conditions were kept constant for both resins. The bottom surface of the casting from resin 4-20586 exhibited irregularly distributed, lower hardness than the top surface, as can be observed from two fluctuating readings in Figure 2-14. The hardness distribution of sample 6-20353 was more uniform through the thickness of the sample than sample 4-20586 as can also be seen from the standard deviation and mean values from Table 2-4. However, the resin formulation 6-20353 is twice the cost of the 4-20586 resin.
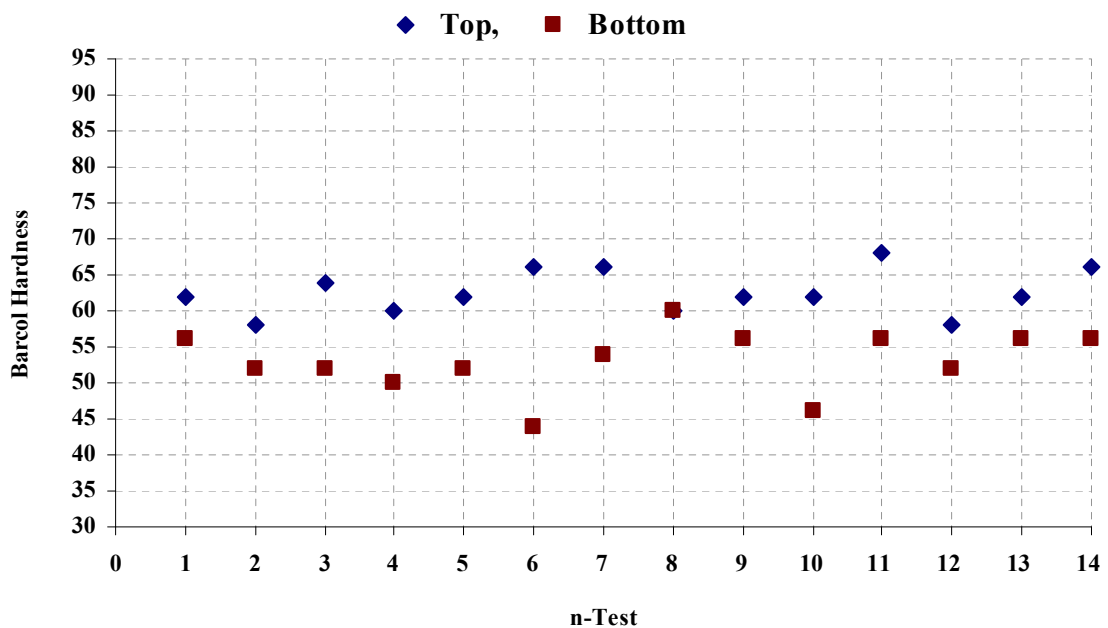
Figure 2-14. Graph of Barcol hardness versus number of test points from each side of the casting for resin system 4-20586. The specimen was cured in 65 mins using the flood lamp (0.1 W/cm^2).
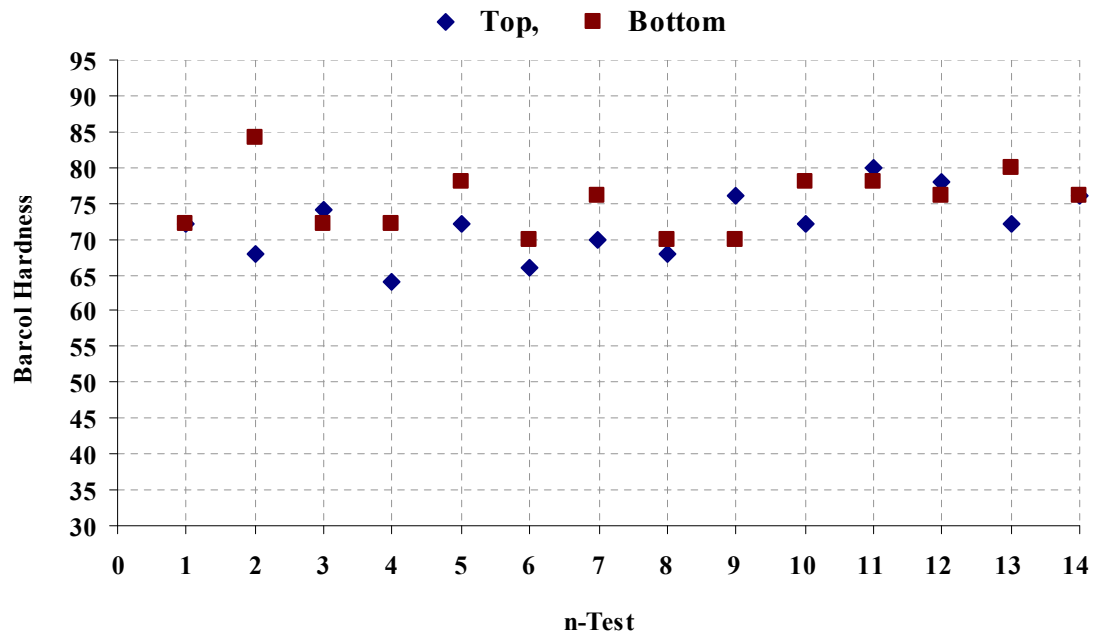
Figure 2-15. Graph of Barcol hardness versus number of test points from each side of the casting for resin system 6-20353. The specimen was cured in 65 mins using the flood lamp (0.1 W/cm^2).

Table 2-4. Barcol hardness test results for castings from epoxy resins 4-20586 and 6-20353

	Sample 4-20586		Sample 6-20353	
	Top Surface	**Bottom Surface**	**Top Surface**	**Bottom Surface**
Mean	63	52	72	75
SD	3.1	4.3	4.7	4.3

2.3.3.2. Resin Systems Based on Epoxy Bisphenol A/F

Bisphenol A/F was used due to its low viscosity compared to Bisphenol A which should result in efficient curing [11]. No work was reported in the literature using this type of epoxy. However, the Dow Chemical Company [21] has such a product that can be used for photocuring of coatings.

Bisphenol A/F with photoinitiators UVI-6992 and UVI-6976

Using a varied compositional ratio of triarylsulfonium hexafluoroantimonate salts (UVI-6976) photoinitiator with bisphenol A/F resulted in an unexpected curing behaviour. The samples were very brittle. Triarylsulfonium hexafluorophosphate salts (UVI-6992) photoinitiator resulted in a less brittle curing result than photoinitiator UVI-6976.

The compositional ratio characterisation of triarylsulfonium hexafluorophosphate salts (UVI-6992) photoinitiator with bisphenol A/F was carried out by varying the compositional ratio of the photoinitiator, as shown in Table 2-5. The curing time for all of the resin systems was 20 minutes. The mould setup was similar for all the mixed resin systems (Section 2.3.2).

Table 2-5. Experimental results of curing 100 PHR (parts per hundred resin) of bisphenol A/F with varied ratios of photoinitiator UVI-6992

Formulation	Photoinitiator ratio (PHR)	Hardness testing ability from top and bottom surfaces	Cured sample colour
1	0.5	unsuccessful, very soft surfaces	Light yellow
2	1.0	Hardness can be tested	Light Yellow
3	2.0	Hardness can be tested	Yellow
4	3.0	unsuccessful , Soft lower surface	Dark yellow
5	4.0	unsuccessful , Soft lower surface	Dark yellow
6	10.0	unsuccessful , lower surface is not cured	Very dark yellow

It was found that the higher the photoinitiator ratio the darker the casting, especially from the top surface which is exposed directly to the lamp radiation (Table 2-5 and Figure 2-16). The casting in Figure 2-16 exhibited darker colour at the top surface facing the flood lamp than the bottom surface. This indicated that, the layer facing the lamp degraded as a result of excess irradiation absorption, which agrees with Narayanan et al. [2]. Bisphenol A/F with 1 PHR UVI-6992 had the best curing behaviour. The casting exhibited a light yellow colour. It was fully cured with a slight hump in the upper and lower sides as well as with air bubbles (Figure 2-17). The air bubbles were generated during the epoxy and photoinitiator mixing process which could be improved by degassing the resin after mixing. The hump was expected to form as a result of shrinkage, and developed after removing from the mould.
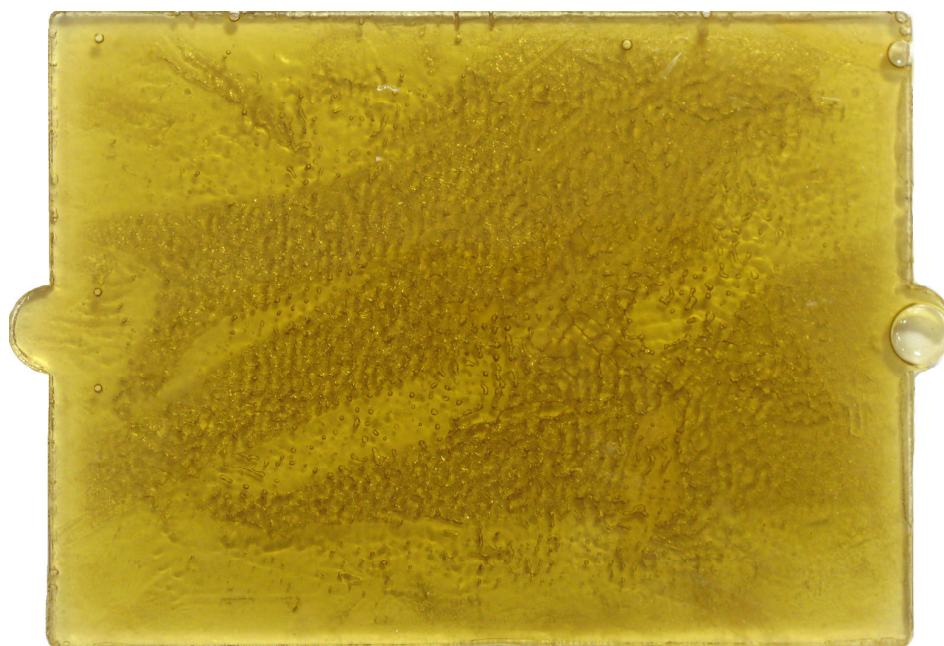
Figure 2-16. Casting of 100 PHR (parts per hundred resin) bisphenol A/F with 10 PHR photoinitiator UVI-6992. The dark yellow colour is due to the high photoinitiator compositional ratio. The specimen was cured in 20 mins using the flood lamp (0.1 W/cm^2).
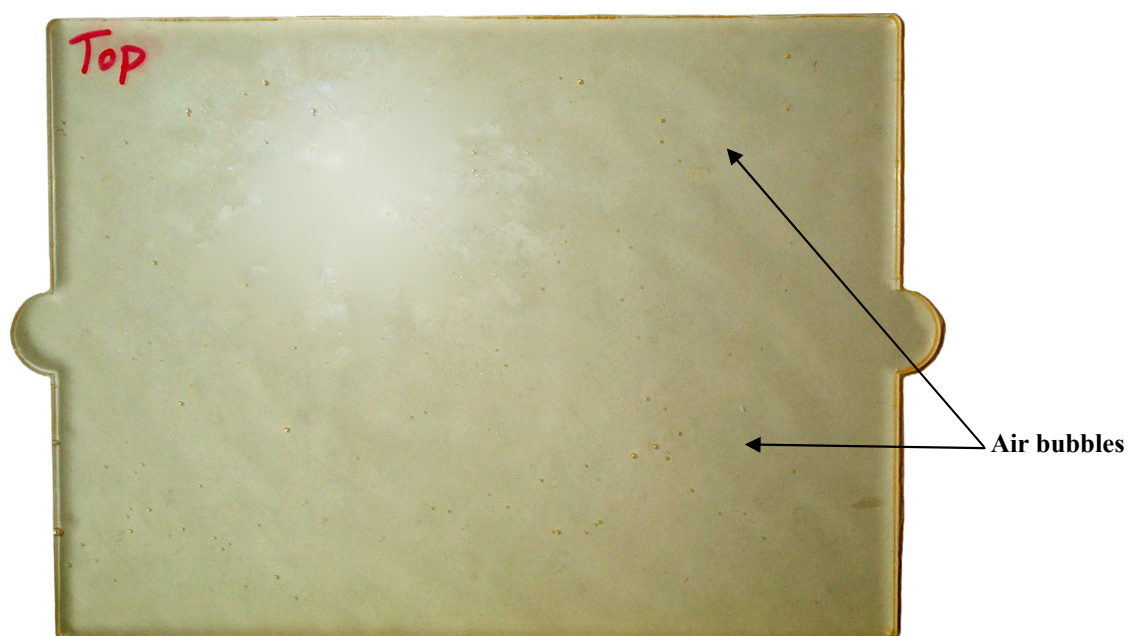
Figure 2-17. Casting of bisphenol A/F (100 PHR) with photoinitiator UVI-6992 (1 PHR). The specimen was cured in 20 mins using the flood lamp (0.1 W/cm^2).

Further tests of hardness were done to understand the degree of curing through the sample. The hardness of the top and lower surfaces was measured using a Barcol Hardness tester and the results are shown in Figure 2-18 and Table 2-6.
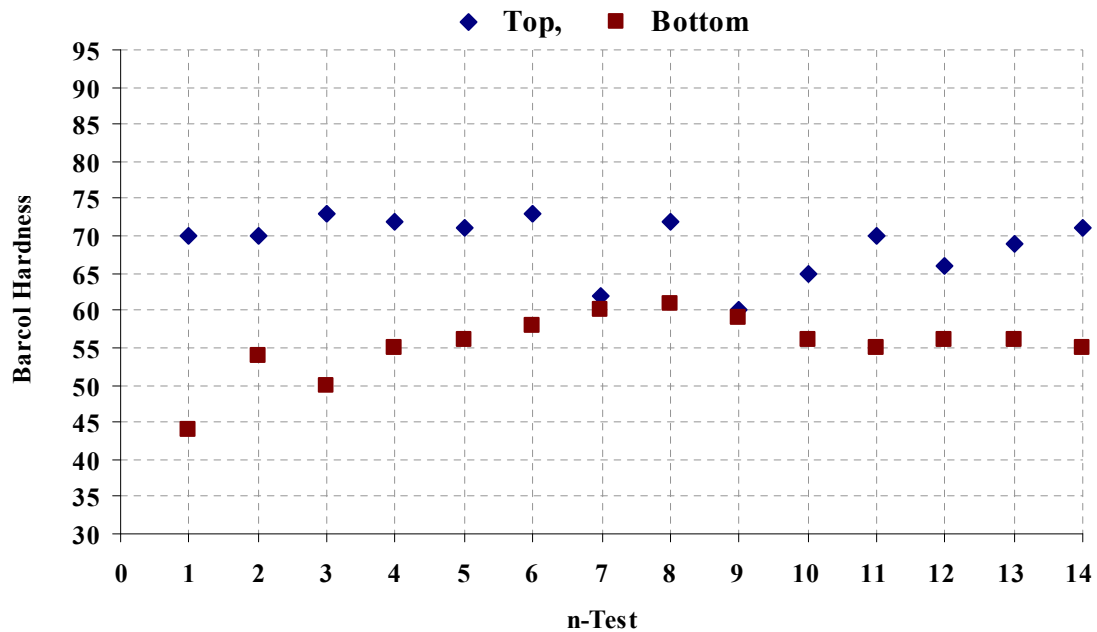
Figure 2-18. Graph of Barcol hardness versus the number of test points from each side of the casting for the resin system: Bisphenol A/F (100 PHR) with photoinitiator UVI-6992 (1 PHR). The specimen was cured in 20 mins using the flood lamp (0.1 W/cm^2).

The results in Table 2-6 show that the top surface has a higher hardness. Standard deviation results illustrate that the hardness distribution values of the top surface are similar to the bottom surface. However, the curing time and variation in hardness between the two surfaces of the casting suggests further improvements could be achieved using additives (monomers) as suggested by Decker et al. [11, 34].

Table 2-6. Barcol hardness test results of the casting from resin formulation of bisphenol A/F (100 PHR) with photoinitiator UVI-6992 (1 PHR). The specimen was cured in 20 mins using the flood lamp (0.1 W/cm^2)

	Top Surface	Bottom Surface
Mean	69	55
SD	**4.1**	**4.3**

Photocuring by adding Oxetane (OXT-101)

Oxetane (OXT-101) was added to the best curing resin system of bisphenol A/F with 1 PHR UVI-6992 photoinitiator, as discussed above. In order to study the effect of the Oxetane, castings with a number of different oxetane ratios were produced. Such additives enhance the reactivity of the epoxy monomers leading to shorter curing times and also improve the toughness [11]. Three different ratios of oxetane were added to epoxy with 1 PHR UVI-6992 and cured for a period of 20 minutes, repeating the procedure done for the epoxy without the additive (Table 2-7).

Table 2-7. Experimental results of curing 100 PHR (parts per hundred resin) of bisphenol A/F with varied ratios of both photoinitiator UVI-6992 and Oxetane OXT-101.

Formulation	Photoinitiator ratio (PHR)	Oxetane ratio (PHR)	Curing Time (minutes)	Hardness measuring ability (Yes: hard, No: soft, No*: very soft)	
				Top Surface	Bottom Surface
1	1.0	5	10	Yes	No
2	1.0	10	20	No	Yes
3	1.0	15	10	No*	No*
4	1.0	15	20	No	Yes
5	1.0	25	20	No	No
6	1.5	10	10	No	No
7	2.0	10	10	**Yes**	**Yes**
8	2.5	15	10	**Yes**	**Yes**
9	3.0	10	10	**Yes**	**Yes**
10	3.5	15	10	**Yes**	**Yes**

The top surfaces hardness of samples with 10, 15 and 25 PHR oxetane were not found to be measurable and behaved like rubber (Table 2-7). The percentage of oxetane was lowered to 5 PHR and the resin mixture was cured for 10 minutes to find out if whether the small amount of oxetane influence the curing behaviour. This resulted in a soft lower surface. To improve the curing behaviour, the addition of different photoinitiator ratios was done. It was found that adding a ratio from 2 PHR to 3 PHR of UVI-6992 photoinitiator with a ratio of oxetane from 10 PHR to 15 PHR into bisphenol A/F resulted in a curing rate faster than the one found earlier with the mixture of bisphenol A/F and 1 PHR UVI-6992 (Table 2-7). The resin systems with the oxetane cured in 10 minutes whereas the one without the additive cured in 20 minutes.

A hardness test was conducted for the casting made from the optimised resin system formulation that consisted of bisphenol A/F with 2.5 PHR UVI-6992 and 15 PHR oxetane. The hardness on the top surface was also found to be greater than the bottom surface, as shown in Figure 2-19 and Table 2-8, compared to the casting without oxetane (Figure 2-18 and Table 2-6). However, the oxetane improved the hardness of the casting comparing to the casting without oxetane. The standard deviation results (Table 2-8) also imply more uniform hardness distribution in the top and bottom surfaces of the casting.
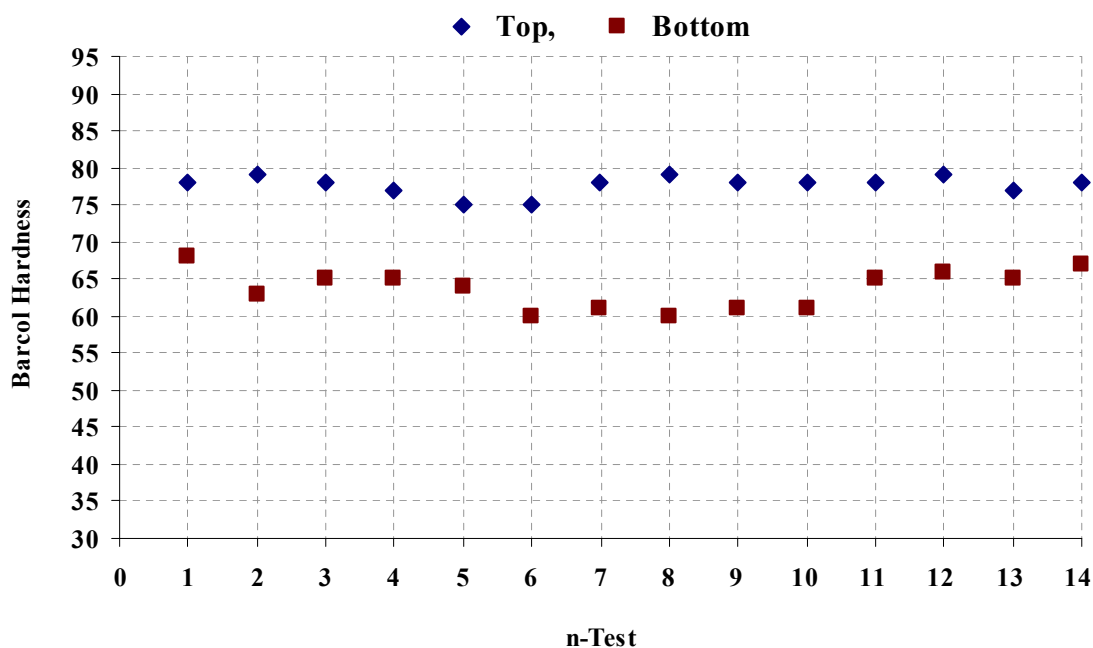
Figure 2-19. Graph of Barcol hardness versus number of test points from each side of the casting for the resin system: Bisphenol A/F (100 PHR) with photoinitiator UVI-6992 (2.5 PHR) and oxetane OXT-101 (15 PHR). The specimen was cured in 10 mins using the flood lamp (0.1 W/cm^2).

Table 2-8. Barcol hardness test results of the casting from resin formulation of bisphenol A/F (100 PHR) with photoinitiator UVI-6992 (2.5 PHR) and oxetane OXT-101 (15 PHR). The specimen was cured in 10 mins using the flood lamp (0.1 W/cm^2)

	Top Surface	Bottom Surface
Mean	78	64
SD	**1.3**	**2.6**

2.3.3.3. Resin Systems Based on Cycloaliphatic Epoxy

Cyracure UVR-6105 cycloaliphatic epoxide resin was selected based on its high cationic reactivity as well as low viscosity compared to the other commercial cycloaliphatic epoxide resins (Appendix C-1 'C2') [21]. This difunctional cycloaliphatic epoxy resin also has been of interest in many other UV curing studies [36-38, 58].

Cyracure UVR-6105 with Photoinitiators UVI-6992 and UVI-6976

Triarylsulfonium hexafluorophosphate salts (UVI-6992) and triarylsulfonium hexafluoroantimonate salts (UVI-6976) photoinitiators were both added to the Cyracure UVR-6105 cycloaliphatic epoxide resin. The resin systems samples with various compositional ratios of photoinitiator were cured using the casting mould (Figure 2-7). The polymerisation of Cyracure UVR-6105 with UVI-6992 photoinitiator ratios less than 2 PHR cured after 20 minutes of radiation exposure, while with UVI-6992 photoinitiator ratios from 2.5 PHR to 4 PHR the samples cured within 10 minutes. Further addition of UVI-6992 photoinitiator inhibited cure of the bottom side of the samples and the top layer of the samples were dark yellow as a result of high photoinitiator concentration. This behaviour also has been reported in the literature from the Dow Chemical Company [21]. It has been

reported [21] that UVI-6992 photoinitiator is not designed for producing thick samples using cycloaliphatic epoxy (Cyracure UVR-6105).

Unlike photoinitiator UVI-6992, photoinitiator UVI-6976 resulted in a more stable curing behaviour with Cyracure UVR-6105. The characterisation process was carried out by varying the ratio of the photoinitiator. The experimental results of the resin characterisation are outlined in Table 2-9.

Table 2-9. Experimental results of curing 100 PHR (parts per hundred resin) of cycloaliphatic epoxy with varied ratios of photoinitiator UVI-6976

Formulation	Photoinitiator ratio (PHR)	Curing time (minutes)	Hardness testing ability from top and bottom surfaces	Cured sample colour
1	0.26	10	Hardness can be tested	Light yellow
2	0.37	6	Hardness can be tested	Light yellow
3	0. 60	2	Hardness can be tested	Yellow
4	1.10	2	unsuccessful , Soft lower surface	Yellow
5	2.10	2	unsuccessful , Soft lower surface	Dark yellow
6	3.20	2	unsuccessful , Soft lower surface	Dark yellow
7	4.20	2	unsuccessful , lower surface is not cured	Dark yellow
8	10.60	2	unsuccessful , lower surface is not cured	Very dark yellow

The polymerisation of Cyracure UVR-6105 occurred more rapidly with photoinitiator UVI-6976 compared to UVI-6992. Cyracure UVR-6105 cured five times faster with UVI-6976 than with UVI-6992. This rapid curing also indicates high resin reactivity. Cyracure UVR-

6105 with 0.6 PHR UVI-6976 showed the best curing behaviour. The casting exhibited a yellow colour. The castings of the samples with a UVI-6976 ratio from 2PHR to 4 PHR were dark yellow with a soft lower surface. Additional ratios of UVI-6976 resulted in a very dark yellow casting and the lower side of the casting did not cure, Table 2-9. Thus, Table 2-9 shows that low concentration of photoinitiator will result in low absorption and long curing time. High concentration of photoinitiator will result in high absorption and limited depth of radiation penetration. In addition, referring to the electromagnetic spectrum in Figure 2-1, the more intense yellow colour the higher absorption of blue radiation.

The hardness test results of the optimised resin system with 0.6 PHR UVI-6976 showed very close hardness distribution values on both the top and bottom surfaces (Figure 2-20), indicating a uniform curing rate through the sample. This can also be observed from the mean and standard deviation values in Table 2-10.
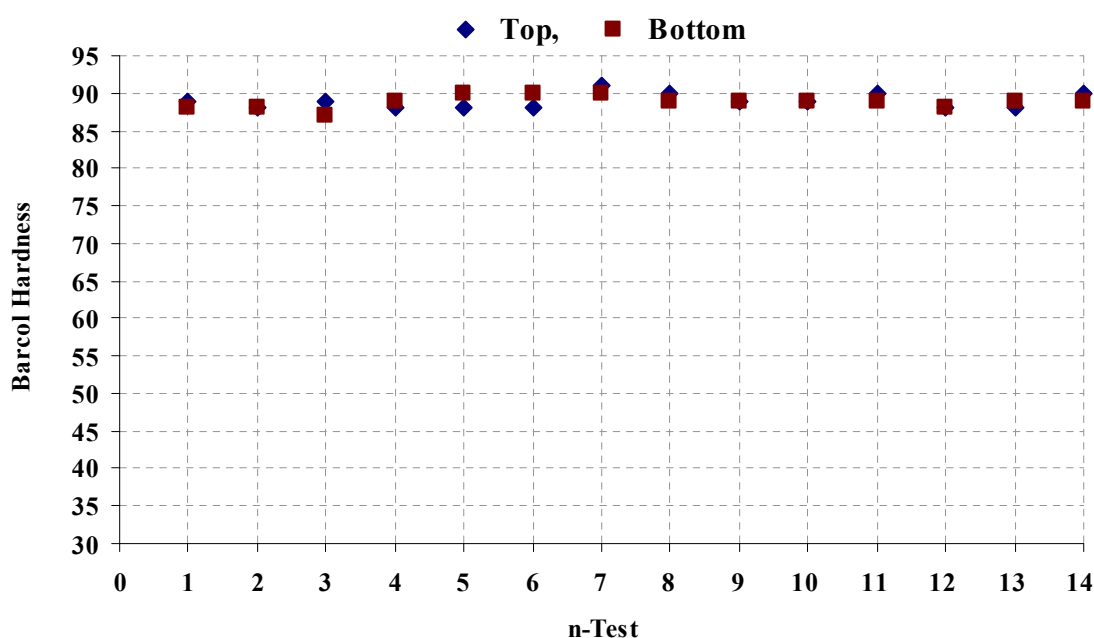
Figure 2-20. Graph of Barcol hardness versus number of test points from each side of the casting for resin system: Cycloaliphatic epoxy (100 PHR) with photoinitiator UVI-6976 (0.6 PHR). The specimen was cured in 2 mins using the flood lamp (0.1 W/cm^2).

Table 2-10. Barcol hardness test results of the casting from a resin formulation of cycloaliphatic epoxy (100 PHR) with photoinitiator UVI-6976 (0.6 PHR). The specimen was cured in 2 mins using the flood lamp (0.1 W/cm^2)

	Top Surface	Bottom Surface
Mean	89	89
SD	**1.0**	**0.9**

Photocuring by adding Oxetane (OXT-101)

Oxetane (OXT-101) was added to the optimised resin system of cycloaliphatic epoxy Cyracure UVR-6105 (100PHR) with photoinitiator UVI-6976 (0.6 PHR). The oxetane ratios were varied from 1.1 PHR to 5.3 PHR as shown in Table 2-11. All of the formulations cured. However, ratios greater than 2.6 PHR required longer radiation exposure, explained by the reduction in the reactivity of the resin systems at those ratios. Addition of photoinitiator UVI-6976 at ratios greater than 0.6 PHR with oxetane was avoided because the resulting samples did not exhibit uniform curing between the top and bottom surfaces of the casting.

Table 2-11. Experimental results of curing 100 PHR (parts per hundred resin) of cycloaliphatic epoxy with varied ratios of both photoinitiator UVI-6976 and Oxetane OXT-101

Formulation	Photoinitiator ratio (PHR)	Oxetane ratio (PHR)	Curing Time* (minutes)	Hardness measuring ability (Yes: hard, No: soft, No*: very soft)	
				Top Surface	**Bottom Surface**
1	0.6	1.1	2	Yes	Yes
2	0.6	1.6	2	Yes	Yes
3	0.6	2.1	2	Yes	Yes
4	0.6	2.6	2	Yes	Yes
5	0.6	3.2	2 ½	Yes	Yes
6	0.6	3.7	2 ½	Yes	Yes
7	0.6	4.2	2 ½	Yes	Yes
8	0.6	4.8	3	Yes	Yes
9	0.6	5.3	3	Yes	Yes

Note: The curing time for each casting was found based on the change in the hardness at the top and bottom surface of the castings at curing intervals 1½, 2, 2 ½, 3 minutes. Hence, the curing time was selected when the hardness was found constant.

As oxetane improves the resin system reactivity and the toughness [11], the optimised resin system with 2.6 PHR of oxetane was selected, Table 2-11. This resin was selected based on its fast curing speed with the highest oxetane content. The castings made with and without oxetane had irregular top and bottom surfaces, expected to be due to shrinkage, as shown in Figure 2-21.
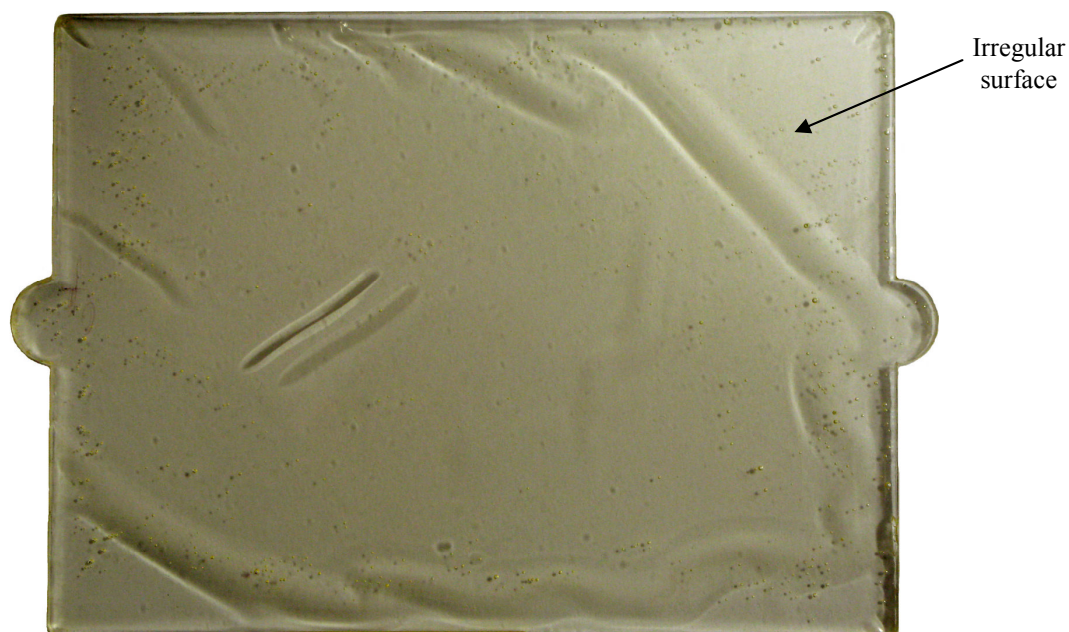
Figure 2-21. Casting of cycloaliphatic epoxy (100 PHR) with photoinitiator UVI-6976 (0.6 PHR) and oxetane OXT-101 (2.6 PHR), showing irregular surfaces. The specimen was cured in 2 mins using the flood lamp (0.1 W/cm^2).

The surface irregularities in the final casting were improved when 750 μm thick Melinex polyester films [78] were used within the mould setup. Further hardness test results for the optimised resin system with 2.6 PHR oxetane showed very similar results (Figure 2-22 & Table 2-12) as for the optimised resin system which did not include oxetane (Figure 2-20 & Table 2-10).
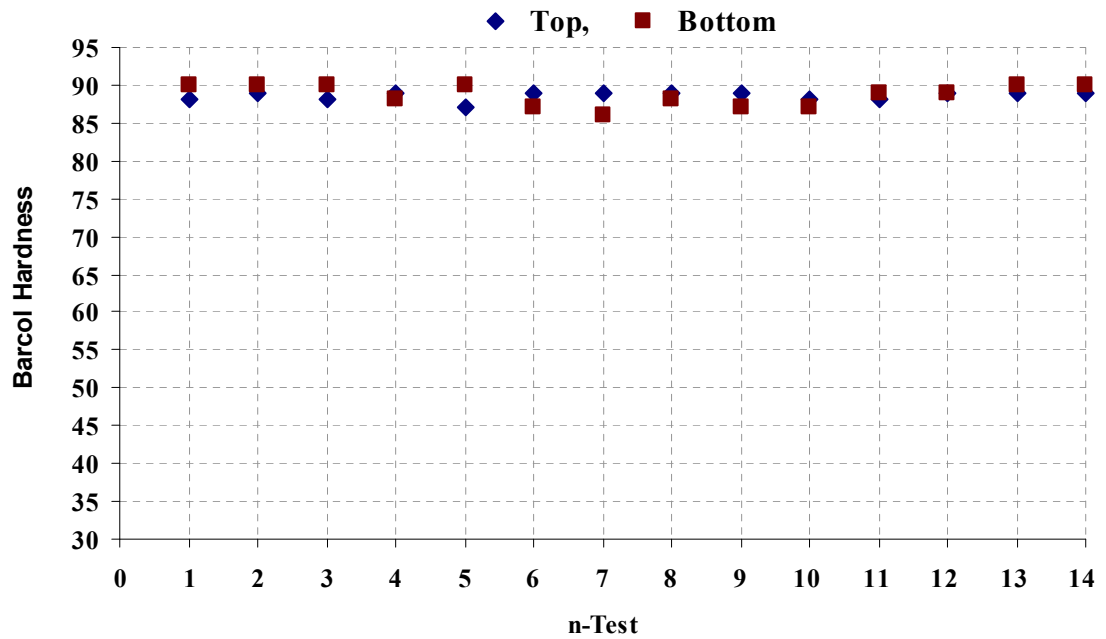
Figure 2-22. Graph of Barcol hardness versus number of test points from each side of the casting for resin system: Cycloaliphatic epoxy (100 PHR) with photoinitiator UVI-6976 (0.6 PHR) and oxetane OXT-101 (2.6 PHR). The specimen was cured in 2 mins using the flood lamp (0.1 W/cm^2).

Table 2-12. Barcol hardness test results of the casting from resin formulation of cycloaliphatic epoxy (100 PHR) with photoinitiator UVI-6976 (0.6 PHR) and oxetane OXT-101 (2.6 PHR). The specimen was cured in 2 mins using the flood lamp (0.1 W/cm^2)

	Top Surface	Bottom Surface
Mean	89	89
SD	**0.7**	**1.4**

Photocuring by Adding Photosensitization Additives

According to the literature, cycloaliphatic epoxy photocuring can be improved further when a photosensitizer is added to the resin composition [13, 29, 37-43]. Photosensitizer additives either enhance or shift the absorption spectrum towards the visible spectrum, as discussed in Section 2.2.5.

Two different types of photosensitizer were used in this study as shown below:

1. H-Nu 470 photoinitiator [60].

2. Anthracene photosensitizer [76].

The H-Nu 470 photoinitiator is an octyloxphenyl-phenyl iodonium hexafluoroantimonate photoinitiator (OPPI) and H-Nu 470 photosensitizer. The H-Nu 470 photosensitizer is only recommended by Spectra Group Ltd. [60] to be used with the OPPI photoinitiator mixed in cycloaliphatic epoxides, because it cannot sensitize sulfonium salt photoinitiators and results in poor curing behaviour with bisphenol A epoxide based formulations.

The cycloaliphatic epoxy (UVR-6105) based resin system was prepared by using the H-Nu 470 photoinitiator, which consisted of 2.5 PHR octyloxphenyl-phenyl iodonium hexafluoroantimonate photoinitiator (OPPI) and 0.1 PHR H-Nu 470 photosensitizer. The experimental work using the H-Nu 470 photoinitiator resulted in efficient curing of thin film samples of less than 1 mm thickness. However, poor curing was observed as the thickness of the resin samples increased in sequence from 1 mm to 5 mm. The poor curing of the thick samples occurred as a result of poor transmission of the emitted irradiation from the flood lamp into the lower side of the sample. The orange colour (Figure 2-23a) of the resin system before and after curing of the top side of the sample could be one reason for the high absorption and blocking the radiation to get into the lower side of the sample. Curing cycloaliphatic epoxy (UVR-6105) using the H-Nu 470 photoinitiator did not improve even when the ratio of the H-Nu 470 photosensitizer was varied.

For the anthracene photosensitizer, the recommended ratio of photosensitizer in a resin system is 10 % of the total weight of the photoinitiator ratio in the resin system [41-43]. Hence, 0.1 PHR of anthracene photosensitizer was added to the above optimised resin system, which consisted of cycloaliphatic epoxy (UVR-6105) with 0.6 PHR of UVI-6976 photoinitiator and 2.6 PHR of oxetane. As the photosensitizer comes in a powder form, the mixed ratios of the resin composition were stirred for 45 minutes to dissolve the photosensitizer in the resin system. This resin system was transparent (Figure 2-23b) compared to the resin system prepared using the H-Nu 470 photoinitiator. The resin system was cured using the casting mould (Figures 2-7 & 2-8) in 12 minutes. This is approximately 6 times longer than without adding the anthracene photosensitizer to the same resin system. The hardness test results of the casting showed similar hardness results (Figure 2-24) compared to the resin system without the anthracene photosensitizer (Figure 2-22 & Table 2-12), as shown in Table 2-13.
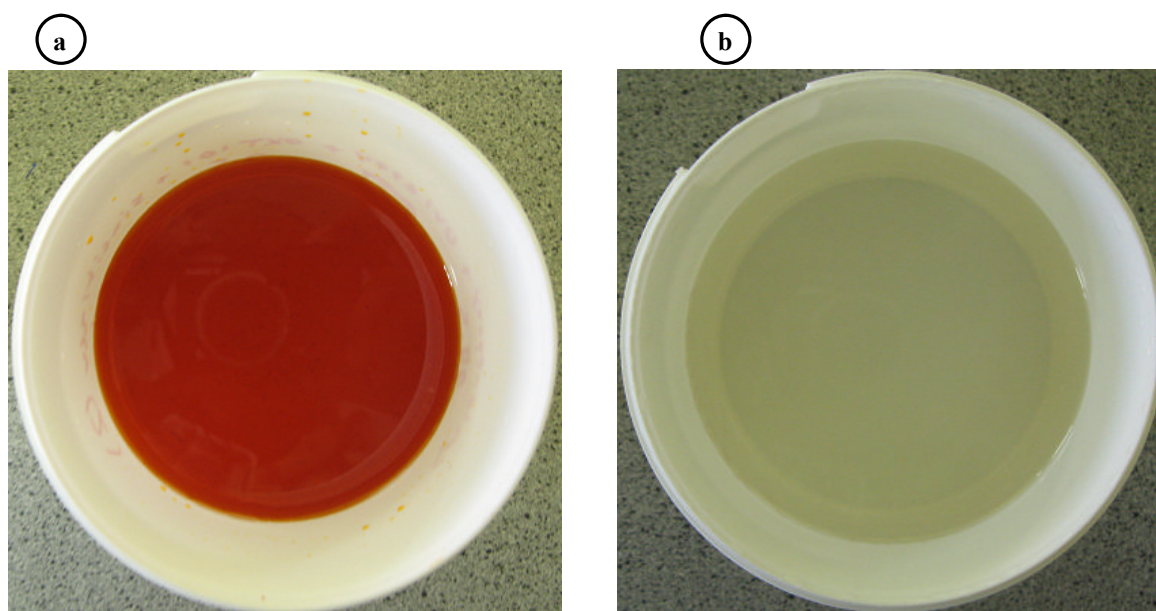
Figure 2-23. Photographical image of two epoxy resin systems with photosensitizers:

(a)   Cycloaliphatic epoxy (100 PHR) with OPPI photoinitiator (2.5 PHR) and H-Nu 470 photosensitizer (0.1 PHR)

(b)   Cycloaliphatic epoxy (100 PHR) with photoinitiator UVI-6976 (0.6 PHR), oxetane OXT-101 (2.6 PHR) and anthracene photosensitizer (0.11 PHR)

Overall, the poor curing behaviour of the resin systems using both photosensitizers contradicts the literature [13, 29, 37-40]. However, this literature related to the thin films, as also reported by Narayanan et al. [2], which differs from the above experimental work which aims to cure deep resin mediums or 'thick components'. Although, neither photosensitizer showed improved curing results, resin system with anthracene photosensitizer were investigated further due to its reactivity that led to curing in a reasonable period compared to the ready formulated resins of Dymax Corporation [22] (4-20586 and 6-20353).
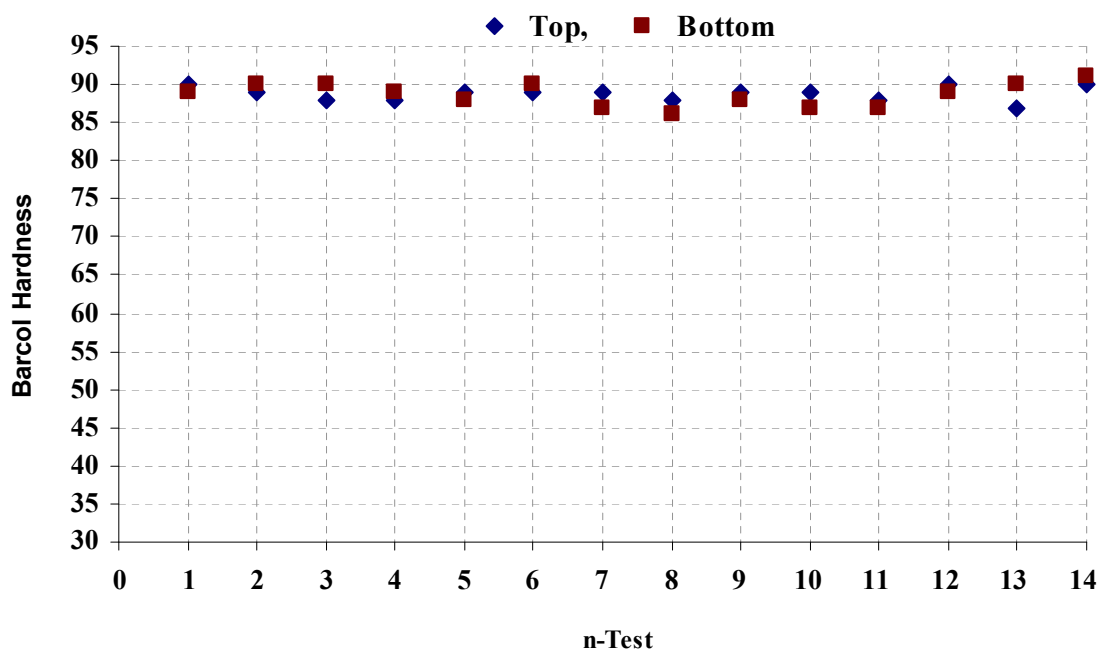
Figure 2-24. Graph of Barcol hardness versus number of test points from each side of the casting for resin system: Cycloaliphatic epoxy (100 PHR) with photoinitiator UVI-6976 (0.6 PHR), oxetane OXT-101 (2.6 PHR) and anthracene photosensitizer (0.11 PHR). The specimen was cured in 12 mins using the flood lamp (0.1 W/cm^2).

Table 2-13. Barcol hardness test results of the casting from resin formulation of cycloaliphatic epoxy (100 PHR) photoinitiator UVI-6976 (0.6 PHR), oxetane OXT-101 (2.6 PHR) and anthracene photosensitizer (0.11 PHR). The specimen was cured in 12 mins using the flood lamp (0.1 W/cm^2)

	Top Surface	Bottom Surface
Mean	89	89
SD	1.2	0.6

2.3.3.4. Optimised Epoxy Resin Systems

In summary, the optimised epoxy resin systems using two types of base epoxy resin, two types of sulfonium salt photoinitiators, oxetane additive and anthracene photosensitizer are outlined in Table 2-14.

Table 2-14. Optimised resin systems of various formulations from the characterisation process. The compositional ratios are described by parts per hundred resin (PHR)

Material	RS1	RS2	RS3	RS4
Epoxy (Bisphenol A/F)	100.0	-	-	-
Cycloaliphatic epoxy (UVR-6105)	-	100.0	100.0	100.0
UVI-6992 photoinitiator	2.5	-	-	-
UVI-6976 photoinitiator	-	0.6	0.6	0.6
Oxetane additive (OXT 101)	15.0	-	2.6	2.6
Anthracene photosensitizer	-	-	-	0.11

Further characterisation of the above optimised resin systems was undertaken to analyse: photocuring energy consumption, effect of additives on the overall resin system viscosity, and the radiation absorption behaviour of the resin systems before and during curing.

2.3.3.5. Viscosity Measurements of the Characterised Resin Systems

Previous studies reported the influence of the viscosity of epoxy resins on the photocuring behaviour [84-85]. These authors suggested that the curing rate of a resin can be improved as the viscosity of a resin decreases. The viscosity can be reduced using an additive which improves the mobility of polymeric chains within the resin. Additives like oxetane are used with epoxy resins to shorten the photopolymerisation period and also to improve the mechanical properties of the final product [52, 55]. Therefore, for further understanding, the viscosity of the four optimised resin systems (Table2-14) was measured. The viscosity study was conducted on the following six samples:

1. **Resin system 4-20586:** (Pre-formulated epoxy resins)

2. **Resin system 6-20353:** (Pre-formulated epoxy resins)

3. **Epoxy 1:** Diglycidyl ether of bisphenol A (DGEBA) and bisphenol F (Bisphenol A/F)

4. **Epoxy 2:** Cycloaliphatic epoxy (Cyracure UVR-6105)

5. **Resin system 1** (RS1 from Table 2-14)

6. **Resin system 2** (RS2 from Table 2-14)

7. **Resin system 3** (RS3 from Table 2-14)

8. **Resin system 4** (RS4 from Table 2-14)

The viscosities of the resins were measured at room temperature 22 °C. The resulting viscosities of the two types of epoxy resins and the optimised resin systems are tabulated in Table 2-15. The commercial pre-formulated epoxy resins exhibited the highest viscosity

comparing to all the resins. Epoxy 1 (bisphenol A/F) has a higher viscosity than Epoxy 2 (Cyracure UVR-6105). On the other hand, resin system RS1, which was made from Epoxy 1 (Bisphenol A/F), acquired the lowest viscosity amongst all the resin systems (Table 2-15) due to the high ratio of oxetane (15 PHR) in the resin composition. Resin system RS1 is about 48 % less viscous than Epoxy 1 (bisphenol A/F). The ratio of the photoinitiator in resin system RS2 indicated a small reduction (0.3 %) in the viscosity compared to Epoxy 2 (Cyracure UVR-6105). But, the ratio of oxetane (2.6 PHR) in resin system RS3 reduced the viscosity by 14 % compared to Epoxy 2 (Table 2-15). Resin system RS4, which is a composition of RS3 with 0.11 PHR anthracene photosensitizer, indicated a further small reduction (16 %) in the viscosity. Hence, by comparing the effect of viscosity reduction resulting from the added ratio of oxetane in both Epoxy 1 and Epoxy 2 resin systems, the viscosity reduction by oxetane has more influence on Epoxy 2 than Epoxy 1.

Table 2-15. Experimentally measured viscosity of two types of epoxy resins and four resin systems as well as the viscosity of the commercial pre-formulated epoxy resins

	Type	Viscosity at 22°C, mPa·s	Viscosity reduction of resin system due to compositional ratio %	Comment
1	4-20586	1200	-	Pre-formulated
2	6-20353	450	-	Pre-formulated
3	Epoxy 1	355	-	-
4	Epoxy 2	292	-	-
5	RS 1	186	48.0 less than Epoxy 1	In-house formulated
6	RS 2	291	0.3 less than Epoxy 2	In-house formulated
7	RS 3	252	14.0 less than Epoxy 2	In-house formulated
8	RS 4	244	16.0 less than Epoxy 2	In-house formulated

2.3.3.6. Energy Consumed for Photocuring of both the Commercial and the Optimised Resin Systems

Radiation exposure H is the total amount of radiation energy input during the resin conversion period and is measured in Joules per centimetre square area (J/cm^2) [86]. The radiation exposure H is a function of irradiance E (W/cm^2) over a period of time t, and it is defined as the time integral of the irradiance:

$$H \; = \; \int_0^t Edt \qquad \qquad \textbf{Equation 2-1}$$

Assuming that E is approximately constant over the exposure time, equation 2-1 is replaced by:

$$H = Et \qquad \qquad \textbf{Equation 2-2}$$

The total delivered energy (Q) of radiation delivered by the flood lamp may be calculated by [86]:

$$Q = E \times t \qquad \qquad \textbf{Equation 2-3}$$

where, Q is the total energy (J / cm^2), E is the irradiance (W/cm^2), t is the duration of illumination (s).

To determine the total delivered energy (Q) by the flood lamp in relation to the emission area (J) [86], Q is multiplied by the emission area of the flood lamp (413 cm^2).

The consumed energy per time may be determined using the following:

$$E_{cons} = P_{output} \times t \qquad \textbf{Equation 2-4}$$

where, E_{cons} is the consumed energy (kWh), P_{output} is the power output (kW), and t is the time during which the device operated (h).

Hence, by knowing that the flood lamp emits an overall intensity of 0.1 W/cm^2, the total delivered radiation energy by the flood lamp for the curing process of the optimised resin systems from Table 2-14 were calculated using equation 2-3 and tabulated in Table 2-16.

Table 2-16. Energy consumed for curing different epoxy resin systems using the flood lamp. The resin systems samples were cast using the casting tool (Figures 2-7 & 2-8) with a volume of 825 cm^2. Lamp power output is 0.4 kW

Resin	Cure time (s)	Q (J / cm^2)	E_{cons} (kWh)	Comment
RS(4-20586)	3900	390	0.433	Commercial pre-formulated epoxy resins
RS(6-20353)	3900	390	0.433	
RS1	600	60	0.067	In-house formulated epoxy resins, as shown in Table 2-14
RS2	120	12	0.013	
RS3	120	12	0.013	
RS4	720	72	0.080	

As shown in Table 2-16, the energy consumed for curing the resin systems prepared in house (RS1, RS2, RS3 and RS4) was less than the pre-formulated commercial epoxy resin

systems (RS4-(20586) and RS6-(20353)). This indicates the importance of resin system optimisation when photocuring thick components. Resin systems RS2 and RS3 were the most efficient in terms of energy consumption. These cycloaliphatic epoxy based resin systems (RS2 and RS3) required 20 % of the energy required for curing the resin system based on Bisphenol A/F (RS1). Adding anthracene photosensitizer to resin system RS3 to make resin system RS4, not only increased the cost of the resin system, but also increased the cost for curing it. Resin system RS4 consumed 6 times more energy to cure compared to resin systems RS2 and RS3 (Table 2-16).

Typical Energy Consumed by Conventional Thermal Curing (Theoretical Study)

In conventional thermal curing processes, a resin formulation is cured using an oven. The oven sizes vary base upon the geometry/size of a part required for the curing process. For relative comparison of the consumed energy between thermal curing and UV curing processes, a typical oven example for thermally curing relatively small size parts (less than 1 m^3), may be the 24 kW Barlow Whitney oven (Figure C-5 in Appendix C-1 'C3').

During the heating process, the Barlow Whitney oven operates full power over the heating time (24 kW). Once the operating temperature is reached, an oven of this type consumes ~ 10 % of the total power output to maintain the operating temperature under controlled ambient extraction conditions. Hence, for the case of Barlow Whitney oven, only ~ 2.4 kW will be consumed after the operating temperature is reached.

For the purpose of studying the consumed energy of thermally cured epoxy formulations, two typical types of commercial epoxy formulations were used, as shown in detail below:

- Dow 4201 and 4200 [21], DGEBA based epoxy adhesives for bonding or sealing applications.

  - Cure cycle (1 h and 20 mins), the power output used for the heating process includes:

    - *Step 1:* Increase in temperature from 25°C to 130°C for the first 10 mins (24 kW),

    - *Step 2:* Then, constant temperature of 130°C for 30 mins (2.4 kW),

    - *Step 3:* Followed by an increase in temperature to 190°C for 10 mins (24 kW)

    - *Step 4:* Finally, constant temperature of 190°C for 30 mins (2.4 kW)

- ST 70 [87], epoxy formulation for curing thick sections with or without glass fibre reinforcements.

  - Cure cycle (2 h and 15 mins), the power output used for the heating process includes:

    - *Step 1:* Increase in temperature from 25°C to 55°C for the first 25 mins (24kW),

    - *Step 2:* Then, constant temperature of 55°C for 60 mins (2.4 kW),

    - *Step 3:* Followed by an increase in temperature to 120°C for 25 mins (24 kW)

    - *Step 4:* Finally, constant temperature of 120°C for 25 mins (2.4 kW)

The energies consumed for the above epoxy formulations were calculated using equation 2-4 and tabulated in Table 2-17. As epoxy formulation of type ST 70 cures in a longer time than formulations of Dow-4201 and Dow-4200, it consumed higher energy; 23.4 kWh and 10.4 kWh, respectively.

Table 2-17. Theoretical study: Energy consumed for thermally curing different epoxy resin systems using the Barlow Whitney oven. The consumed energy was calculated using equation 2-4

	P_{output} (kW)	Time (h)		E_{cons} (kWh)	
		Dow 4201 and 4200	ST 70	Dow 4201 and 4200	ST 70
Step 1	24.0	0.167	0.417	4.0	10.0
Step 2	2.4	0.500	1.000	1.2	2.4
Step 3	24.0	0.167	0.417	4.0	10.0
Step 4	2.4	0.500	0.417	1.2	1.0
			Total	**10.4**	**23.4**

The energy consumed for curing epoxy formulations using thermal curing is much higher than that of the UV curing process, as can be observed from the values in Tables 2-16 and 2-17. However, in case of the Barlow Whitney oven (1 m^3 space), larger parts can be thermally cured compared to a single flood lamp. For that reason, for photocuring larger size parts either multiple flood lamps or controlled positioning of the flood lamp would be required. In addition, for close comparison between the conventional thermal curing and UV curing (flood lamp) processes, the following example was suggested:

- If six part of dimensions 70 cm wide, 70 cm long and 0.5 cm thick needs to be cured using the different processes, then the curing condition may be as follows:

  - ■ ***Thermal curing process:*** the six parts can be all fit in the Barlow Whitney oven (1 m^3 space), hence, the consumed energy would be as shown earlier in Table 2-17

  - ■ ***Photocuring process:*** the emission area of the flood lamp is 413 cm^2 which is of about twelve times less than the area of the part ($70 \times 70 = 4900$ cm^2). The consumed energy for different epoxy formulation was calculated using the values in Table 2-16 (E_{cons} of 6 parts = E_{cons} of emission area (413 cm^2) $\times$ 12 $\times$ 6) and tabulated in Tables 2-18.

The calculated values of the consumed energy for the photocuring process (Tables 2-18) show an increased consumption of energy for the pre-formulated epoxy resins comparing to the thermal cured resins, Tables 2-17. However, the in-house prepared epoxy formulations are still ~ 10 times more efficient than the thermally cured formulations, mainly formulations RS2 and RS3.

Table 2-18. Theoretical study: Energy consumed for curing six parts (dimensions: 70 cm wide, 70 cm long and 0.5 thick) using different epoxy resin systems using the flood lamp

Resin	E_{cons} (kWh) UV Photocuring
RS(4-20586)	31.176
RS(6-20353)	31.176
RS1	4.824
RS2	0.936
RS3	0.936
RS4	5.760

2.4. Optical Properties of the Optimised Epoxy Resin Systems in a Liquid State and During Photopolymerisation (Spectroscopic Experiments)

2.4.1. Objective

The aim of this study is to investigate the absorption spectrum of the optimised resin systems before and during the photocuring process. The absorption spectra of the optimised resin systems provide information regarding the photocuring efficiency when compared to the emission spectrum of the radiation source. Monitoring the emitted radiation passing through the resin systems during the photocuring process determines the change in optical properties, such as transmission or absorption, through the polymerisation process.

2.4.2. Theoretical Consideration of Radiation Absorption

In radiation absorption, the electromagnetic radiation absorbed in a material can be described by the optical density (OD) value, which can be determined by:

$$OD = -\log_{10}\left(\frac{I}{I_0}\right)$$

Equation 2-5

where I_0 is the input intensity onto a material and I is the transmitted intensity through a material.

The absorption of a material can also be described in terms of the properties of the material through which the electromagnetic radiation is travelling using the Beer-Lambert law (Appendix D-1). When photocuring polymers, the amount of energy transferred by the light is critical for initiation of the reactive species within a photoinitiator [11-13]. The total rate of energy absorption [88] for sample length (depth of resin l) by the photoinitiator to produce reactive species, which determines the efficiency of the curing process, is given by:

$$e = \int_{0}^{\infty} E_{\lambda} \left(1 - e^{-k_{\lambda}l} \right) d\lambda \qquad \text{Equation 2-6}$$

where λ is the wavelength, κ_{λ} is the response spectrum of the resin system and E_{λ} is the emission spectrum of the irradiating light source. This implies that the maximum curing efficiency can be achieved if E_{λ} and κ_{λ} are well matched (More details and examples of matching photocuring system can be found in Appendix B-1 'B1'). The response spectrum κ_{λ} represents both ε, the extinction coefficient of the absorbing species (L mol^{-1} cm^{-1}), and c, the concentration of absorbing species of a material (mol L^{-1}):

$$k_{\lambda} = \varepsilon_{\lambda} \cdot c \qquad \text{Equation 2-7}$$

Usually, the experimental absorption measurements unit is OD (optical density), when a spectrometer is used. However, for understanding the absorption efficiency of a resin system the response spectrum κ_{λ} should be used to carry on the matching comparison between the absorption band of a resin medium with the emission spectrum of a radiation source. The response spectrum κ_{λ} may also be used to monitor the change in radiation absorption during the photopolymerisation process of a resin. The response spectrum κ_{λ} can

be found using Beer-Lambert law, equations 2-5 and 2-7, as shown in equation 2-7, (for more details on determining κ_λ, see Appendix D-1):

$$k_\lambda = \frac{-\ln\left[10^{-OD}\right]}{l}$$

Equation 2-8

Hence, by using equation 2-8, the experimentally collected spectral data of absorption with units of OD can be converted to the response spectrum k_λ per cm^{-1}.

2.4.3. Experimental Details

Here, the absorption spectrum of the photoinitiators, the optimised resin systems and the radiation absorbed by the optimised resin systems during the photocuring process are investigated by studying their response spectra κ_λ (equation 2-8). The change in the response spectrum κ_λ during photocuring for the optimised resin systems was found from the transmitted intensities at wavelength 368 nm (UV-A). The experimental work was conducted for the optimised resin systems from Table 2-14 and the photoinitiators used in the optimised resin systems.

Material:

The absorption measurements were carried out for the following samples:

1) **Photoinitiators:** (A) Triarylsulfonium hexafluorophosphate salts (UVI-6992) and

    (B) Triarylsulfonium hexafluoroantimonate salts (UVI-6976)

2) **Resin system 1** (RS1 from Table 2-14)

3) **Resin system 2** (RS2 from Table 2-14)

4) **Resin system 3** (RS3 from Table 2-14)

5) **Resin system 4** (RS4 from Table 2-14): Resin system 3 with Anthracene photosensitizer (≥99% purity) 0.11 PHR

Equipment and Methods:

Figure 2-25 illustrates the positioning of the equipment used for monitoring the absorption spectrum during photocuring of the optimised resin systems and the photoinitiators.
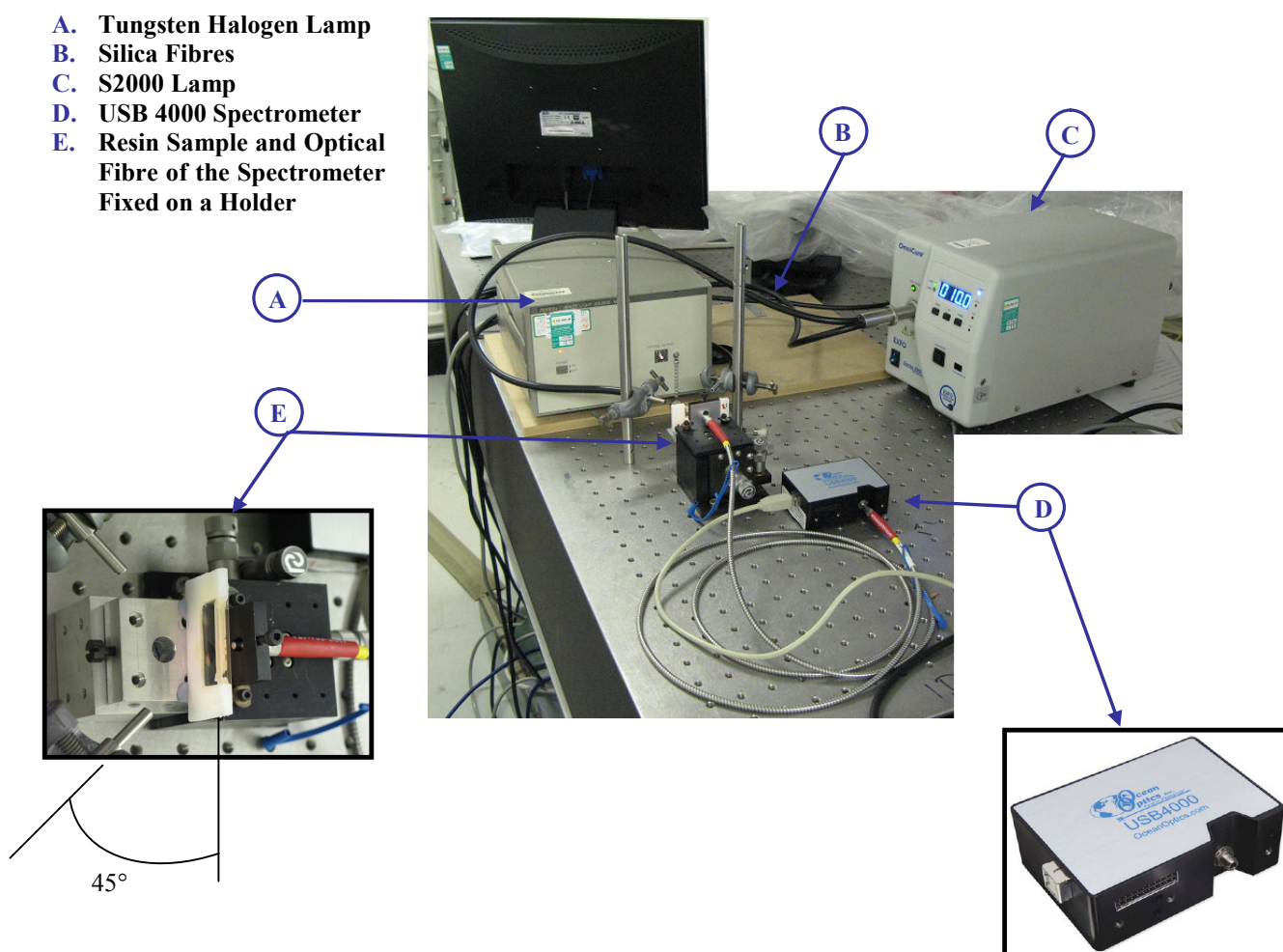
The absorption spectrum of the photoinitiators, optimised resin systems and the radiation absorbed by the optimised resin systems during the photocuring process were conducted using a 60 watt tungsten halogen lamp (Figure 2-25A). The lamp emits radiation continuously over a range of wavelengths from 300 nm to 1000 nm. The tungsten halogen lamp was tested to determine whether if would it photocure the resin systems by a continuous exposure time of ten minutes. All samples indicated no curing. Thus, it was kept on through all the experiments.

For the photocuring process of the optimised resin systems, an OmniCure S2000 (EXFO Corp.) radiation source (Figure 2-25C) with a nominal power of 200 W was used. This radiation source was designed to deliver a light beam for spot curing applications. It is

equipped with a high pressure mercury vapor bulb with major emission peaks at wavelengths of 365 nm, 406 nm and 440 nm. A reflector within the radiation source is set-up to deliver a light beam through two silica light guides with a diameter of 3 mm and length of 1000 mm (Figure 2-25B). Irradiance (radiant power per unit area) is approximately 30 W/cm^2 over the spectral range from 280 nm to 450 nm.

The spectral outputs of all the experiments were measured using a USB4000 spectrometer (Ocean Optics [89]), as shown in Figure 2-25D. The spectrometer determined the absorbance spectra which indicate how much light a sample absorbs, in the range from 200 nm to 850 nm. The radiation was collected using a 1 mm diameter optical fibre with an acceptance angle (θ_{ac}) of 12.4°. Data processing of the absorption readings (OD) were conducted using software provided with USB4000 spectrometer. The samples were held within a container made of a polypropylene body and two microscope slips joined using epoxy permanent glue. Dimensions of the container were: 40 mm wide, 20 mm height and 5 mm thick (Figure 2-26). The container was positioned using a holder as shown in Figure 2-25E.

As the aim of the resin optimisation process is to develop a highly reactive formulation for closed mould curing application using the BlueWave 200 mercury (Hg) lamp [22]. The absorption spectrums of all samples were matched with a typical emission spectrum of the BlueWave 200 Hg lamp with major emission peaks at wavelengths of 368 nm, 406 nm and 440 nm. This lamp is described and extensively used in the following Chapters (Chapter 3, 4 and 5).

A. **Tungsten Halogen Lamp**
B. **Silica Fibres**
C. **S2000 Lamp**
D. **USB 4000 Spectrometer**
E. **Resin Sample and Optical Fibre of the Spectrometer Fixed on a Holder**

Figure 2-25. Positioning of the equipment used for the all of the absorption measurements. The tungsten halogen lamp emission point is 80 mm away from the sample. The silica fibres of the OmniCure S2000 lamp are 50 mm away and positioned at 45° to the resin sample.
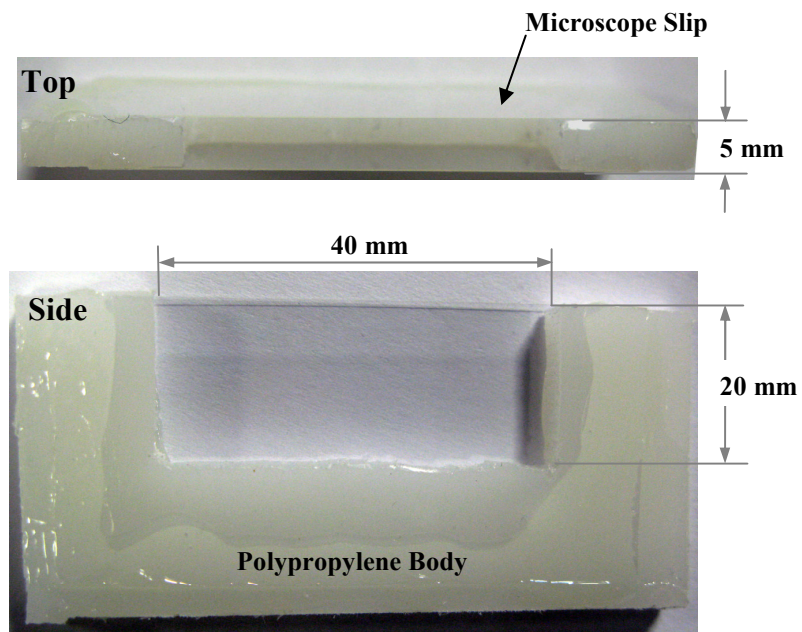
Figure 2-26. In house made container in which the liquid samples were poured.

2.4.4. Results and Discussion

2.4.4.1. Absorption Spectra of Photoinitiators and Resin Systems

Although the photoinitiators of triarylsulfonium hexafluorophosphate salts (UVA-6992) and triarylsulfonium hexafluoroantimonate salts (UVA-6976) resulted in a different curing behaviour during the characterisation of the two types of epoxy resins (Section 2.3), the response spectrum κ_λ of the salts indicated a good matching with the typical emission spectrum E_λ of the Hg lamp (BlueWave 200 lamp) that overlapped the peak emission at 368 nm. The spectra for both salts were found to be very similar, as shown in Figures 2-27 and 2-28.
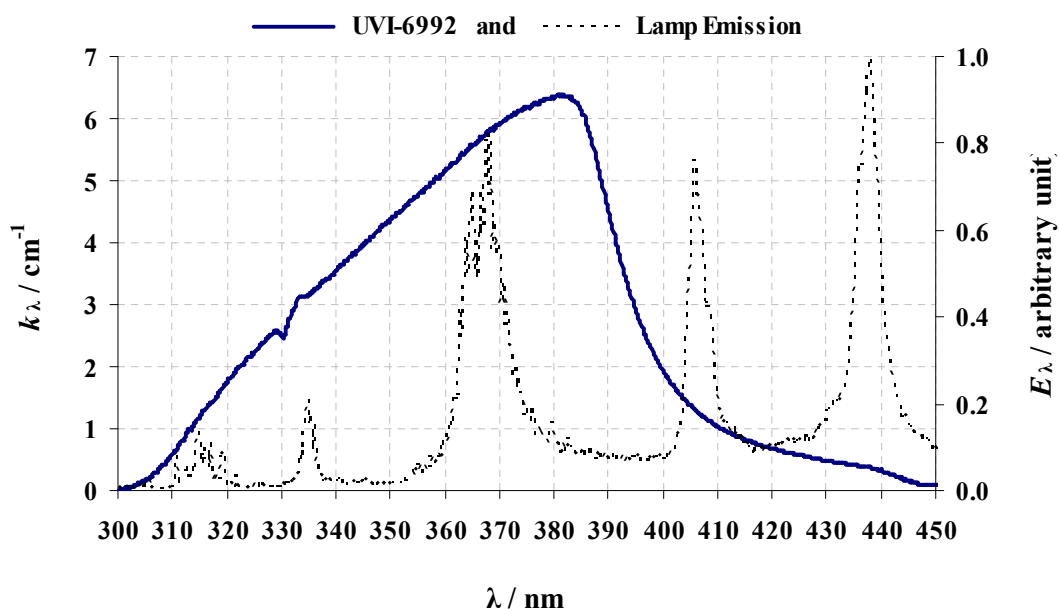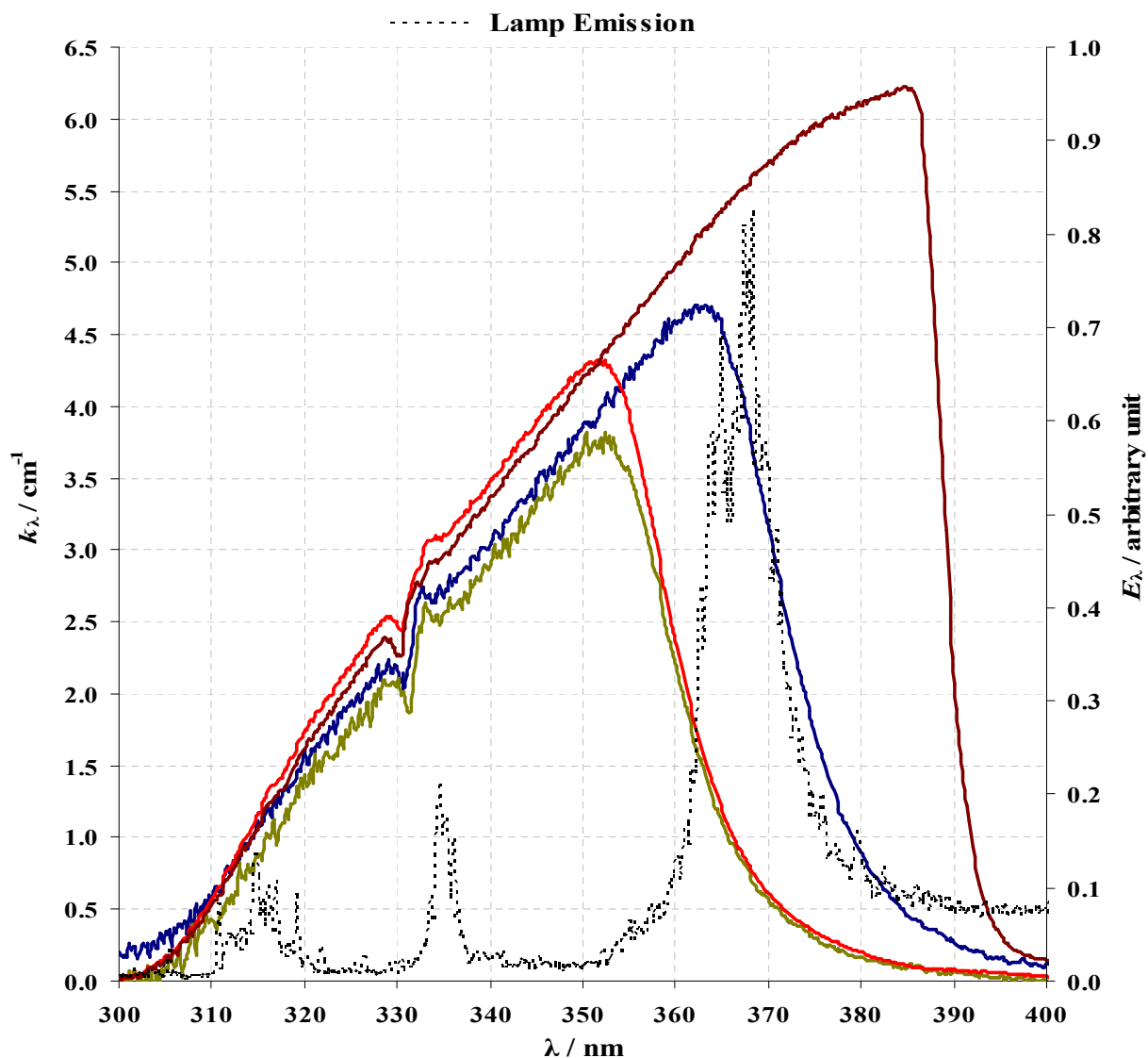

Figure 2-27. Response spectrum κ_λ of photoinitiator triarylsulfonium hexafluorophosphate salts (UVI-6992) and the emission spectrum E_λ of Hg lamp (BlueWave 200).
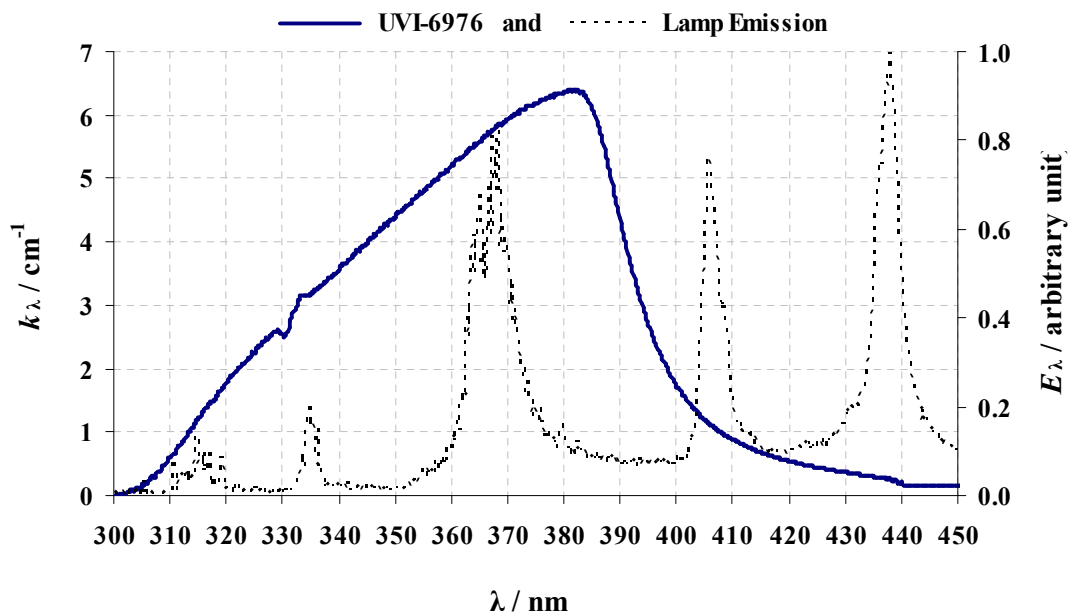
Figure 2-28. Response spectrum κ_λ of photoinitiator triarylsulfonium hexafluoroantimonate salts (UVI-6976) and the emission spectrum E_λ of Hg lamp (BlueWave 200).

The response spectrum κ_λ of both photoinitiators overlaps the emission peak of the Hg lamp at wavelength 368 nm in the UV-A spectrum and covers some of the peak at wavelength 408 nm of the Hg lamp emission E_λ (Figures 2-27 and 2-28). For resin systems RS1, RS2 and RS3, the absorption measurements showed a variation in the response spectrum κ_λ for each resin system (Figure 2-29). The resulting response spectra of all these three optimised resin systems shifted and covered some of the emission peak at wavelength 368 nm. This shifting behaviour of the response spectra took place mostly as a result of the epoxy base resin in all of the optimised resin systems. Generally, all of the response spectra κ_λ lay in the 300 nm to 400 nm spectral range and the difference between the response spectra κ_λ is in the right side of the spectra. Resin system RS1of epoxy (bisphenol A/F) shows a higher response spectrum than resin systems RS2 and RS3 of cycloaliphatic epoxy. Resin system RS1 also covers most of the major emission peak at wavelength 368 nm of Hg lamp.

Figure 2-29. Emission spectrum E_λ of Hg lamp (BlueWave 200) and response spectra κ_λ of:

▬ RS1.   Resin system 1: Epoxy (Bisphenol A/F) 100 PHR with triarylsulfonium hexafluorophosphate photoinitiator UVI-6992 2.5 PHR and oxetane (OXT 101) 15 PHR.

▬ RS2.   Resin system 2: Cycloaliphatic epoxy (Cyracure UVR-6105) 100 PHR with triarylsulfonium photoinitiator (UVI-6976) 0.6 PHR.

▬ RS3.   Resin system 3: Cycloaliphatic epoxy (Cyracure UVR-6105) 100 PHR with triarylsulfonium hexafluoroantimonate photoinitiator (UVI-6976) 0.6 PHR and oxetane (OXT 101) 2.6 PHR.

▬ RS4.   Resin system 4: RS3 with Anthracene photosensitizer 0.11 PHR.

Resin system RS3 has a higher absorption response of about 1 cm^{-1} at wavelength 353 nm than resin system RS2. This could be explained as a result of the oxetane additive in resin system RS3. Resin system RS4, which is a composition of resin system RS3 with anthracene photosensitizer, has the highest response spectrum among all the resin systems. Thus, adding anthracene photosensitizer to resin system RS3 improves its absorption. The response spectrum of RS4 overlaps the entire major peak at wavelength 368 nm of the Hg lamp emission.

2.4.4.2. Photopolymerisation of Epoxy Resin Systems Monitored by Spectral Change

In this set of experiments, the S2000 radiation source was used for curing samples of the resin systems (RS1, RS2, RS3 and RS4). Absorption spectrum data was gathered using the tungsten lamp and the spectrometer (USB4000). An initial absorption reading was recorded before curing the samples. The rest of the absorption readings were then recorded continuously after a sequence of irradiation for 10 seconds during each experiment. The response spectra κ_λ (equation 2-8) were calculated from the collected absorption spectrum data. The change in response spectrum κ_λ is described at wavelength 368 nm, at which the highest irradiation is emitted from the S2000 radiation source. The fully cured condition of each sample was determined by: observing the change in colour and physically by indenting the polymerised sample from the top open passage of the container (Figure 2-26) with a 10 cm long steel needle.

For resin RS1, the absorption at κ_{368} increased gradually in the first two minutes of irradiation exposure (Figure 2-30); from 3.48 cm^{-1} to 5.69 cm^{-1}. The sample fully cured in the fourth minute and the measured κ_{368} value was 5.64 cm^{-1}. The absorption at κ_{368} then

decreased in small rates after the fourth minute until it reached a minimum κ_{368} of about 5.54 cm^{-1} by the end of the experiment.

The absorption at κ_{368} of RS2 increased rapidly from 0.5 cm^{-1} until it reached a maximum of 3.85 cm^{-1} at the first half minute of the curing process (Figure 2-31). The absorption at κ_{368} then decreased steadily to 2.62 cm^{-1} after one minute and forty seconds at which the sample was fully cured. The absorption at κ_{368} increased slightly to 2.74 cm^{-1} by the end of the experiment.

The absorption at κ_{368} of RS3 increased rapidly from 0.5 cm^{-1} until it reached a maximum of 2.8 cm^{-1} after 10 seconds of the curing process (Figure 2-32). The absorption at κ_{368} thereafter dropped suddenly in the next 40 seconds to 1.53 cm^{-1}, by which time the sample was fully cured. The absorption at κ_{368} of the cured sample of resin RS3 showed a constant behaviour at ≈ 1.5 cm^{-1} for the rest of irradiation process.

The overall change in the absorption at κ_{368} of resin system RS4 was very small, as shown in the spectrum axis of Figure 2-33. The absorption at κ_{368} readings in the first four minutes of the curing process resulted in noise; hence, the reading was ignored. The change in the absorption at κ_{368} readings caused by curing started from the fourth minute to the ninth minute by a small, gradual increase of κ_{368} from 5.11 cm^{-1} to 5.28 cm^{-1}, respectively. The absorption at κ_{368} after that dropped to 5.25 cm^{-1} in the tenth minute. The sample was fully cured at the ninth minute.
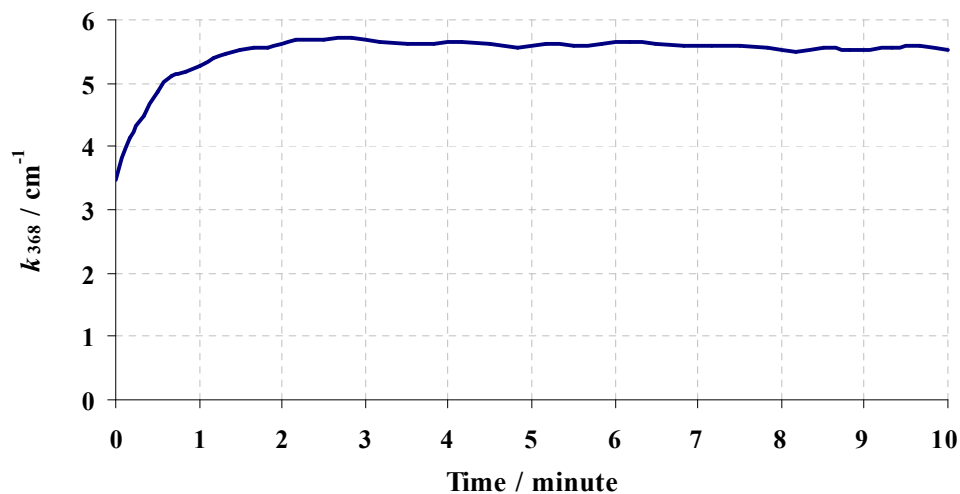
Figure 2-30. Change in response absorption κ_{368} during the curing of 5 mm thick Resin system 1 (RS1): Diglycidyl ether of bisphenol A (DGEBA) and bisphenol F (Bisphenol A/F) 100 PHR with UVI-6976 2.5 PHR and oxetane (OXT 101) 15 PHR.
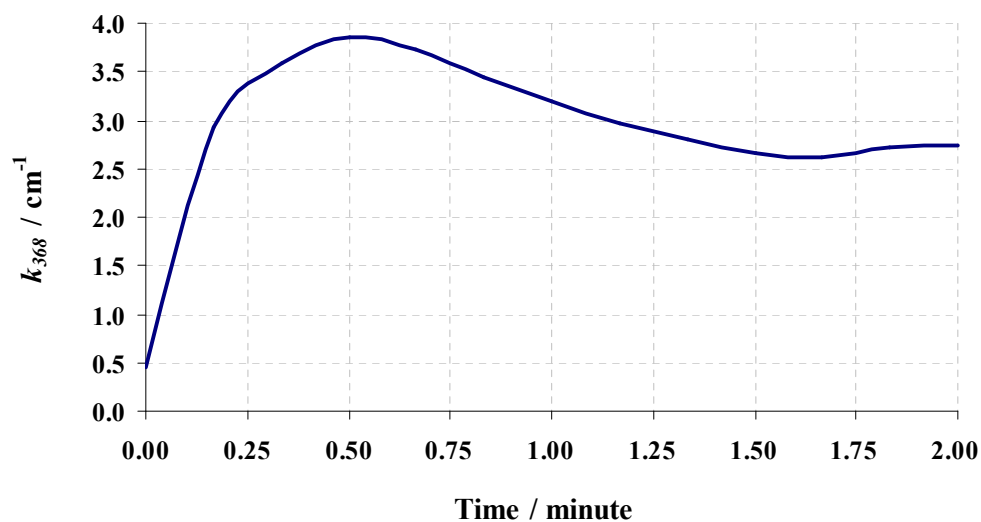
Figure 2-31. Change in response absorption κ_{368} during the curing of 5 mm thick Resin system 2 (RS2): Cycloaliphatic epoxy (Cyracure UVR-6105) 100 PHR with triarylsulfonium hexafluoroantimonate salt photoinitiator (UVI-6976) 2.65 PHR.
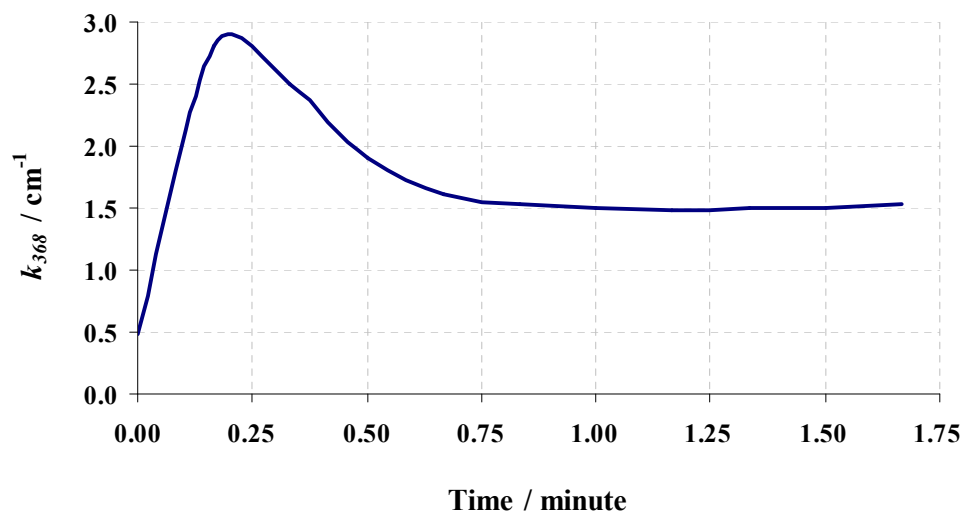
Figure 2-32. Change in response absorption κ_{368} during the curing of 5 mm thick Resin system 3 (RS3): Cycloaliphatic epoxy (Cyracure UVR-6105) 100 PHR with triarylsulfonium hexafluoroantimonate salt photoinitiator (UVI-6976) 0.6 PHR and oxetane (OXT 101) 2.65 PHR.
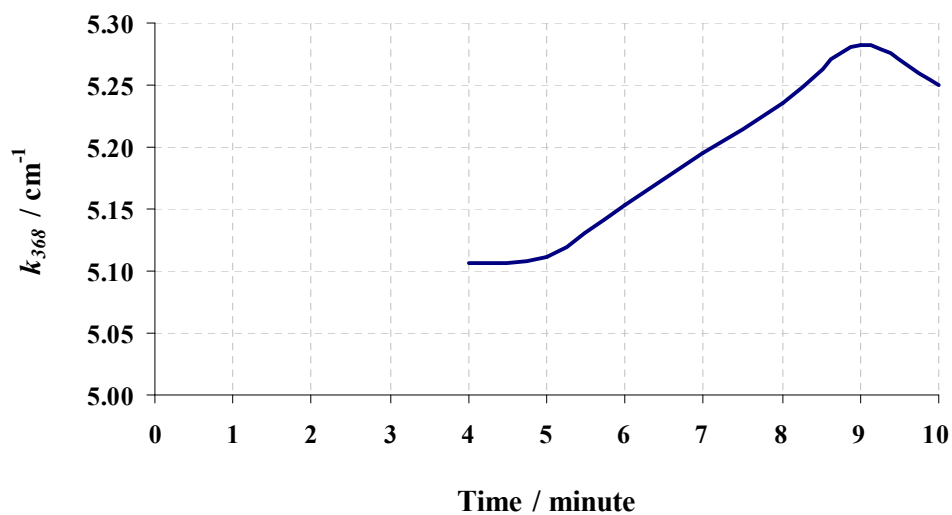

Figure 2-33. Change in response absorption κ_{368} during the curing of 5 mm thick Resin system 4 (RS4): Resin system 3 with Anthracene photosensitizer 0.11 PHR.

All the cured samples indicated higher absorption at wavelength of 368 nm than the initial reading of the base uncured resin formulation. Samples cured from resin systems RS2 and RS3 showed a faster curing rate (within 2 minutes) than the samples cured from resin systems RS1 and RS4 which cured after 4 minutes and 9 minutes, respectively. However, the cured samples of RS2 and RS3 exhibited higher internal stress than the cured samples of RS1 and RS4 as can be observed from the crack in Figure 2-34. The absorption at κ_{368} of the cured sample of RS1, with epoxy bisphenol A/F, decreased slightly after the sample was cured. This indicated the high absorption of the cured sample compared to the resin before curing. The slow change in the absorption spectrum at κ_{368} of the cured sample of RS1 is also related to its yellow colour which was darker than the other samples [64-65, 67].
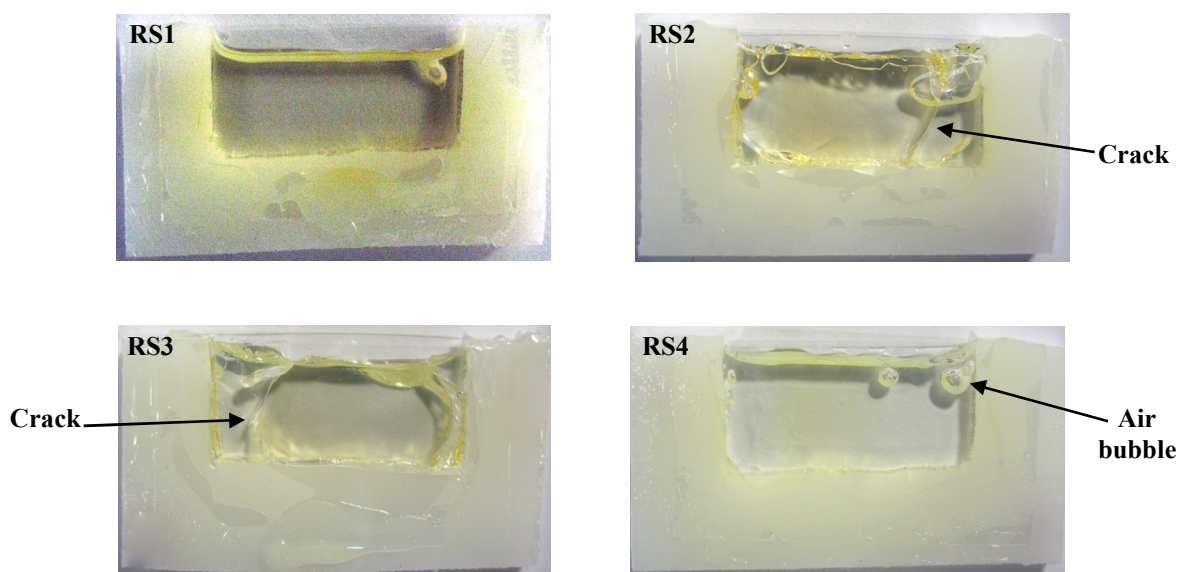
Figure 2-34. Cured samples of: resin system 1 (RS1), resin system 2 (RS2), resin system 3 (RS3) and resin system 4 (RS4).

The curing rate of resin systems RS2 and RS3 were approximately three times faster than resin system RS1, which is in agreement with the literature due to the higher reactivity of cycloaliphatic epoxy resins compared to the DGEBA epoxy resins [28, 46, 53]. The addition of oxetane additive in RS3 resulted in more transmission of light (Figures 2-31 and 2-32) through the cured sample compared to the other samples. The cured sample of RS3 also exhibited less yellowing than RS1, RS2 and RS4 (Figure 2-34). Hence, resin system RS3 will allow more radiation to go through it as it cures compared to all the other resin system. Generally, the yellow colour of the cured epoxy samples increases the radiation absorption in the UVA band as reported by Asilturk et al. [66] which may explain the higher κ_λ values of the cured samples of the different resin formulations compared to the initial κ_λ values, as shown in Figures 2-30 to 2-33.

The sample of resin system RS4, which is a composition of RS3 with a photosensitizer, was expected to have the fastest curing behaviour according to the literature [16, 29, 37-43]. In addition, RS4 in its initial liquid state had a response spectrum that overlapped the entire major emission peak at wavelength 368 nm of the Hg lamp (Figure 2-29). But in contrast, among all of the resin systems, resin system RS4 took a longer time to cure. The casting of resin system RS4 took 6 times longer to cure than RS2 and RS3, as discussed earlier in Section 2.3.3. Although the cured sample of RS4 exhibited the lightest yellowing colour (Figure 2-34), it had high absorption after curing (Figure 2-33). This indicates that the photosensitizer is still causing high radiation absorption even after the full curing of the sample. One explanation is that the sample surface facing the radiation source was absorbing highly and limited the irradiation intensity to penetrate efficiently to cure deeper in the medium.

Overall, the curing response spectrum results of all the resin systems used in this work suggests that resin system RS3 is the most reactive resin system for curing thick components as it allows the irradiation emission to penetrate deeper as the resin cures.

2.5. Interpretation of the Overall Epoxy Optimisation Results

Photocuring efficiency of different epoxy resin systems, during the characterisation process, resulted in a different curing behaviour. Table 2-19 shows an overall summary of the information gathered from the characterisation of the in-house formulated resin systems used in this chapter.

Table 2-19. Characterisation results summary of the in-house optimised epoxy resin systems. Refer to Table 2-14 for the compositional ratio of the resin systems listed in this Table

Resin system	Viscosity (mPa·s)	Curing time (minutes)	Average hardness		Q (J / cm^2)	κ at 368 nm before curing (cm^{-1})	κ at 368 nm after curing (cm^{-1})
			Top	Bottom			
RS1	186	10	78	64	60	3.48	5.54
RS2	291	2	89	89	12	0.50	2.74
RS3	252	2	89	89	12	0.50	1.50
RS4	244	12	89	89	72	5.11	5.28

Generally, resin system RS1 demonstrated improved curing results, such as curing speed and overall hardness, compared to the two commercial pre-formulated epoxy resin systems [22]. However, the variation in the hardness of the top and the bottom surfaces (Table 2-19) of the casting from resin system RS1 may have resulted from the continuous high absorption at κ_{368} (5.69 cm^{-1} at 368 nm wavelength) of the RS1 starting from the second minute of irradiation (Figure 2-30). Thus, the hardness of the casting cured from RS1 is irregularly distributed across its surface. This absorption disadvantage not only varied the hardness of the top and bottom surfaces, it also increased the curing period and eventually

the cost. Nevertheless, oxetane OXT-101 additive in a resin system based on bisphenol A/F epoxy increased the resin system (RS1) conversion speed during photocuring process.

Resin system RS4 exhibited the lowest viscosity compared to the other two resin systems made from cycloaliphatic epoxy. As it is based upon the most reactive resin system (RS3) it was expected to be more reactive. However, RS4 took 6 times longer to cure than resin systems RS2 and RS3. Hence, the curing behaviour result of RS4 contradict the literature [13, 29, 37-43] and suggests that anthracene and H-Nu70 photosensitizers are more applicable in resin formulation used for curing thin films, rather than for thick laminates or components. In addition, the casting made from resin system RS4 showed improved hardness results compared to resin system RS1. However, it is less efficient than RS1 in terms of curing speed and energy consumption. Unlike resin systems RS1 and RS4, resin systems RS2 and RS3 have more efficient curing behaviour. These resin systems cured in 2 minutes, consumed a total energy Q of 12 J/cm^2 and exhibited uniform hardness distribution through the casting. The added oxetane ratio in resin system RS3 reduced its viscosity, and also produced a lower absorption at κ_{368} of the casting after curing compared to RS2, 1.50 cm^{-1} and 2.74 cm^{-1}, respectively. This improvement allows the irradiation emission at wavelength 368 nm to penetrate deeper in RS3 making it more suitable for thick components. The lower viscosity of RS3 compared to RS2 (Table 2-19) also makes it more advantageous for closed mould processes, like Resin Transfer Moulding. Thus, resin system RS3 is the most efficient option among the other optimised epoxy resin systems to be photocured by irradiation emitted from the side of an embedded side emitting optical fibre.

2.6. Chapter Conclusions

- Photopolymerisation of thick resin samples (5 mm) resulted in different curing behaviour for various epoxy resin formulations. The epoxy resin formulation optimisation process resulted in four main resin systems. Three of these were based on cycloaliphatic epoxy and one on bisphenol A/F epoxy.

- Efficient photocuring results for the base epoxy resins bisphenol A/F and cycloaliphatic epoxy were reached when triarylsulfonium hexafluorophosphate salts and triarylsulfonium hexafluoroantimonate salts photoinitiators, respectively, were used with each base epoxy resin.

- In-house formulated resin systems from bisphenol A/F and cycloaliphatic epoxides cured faster than the commercially available, ready formulated epoxy resin systems (65 minutes). Resin system from bisphenol A/F cured in 10 minutes. Resin systems from cycloaliphatic epoxides with and without oxetane additive cured in 2 minutes. The samples cured from the in-house formulated resin systems exhibited more uniformly distributed hardness than the commercial epoxy resin systems.

- Adding oxetane to the resin system of bisphenol A/F epoxy improved the curing speed and the overall hardness distribution of the casting. The Barcol hardness of the casting from bisphenol A/F epoxy with oxetane improved by 12 % on the top surface (78) and 14 % on the bottom surface (64) compared to the formulation without oxetane. The castings produced from resin systems of cycloaliphatic epoxy were found to be harder (89 Barcol hardness) with a more uniform hardness distribution than those produced from the resin system of bisphenol A/F epoxy.

- Adding the H-Nu470 phtoinitiator to cycloaliphatic epoxy resin resulted in poor curing for thick components, and anthracene photosensitizers slowed the curing process by 10 minutes when added to the optimised resin system from cycloaliphatic epoxy which cured in 2 minutes.

- The effect of viscosity reduction by the oxetane additive had an influence on both the cycloaliphatic epoxy and the bisphenol A/F. The optimised resin system from bisphenol A/F epoxy had a 48 % reduction in viscosity (186 mPa·s) compared to the base resin (355 mPa·s). The optimised resin system from cycloaliphatic epoxy was 14 % less viscous (252 mPa·s) than the base resin (292 mPa·s).

- Resin systems based on cycloaliphatic epoxy consumed a lower energy (12 J/cm^2) than the bisphenol A/F based resin system (60 J/cm^2). For the condition of curing similar size parts, the consumed energy for photocuring the in-house prepared formulations (mainly RS2 and RS3) found to be more than 10 times less than that of the typical epoxy formulations cured using the conventional thermal curing process.

- The response spectrum κ_λ of the two sulfonium photoinitiators, used with both bisphenol A/F and cycloaliphatic epoxides, absorb radiation ranging from wavelength 300 nm to wavelength 440 nm of the electromagnetic spectrum. However, the response spectrum κ_λ of all of the optimised epoxy resin systems reduced to a range of 300 nm to 395 nm as a result of optimised resins compositions. Albeit, the response spectrum κ_λ of the optimised epoxy resin systems varied.

- None of the optimised epoxy resin systems showed complete transparency of the wavelength 368 nm (at which the highest intensity is emitted by the Hg lamp in the UVA band) after curing. The absorption of the cured samples from the optimised resin systems varied. Optimised resin systems based on bisphenol A/F and cycloaliphatic epoxy with the anthracene photosensitizer cured in a longer time as a

result of high absorption during curing (absorption at κ_{368} after curing, 5.3 cm^{-1} and 5.28 cm^{-1}; respectively).

- The two resin systems of cycloaliphatic epoxy (100 PHR) with photoinitiator UVI-6976 (0.6 PHR) and with and without oxetane OXT-101 (2.65 PHR) cured faster as a result of a decrease in absorption during curing (absorption at κ_{368} after curing, 2.74 cm^{-1} and 1.50 cm^{-1}, respectively).

# Chapter 3

Characterisation of Side Emitting Optical Fibres

3.1. Introduction

For photocuring epoxy in a closed mould application, use of side emitting optical fibres was proposed. As discussed in the previous chapters, the radiation emitted from the side of the fibre should match the absorption spectrum at which the epoxy photo-reacts and the amount of radiation energy transferred to the epoxy medium is critical for efficient initiation of the photoreactions. This chapter covers an experimental characterisation of several commercially available side emitting optical fibres in order to determine the characteristics, optical transmission and the side emission performance of each side emitting optical fibre.

3.2. Background

3.2.1. Introduction

Optical fibres are a form of a wave guide through which electromagnetic (EM) radiation or 'light waves' are transmitted. Optical fibres come as either mono-mode or multi-mode. Mono-mode optical fibres are used extensively in telecommunication and data transfer applications. Multi-mode optical fibres are more desirable for illumination purposes, due to their large core characteristic [3, 89-91]. In light guiding applications, the optical fibres require a light source and a clear material, such as glass or polymer, for the radiation to transmit through [92]. Optical fibre, usually, consists of three parts: core, cladding and outer protective jacket layer, as shown in Figure 3-1.
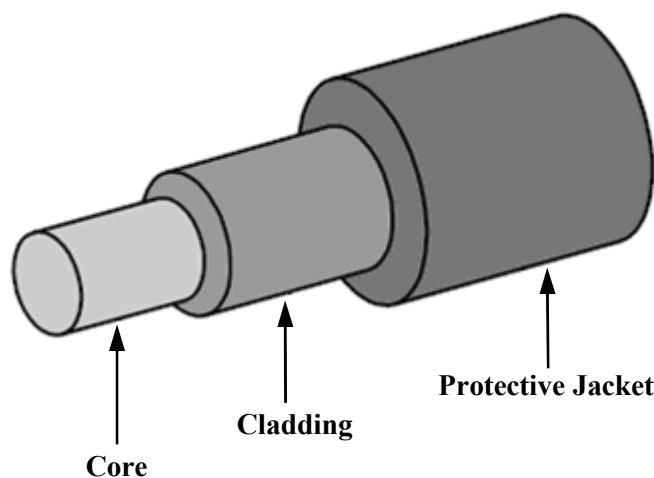

Figure 3-1. Typical structure of optical fibre.

For the EM radiation to be transmitted through an optical fibre, the refractive index of the core (n_1) must be greater than the refractive index of the cladding (n_2), otherwise the radiation will be lost immediately after it is launched into the fibre. Hence, for guiding of

EM radiation through an optical fibre, the condition $n_1 > n_2$ at the core/cladding interface must always be achieved.

The speed of light depends on the material through which it is travelling. The refractive index of a material describes the speed that the light travels through it. For example, the higher the refractive index of a material, the slower the speed of light, and the lower the refractive index, the higher the speed of light, Figure 3-2. The refractive index of a material can be expressed by following formula:

$$\text{Refractive index} \quad = \quad \frac{\text{Speed of light in free space}}{\text{Speed of light in the material}}$$

where, the speed of light in free space $= 3 \times 10^8$ m/s.
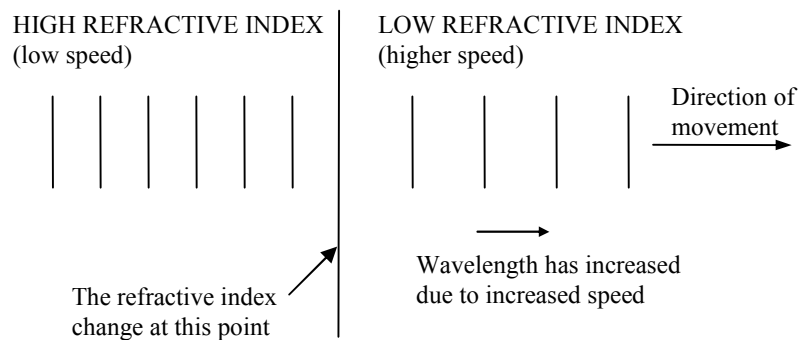
Figure 3-2. Variation in refractive index effect in light rays speed [92].

Factors that affect the amount of light that is transmitted through a material are absorption and scattering of the light. The absorption of radiation results in heat generation in a

material. Absorption and scattering together are known as attenuation. Attenuation is measured in decibels per kilometre (dB/km) for communication fibre [93].

3.2.2. Snell's Law and Total Internal Reflection

Transmission of light rays through an optical fibre is dependent upon the angles at which the light rays are launched at the end face of the fibre. The angles of the incoming ray are called the angles of incidence and the outgoing rays are known as the angles of refraction. These angles can be measured with respect to the normal as shown in Figure 3-3a. The relationship between these angles and the refractive indices of the materials of the fibre (core/cladding) is described by Snell's law:

$$n_1 \sin \psi_1 = n_2 \sin \psi_2$$

Equation 3-1

where, n_1 and n_2 are the refractive indices of the core and cladding; respectively, $\sin \psi_1$ is the angle of incidence and $\sin \psi_2$ is the angle of refraction.
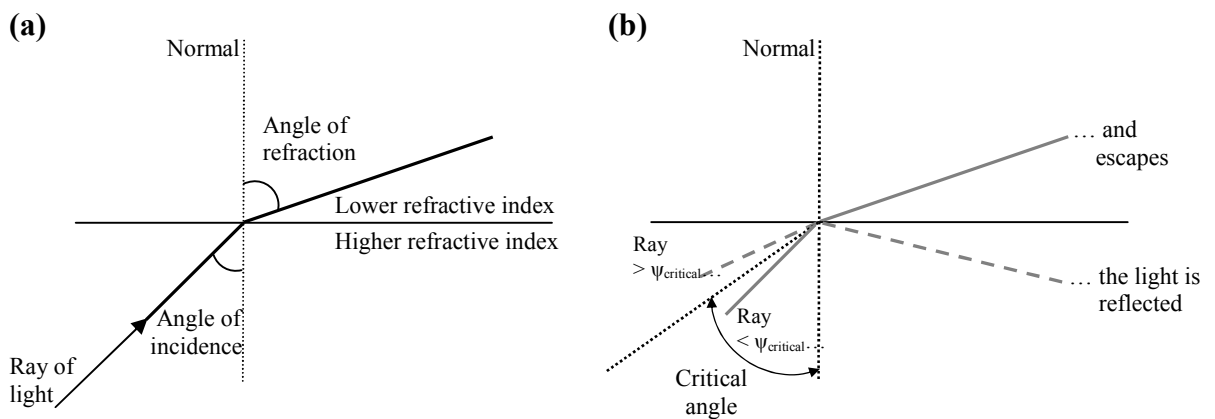

Figure 3-3. (a) Light ray angles when passing through materials with different refractive indices, and (b) total internal reflection (TIR).

As shown in Figure 3-3a, the angle of the ray increases when it enters the material with lower refractive index. For the light rays to be guided through the fibre, the angle of incidence has to be greater than the critical angle ($\psi_{critical}$). The critical angle ($\psi_{critical}$) is the angle which, if exceeded, rays will not be guided or 'refracted' in the core of an optical fibre, and it is expressed as follows:

$$\psi_{critical} = \arcsin\left(\frac{n_2}{n_1}\right)$$

Equation 3-2

Total internal reflection (TIR) of the light rays through an optical fibre (Figure 3-3b) occurs under the condition that the angles of incidence of the light rays at the core/cladding boundary are greater than the critical angle. As a result, the boundary region acts as a mirror and the transmitted light rays reflect back from the core/cladding boundary into the core of the fibre.

In addition, the launched light ray into an optical fibre may undergo both reflection and refraction when it travels from a medium to another, as shown in Figure 3-4. The reflection and refraction of incident ray also vary accordingly with the material refractive index. For instance, higher refractive index would result in higher reflection than refraction of the incident light ray. The coefficient of the reflected light ray can be described by Fresnel's law of reflection:
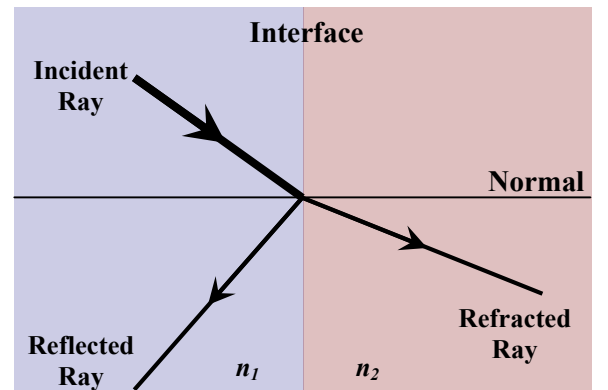
Figure 3-4. Schematic illustration showing the refraction and reflection of the incident ray due to travelling through medium with different refractive index values.

$$R = \left(\frac{n_1 - n_2}{n_1 + n_2} \right)^2 \qquad\qquad \textbf{Equation 3-3}$$
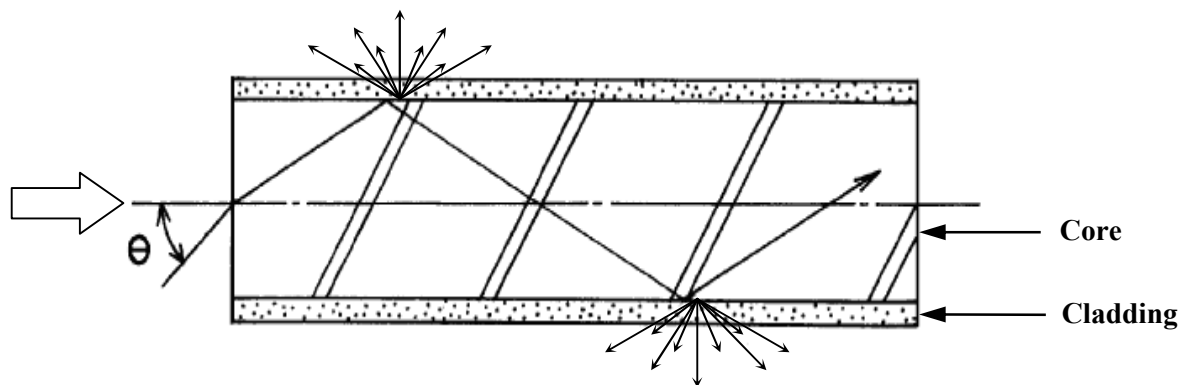
3.2.3. Side Emitting Optical Fibres

Initially side emitting optical fibres were used for illumination purposes, as suggested by Spigulis et al. [7] and Sillyman et al. [3]. But during the last decade, side emitting optical fibres were found of interest in other applications such as waste-water disinfection, medical phototherapy, photocuring of polymers and sensing [14-16, 25, 95-98].

EM radiation emission along the side of an optical fibre is achievable by either controlling the radiation launching conditions or by designing a side emission mechanism in an optical fibre. Side emission caused by controlling the launching conditions happens when the angles of incidence of the launched radiation are smaller than the critical angle ($\psi_{critical}$). For the side emission mechanisms, numerous patents and publications exist relating to the design of side emitting fibres [3-10]. Generally, the proposed design methodologies to cause radiation to be emitted from the side of an optical fibre are as follows:

- Including scattering particles in the core of the fibre, Figure 3-5

- Including scattering particles in the cladding of the fibre, Figure 3-6

- Adding micro-cuts or notches in the cladding of the fibre, Figure 3-7

- Creating micro-bends along an optical fibre geometry

- Varying the materials of the core or the cladding of optical fibres to result in different refractive index values, so that the $n_{core} > n_{cladding}$ condition causes side emission
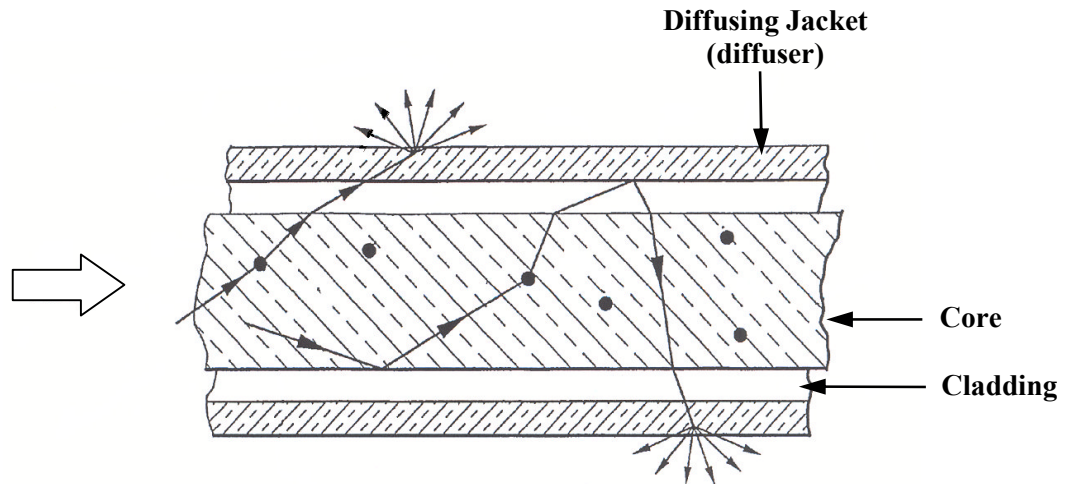
Figure 3-5. Side emitting fibre with scattering particles in the core [5].

Figure 3-6. Side emitting fibre with scattering particles in the cladding [6].
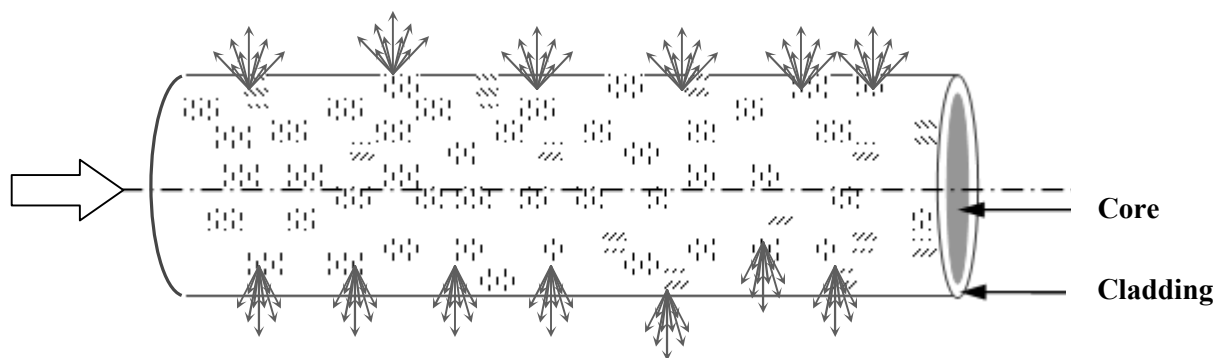
Figure 3-7. Example of side emitting fibre with micro-cuts or notches in the cladding.

Each one of the optical fibres (Figures 3-5, 3-6 and 3-7) are made from parts of different materials so that the fibres met the light guidance requirement ($n_{core}>n_{cladding}$) for total internal reflection. An addition of a diffuser layer over the cladding (Figure 3-5) is also used to protect the fibre from mechanical damage, especially for fibres with silica core. The scattering mechanisms in the claddings of the fibres are used to leak out the light rays getting into the claddings. Generally, side emission occurs when radiation from a radiation source is launched at the end face of fibre, this then travels through the core to the other parts of the fibre until it passes through the side of the fibre. This process may possibly cause a loss of radiated light due to the optical properties of the fibre parts, such as material absorption which can be caused from fibre parts and/or scattering particles.

Zajkowski et al. [8] reported that the emission along the fibres drops exponentially under the condition of uniform treatment along the fibre length. However, other treatment techniques show the possibility of making an optical fibre emit uniformly along the side of the fibre. Spigulis et al. [7] showed an improved side emission along an optical fibre, consisting of a silica core fibre with scattering mechanism particles. Creating notches with controlled distances in the cladding of an optical fibre can also result in an improved uniformity of side emission along the length of the fibre, as demonstrated by Sillyman et al. [3].

For efficient side emission results, the selection of a side emitting optical fibre for an application should be based on the optical transmission of the materials from which the fibre parts (core, cladding, diffusing jacket and scattering particles) are made with respect to the required transmission of the EM spectral band. Impurities such as iron, copper, cobalt, nickel, manganese and chromium have the effect of absorbing the radiation increasing attenuation, and consequently, decreasing the overall radiation intensity in the fibre [93, 99-100]. The UV absorption in a fibre can result from [98-99, 101]:

- Intrinsic and extrinsic absorption
- Absorption from impurity ions, such as Cr^{3+}, Fe^{3+} and Cu^+
- Processing conditions used, such as crucible material, and atmosphere; Pt and CCl_4 being a particularly bad combination

3.3. Characterisation of Commercial Side Emitting Optical Fibres

3.3.1. Objective

A characterisation of various types of commercial side emitting optical fibres was undertaken to investigate their design; such as the number of parts in each fibre, material of the parts, type of scattering mechanism and the location of the scattering mechanism. The other objective is to study the spectral transmission behaviour of the commercial side emitting optical fibres. The aim behind this work is to determine the most efficient side emitting optical fibre to be used for epoxy curing in a closed mould application by spectral emission in the UVA band (315 nm - 400 nm).

3.3.2. Fibre Characterisation Experiments

3.3.2.1. Experimental Details

Materials

The characterisation was conducted on 7 commercial side emitting optical fibres. The fibres are listed in Table 3-1 and shown in Figure 3-8.

Table 3-1. Types of the commercial side emitting optical fibres and untreated fibre used for the characterisation process

	Fibre	Outer diameter (µm)	Designed loss of total radiation per length (m)	Supplier
Glass core fibres	1	727	Not provided	Light Tech, Inc. [102]
	2	1083	20	Light Tech, Inc. [102]
	3	1259	2	Light Tech, Inc. [102]
	4	1540	Not provided	Light Tech, Inc. [102]
	5	937	Not provided	Fiber Tech GmbH [103]
Polymer optical fibre (POF)	6	1000	Not provided	Mitsubishi Rayon of Japan [104]
	7	1551	Not provided	Mitsubishi Rayon of Japan [104]
	8	1000	Not designed for side emission	Mitsubishi Rayon of Japan (not treated) [104]
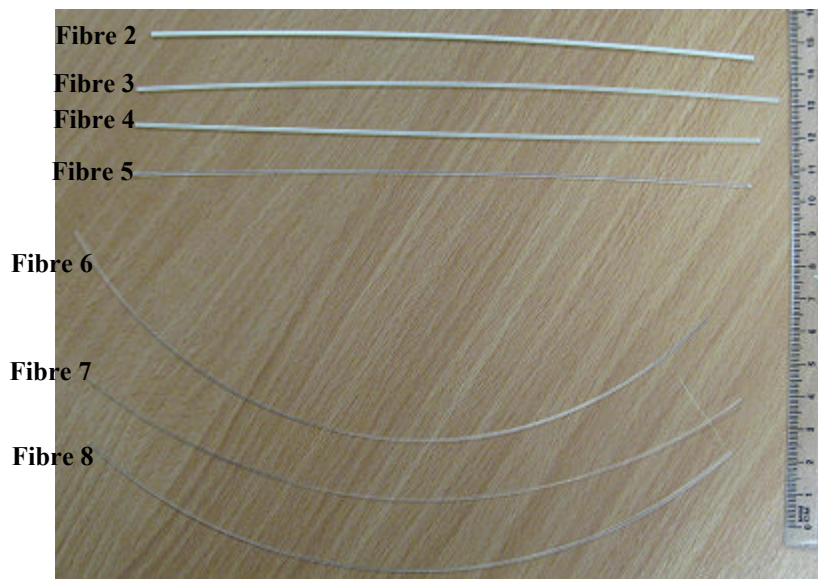
Figure 3-8. Photographic image of the different types of optical fibres as listed in Table 3-1: Silica core fibres 2 to 4, PMMA optical fibres 5 to 7.

Testing techniques

To determine the number of fibre parts, part materials, cross-sectional dimensions and scattering mechanisms, the following testing techniques were conducted:

1. **Scanning Electron Microscopy (SEM)** (Jeol Winsem, JSM-6400)**:**

   - Identification of optical fibre parts (core, cladding, diffusing jacket)

   - Finding the location of scattering particles to study their distribution and dimensions

2. **Energy Dispersive X-ray spectroscopy (EDX)** (Jeol Winsem, JSM-6400)**:**

   - Identification of optical fibre part materials

   - Determine the material of scattering particles

3. **Fourier Transform Infrared Spectroscopy (FTIR)** (Bruker, Tensor 27)**:**

- Used for determining the polymeric material of the optical fibre parts. This technique was used for confirming the polymeric materials of the optical fibres found using **EDX**.

4. **Transmission Light Microscope** (Nikon Digital Camera, DXM 1200F)**:**

- Measurements of cross-sectional dimensions of optical fibre parts

- Study the surface perforations of PMMA optical fibres

The sample preparations of the optical fibres for the above testing techniques are reported in Appendix E-1.

Quantification of the volumetric density of particles from the SEM-secondary electron images is possible by using computer software like Image J [105]; which relies on differentiating the variation of the image contrast or 'pixels' for measuring the particles density. Such software requires images which are gathered from a polished or 'flat' sample. But polishing the optical fibres will contaminate the samples and will result in improper information. Thus, an alternative technique was used. The particle volume density was estimated from an area of 400 μm^2 (20μm x 20μm) of all fibre microstructure SEM (scanning electron microscopy) images using the scale bar provided with each image, Figure 3-9 shows an example. For each fibre, the calculation was carried out from an average of three locations at which low, medium and highest numbers of particles were observed. The particles were assumed to be circular. The estimated particle volume fraction V_P was calculated using the following,

$$V_P \quad = \quad \frac{\text{Particles Areas}}{\text{Total Area (400 } \mu m^2)} \qquad \qquad \textbf{Equation 3-4}$$

where, the shape of the particles were assumed to be circular ($A_{Particles} = \frac{1}{4}\pi d^2$), Figure 3-9.
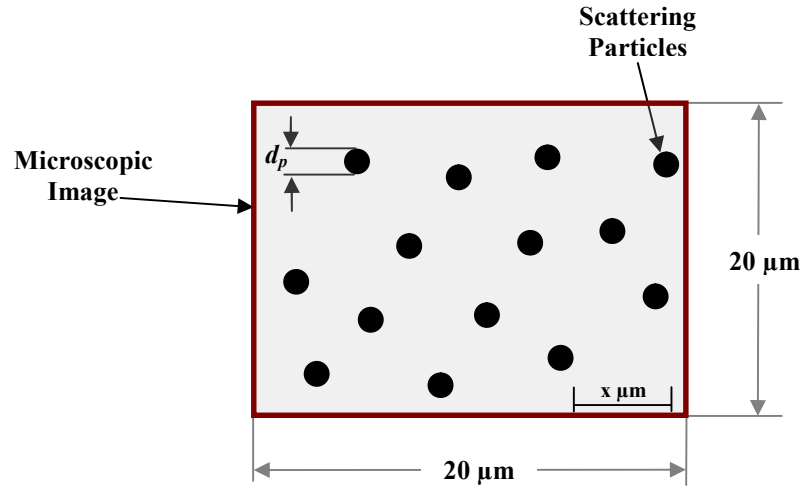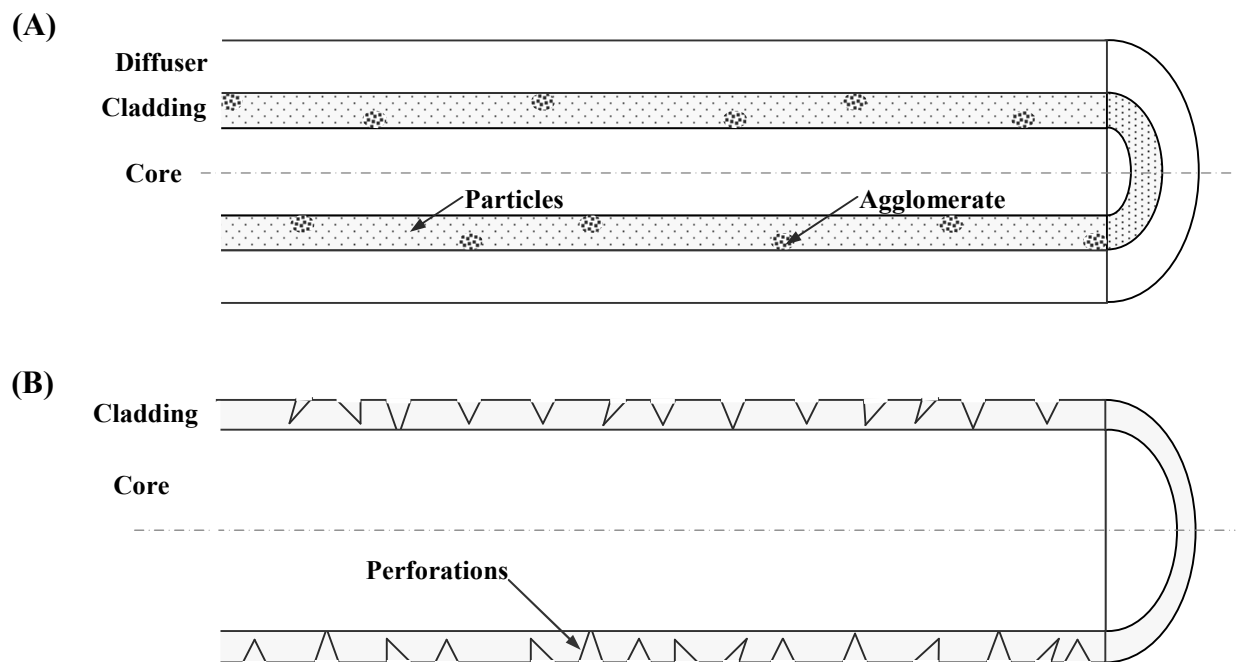

Figure 3-9. Schematic illustration of the estimated particle volume friction V_P measurements from a microscopic image.

3.3.3. Results and Discussion

The testing results for all of the commercial side emitting optical fibres are summarised in Table 3-2. Generally, the fibres can be categorized into two main types, Figure 3-10:

(A) *Silica core fibres* (1, 2, 3, 4 and 5, Table 3-2), each fibre consists of 3 parts: silica core, polymeric cladding and diffuser. The side emission (scattering mechanism) results from particles embedded in the polymeric cladding of the fibre

(B) *Polymer optical fibre* (POF) (6 and 7, Table 3-2) made out of 2 parts: PMMA core and fluorinated cladding with surface perforations such as micro-holes used as a scattering mechanism in the cladding of the fibres

Figure 3-10. Schematic illustration of the design cross-section of the two types of side emitting optical fibres (not to scale):

(A) Glass optical fibre consisting of core, cladding and diffuser. The cladding of the fibre contains particles and agglomerates to cause side emission

(B) Polymeric optical fibre made with core and cladding. The side emission mechanism of this fibre occurs by means of irregularly distributed surface perforations on the cladding of the fibre

Core, cladding and diffuser of fibres 1-4 are found to be of the same materials compared to fibre 5. They are made of a silicon dioxide (silica (SiO_2)) core, Poly(Dimethylsiloxane) cladding and Poly(Amide-6) diffuser with ZnO particles embedded in their claddings, as shown in the EDX spectrum in Figure 3-11. Fibre 5 is also made of silicon dioxide (silica (SiO_2)) core and Poly(Dimethylsiloxane) cladding, however, its scattering particles and diffuser material were found to be Al_2O_3 (Figure 3-12) and Poly(Vinyl Chloride), respectively. The scattering particle distributions of all fibres were found to be inconsistent across the microstructure of the fibre claddings as shown in the SEM-secondary electron images of Figures 3-13 to 3-17. The scattering particles in fibres 1-5 were found either individually or accumulated as agglomerate. The formation of agglomerates could have resulted from insufficient mixing of the particles with the cladding material during the manufacturing of these fibres. The refractive indices listed in Table 3-2 vary slightly across the range of wavelengths discussed here, and therefore the wavelength-dependence is not considered, as long as the condition $n_{core}>n_{cladding}$ is satisfied to achieve total internal reflection at all wavelengths.

The resulted volume fraction V_P form an area of 400 μm^2 from the resulted microscopic images, as shown from an example in Figure 3-16, is given in Table 3-2 for semi-quantitative comparison of the different fibre specimens (fibres 1-5). Fibres 4 and 5 contain the highest density (Table 3-2) of particles and a larger number of agglomerates, ~ 40 μm and 50 μm diameter; respectively, compared to the other fibres, as shown in Table 3-2 as well as in Figures 3-16 and 3-17. Fibre 1 has a very low quantity of particles (Table 3-2 and Figure 3-13). The particles in fibre 5 were distributed mainly as agglomerates (Figure 3-17). Thus, it is expected that an increase in particle density may result in larger and higher number of agglomerates.

Both fibre 6 and 7 were found to be made of a PMMA core with Poly(Vinylidene Fluoride) cladding. The scattering mechanism of these fibres is a perforation as a result of pinched

micro-holes on the outer surface of the cladding. The SEM-secondary electron microscopy and Transmission Light Microscope imaging tests on samples from fibres 6 and 7 were conducted in order to observe the perforation on the side surface of the claddings of these fibres. The micro-holes in these claddings were found to be irregular in sizes, Figures 3-18 and 3-19. The sizes of the micro-holes varied from 15 μm to 45 μm, and both of the fibres exhibited a medium density of irregular micro-holes. The distributions of micro-holes along the cladding outer surface were found to be inconsistent. The treatment appears to be done only on part of the fibre claddings all through the fibres length, while the other sides were untouched (Figure 3-19A). This could be a design methodology to control the side scattering efficiency with respect to length. The sizes of the micro-holes on the cladding not only varied in size, but also varied in depth as some of the micro-holes reached the core of the fibre, as shown in Figure 3-19B.

Table 3-2. Characterisation results of commercial side emitting optical fibres parts and scattering particle materials with particles size and distribution. The refractive indices for all fibres materials were estimated in the UV-A and visible blue spectrum [106, 107] (wavelength-dependence is not considered here)

Fibre	Optical Fibre Parts Material			Fibres Parts		Scattering Particles Material & Refractive Index	Particles or Micro-Holes Sizes (µm) & Density	Presence of Agglomerate / Size (µm)	Comments of Scattering Medium
	Core	Cladding	Diffuser	Diameter (µm)	Refractive Index				
1	Silicon Dioxide (SiO_2)	Polydimethylsiloxane (PDMS)	Polyamide-6 (PA6)	Core : 386 Cladding : 536 Diffuser : 727	Core : 1.47 Cladding : 1.40 Diffuser : 1.53	Zinc oxide (ZnO) 2.22	$0.5 < S_P^* < 2$ Very low density, $\sim 1.0 \times 10^{-2}$	$2 < S_G^* < 5$	Both particles and agglomerate sizes were found irregularly distributed along the fibres
2	Silicon Dioxide (SiO_2)	Polydimethylsiloxane (PDMS)	Polyamide-6 (PA6)	Core : 550 Cladding : 743 Diffuser : 1083	Core : 1.47 Cladding : 1.40 Diffuser : 1.53	Zinc oxide (ZnO) 2.22	$0.1 < S_P^* < 3$ Low density, $\sim 2.9 \times 10^{-2}$	$1.5 < S_G^* < 9$	
3	Silicon Dioxide (SiO_2)	Polydimethylsiloxane (PDMS)	Polyamide-6 (PA6)	Core : 796 Cladding : 938 Diffuser : 1259	Core : 1.47 Cladding : 1.40 Diffuser : 1.53	Zinc oxide (ZnO) 2.22	$1 < S_P^* < 2$ Medium density, $\sim 7.1 \times 10^{-2}$	$6 < S_G^* < 40$	
4	Silicon Dioxide (SiO_2)	Polydimethylsiloxane (PDMS)	Polyamide-6 (PA6)	Core : 750 Cladding : 1050 Diffuser. : 1540	Core : 1.47 Cladding : 1.40 Diffuser : 1.53	Zinc oxide (ZnO) 2.22	$0.1 < S_P^* < 3.5$ High density, $\sim 11.8 \times 10^{-1}$	$1 < S_G^* < 50$	
5	Silicon Dioxide (SiO_2)	Polydimethylsiloxane (PDMS)	Ethylene tetrafluoroethylene (ETFE)	Core : 607 Cladding : 734 Diffuser : 937	Core : 1.47 Cladding : 1.48 Diffuser : 1.54	Aluminium oxide (Al_2O_3) 1.79	$0.5 < S_P^* < 2$ High density, $\sim 12.5 \times 10^{-1}$	$1 < S_G^* < 10$	
6	Polymethyl methacrylate (PMMA)	Polyvinylidene Fluoride (PVDF)	-	Core : 980 Cladding : 1000	Core : 1.48 Cladding : 1.41	side surface pinched micro-holes	$15 < S_H^* < 45$	-	Irregularly distributed micro-holes
7	Polymethyl methacrylate (PMMA)	Polyvinylidene Fluoride (PVDF)	-	Core : 1494 Cladding : 1551	Core : 1.48 Cladding : 1.41	side surface pinched micro-holes	$15 < S_H^* < 45$	-	
8	Polymethyl methacrylate (PMMA)	Polyvinylidene Fluoride (PVDF)	-	Core : 980 Cladding : 1000	Core : 1.48 Cladding : 1.41	Not treated (normal optical fibre)			

Note:
- ❖ S_P is Scattering Particles size
- ❖ S_G is Scattering Particles agglomerates size
- ❖ S_H is Micro-Holes sizes

❖ **The estimated particle volume fraction V_P was found from SEM-BSE image from 20 particles and the distance between them (for all of the optical fibres)**
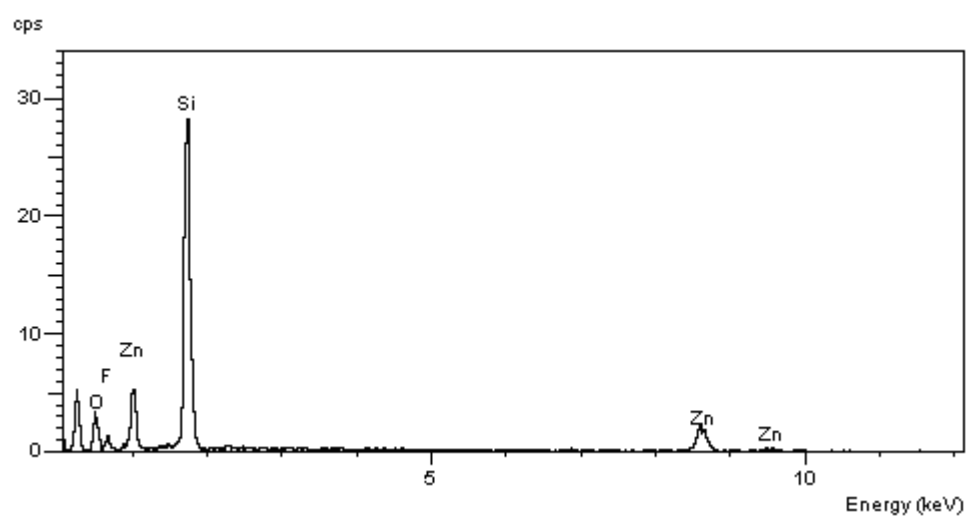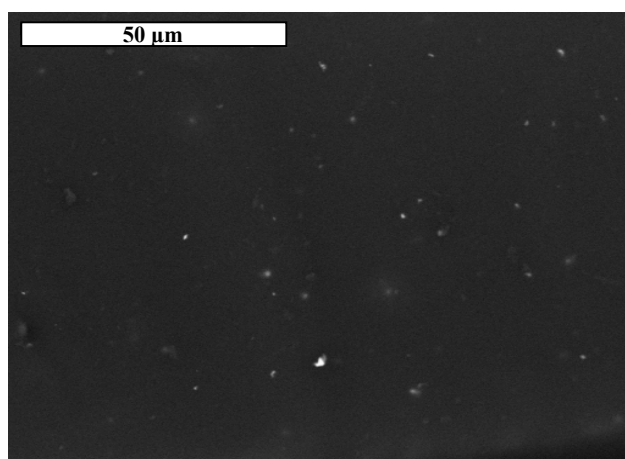
Figure 3-11. EDX spectrum of fibre 3 scattering particles. The scattering particles material was identified by the zinc, Zn, peaks.
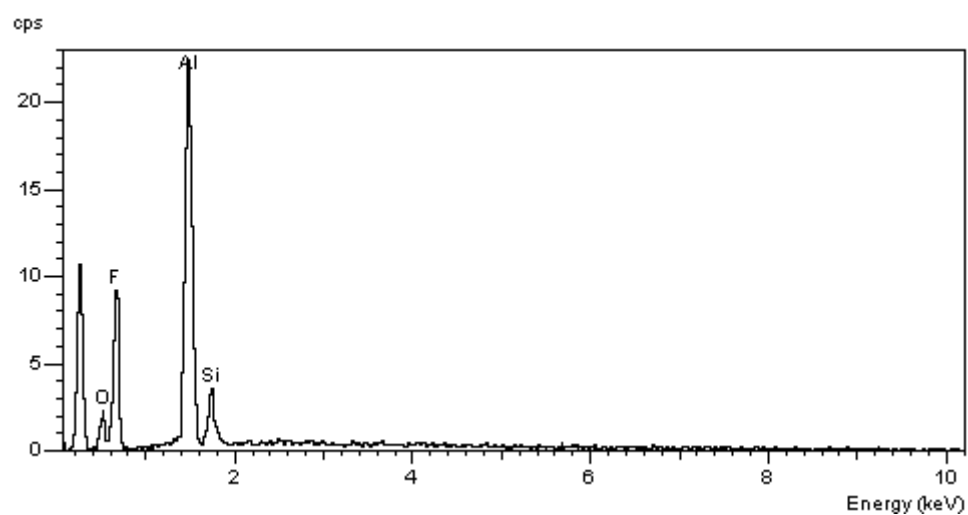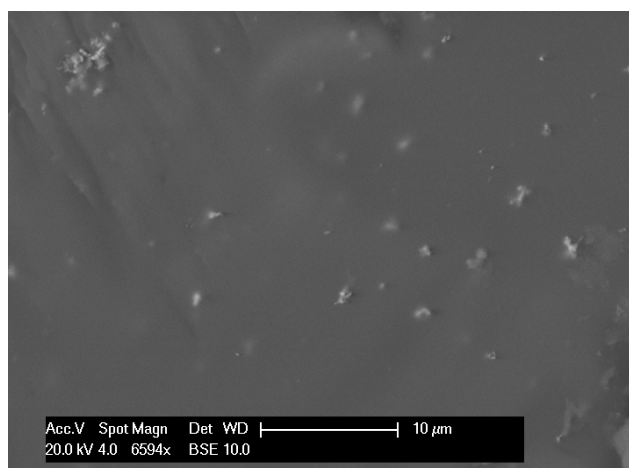

Figure 3-12. EDX spectrum of fibre 5 scattering particles. The scattering particles material was identified by the aluminium, Al, peak.
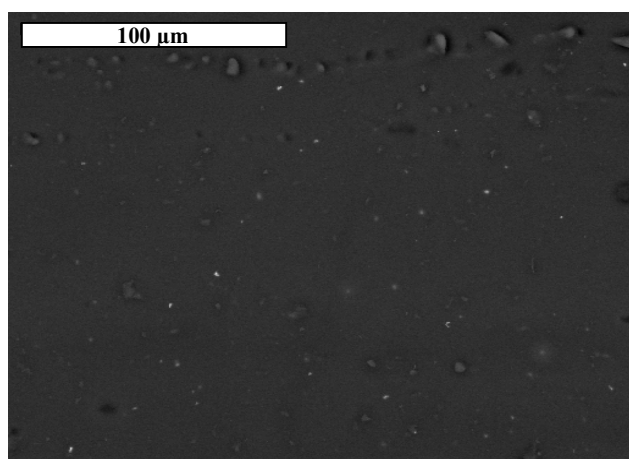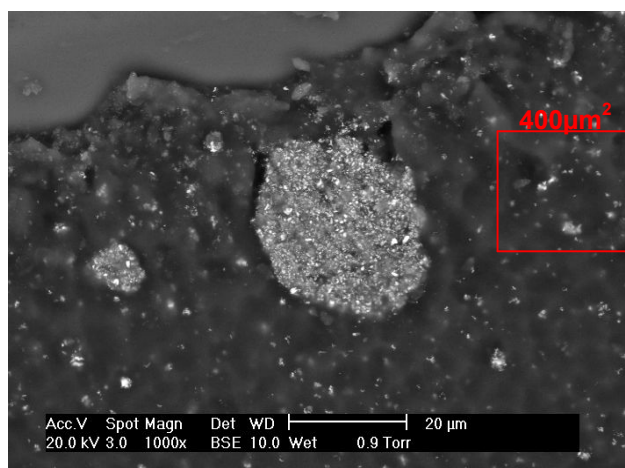
Figure 3-13. SEM-BSE image of fibre 1 cross-section showing ZnO scattering particles.

Figure 3-14. SEM-BSE image of fibre 2 cross-section showing ZnO scattering particles.

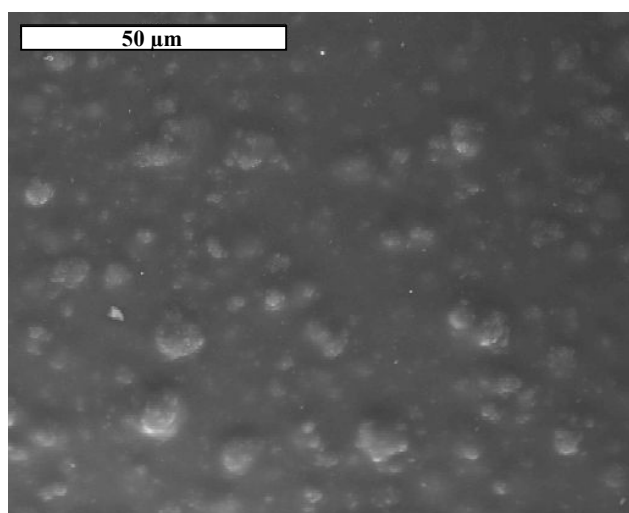**Figure 3-15.** SEM-BSE image of fibre 3 cross-section showing ZnO scattering particles and agglomerate.

Figure 3-16. SEM-BSE image of fibre 4 cross-section showing ZnO scattering particles and agglomerates.

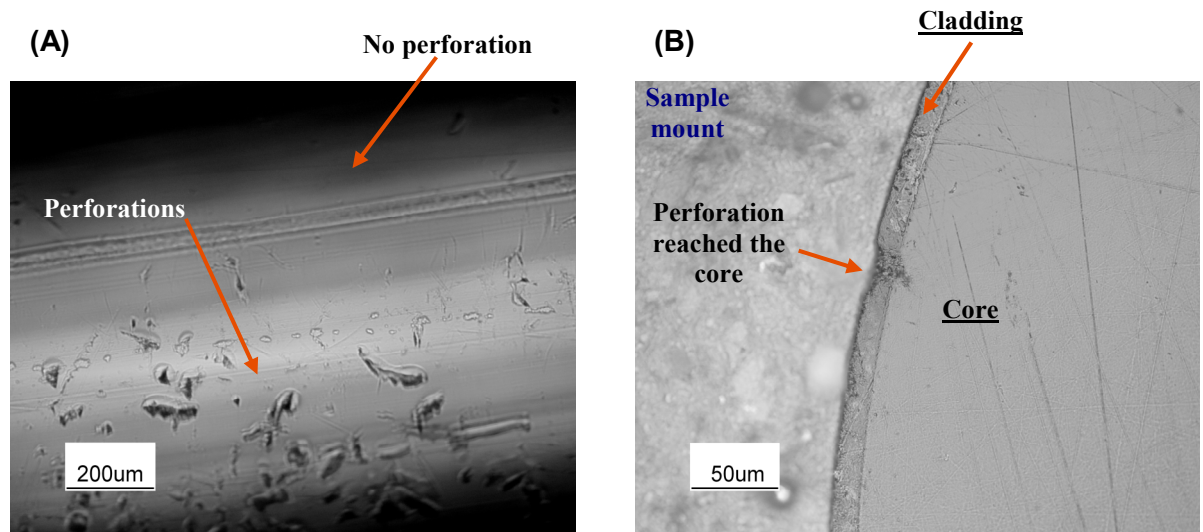**Figure 3-17.** SEM-BSE image of fibre 5 cross-section showing Al_2O_3 scattering particles and agglomerates.
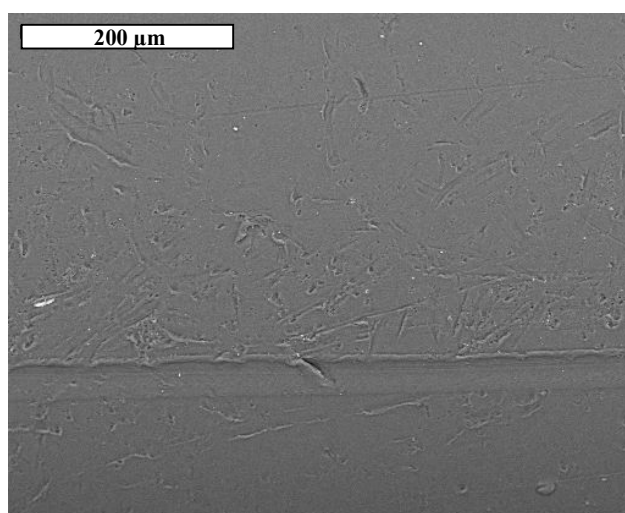
Figure 3-18. SEM-BSE image of fibre 6 showing side surface micro-holes.

Figure 3-19. Transmission Light Microscope images of fibre 6 showing side surface micro-holes:

    (A) Side view image of irregular perforations

    (B) Fibre 6 end cross-section showing pinched micro-hole that reached the core

3.4. Side Emission Spectral Analyses of Fibres (Spectroscopic Measurements)

Optical transmission of the commercial side emitting optical fibres in the spectral range from 280 nm to 450 nm (UVA and visible blue bands) is investigated while coupled to a high radiation emission source comprising a mercury lamp delivering a nominal flux density of 40 W/cm^2.

3.4.1. Experimental Details

3.4.1.1. Equipment Involved in Measuring Spectral Output

For the experiments carried out in this study, a BlueWave 200 [22] radiation source (mercury 'Hg' lamp) was used with a nominal power of 200 W, designed to deliver a light beam for spot curing applications, as shown in Figure 3-20. This radiation source was equipped with a mercury (H) bulb with major emission peaks at wavelengths of 368 nm, 406 nm and 440 nm (see Figure 3-21) and a reflector set-up to deliver a light beam through a mono-refractive index silica glass rod light guide of diameter of 5 mm. The effective flux density (radiant power per unit area) was approximately 40 W/cm^2 over the spectral range from 280 nm to 450 nm. The lamps intensities at various spectral bands were supplied as follows [22]:

Total	(280-450 nm)	40+ W/cm^2
Visible	(400-450 nm)	17+ W/cm^2
UVA	(320-395 nm)	17+ W/cm^2
UVB	(280-320nm)	7 W/cm^2

Figure 3-20. BlueWave 200 [22].
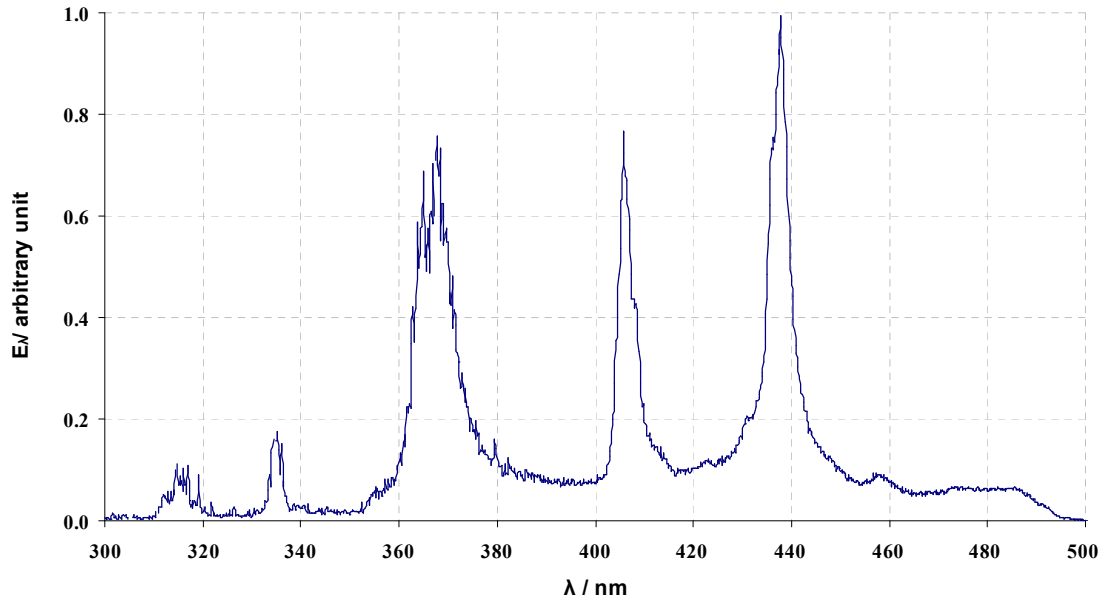
Figure 3-21. Example figure of the emission spectrum E_λ of the BlueWave 200 lamp (Hg lamp), recorded using USB 4000 at a distance 50 cm away from the lamp.

The transmission spectrum was monitored during the experiments using a USB4000 spectrometer (Ocean Optics [89]). The USB4000 spectrometer used here is the same as the one shown in Figure 2-25D of Chapter 2. The radiation was collected from the side of the fibre samples using a 1 mm diameter commercial silica glass optical fibre with half cone acceptance angle (θ_{ac}) of 12.4° and passed directly into the spectrometer. The spectrometer enabled measurement of the absolute spectral irradiance E_λ of the radiation emitted from the side of the fibre samples, in the range of 200 nm to 850 nm wavelength.

3.4.1.2. Experimental Preparations

Fibre samples of 1 m long (Table 3-1) were each fitted with three in-house made hollow brass connectors (10 mm long and 6 mm diameter) along their length. The three brass connectors were attached to each optical fibre using an epoxy adhesive. One brass connector was for connecting the fibre with the Hg lamp and the other two were used for positioning the fibre.

After fitting these connectors, the launch face of the fibre was polished to a 1 μm finish to reduce refraction and diffuse scattering. During each experiment, two of the three fibre connectors were clamped to two holders to position the fibre in a straight line on a scaled base rail, as illustrated in Figure 3-22. The third connector of the fibre was then abutted to the end of the silica glass light guide of the Hg lamp and secured using a self-made aluminium tube fitting (50 mm long, 7 mm inside diameter and 2 mm wall thickness), which allowed centring of the polished launch face end of the fibre sample relative to the light beam (Figure 3-22). The silica glass optical fibre of the spectrometer, which was used for data collection, was clamped to a movable holder on the scaled base rail (Figure 3-22).

The two holders of the optical fibre connecters were fixed throughout the experiments and each fibre was aligned with the silica glass light guide of the Hg lamp during the experiments for consistent collection of measurements along the fibres. The holder of the silica glass optical fibre of the spectrometer was used for collecting data from several longitudinal (x-axis) and radial (r-axis) positions.

The spectral data from the side surface of each fibre sample was collected at intervals of 5 cm along the fibre length. The data was collected in five steps axially at each longitudinal location (x). At each location, the end face of the silica glass optical fibre of the spectrometer was moved radially (r) away from the outer surface of the optical fibre at intervals of 2 mm starting from 2 mm to 10 mm.
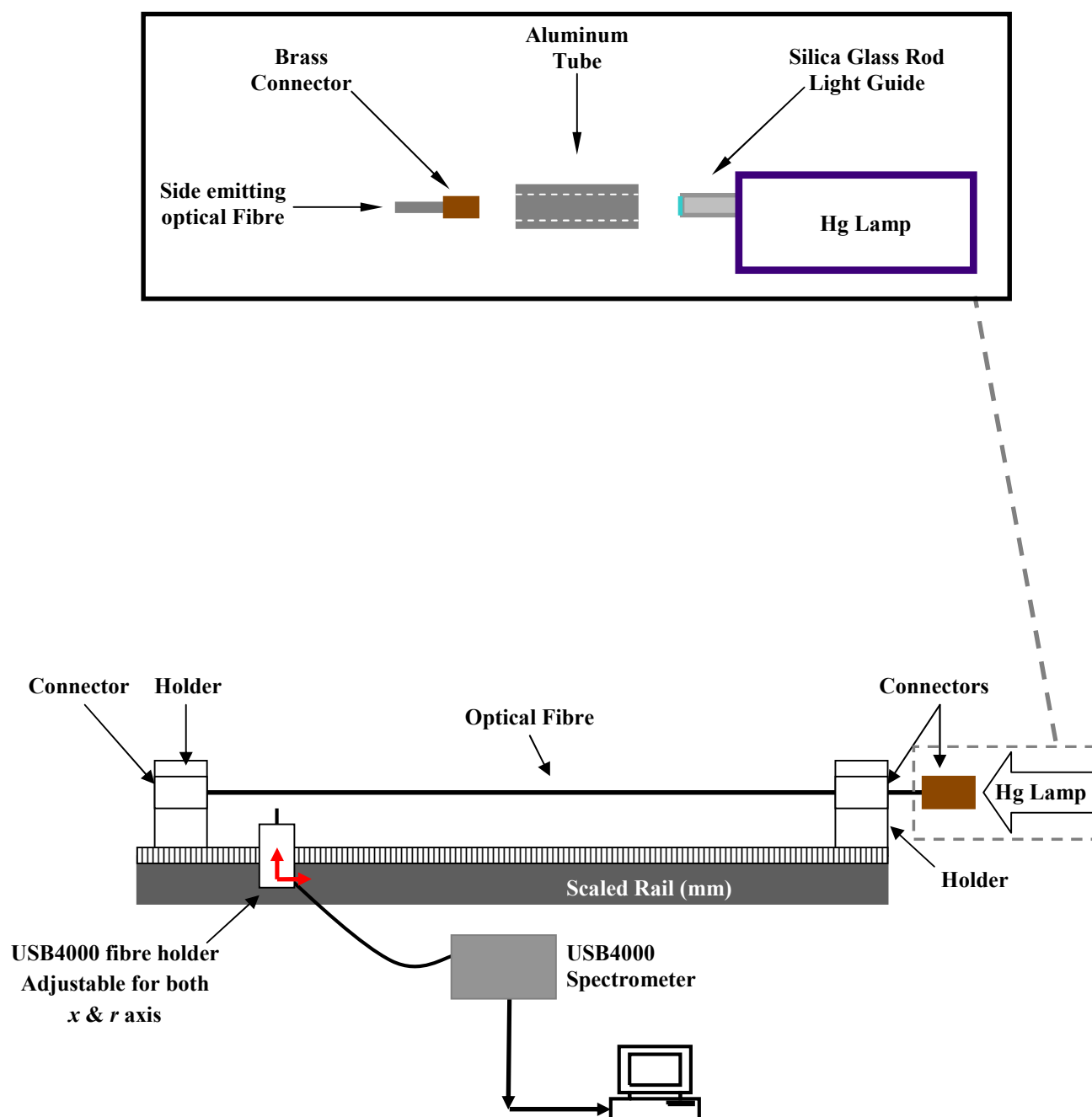
Figure 3-22. Schematic illustration of the entire spectroscopic data collection experimental setup.

3.4.2. Results and Discussion

In the photocuring process, as discussed in Chapter 2, the photoinitiator within an epoxy resin formulation is activated by a radiation in the UVA band (315 nm to 400 nm). Hence, the objective of this investigation is to study the performance of the spectral transmission from the side of fibres 1-7 in the UVA band using the Hg lamp with an emission output of 40 W/cm^2.

3.4.2.1. Optical Transmission from the Side of the Fibres

Fibres 1-5 have a scattering mechanism of the type shown in Figure 3-10a, and side emission takes place due to the particles in the cladding. In these fibres, the Hg lamp emission is launched at one end of the fibre from which the light rays enter the core and then some of the light rays escape to the cladding due to the small difference between their refractive indices (Table 3-2). The light rays then get into the medium where the randomly distributed particles are located in the cladding which causes the light rays to scatter in different directions depending upon the angle at which the light rays hit the particles. The light rays with an angle greater than the critical angle will be diverted out of the side surface of the fibre as a side emission. The scattered light rays with an angle smaller than the critical angle, may either be guided back into the core of the fibre or scattered out of the fibre by hitting another randomly distributed particle.

In the case of fibres 6-7 (Figure 3-10b), the light rays launched by the Hg lamp into the core of the fibre are expected to scatter out more efficiently when the light rays reach the irregularly distributed micro-perforations in the fibre cladding. As there is no added scattering material in these fibres there will be no back reflection or absorption, hence, once the light rays hit the micro-perforations they get diverted outward.

The polydimethylsiloxane cladding material of the silica core fibres 1-5 is transparent to UVA (315 nm to 400 nm) band, as reported by Masson et al. [108] and DeGroot et al. [106]. The diffuser materials of fibres 1-4 (Polyamide-6) and fibre 5 (Ethylene tetrafluoroethylene) generally exhibits high optical transmission in the UVA and visible bands [13, 25, 37]. The PMMA and the polyvinylidene fluoride (PVDF) materials of the core and the cladding, respectively, of fibres 6-8, were reported to be highly transparent in the UVA band [109, 110]. Yu et al. [111] observed a 100 % transmission of the PMMA in the UVA band when irradiated for 1 minutes using high-pressure mercury UV lamp (70 mW/cm^2). However, the polymeric materials of the fibres degraded when left for more than 3 minutes under continuous irradiation from the Hg lamp. This indicates that the polymeric materials of the fibres absorbed the UV irradiation and initiated a photochemical reaction that resulted in a photo-oxidation process which is in agreement with the literature [19, 100, 112]. This phenomenon is further discussed in Chapter 4.

The launched radiation from the Hg lamp into fibres 1-4 showed very low transmission at wavelengths below 380 nm when measured from the side of the fibres. Figure 3-23 shows an example of a typical spectrum emitted from the side of these fibres. The high absorption in the UVA band below wavelength 380 nm was expected to be caused by the zinc oxide (ZnO) particles contained in the claddings of these fibres, which has been reported by many authors [113-117].

In contrast, fibres 5-7 transmitted almost an identical spectral output of side (see for instance Figures 3-24 and 3-25) emission as the spectrum of the Hg lamp (Figure 3-21). The cladding on fibre 5 comprises aluminium oxide (Al$_2$O$_3$) scattering particles. The absorbance of aluminium oxide (Al$_2$O$_3$) in the UVA band is relatively low as discussed by Gluhoi et al. [118] and Demiryont et al. [119]. This explains why the transmission spectrum of the fibre and emission spectrum of the Hg lamp were identical. Thus, the aluminium oxide (Al$_2$O$_3$) scattering particles in the cladding of fibre 5 are more suitable to be used with the spectral emission in the UVA band compared to the zinc oxide (ZnO) scattering particles in fibres 1-

4. However, the high side emission of the 1 metre long polymeric fibres 6-7 (design type Figure 3-10b) in the UVA band make them even more suitable for delivering higher amounts of side emission compared to fibre 5 (design type Figure 3-10a). Other advantages of the polymeric fibres 6-7, beside their material low absorption in the UVA band, are their large core, thin cladding (Table 4-2), no diffuser layer and no absorbing scattering particles.
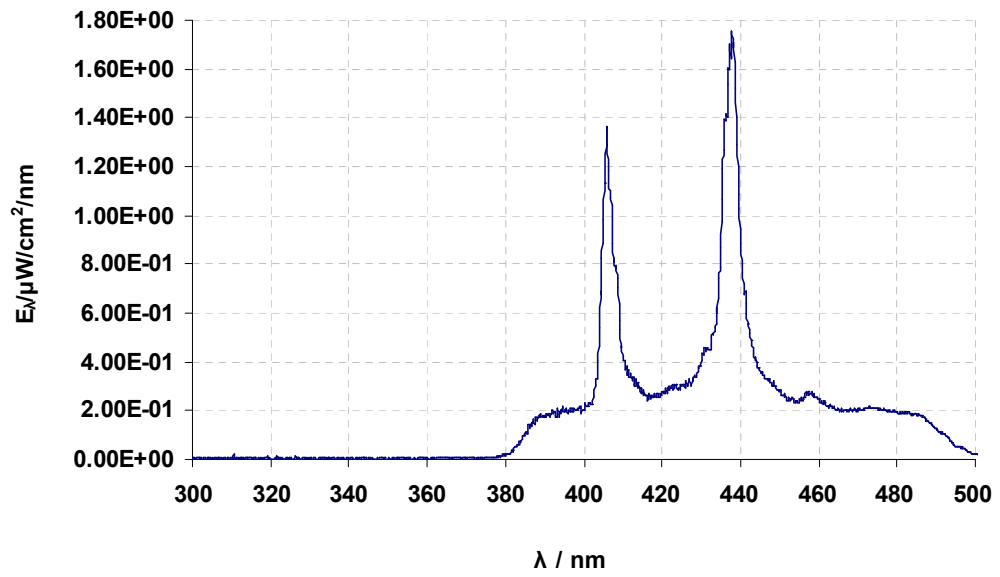
Figure 3-23. Emission spectrum E_λ of fibre 4, recorded at $x_n = 68.95$ cm and $r_n = 0.2$ cm. A typical example of the emission spectrum E_λ from the side of fibres 1-4 which contain ZnO particles in their claddings for side emission applications.
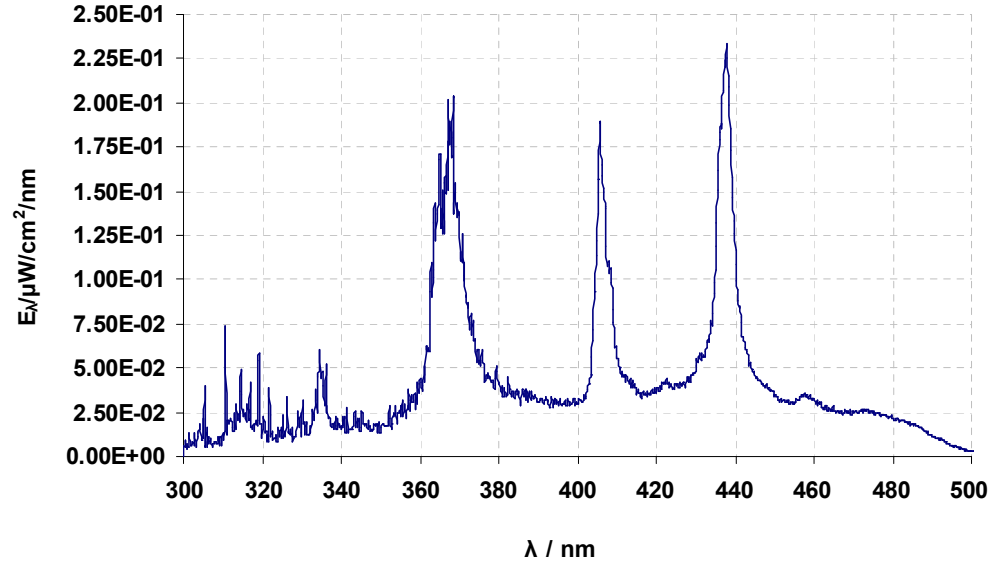
Figure 3-24. Side emission spectrum E_λ of fibre 5, recorded at x = 8.45 cm, r = 0.2 cm. This fibre contains Al_2O_3 particles in the cladding which caused the side emission.
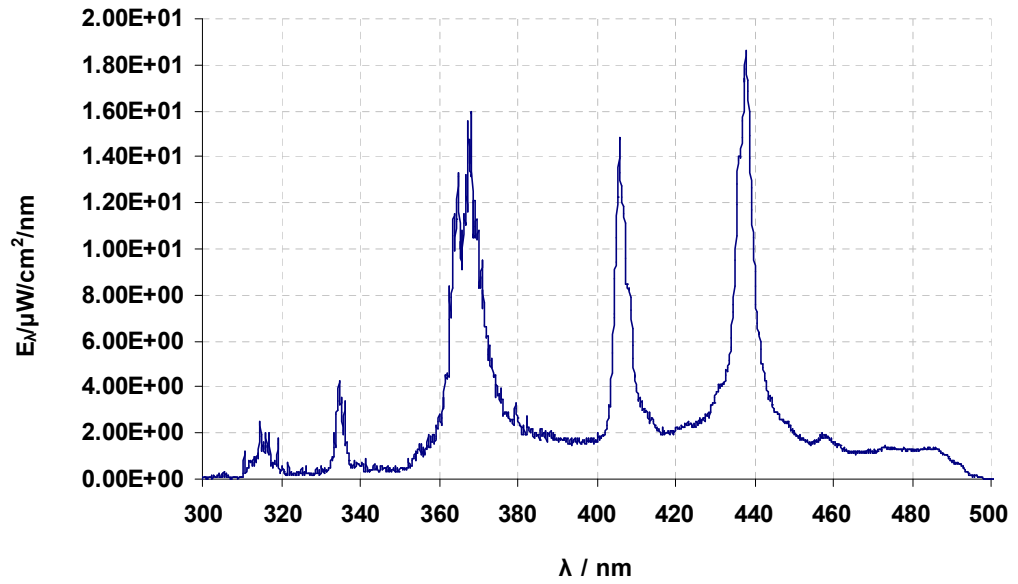
Figure 3-25. Side emission spectrum E_λ of fibre 6, recorded at x = 18.65 cm, r = 0.2 cm. The micro-perforations in the cladding of the fibre caused the side emission.

3.4.2.2. Irradiance (E_λ) Distribution along the Side of the Fibres

The photocuring of epoxy resin formulations, as shown from the response spectrum k_λ of the optimised formulations in Chapter 2, take place by an emission in the UVA band. Therefore, the irradiance E_λ measurements from the side of the 1 metre long samples of all fibres were studied in the UVA band at the emission wavelength of 368 nm. Furthermore, for a fibre to perform efficiently while embedded in a closed mould for a resin curing application, it should emit from its side sufficient UVA irradiation to cause the photocuring process. The higher the side emission the faster the polymerisation of the resin will be.

For fibres 1-5, with the particles in their claddings, the side emission was found to drop exponentially when measured either along the fibres or radially away from the outer surface of the fibres, as shown in Figures 3-26 to 3-29. However, fluctuation in the exponential decay along fibre 4 and fibre 5 were observed, Figures 3-28 and 3-29, respectively. This behaviour is more likely to have been caused by the irregularity of the high number of particles and particles agglomerates distributed within the claddings of these fibres as shown earlier in Figures 3-16 and 3-17. Although, the silica core of fibre 4 is larger than the core of fibre 2, the increased number of ZnO particles in the cladding of fibre 4 was found to reduce the side irradiance E_λ at wavelength 368 nm further when compared to fibre 2, as can be observed from Figures 3-26a and 3-26b.

The spectral emission measurements along the side of the 1 m long samples of the polymer optical fibres (POF) 6-7 indicated fluctuations in intensities as shown in Figures 3-30 and 3-31. Although fibre 8 was not treated, it was found to emit small amounts of radiation from the fibre side, Figure 3-32. The side emission of the untreated fibre was checked by launching radiation into the fibre from a tungsten halogen lamp [89] (emission intensity continuously increasing from 300 to 1000 nm), and no side emission was detected. Hence, the resulting side emission from the untreated fibre (fibre 8) occurs only when a high flux

density radiation source (Hg lamp) is employed. Theoretically, the launched radiation from the Hg lamp into fibre 8 should cause total internal reflection, as the cone of acceptance (θ_{ac}) of the PMMA core fibre is greater than the divergent angle of the silica rod light guide of the Hg lamp, see Appendix F-1 for more details. However, the POF part materials and design cause intrinsic and extrinsic losses as discussed by Zubia et al. [98], Takezawa [100] et al. and Appajaiah et al. [101]. These are the most likely reasons for the measurable side emission from the untreated fibre 8 when connected with the high emission Hg lamp. Furthermore, the untreated PMMA core fibre (fibre 8) generally emitted higher side emission at wavelength 368 nm than all of the treated silica core fibres.

A number of high intensity readings were recorded for fibres 6-7 (Figures 3-30 and 3-32). These resulted from the partially treated surface perforations as discussed earlier in relation to Figure 3-19a. The perforations in the cladding of these fibres were not made as a straight line of perforations perpendicular to the fibre length, instead, the perforations were oriented angularly along a helical axis which led to the collection of spectral data from both the treated and the untreated cladding surface, as can be seen from the schematic illustrated in Figure 3-33. This indicates that the non uniformity of side emission along the length of fibres 6-7 was due to the varying positions of perforations along the fibre, as shown in Figures 3-30 and 3-31. Therefore, the side emissions of the treated fibres 6-7 took place from both the micro-perforations in the cladding as well as from the untreated surface which emitted radiation due to intrinsic and extrinsic losses within the fibres. The intrinsic and extrinsic losses of the polymeric fibres are discussed further in Chapter 5.

Additionally, the side emission from most of the fibres dropped exponentially. The exponential decay of the side emission along each fibre sample (1 m long) was analysed by determining the attenuation coefficients k at wavelength 368 nm, as shown in Table 3-3. Fibre 2 is designed to lose the launched radiation from its side over a length of 20 metres from the fibre launch face, while fibre 3 loses the launched radiation in a length of 2 metres. The characterisation work on these two fibres suggests that the low density of ZnO particles

(Table 3-2 and Figure 3-14) in the cladding of fibre 2 resulted in a reduced loss of the launched radiation compared to fibre 3, which contains a medium density distribution of ZnO particles, as shown in Figure 3-26a and Figure 3-27a, respectively. These experimental observations were confirmed by the attenuation coefficients k values (Table 3-3) of fibre 2 and fibre 3, 6.4 x 10^{-3} cm^{-1} and 1.9 x 10^{-2} cm^{-1}, respectively. Generally an increase of particles in the claddings caused an increase in the attenuation coefficients k. However, the high absorption caused from the randomly distributed high density of ZnO particles and agglomerates in fibre 4 resulted in irregular side emission (Figure 3-28a) from this fibre which resulted in a lower attenuation coefficients k compared to fibre 3 (medium density of ZnO), as shown in Table 3-3.

(a)

◆ **2 mm,** ■ **10 mm (radial distance at which the data was collected)**

(b) △ **8.45 cm,** ○ **83.45 cm (longitudinal distance at which the data was collected)**
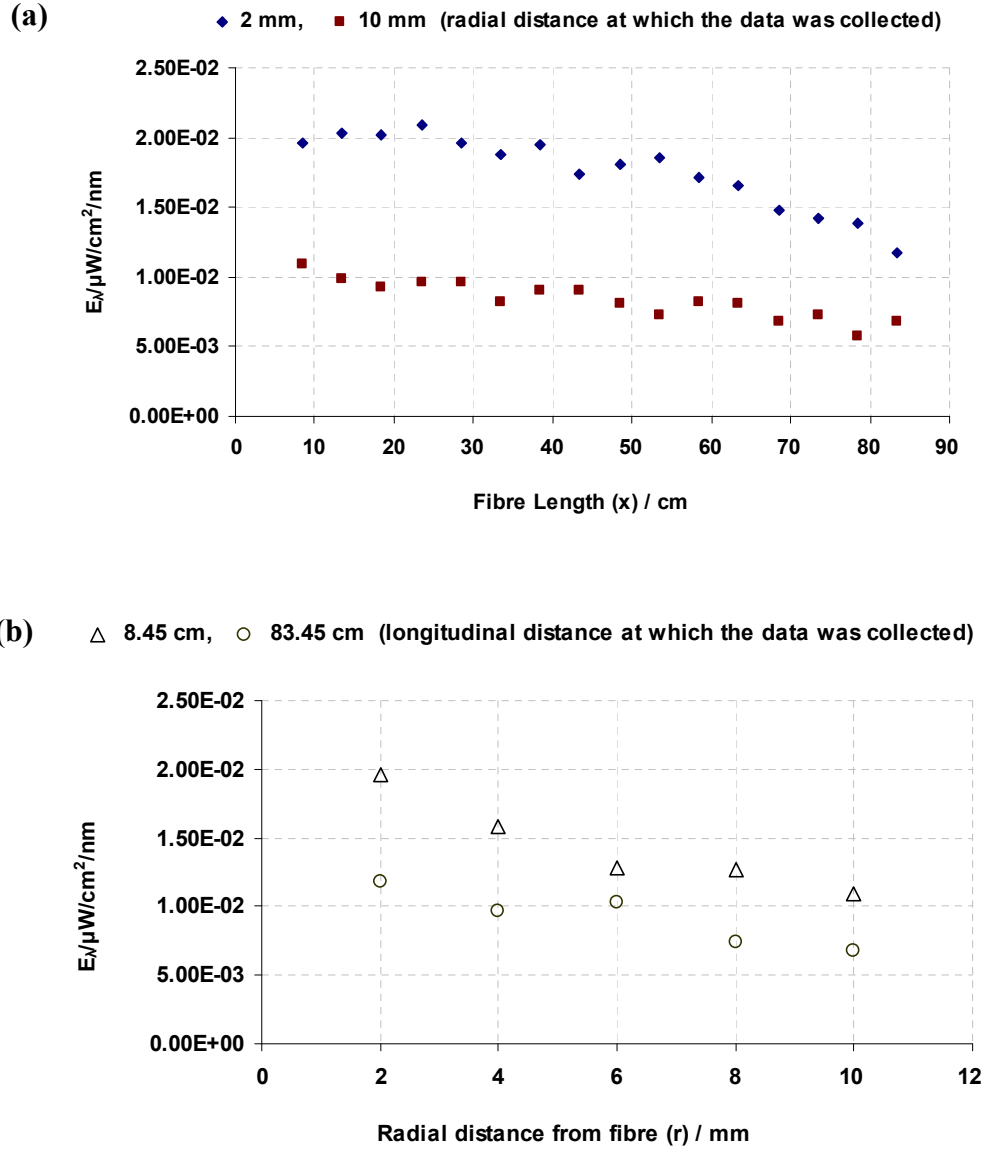
Figure 3-26. Irradiance E_λ at λ=368 nm from fibre 2 (containing ZnO particles in the cladding of the fibre):

(a) As a function of the position x along the fibre, showing spectral output collected at radial distance r from the side of the fibre

(b) As a function of the radial distance from the recorded spectral outputs at positions 8.45 cm and 83.45 cm along the fibre

(a)

◆ **2 mm,** ■ **10 mm (radial distance at which the data was collected)**

(b)

△ **8.85 cm,** ○ **83.85 cm (longitudinal distance at which the data was collected)**
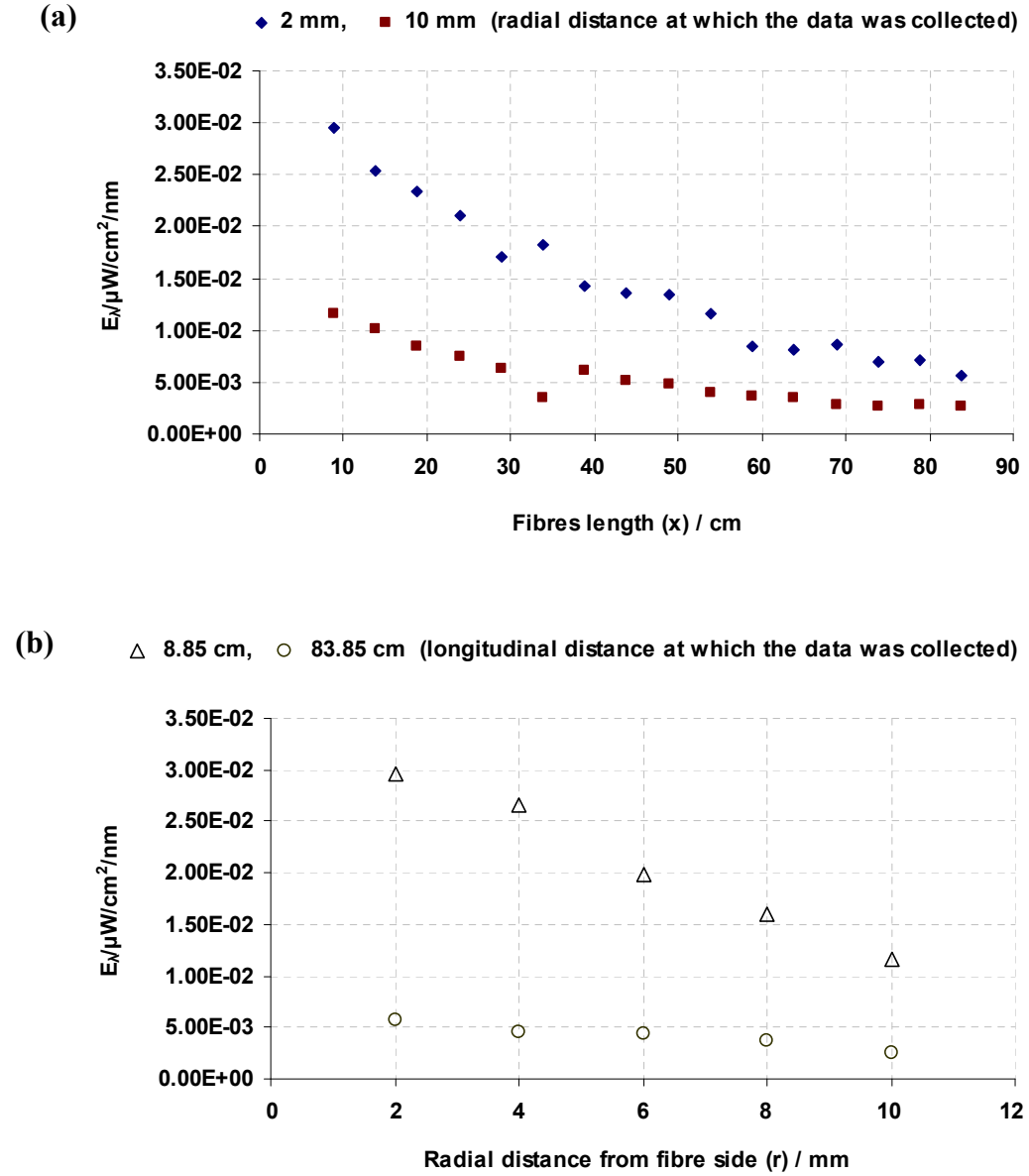
Figure 3-27. Irradiance E_λ at λ=368 nm from fibre 3 (containing ZnO particles in the cladding of the fibre):

(a) As a function of the position x along the fibre, showing spectral output collected at radial distance r from the side of the fibre

(b) As a function of the radial distance from the recorded spectral outputs at positions 8.85 cm and 83.85 cm along the fibre
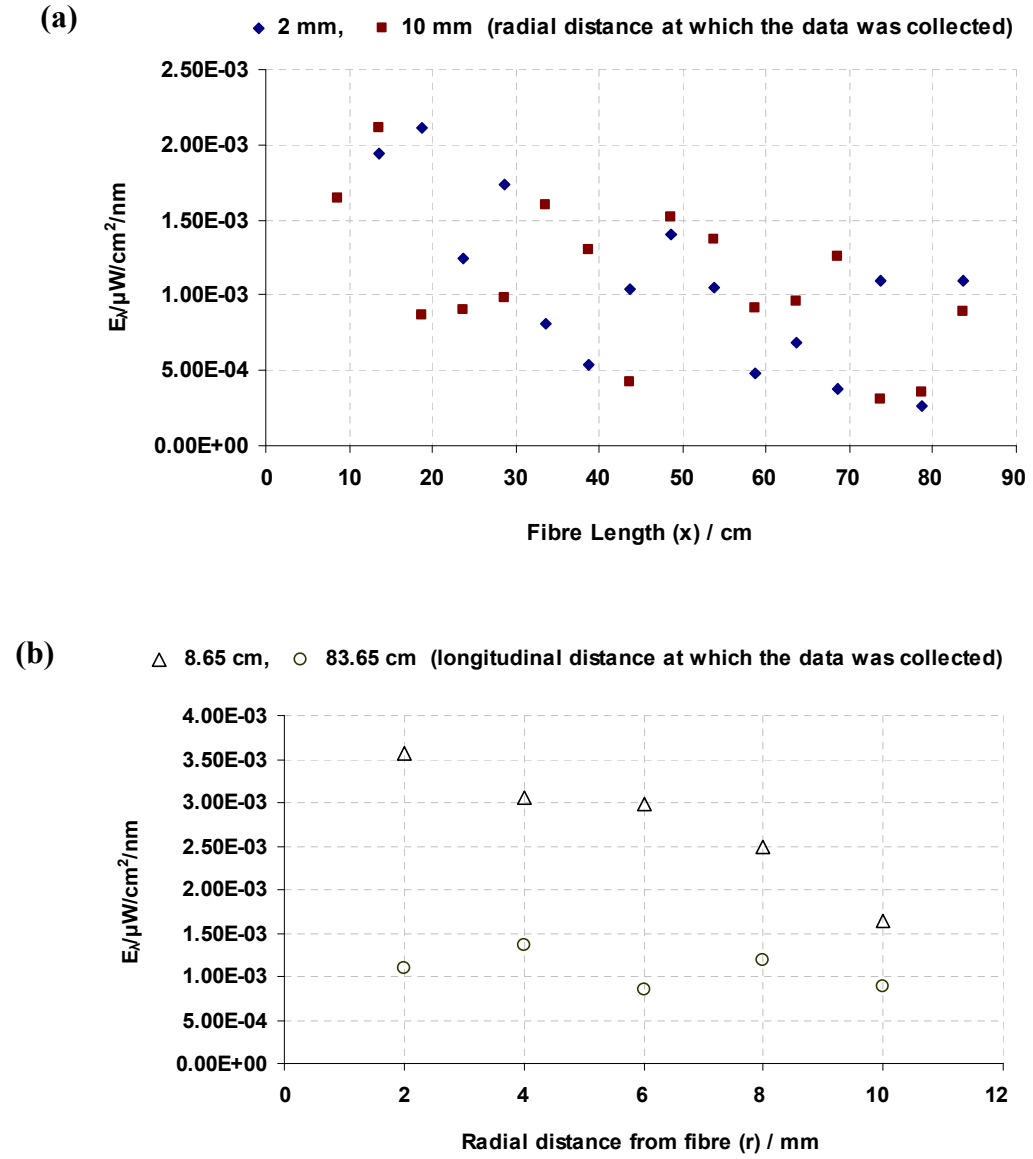
(a)

(b)

Figure 3-28. Irradiance E_λ at $\lambda=368$ nm from fibre 4 (containing ZnO particles in the cladding of the fibre):

(a) As a function of the position x along the fibre, showing spectral output collected at radial distance r from the side of the fibre

(b) As a function of the radial distance from the recorded spectral outputs at positions 8.65 cm and 83.65 cm along the fibre

(a)

◆ **2 mm,** ■ **10 mm (radial distance at which the data was collected)**

(b) △ **8.45 cm,** ○ **83.45 cm (longitudinal distance at which the data was collected)**

Figure 3-29. Irradiance E_λ at λ=368 nm from fibre 5 (containing Al_2O_3 particles in the cladding of the fibre):

(a)   As a function of the position x along the fibre, showing spectral output collected at radial distance r from the side of the fibre

(b)   As a function of the radial distance from the recorded spectral outputs at positions 8.45 cm and 83.45 cm along the fibre
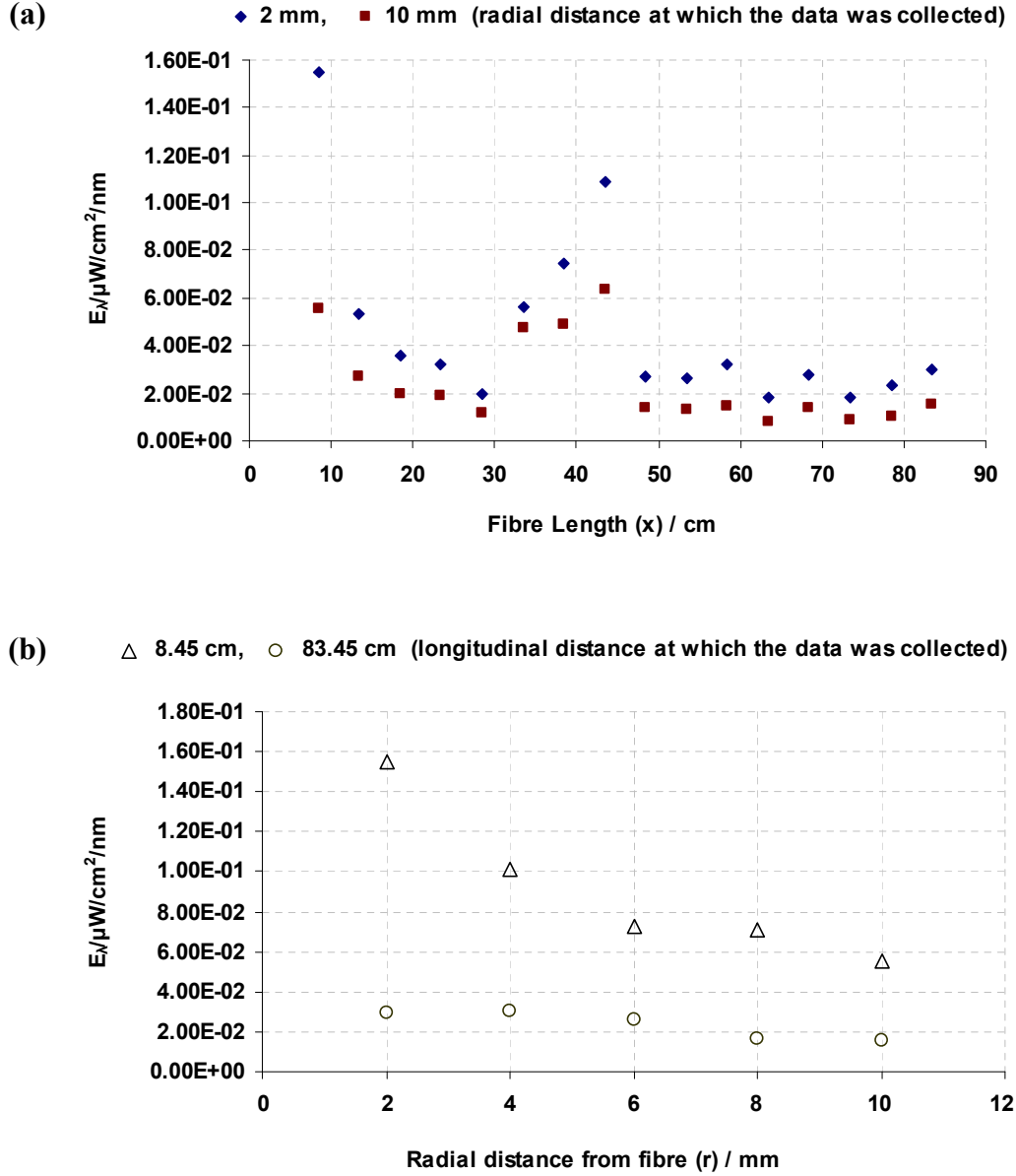
(a)

◆ **2 mm,** ■ **10 mm (radial distance at which the data was collected)**

(b)

△ **8.65 cm,** ○ **83.65 cm (longitudinal distance at which the data was collected)**

Figure 3-30. Irradiance E_λ at $\lambda=368$ nm from fibre 6 (micro-perforations in the cladding of the fibre):
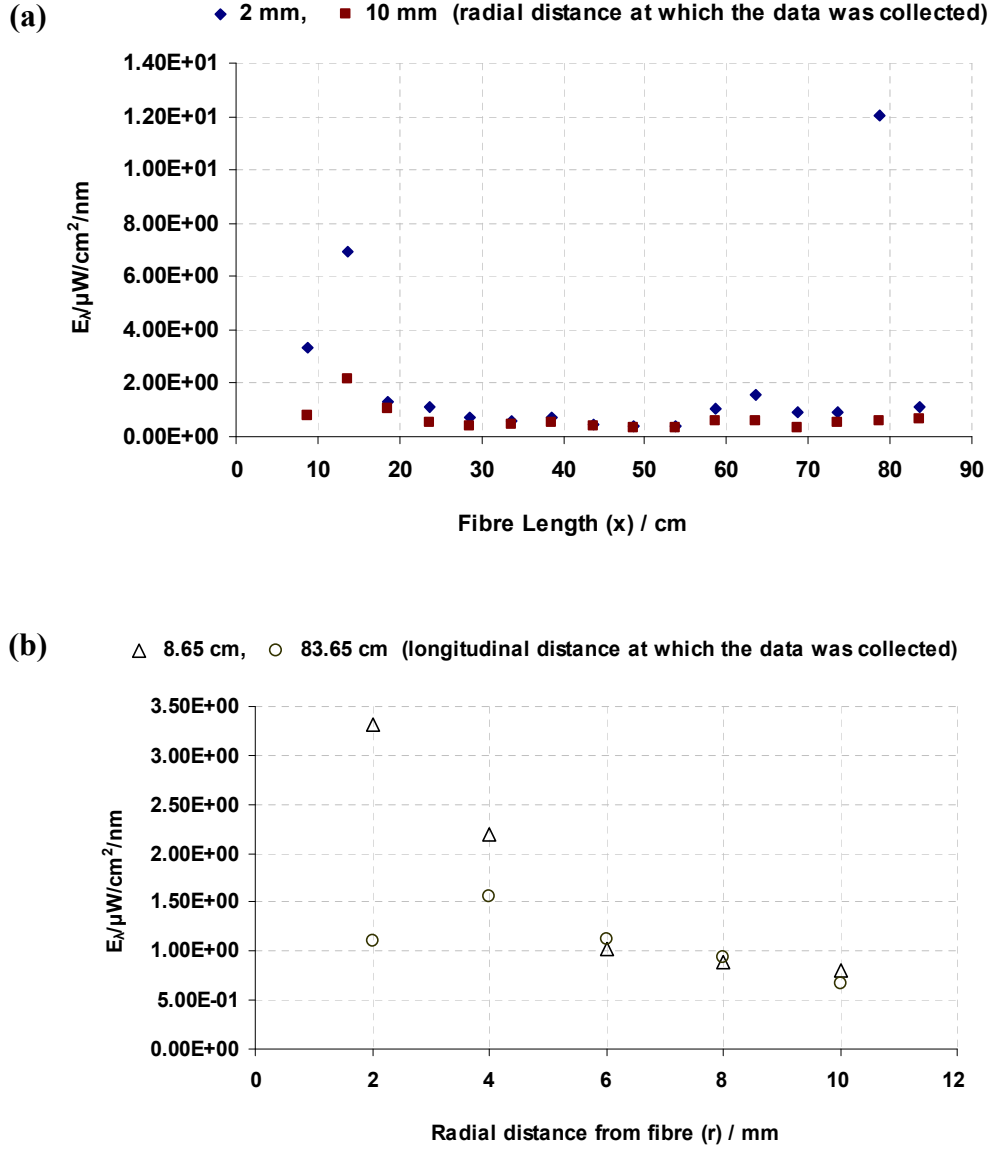
(a) As a function of the position x along the fibre, showing spectral output collected at radial distance r from the side of the fibre

(b) As a function of the radial distance from the recorded spectral outputs at positions 8.65 cm and 83.65 cm along the fibre

(a)

(b)

Figure 3-31. Irradiance E_λ at $\lambda=368$ nm from fibre 7 (micro-perforations in the cladding of the fibre):
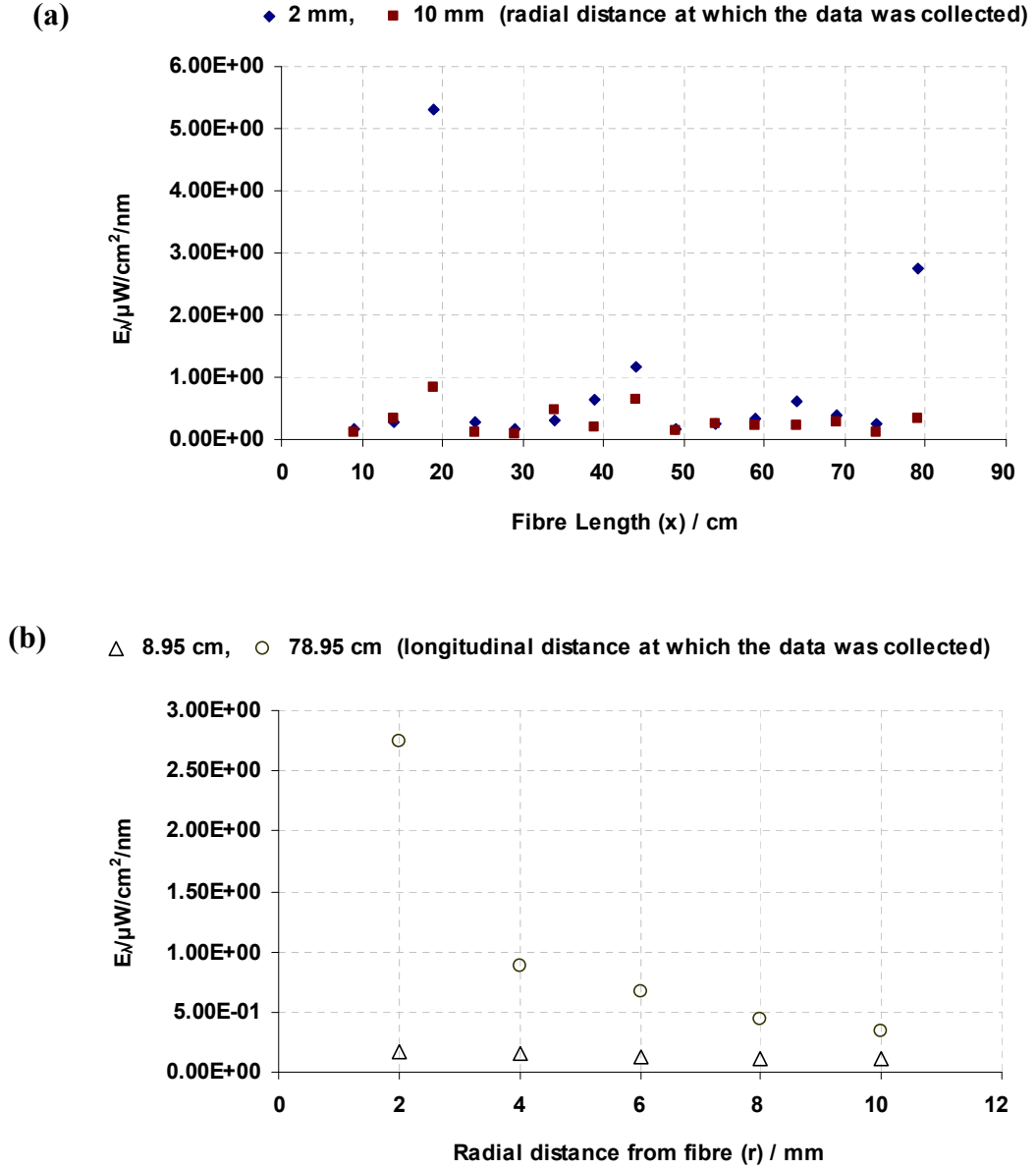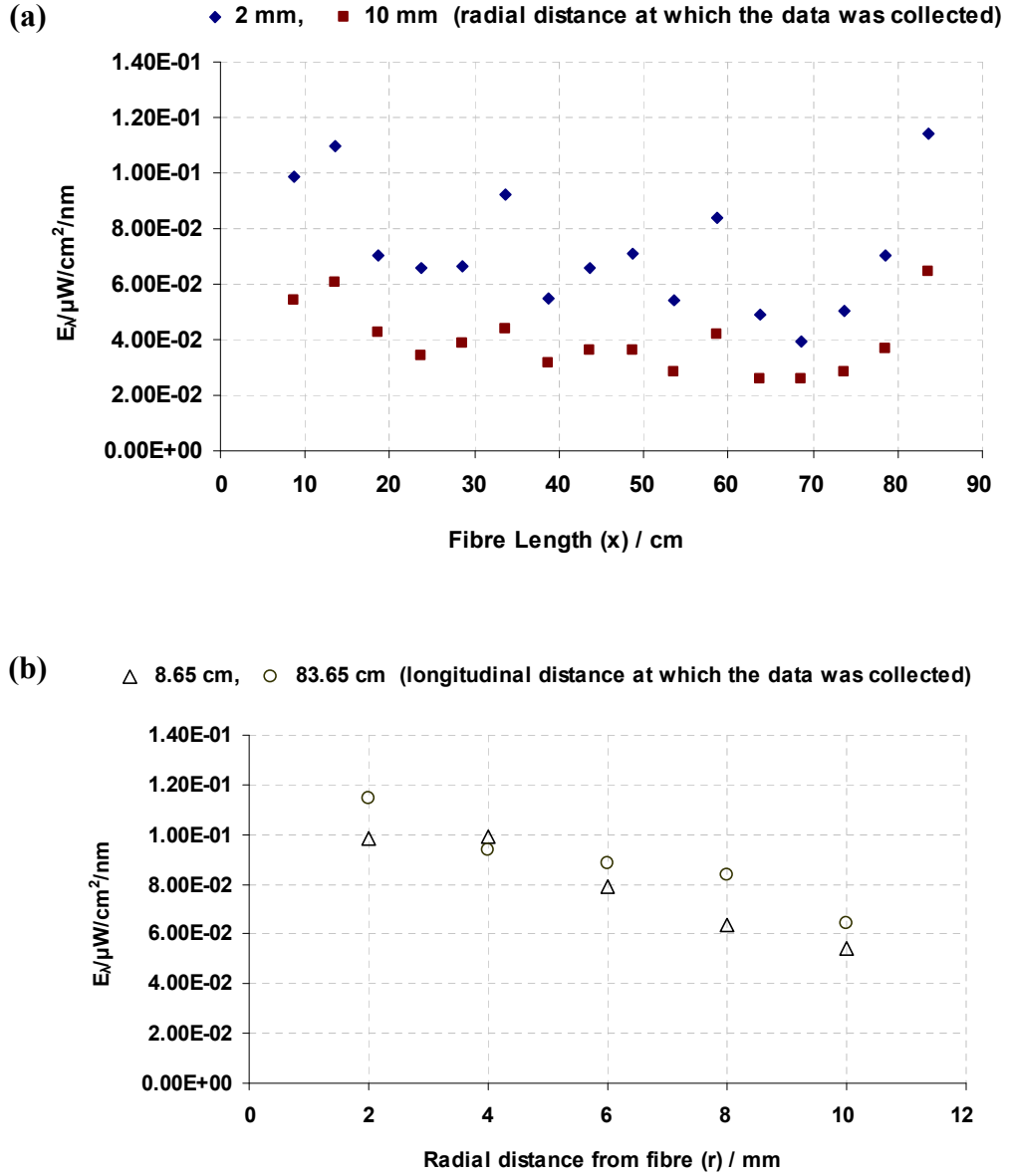
(a) As a function of the position x along the fibre, showing spectral output collected at radial distance r from the side of the fibre

(b) As a function of the radial distance from the recorded spectral outputs at positions 8.95 cm and 78.95 cm along the fibre

(a)   ◆ **2 mm,**   ■ **10 mm (radial distance at which the data was collected)**

(b)   △ **8.65 cm,**   ○ **83.65 cm (longitudinal distance at which the data was collected)**


Figure 3-32. Irradiance E_λ at λ=368 nm from fibre 8 (not designed for side emission application):

(a)   As a function of the position x along the fibre, showing spectral output collected at radial distance r from the side of the fibre

(b)   As a function of the radial distance from the recorded spectral outputs at positions 8.65 cm and 83.65 cm along the fibre

Table 3-3. Attenuation coefficients k determined from the exponential decay in spectral irradiance, at wavelength 368 nm, along the side of fibres and at a radial distance of 10 mm

Fibre	k / cm^{-1}
1	1.0×10^{-3}
2	6.4×10^{-3}
3	1.9×10^{-2}
4	1.3×10^{-2}
5	1.7×10^{-2}
6	-
7	-
8	4.2×10^{-3}
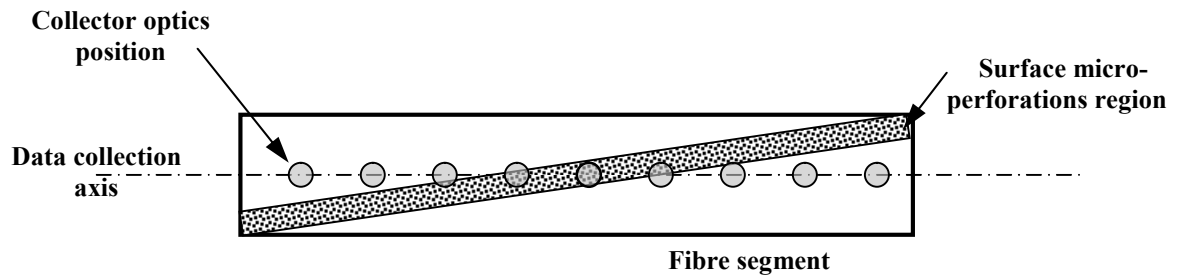
Figure 3-33. Schematic illustration of the surface micro-perforations of fibres 6-7 and the positions of the spectrometer during the experiment, which resulted in a fluctuation in the irradiance E_λ measurements shown in Figures 3-30 and 3-31.

3.5. Chapter Conclusions

- Seven commercial side emission optical fibres were characterised regarding their design characteristics.

- The designs of the fibres were found to be of two different types:

  o Fibres with a silica core, silicone cladding (polydimethylsiloxane (PDMS)) and with a diffuser of either Polyamide-6 (PA6) or Ethylene tetrafluoroethylene (ETFE).

  o Polymer optical fibres with a polymethyl methacrylate (PMMA) core and a cladding from fluorinated polymer (polyvinylidene fluoride (PVDF)).

- For the side emission application, the fibres with a silica core were made with scattering particles (ZnO or Al_2O_3) embedded in the cladding of the fibres. The scattering particles in the claddings of the fibres were found either individually or accumulated in the form of agglomerates. The density of the scattering particles varied for different fibres. The scattering particles were also found to be irregularly distributed across the claddings of the fibres.

- The side emission mechanism of the PMMA core fibres was made by irregularly distributed microperforations on the outer cladding surface of fibres. Some of the microperforations even reached the core of the fibres.

- The optical transmission of the commercial side emitting optical fibres was investigated using an Hg lamp (40 W/cm^2) which emits radiation in the spectral range from UVA to visible blue. The side emission measurements of the silica core fibres with ZnO scattering particles in their claddings showed high absorption in the UVA band, especially below wavelength 380 nm.

- Silica core fibres with Al_2O_3 particles and PMMA core fibres transmitted similar spectral emission as the Hg lamp.

- The intensity decayed exponentially along the fibres which contained more uniform scattering particles. The exponential decay of the intensity from the sides of the fibres was found to increase with fibres containing a higher density of scattering particles.

- Hence, the higher the scattering, the higher the intensity emitted from the side of the fibre. The measured intensities from the side of the PMMA core fibres indicated fluctuation due to the irregular distribution of the microperforations, but resulted in these fibres showing the highest degree of side emission.

- Thus, PMMA core fibres show high potential to cure the optimised epoxy formulation RS3 (see Table 2-14 of Chapter 2) in a closed mould process due to their high side emission transmission in the UVA band which is desired for the photocuring process. But fibres from this type required further stabilising for use with a high emission Hg lamp (40 W/cm^2) and also further enhancement to their side emission; these are discussed in the following Chapters (4 & 5).

Chapter 4

Effect of Degradation on the Transmission of PMMA Optical Fibres

4.1. Introduction

Polymer optical fibres (POFs) have been developed over the past three decades [98]. The improved transmittance of these optical fibres has raised interest in adopting them for many applications [14-16, 94-98]. However, these optical fibres undergo degradation when exposed to UV radiation [19], which limits their transmission stability over time. This chapter discusses the effect of polymer degradation on the transmission of PMMA optical fibres when exposed to high intensity UV-A and visible blue radiation, and it also demonstrates the transmission of the PMMA optical fibres by using a cooling device between the radiation source and the PMMA optical fibres.

4.2. Background

Polymethylmethacrylate polymer optical fibres (PMMA POFs) are of low cost and exhibit high ductility, large core diameter, relative immunity to dust and easy handling characteristics providing great potential for their replacement of silica glass-based optical

fibres for short length applications [90-91]. Although a PMMA POF exhibits far greater overall optical attenuation than silica glass optical fibres, specialised step index (SI)-POFs often already replace silica glass fibres for short distance applications like local area networks (LAN) and automotive applications [120]. The PMMA POF is of interest for other applications such as illumination, waste-water disinfection, photocuring of polymers and sensing [14-16, 94-98]. However, one problem is that PMMA POF can exhibit increased attenuation when operated at temperatures greater than 100 °C [98].

High intensity light sources can generate heat at a polymeric fibre coupling as a result of photon absorption of the polymeric material. The enthalpy absorbed ($\Delta H_{absorption}$) increases with time and radiation intensity. The photon absorption causes the molecular structure to become energy rich or 'excited'. The magnitude of absorbed energy that allows the molecular species of a material to begin to react is the activation energy. When the appropriate activation energy for dissociation (E_a) is reached, a photochemical reaction may take place causing the polymer to dissociate, form free radicals and undergo further reactions. Such photochemical reactions, in turn, can generate further heat ($\Delta H_{reaction}$) [19, 121]. Hence, the photon irradiated polymer will acquire heat generated from both material absorption ($\Delta H_{absorption}$) and photochemical reactions ($\Delta H_{reaction}$).

Silica-based glass optical fibres have a more strongly chemically bonded matrix and have higher operating temperatures, and activation energy for dissociation (E_a), compared to the PMMA POF. This allows silica glass optical fibres to be coupled to radiation sources with high radiation intensity without employing any cooling means at the coupling point.

The increase in temperature when radiation is coupled to the fibre changes the structure of the irradiated material and affects the optical properties of PMMA POF. Meseguer et al. [122] reported that the refractive index, at 450 nm wavelength, of PMMA decreases at temperatures higher than 50 °C; this would tend to result in smaller Fresnel reflection loss at the fibre end and hence greater power coupling into the fibre. Enhanced fluctuations in density and refractive index of the fibre materials with temperature increase [123] could

result in some light being scattered out of the fibre, hence not absorbed and so would not contribute to heating of the fibre. A major factor contributing to the degradation of the PMMA POF is photo-degradation, especially when UV (ultraviolet) radiation is introduced. The photodissociation of PMMA results in a random scission of the polymer chain backbone by a free radical process that occurs as a result of three simultaneous major reactions: random homolytic scission of main chain C=C bonds; photolysis of the ester side groups and photodissociation of the methyl side groups [19]. The photo-degradation of PMMA in air generates products like methane, hydrogen, carbon monoxide and carbon dioxide which, if they dissolve in the PMMA, may change the original optical properties of the PMMA [19]. For instance carbon monoxide and carbon dioxide dissolution can contribute to PMMA transmission loss in the 300 nm to 450 nm spectral band, as reported by Yu et al. [111]. These authors also reported that UV-irradiated PMMA films, in the presence of oxygen (ambient air), exhibit an increase in refractive index as well as mass loss. On the other hand, Kashiwagi et al. [124] reported that the thermal-oxidative degradation of PMMA took place at lower temperatures (50 °C - 60 °C) in ambient air than in a nitrogen gas medium, as would be expected due to the lower partial pressure of oxygen in nominal nitrogen gas than in air.

Most of the reported work regarding the utility of the PMMA POF under high UV flux has been at 254 nm wavelength, in the UVC electromagnetic spectrum, using a low pressure mercury lamp with flux density output $\approx$ 100 μW/cm^2 [125-126]. Wochnowski et al. [121] concluded that irradiating PMMA at 248 nm, in a gas atmosphere controlled vacuum chamber to examine the volatile defragmentation products ablated from the irradiated PMMA surface, resulted in complete ester side chain cleavage, while at 193 nm only an incomplete ester side chain scission took place. The ester side chain cleavage (main chain scission) caused the formation of carbon, carbon double bonds C=C in the polymeric main chain which act as absorption centres. Pakhomov et al. [126] reported that the absorption centres C=C and C=O bonds formed in the PMMA as a result of UV irradiation at wavelength 254 nm with flux density output $\approx$ 100 μW/cm^2 for 1 hour, caused the PMMA

POF gradually to lose light transmission. Although, the study on PMMA under UV irradiation using laser pulses by Wochnowski et al. [121] showed no modification of the PMMA polymer structure at longer wavelength (308 nm). Yao et al. [127] demonstrated photo-degradation of PMMA on irradiation at the wavelength 360 nm in ambient atmosphere which caused changes to the chemical and physical properties of PMMA. Hence, the main chain scission of the PMMA by UV can also be achieved at longer wavelengths (i.e. at least 360 nm) especially at high intensities [127].

Overall, thermal- and photo-degradation factors result in a change in the optical properties of the POF at the launch face under UV irradiation at $\leq$ 360 nm and lead to a drop in the total radiation intensity launched [128], thus reducing the optical transmission stability of the fibres. The effect of degradation on PMMA optical transmission has been studied for decades [19, 111, 121-128]; however, reports related to coupling a PMMA POF with powerful radiation sources in the UVA-band (315 nm to 400 nm) are sparse [123, 125].

4.3. Effect of Degradation on the Transmission of PMMA Optical Fibres

4.3.1. Objective

In this chapter, the effect of thermal- and photo-degradation on the transmission of a PMMA POF is investigated under irradiation with a mercury (Hg) lamp (main peak emissions: 335 nm, 365 nm, 406 nm and 438 nm) with effective flux density of ~ 40 W/cm^2 over the spectral range: 280 nm to 450 nm in the ambient atmosphere. A technique for connecting a POF to a high intensity radiation source to achieve longer operation periods is discussed.

4.3.2. Experimental Details

The degradation study was based on four sets of experiments, using the source as described above, each on a 200 mm long sample of the PMMA POF conducted in ambient air as follows:

Experiment series 1: Determination of transmitted power under constant source power of 40 W/cm^2 with time;

Experiment series 2: Determination of transmitted power under constant source power of 40 W/cm^2 with time, using a cooling device at the PMMA POF launch face;

Experiment series 3: Determination of spectral transmission under constant source power of 40 W/cm^2 with time, using a cooling device at the PMMA POF launch face,

Experiment series 4: Determination of the transmission recovery behaviour for the irradiated PMMA POF in experiment 2 over a rest period under ambient conditions post-irradiation

Materials

A commercial untreated PMMA POF (CK-30) of 738 µm core-diameter with a poly(vinylidene fluoride) (PVDF) cladding of 12 µm thickness was used in this study. The POF was purchased from LasIRvis Optoelectronic Components Ltd [130].

Experimental equipment and setup

For the experiments, a BlueWave 200 radiation source was used. This radiation source is described in Section 3.4.1.1 of Chapter 3. The emission spectrum of this lamp is shown in Figure 4-1.
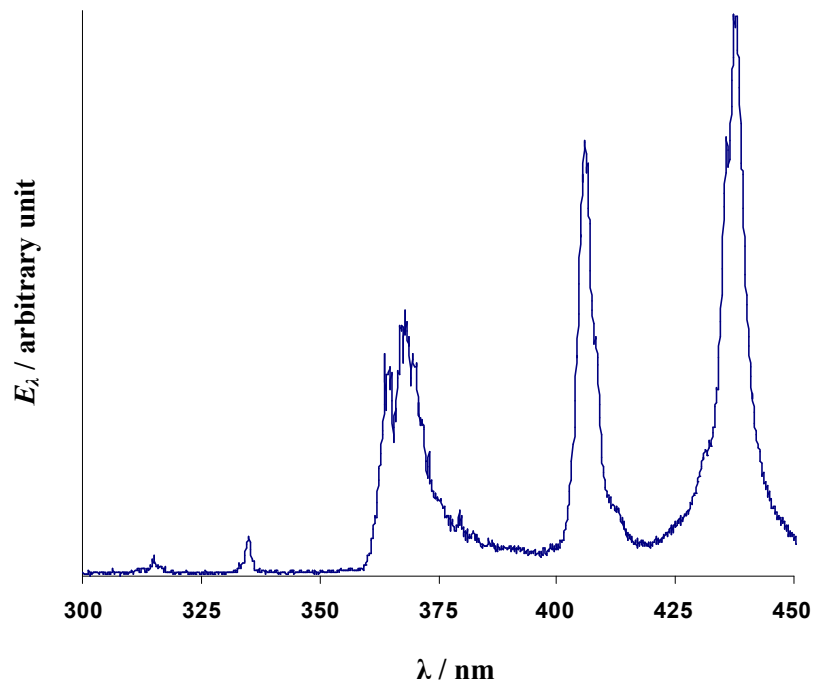

Figure 4-1. Emission spectrum E_λ of the BlueWave 200 mercury lamp collected from the near-end of the 5 mm diameter silica glass light guide. The spectrum was recorded using a USB4000 spectrometer (Ocean Optics). These equipments are described in Section 3.4.1.1 of Chapter 3.

The PMMA POF samples were all fitted with in-house made, hollow metal (brass or aluminium) connectors at the launch ends (10 mm long and 6 mm diameter) to expose the fibre end. After fitting these connectors, the launch face at the connector and the exit end of each fibre was polished to a 1 μm finish using diamond polish to reduce refraction and diffuse scattering.

For Experiment series 1 (Figure 4-2), the launch face of the PMMA POF sample was fitted with a brass connector (in-house). The PMMA POF sample was then abutted to the end of the silica glass light guide and secured using a house-made aluminium tube fitting (50 mm long, 7 mm inside diameter and 2 mm wall thickness), which allowed centring of the polished launch face of the PMMA POF relative to the light beam. In Experiment series 2, 3 and 4, the launch face of the PMMA POF samples was fitted with aluminium connectors (in-house) and thermally coupled to the silica glass light guide using a cooling device, as shown in Figure 4-3. The cooling device also allowed centring of the samples relative to the light beam using a built-in aluminium tube fitting (Figure 4-4), surrounded by water ice. The built-in aluminium tube was 54 mm long with two inside diameters (7 mm diameter for 30 mm length, to hold the aluminium connector of the PMMA POF, and 10 mm diameter for 24 mm length at the other end for connecting the silica rod light guide protective stainless steel casing). The cooling device body was made from aluminium for efficient heat conduction and had a brass sleeve (10 mm long, 6 mm inside diameter and 1 mm wall thickness) for coupling with the aluminium connector of the PMMA POF to avoid cold welding of the aluminium connector of the fibre with the cooling device.
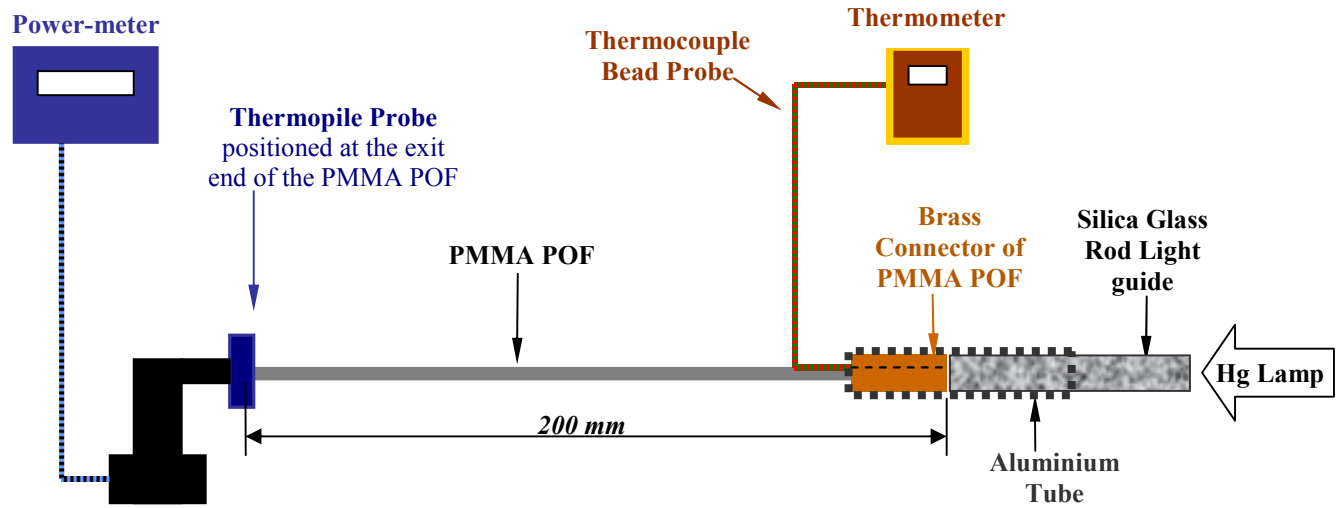
Figure 4-2. Schematic arrangement of: (i) the launch conditions of the Hg lamp radiation into the PMMA POF, (ii) measurement of power transmission through the PMMA POF and (iii) temperature measurement at the launch end face of PMMA POF for Experiment series 1 (not to scale).
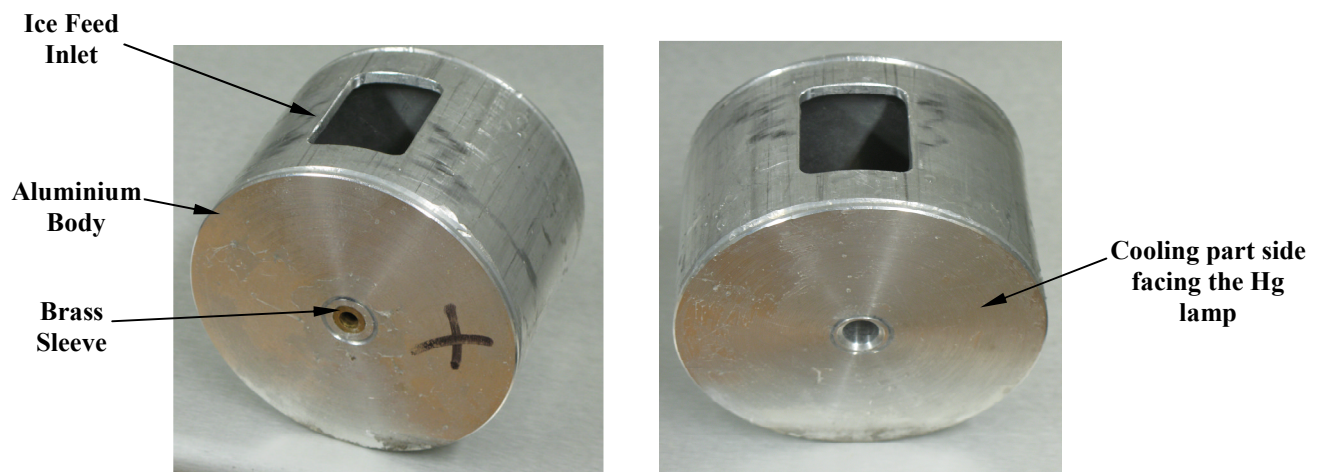
Figure 4-3. Cooling device.
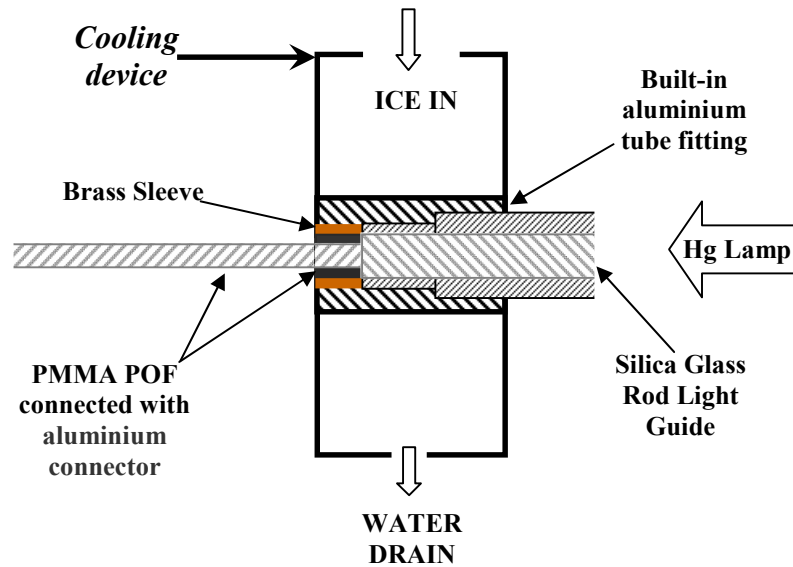
Figure 4-4. Schematic illustration of the cooling device in functioning state using dry water ice, while connected with both the silica rod light guide and the PMMA POF (not to scale).

For Experiment series 1 and 2, a power-meter (Molectron PM500A analogue power-meter with a thermopile probe, equipment error ± 7 mW, Figure 4-5) was used at the exit face of the PMMA POF to study the change in power transmission through the PMMA POF.


Figure 4-5. PM500A analog power-meter.

The thermopile probe of the power-meter was placed (Figure 4-2) at the polished exit end of the PMMA POF. A thermocouple bead probe was attached similarly to both brass and aluminium connectors of the PMMA POF samples, as shown for the brass connector in Figure 4-2, to measure the temperature at the coupling between the end of the silica glass light guide and the PMMA POF launch face. The total error of both the thermocouple bead

probe and thermometer (single channel K type thermometer, 206-3722) was ± 2.85 °C. Both the thermocouple and power-meter readings were recorded at five second intervals during each experiment.

The transmission spectrum of the PMMA POF was monitored during Experiment series 3 using a USB4000 spectrometer (see Section 3.4.1.1 of Chapter 3 for description). The overall experimental setup is depicted in Figure 4-6. The radiation was collected from the exit end of the PMMA POF using a 1 mm diameter commercial silica glass optical fibre with half cone acceptance angle (θ_{ac}) of 12.4°. The spectrometer enabled measurement of the spectral irradiance (E_λ) of the radiation emitted from the exit end of the PMMA POF, in the range 200 nm to 850 nm wavelength.

Finally, the topographical change to the launch face of PMMA POF was investigated using scanning electron microscopy (SEM) (Jeol Winsem, JSM-6400). The samples were coated with carbon using a Polaton SC-7640 sputter coater, prior to examination, to protect the samples from electronic charging and possible degradation.
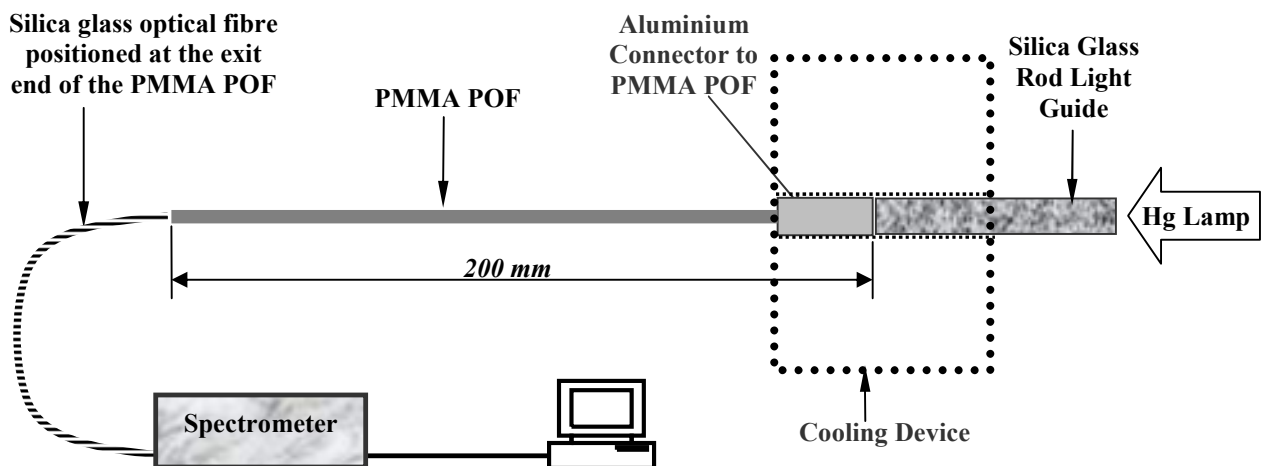
Figure 4-6. Schematic arrangement of measurement of spectral output transmission from the PMMA POF with the cooling device in place at the launch end of the PMMA POF in Experiment series 3.

4.4. Results and Discussion

4.4.1. Power Transmission of PMMA POF without Cooling Device

(*Experiment Series 1*)

Experimental series 1 was carried out without the cooling device surrounding the launch face of the PMMA POF (Figure 4-2). The transmitted power of the PMMA POF was found to drop from 150 mW to 80 mW after 5 mins of irradiation by the Hg lamp at 40 W/cm^2 over the spectral range from 280 nm to 450 nm (Figure 4-7), while simultaneously the temperature at the launch face of the PMMA POF increased from 15 °C to 82 °C. During the first 5 mins of irradiation, the power transmitted by the PMMA POF dropped on average by a nominal 14 mW per min from the initial value of 150 mW to a value of 80 mW, and followed by a nominal drop of 3.3 mW per min until the end of the 8 mins. No loss of power transmission was observed from 9 mins to 13 mins. The temperature reached a maximum of 92 °C after 7 mins, and then fluctuated between 88 °C and 79 °C until 13 mins. It is proposed that the thermal- and photo-oxidation effects were responsible for the loss in transmission and the temperature rise. The total power loss was 53 % after 13 mins and was accompanied by no change in colour of the launch face of the PMMA POF. However, irradiation for 13 mins caused the launch face of the PMMA POF sample to undergo a physical change in shape (Figure 4-8). The SEM-secondary electron image (Figure 4-8a) of the carbon coated launch face of the PMMA POF sample indicates a topographical change at the centre of the launch face which increased in size relative to the surrounding peripheral region. While in Figure 4-8b, at higher magnification, the interface between the swollen central region and the unchanged peripheral region may be seen to exhibit an irregular topographical surface surrounding the swell.
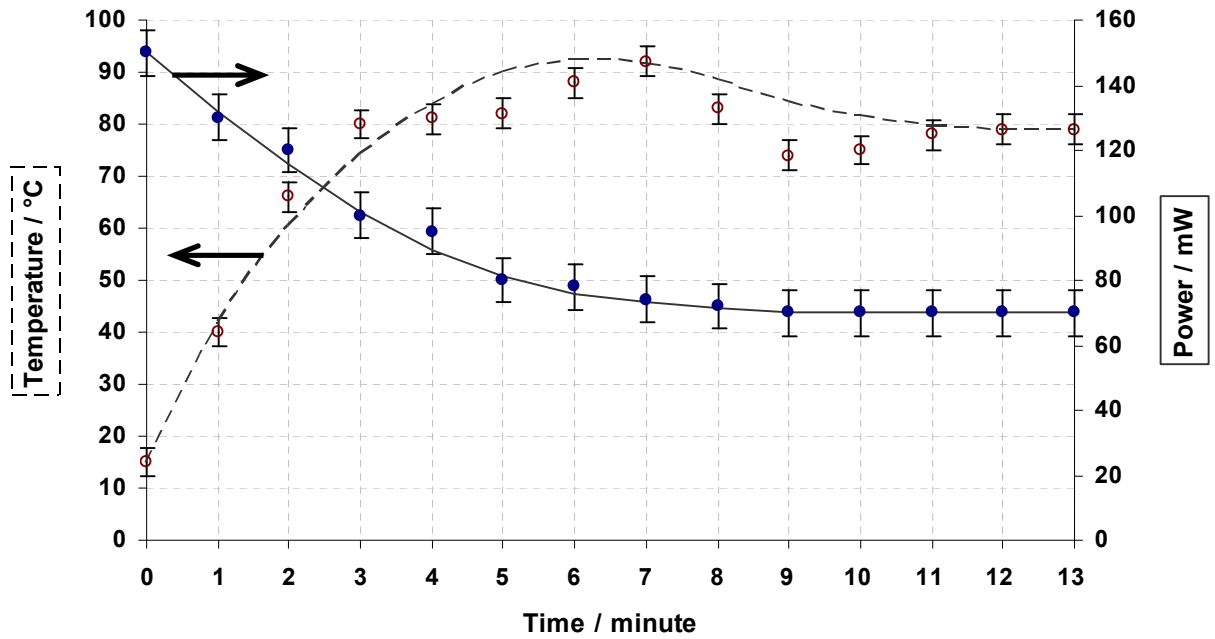
Figure 4-7. Power output (●) and temperature (○) variation with time for the PMMA POF irradiated for 13 mins by 40 W/cm^2 output source.
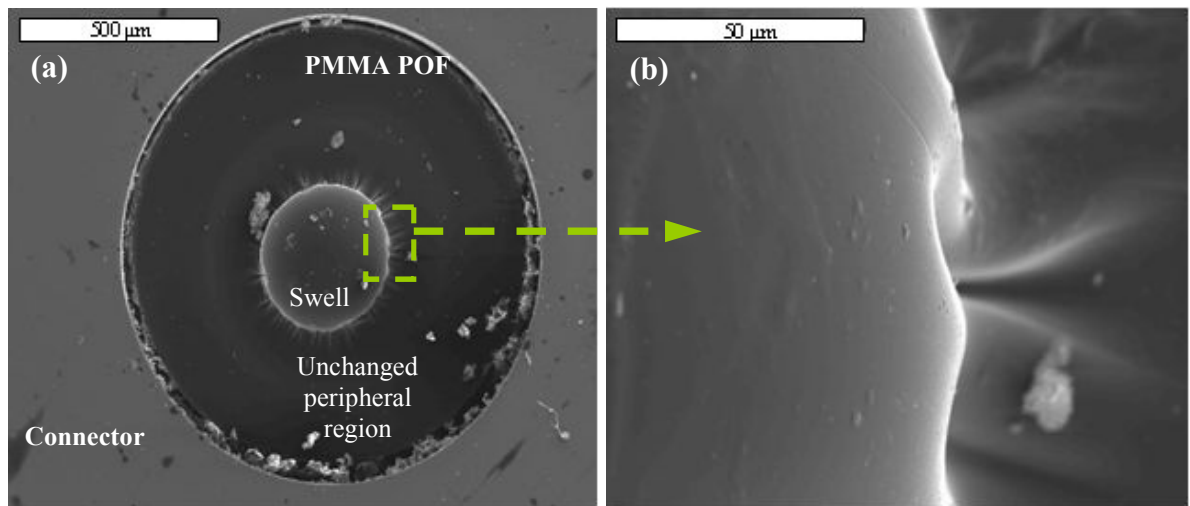
Figure 4-8. Scanning electron microscopy (SEM) secondary electron images of the physical change to the PMMA POF launch face (carbon coated) irradiated for 13 mins by 40 W/cm^2 output of the Hg lamp source (the temperature rose to 92 °C): (a) the region of the swell is approximately circular of ~ 370 µm diameter, while (b) shows at higher magnification the interface between the swollen central region and the unchanged peripheral region. The variation in contrast is the result of different topographical levels.

The topographical change of the PMMA POF launch face during irradiation will have contributed to the transmission loss, as the irregular surface will have increased refraction and scattering. It suggested that the change in shape of the PMMA POF launch face occurred as a result of photo-thermal effects caused by the heat generated in the POF launch face material from both radiation absorption ($\Delta H_{absorption}$) and photochemical reaction ($\Delta H_{reaction}$) [19]. The topographical change observed at the centre of the PMMA POF launch face was due to that region being in receipt of the highest temperature rise during the exposure, which could have caused a higher oxidation effect in that region [124]. Longer exposure from the Hg lamp for up to 40 mins resulted in a more severe physical change of the launch face of the fibre. A chemical reaction is proposed to have occurred. Material loss was observed, proposed to have volatilised, and a change in colour from transparent to black was observed as shown in the photographic images of Figures 4-9a and 4-9b. It is suggested that these physical changes to the launch-face of the PMMA POF, after longer exposure to the Hg lamp, were caused by an increase in temperature and directly lead to the reduction of power transmission through the PMMA POF. These observations fit the increased sensitivity of PMMA to UV degradation as the temperature is increased as reported by others (see for instance ref.19) as at higher temperatures the PMMA is reported to become more sensitive to UV degradation.
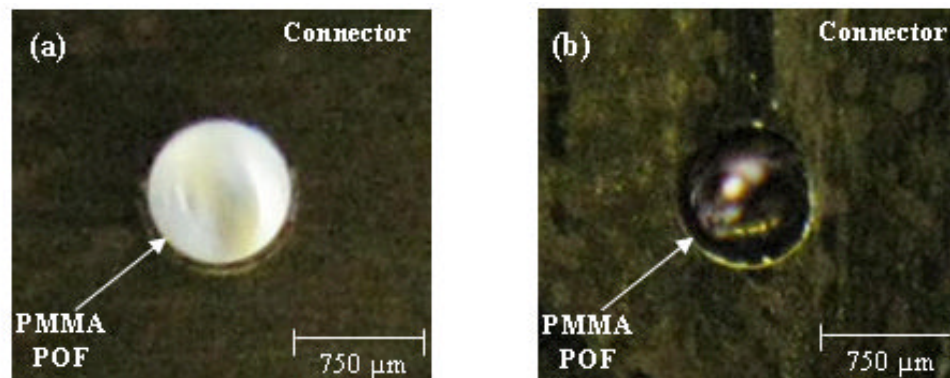

Figure 4-9. Photographic images showing the loss of PMMA POF material and change in colour from white to black after 40 mins of continuous irradiation at 40 W/cm^2 of the Hg lamp source power. The launch face of the PMMA POF is shown: (a) before irradiation and (b) after irradiation. These effects are proposed due to photo-thermal ablation.

4.4.2. Power Transmission with Cooling Device (*Experiment Series 2*)

Experiment series 2 was the same as Experiment series 1 but with the addition of the cooling device at the connector (Figure 4-2 & Figure 4-4) that connected the PMMA POF to the silica glass light guide. The experiment was conducted for a maximum time of 1 h with a new PMMA POF in place. The temperature reading from the PMMA POF connector after 1 min was 35 °C (Figure 4-10). The temperature then dropped slightly throughout the experiment until it reached a constant value of 32 °C after 8 mins. An increase in the transmitted power was observed from 140 mW to 145 mW in the first 4 mins of the experiment. That most probably had occurred due to the drying off of the condensed water mist layer, formed by the cooling device, on the silica rod light guide exit end surface. The power output then showed a constant value of 145 mW after 4 mins up to 7 mins, followed by an average nominal drop of 1.2 mW min^{-1} during 53 mins of continuous radiation exposure (Figure 4-10). The power output of the PMMA POF reached 135 mW at 13 mins. Thus there was a power loss of 7 %, at 13 mins compared to a loss of 53 % without employing the cooling device. After 1 h, the power transmitted reached 80 mW, with an overall power loss of 45 %. The temperature readings (32 °C to 35 °C) were below the maximum operational temperature (70 °C) of the PMMA POF as provided in the material data sheet [130]. However, the relatively modest drop in power transmission during 1 h (Figure 4-10) suggested that still a limited photo-degradation of the PMMA had occurred, presumably caused by photochemical reaction. Because no physical degradation of the launch face was observed visually or by SEM-secondary electron imaging (Figure 4-11), the modest drop in power transmission might have been due to products such as carbon dioxide from photo-degradation process dissolved in the PMMA [19, 111, 122-123].
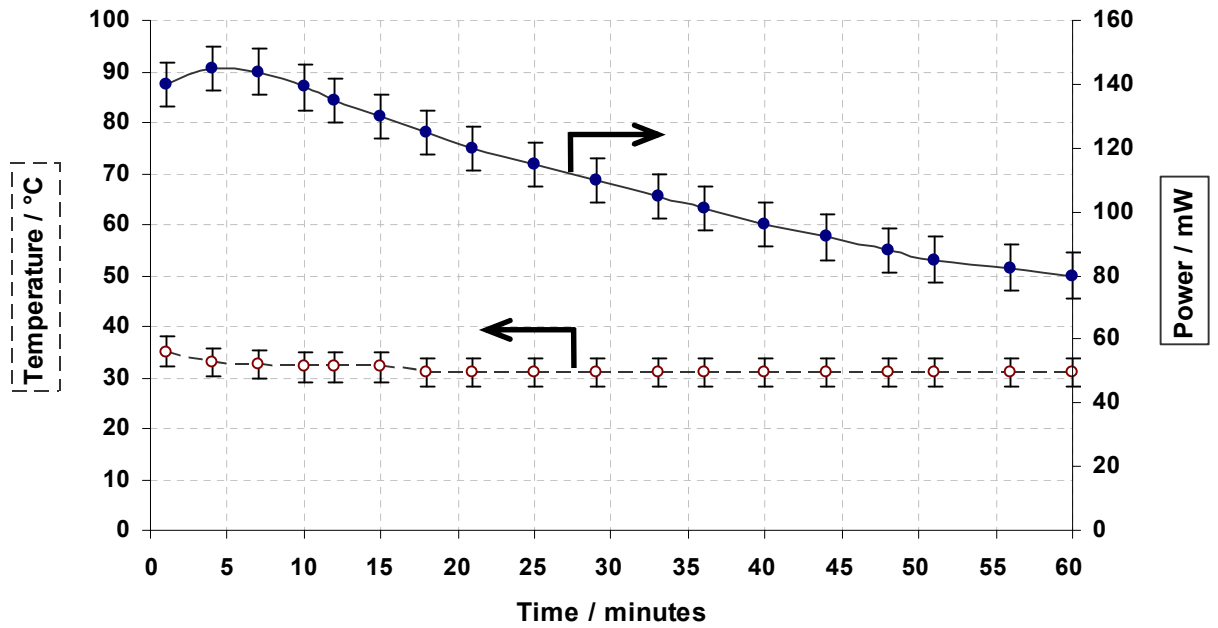
Figure 4-10. Power output (●) and temperature (○) variation with time for the PMMA POF under 40 W/cm^2 of the Hg lamp source radiation with the cooling device in place at the launch face of the PMMA POF and irradiating for up to 1 h.
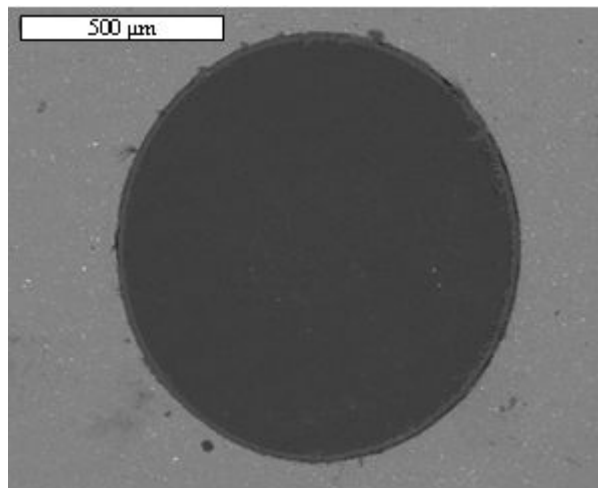

Figure 4-11. Scanning electron microscopy (SEM), secondary electron image of the launch face of the PMMA POF tested with the 40 W/cm^2 output Hg lamp source with the cooling device in place for 1 h. Note, there is no evidence of thermal degradation and the launch face appears smooth and unchanged.

Additionally, the photochemical reaction may have increased slightly the refractive index of PMMA as irradiation from the Hg lamp causes an increase in the refractive index of the PMMA as reported by Yu et al. [111]. A gradual increase in the refractive index of PMMA film samples (1.14 μm to 8.74 μm) was observed by Yu et al. [111] when the PMMA was continuously irradiated with Hg lamp (500 W) and the changes in the refractive index were evident by a prism coupler. Thus, the changes in optical properties of the PMMA could have reduced the radiation launched successfully into the PMMA POF, as a result of refractive index increase at the launch face, due to greater Fresnel reflection loss. However, it is unlikely that the refractive index could have changed enough to account for the observed power loss. Nevertheless, the fact that photo-degradation did take place at the PMMA POF launch face was validated by re-polishing the launch face of two new PMMA POF samples irradiated for 13 mins and 1 h, respectively, then repeating the experiment with the cooling device at the connector. The power transmission through the re-polished PMMA POF irradiated for 13 mins was approximately 97 % of the initial value, indicating that the photo-degradation only caused a thin layer of the PMMA POF material to exhibit a change in optical properties. Similar behaviour has also been reported by Pakhomov et al. [128]. However, the PMMA POF sample irradiated for 1 h did not exhibit the initial readings even after re-polishing; almost certainly, therefore, the degradation went deeper into the material beyond the superficial surface.

### 4.4.3. Spectral Transmission of PMMA POF with Cooling Device (*Experiment Series 3*)

Absorption Spectra

The PMMA POF used in this study was coupled with the cooling device at the silica glass rod light guide of the Hg lamp with 40 W/cm^2 source output. Radiation was transmitted through the system for 1 h. The transmitted radiation through the PMMA POF was evaluated from continuously collected spectra at the exit end of the PMMA POF during the experiment (Figure 4-6). The acquired spectra were similar in nature to the emission spectrum of the Hg lamp (Figure 4-12). However, the PMMA POF did not transmit the peak emission wavelength of 315 nm (Figure 4-12) indicating high absorption of the launched emission at wavelengths below 320 nm by the fibre material. In contrast, Wochnowski et al. [121] and Sutcliffe et al. [134] reported that PMMA material has low absorption at wavelengths ≥ 308 nm, Torikai et al. [131-132] extensively studied the effect of wavelength-dependent photo-degradation and concluded that wavelengths below 320 nm contribute significantly to the photo-degradation of the PMMA material. Hence, when the cooling device was used here, radiation absorption at wavelengths below 320 nm (Figure 4-12) could have contributed to photochemical reaction at the launch face of the PMMA POF. However, it must be noted that compared to the large intensity peak emission at 368 nm of the Hg lamp (Figure 4-12), the intensity of emission < 320 nm is small. Thus, it cannot be ruled out that irradiation at the peak wavelength 368 nm also contributed to the drop of power transmission (Figure 4-10). The transmission loss against time of the transmitted spectral irradiance through the PMMA POF was also evaluated for the transmitted wavelength emission peaks. The spectral results of the transmitted irradiation through the PMMA POF for up to 1 h indicated that the loss of transmission increases from the longer wavelength emission peak (438 nm) towards the shorter wavelength emission peak (335 nm) as shown in Figure 4-13.
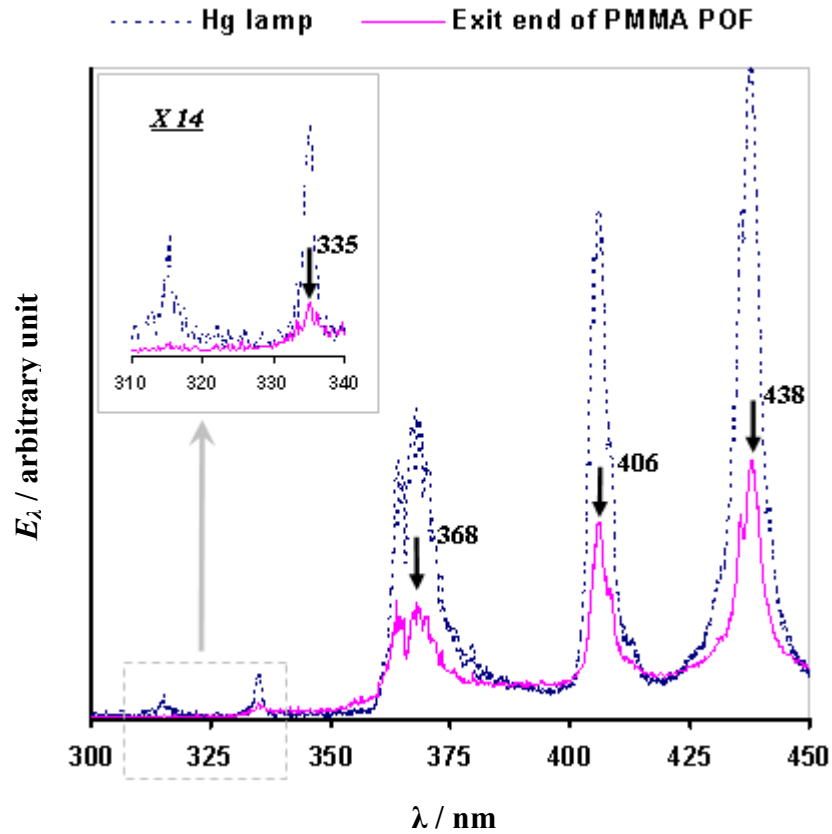
Figure 4-12. Emission spectra E_λ recorded from: the end of silica glass rod light guide whose launch face was abutted to the Hg lamp (·····) and exit face of the PMMA POF sample (—) after radiation using 40 W/cm^2 output power of the source for 5 seconds with cooling device in site at the fibre launch end. (Note that arrowed peaks refer to the wavelengths whose absorbance was monitored with time of irradiation during Experiment series 3.)
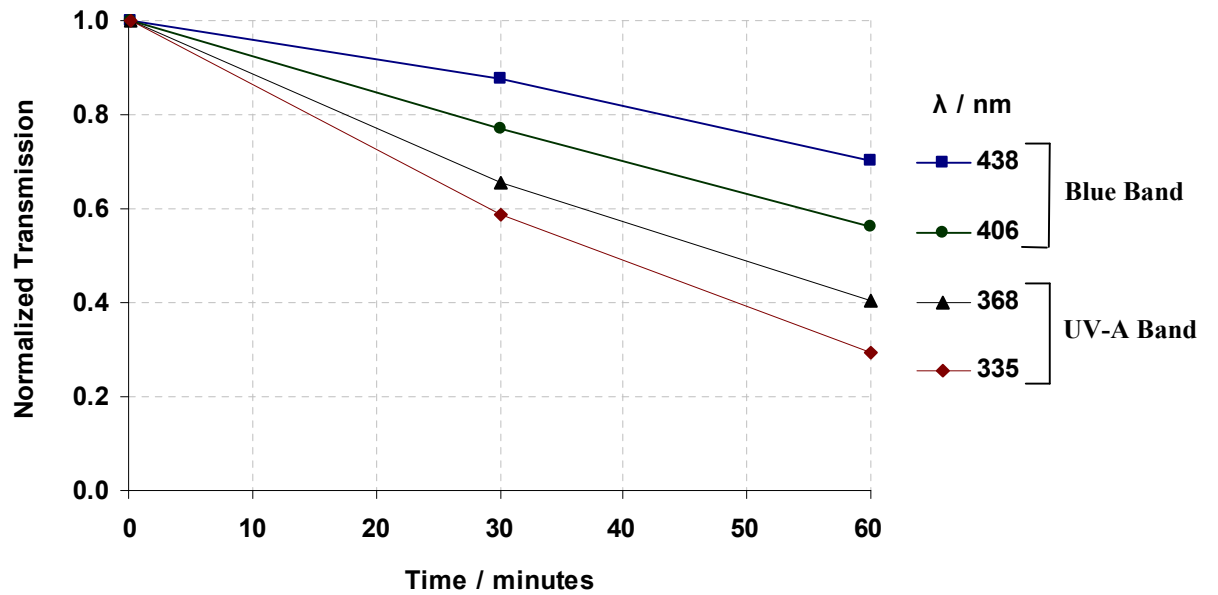
Figure 4-13. Spectral results showing power transmission loss with time collected from the polished exit end of the PMMA POF using the 40 W/cm^2 output Hg lamp source with the cooling device in place at the fibre launch end. The results represent the drop in transmission after 5 seconds, 30 minutes and 60 minutes at wavelengths: 335, 368, 406 and 438 nm. The collected spectral irradiance values at the exit end of the PMMA POF were normalized for all wavelengths to 1 after dividing them by the initial spectral irradiance.

Absorption Coefficient

While most of the previous work on PMMA absorption behaviour [125, 127, 132-134] has been focused on irradiation wavelengths smaller than 300 nm, recently Yao et al. [127] investigated the photo-degradation effects of PMMA bulk samples irradiated at the single wavelength of 360 nm (500 W intensity) for up to 140 h with a controlled temperature of 33 °C. They found that the photo-degradation caused by this continuous UV irradiation resulted in rupture of the PMMA chemical bonds with time [124, 127] with main-chain scission reactions of the polymer and substitution.

The absorbance A (no unit) of the PMMA material depends on the irradiation exposure period, and by the Beer-Lambert law,

$$I = I_0 e^{-A}$$
(Equation 4-1)

$$\text{where} \quad A = \varepsilon c l$$
(Equation 4-2)

where, I_0 is the input intensity (W), I is the transmitted intensity (W), l is path length (cm), c is the concentration of absorbing species (mol L^{-1}), ε is the extinction coefficient of the absorbing species (L mol^{-1} cm^{-1}).

Absorbance was found to increase under continuous irradiation due to gradual development of absorbing products that caused more loss of the transmitted radiation through the PMMA POF, as shown earlier in Figure 4-13. The absorption coefficient α for a fixed path length can be described by rearranging the Beer-Lambert law:

$$\alpha = -\frac{\ln\left(I/I_0\right)}{l}$$
(Equation 4-3)

Let α_1 be the initial absorption coefficient of the PMMA core material of the POF. As the irradiation exposure proceeds, α will vary due to the formation of the degraded PMMA products caused by the photochemical and photothermal reaction [19], such as macro-radicals and colour centres [125, 127, 134]. This variation in α may also be described by the following:

$$\alpha_{PMMA} \xrightarrow{\ UV\ } \sum \alpha_i \qquad \text{(Equation 4-4)}$$

$$\text{where} \qquad \alpha_i \propto c_i \qquad \text{(Equation 4-5)}$$

$$\text{and} \qquad \alpha_i = \varepsilon_i c_i \qquad \text{(Equation 4-5)}$$

where, i is the number of the new species resulting from the photochemical reaction process of a polymeric material.

The concentration of absorbing species (c_i) and the absorption coefficient (α_i) of the resulting product of the PMMA photo-degradation have different transmission properties compared to the original PMMA material. During progressive photochemical reaction of the PMMA material, the concentration of absorbing species (c) of the original PMMA material decreases while that of the degraded product absorbing species increases and results in changed transmission. In addition, extra loss due to reflection and/or scattering will be incurred if the product species have a different refractive index from the PMMA starting material, which is likely.

Typical values of α after 30 mins and 60 mins of continuous exposure to the Hg lamp of the PMMA POF at different wavelengths were calculated by substituting the collected spectral data into equation 4-3. These are tabulated in Table 4-1. The resulting values of α_λ after 30 mins and 60 mins of continuous exposure indicated that proportionally larger amounts of optical loss occurred for the PMMA POF in the UV-A band relative to the rest of the

spectrum (Figure 4-14). The highest residual value of the nominal absorption coefficient for the PMMA POF after 30 mins and 60 mins of Hg lamp exposure, respectively, was found at wavelengths of 335 nm; $\alpha_{335nm} = 2.7x10^{-2}$/cm and $\alpha_{335nm} = 6.1x10^{-2}$/cm, respectively.
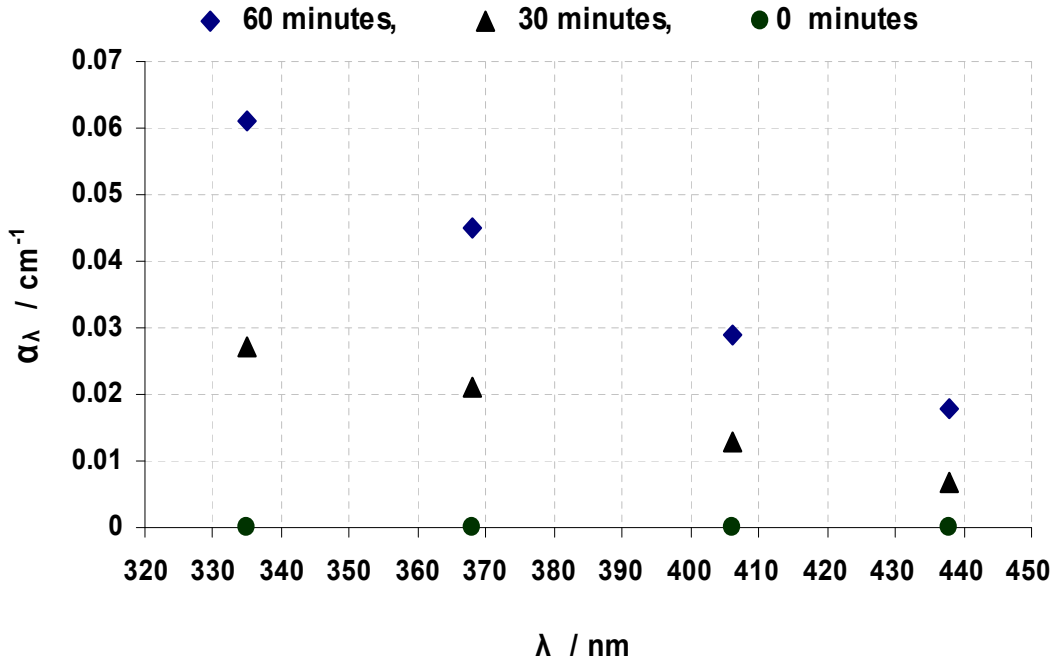
Figure 4-14. Spectral nominal absorption coefficient (α_{λ}) at 335 nm, 368 nm, 406 nm and 438 nm of a PMMA POF for two periods of continuous 40 W/cm^2 Hg lamp irradiation exposure: 30 minutes (▲) and 60 minutes (♦), compared to the initial zero minute (●) values.

Although, the residual nominal α_{λ} values at 335 nm and 368 nm were found to be higher than the values at 406 nm and 438nm, the relative change in nominal absorption coefficient $\Delta\alpha_{\lambda}$ was greater at 438 nm than at 335 nm, 368 nm and 406 nm, as shown in Table 4-1. The Hg lamp emission in the blue band (i.e. 400 nm to 450 nm) does not degrade the launch face of the PMMA POF, due to the low nominal absorption of PMMA in the blue band [109-110, 129, 135-136]. Furthermore, the Hg lamp emission in the UV-A band, especially

at 315 nm, had a more significant influence in changing the optical properties at the launch face of the PMMA POF and consequent drop in the overall transmitted spectral flux [129, 131-132].

Table 4-1. Nominal absorption coefficient (α_{λ})at wavelengths 335, 368, 406 and 438 nm (marked on Figure 4-12) of PMMA POF connected under continuous Hg lamp radiation exposure for 30 mins and 60 mins, and the relative change ($\Delta\alpha_{\lambda}$) form 30 mins to 60 mins. (Found from the experimentally collected absolute spectral irradiance data and by using equation 4-3).

Spectral band	Wavelength / nm	α_{λ} / cm^{-1}		$\Delta\alpha_{\lambda}$
		30 min	60 min	
UV-A	335	2.7×10^{-2}	6.1×10^{-2}	1.3
	368	2.1×10^{-2}	4.5×10^{-2}	1.1
Blue	406	1.3×10^{-2}	2.9×10^{-2}	1.2
	438	0.7×10^{-2}	1.8×10^{-2}	1.6

Note, the relative change was calculated using, $\Delta\alpha_{\lambda} = \dfrac{\alpha_{\lambda}(initial) - \alpha_{\lambda}(end)}{\alpha_{\lambda}(initial)}$

4.4.4. Light Transmission Recovery of the PMMA POF Post-exposure to Hg Lamp Source (*Experiment Series 4*)

The transmission of a degraded PMMA POF was found to recover to some extent if left in ambient conditions after the Hg lamp had been switched off. Earlier work [125-126] on the phenomenon of PMMA POF transmission recovery was studied after UVC irradiation, in particular at 254 nm wavelength with a flux density of 100 $\mu W/cm^2$.

For instance, Pakhomov et al. [126] observed yellowing of a 1 mm diameter PMMA POF after 1 h of continuous irradiation from an Hg lamp at 254 nm which appeared to have caused transmission loss. However, when the PMMA POF was tested after a period of rest at room temperature, the yellowing disappeared and the spectral light transmission had almost completely recovered. However, longer exposure (several hours) of the PMMA POF to 254 nm radiation caused a permanent yellow colour and significant light losses, even after long rest periods. The recovery behaviour of the PMMA POF was further studied by Taguenang et al. [125]. These authors demonstrated molecular recovery of an irradiated 1 mm diameter PMMA POF with time using Raman spectroscopy: a powerful technique for identifying molecular species. The reported study showed some evidence of PMMA recovery by continuous growth of Raman bands (between wavenumbers 600 cm^{-1} and 1600 cm^{-1} [125]) of PMMA molecular species during the two weeks subsequent to the irradiation dose of 1h and 50 mins.

Here, the PMMA POF transmission recovery was investigated after UVA irradiation from an Hg lamp at major peak 368 nm with an overall peak flux density output $\approx$ 17 W/cm^2 (Section 3.4.1.1 of Chapter 3), which is of a higher flux density than what has been used in the work by both Pakhomov et al. [126] and Taguenang et al. [125], but of lower photon energy.

Monitoring of the transmission recovery of the PMMA POF in the current work was conducted on PMMA POF which had been irradiated for 1 h under ambient conditions and with the cooling unit in place (Figure 4-4). The transmission loss is shown in Figure 4-10. The transmission recovery of the irradiated PMMA POF was determined by a once weekly measurement using the power-meter.

Although, the PMMA POF transmission decreased during the irradiation period (Figure 4-10), the irradiated launch face of the PMMA POF did not exhibit a yellow colour after 1 h irradiation as observed by Pakhomov et al. [126]. The PMMA POF showed a 6.9 % recovery in overall power transmission after 1 week. This recovery carried on with time (Figure 4-15) until an overall recovery after 5 weeks of power transmission reached 86 % of the original transmission. No further recovery was observed when the PMMA POF was left for a longer rest period of up to 7 weeks. This irreversible behaviour of the PMMA after 5 weeks was due to irreversibly formed absorption centres, such as carbon monoxide and carbon dioxide dissolution, based on the lose of the C=C and C=O bonds via UV degradation, as has been found by Yu et al. [111] and also suggested by Pakhomov et al. [126], respectively. In conclusion, here it has been shown that the PMMA POF also exhibited transmission recovery when irradiated with UVA as had previous work [125-126] when irradiating the PMMA POF with UVC.

Generally, the similarity in the reported work regarding the transmission recovery of PMMA material post UV irradiation by Taguenang et al. [125], Pakhomov et al. [126] and also the work presented in this Chapter is that all of the studies were conducted under normal air atmosphere conditions. Hence, the degraded PMMA material under a short period of UV irradiation may have reacted with the component of air (such as oxygen or nitrogen) and resulted in the regeneration of the PMMA molecules. This suggestion may be validated by investigating PMMA in the presence of individual chemicals.
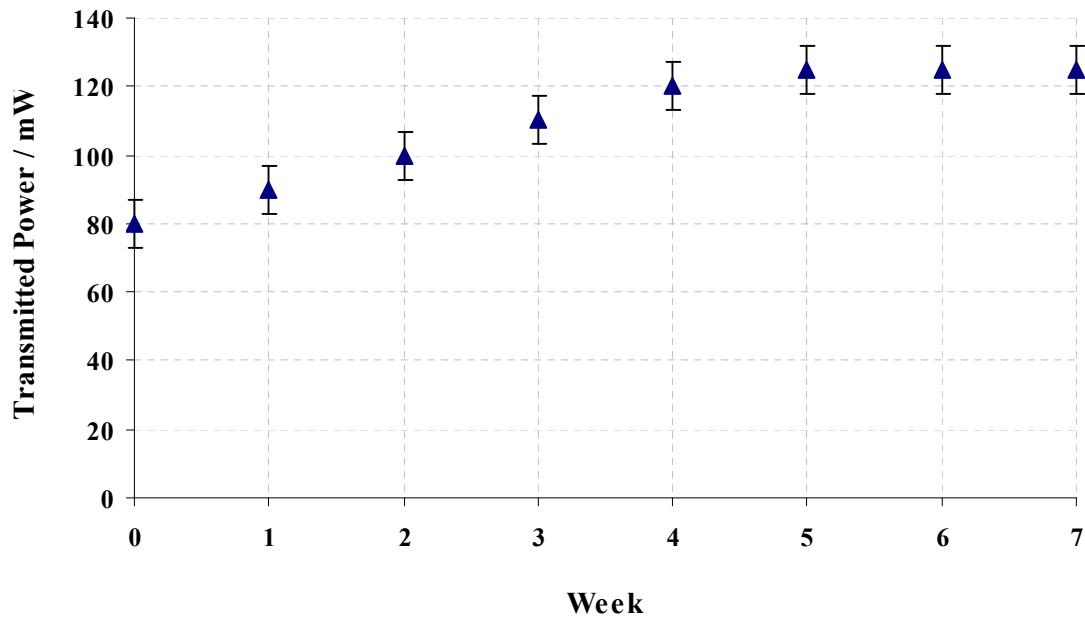
Figure 4-15. Transmission recovery measurements of the PMMA POF irradiated by the Hg lamp at 40 W/cm^2 for 1 hour with the cooling device in place at the fibre launch end. After the lamp was switched off (zero week) the PMMA POF was left to rest at room temperature (23 °C) in the dark and tested for total power transmission once each consecutive week after irradiation, up to 7 weeks.

4.5. Chapter Conclusions

The utility of PMMA POF under high flux at peak emissions: 335 nm, 368 nm, 406 nm and 438 nm in the UVA and blue electromagnetic spectrum has been studied by investigating the stability of the optical transmission. The radiation generated by the Hg lamp caused the PMMA POF to undergo physical and chemical changes at the coupling which led to a drop in the radiation launched into and transmitted by the PMMA POF. Any thermal effect due to radiation absorption using the Hg lamp was better controlled when a cooling device was used. Without the cooling device the photo-degradation effect was evident after only 7 mins. The radiation transmission through the PMMA POF was found to have dropped (by an average of 1.2 % per minute) 53 % at 13 mins. The lower degradation when using the cooling device indicates that the PMMA became more sensitive to UV-A radiation degradation at high temperatures.

The photo-degradation effect was analysed in more detail by monitoring the transmitted spectral intensity. A drop in transmission of the PMMA POF with time was observed in both the UV-A and blue bands. The PMMA POF did not transmit well below the wavelength of 320 nm. The transmission loss increased gradually from 450 nm to 335 nm wavelengths demonstrating relatively larger nominal absorption in the UV-A band. The highest nominal absorption coefficient (α_λ) of the PMMA POF continuously exposed to the Hg lamp was found at 335 nm wavelength, when tested using the cooling device after 30 mins and 60 mins was 2.7×10^{-2} cm^{-1} and 6.1×10^{-2} cm^{-1}, respectively. Although, emission from the UV-A band caused photo-degradation, the relative change in the nominal absorption coefficient $\Delta\alpha_\lambda$ during continuous irradiation exposure indicated relatively more loss at a wavelength of 438 nm in the blue band.

The irradiated PMMA POF launch face recovered a percentage of the loss in transmission with time. After 1 h of irradiation with the cooling device in place, the PMMA POF

transmission was reduced to 44.8 % of its initial value; this recovered to a maximum of 86 % after 5 weeks.

Chapter 5

PMMA Optical Fibres: Attenuation, Side Emission Enhancement and Curing of Epoxy in a Closed Mould

5.1. Introduction

In Chapter 3, various types of commercial side emission optical fibres were characterised. They were found either to consist of a silica core with a cladding containing scattering particles (Al_2O_3 or ZnO), or of a core of poly(methyl methacrylate) (PMMA) and a poly(vinylidene fluoride) cladding with micro-perforations. The PMMA core fibres exhibit generally a higher intensity of side emission, particularly in the UVA band, and thus prove more suitable for photocuring applications than typical commercial silica core fibres. But the measured intensities along the two PMMA side emitting optical fibres (fibres 6-7 from Table 3-2 of Chapter 3) were inconsistent for both fibres (Figures 3-30 & 3-31). In addition, most of the readings along the two fibres indicated a higher ratio of lower intensities than the recorded high intensities which are more effective for the curing process. Hence, in order to improve the efficiency of the photocuring process, further enhancement of the emitted radiation intensity (at a given intensity of the lamp emission launched into the PMMA core of the fibres) is desirable. In this context, this study aims at the characterisation of the transmission of PMMA optical fibres, the enhancement of their side emission efficiency in the spectral range from UV-A to visible blue and using the enhanced fibre for epoxy curing.

5.2. Background

5.2.1. Attenuation of Polymer Optical Fibres (POF)

Attenuation in POFs varies with the radiation wavelengths transmitted through them, which classify them for applications at specific wavelengths. For example, the polystyrene (PS) POF has less attenuation in the red band [98], whereas the PMMA POF transmits highly in the UVA and visible blue bands [109-111].

Attenuation in POFs is not constant with fibre diameter. As the core diameter decreases, the attenuation increases. This phenomenon has been demonstrated for the PMMA POF made by different manufacturers [98]. Humidity is known to impose significant attenuation in a PMMA POF when absorbed into the cores [91]. This attenuation mechanism can be eliminated by making the cladding material from a fluorinated polymer. Loss of a launched power in POFs can result from three factors: Optical fibre *coupling*, as well as *intrinsic* and *extrinsic* loss mechanisms [92-93, 98-99, 137].

The attenuation caused by poor coupling results in either a drop of the total radiation launched or in side emission. Poor coupling often occurs when the end face cross-sectional area of the fibre is connected at an angle to the surface of the radiation source, making the incident angle of some rays larger than the critical angle. Often this angled coupling results when the outer diameter of the optical fibre is significantly smaller than the inner diameter of the connecting unit of the radiation source. This allows the fibre to become angled within the connector. To overcome these problems the end face is processed using a hot plate so that the POF is deformed to fill the tolerance gap between it and the connector [90], and it also gives a smoother/flatter face. This method provides the lowest coupling loss for POFs.

Intrinsic loss mechanisms are the principle form of attenuation within POFs. This attenuation can not be eliminated as it arises from the material composition of the POFs.

Intrinsic loss attenuation includes both *material absorption* (by vibration modes and electronic transitions) and *Rayleigh scattering* (by density fluctuation, orientation fluctuation and composition fluctuation).

Extrinsic loss mechanisms are unlikely to appear in an ideal optical fibre. This loss is caused by the damage occurring during manufacturing process and the handling of the fibre. Extrinsic loss results in: *radiation absorption* especially in the UV band (by metallic, organic pollutants and crucible material), *dispersion* (by dust particles, microfractures, bubbles, and other structural imperfections) and *scattered radiation losses* (by microbends, macrobends and micro-cuts in the fibre geometry).

Other loss from a fibre is caused by bend radii. This type of attenuation has been analysed and studied for the multimode step index optical fibres by authors such as Durana et al. [138], Badar et al. [139] and Boechat et al. [140]. These authors suggest that the attenuation increases as the bend radii of a fibre decreases.

5.2.2. PMMA Polymer Optical Fibres (POF) for Epoxy Curing

In photocuring applications, activation of the photoinitiators is directly linked to the flux emitted into the resin medium. In most of the reported work in this field, the speed of the curing process is correlated to high flux that is not achievable with side emission optical fibres [11-13]. However, as the PMMA POF becomes more stable with the high emission Hg lamp (40 W/cm^2), as discussed in Chapter 4, they showed high potential for curing epoxy in a closed mould application compared to silica core optical fibres. This is due to their large core advantage, lack of a diffuser and absence of radiation absorbing scattering particles, as discussed in Chapter 3.

5.3. Experimental Investigation of PMMA Optical Fibres

5.3.1. Objective

In addition to the previously found characteristics of the PMMA POF, this chapter investigates techniques for further understanding the attenuation of the PMMA POF as well as for enhancing the side emission efficiency of the PMMA POF.

The study in the chapter also aims to photocure components from the optimised epoxy resin system RS3 (Section 2.3.3.4 of Chapter 2) using in-house treated, side emitting PMMA optical fibres. Polyester resin is also cured to compare its curing rate with epoxy resin.

5.3.2. Experimental Details

The study of the PMMA optical fibres was based on four sets of experiments:

- **Experiment series 1:** determination of the fibre attenuation (intrinsic and extrinsic),

- **Experiment series 2:** quantification of side emission at fibre bends,

- **Experiment series 3:** modification of the fibres to improve the side emission efficiency, and

- **Experiment series 4:** using the side emitting PMMA optical fibre which has been enhanced during Experiment series 3 for curing 1.5 mm and 5 mm thick components from epoxy resin, and to cure a 1.5 mm thick component from polyester resin

Materials

A BlueWave 200 radiation source (Hg lamp) was used for all the experiments. This radiation source is described in Section 3.4.1.1 of Chapter 3.

The different commercial PMMA POFs used in this study are described in Table 5-1. The PMMA POFs were purchased from Mitsubishi Rayon of Japan [104] and LasIRvis Optoelectronic Components Ltd [130].

**Table 5-1.** The commercial PMMA POFs used in this study

Fibre	Core material	Cladding material	Fibre diameter / µm	Core diameter / µm	Cladding thickness / µm	*Average Ratio of Core / Cladding*	Fibre treatment
1			500	486	7	0.972	Untreated [130]
2	Poly(methyl methacrylate)	Poly(vinylidene fluoride)	750	738	6	0.984	Untreated [130]
3			1000	980	10	0.980	Untreated [130]
4			1551	1494	29	0.980	Untreated [130]
5			1551	1494	29	0.980	Surface micro-perforation [104]

Experimental equipment and setup

In Experiment series 1, 2, 3 and 4, the PMMA POF samples were all fitted with in-house made, hollow aluminium connectors at the launch ends (10 mm long and 6 mm diameter) to expose the fibre end. After fitting these connectors, the launch face of the connector and the exit end of each fibre was polished to a 1 μm finish using diamond polish to reduce refraction and diffuse scattering at the end face. The fibres were connected to the radiation source via a cooling device, as described in Section 4.3.2. This allowed centring of the fibres relative to the emitted light beam and protected the launch faces from thermal degradation due to heating induced by the high-power irradiation, which could potentially reduce the intensity of radiation launched into the fibre.

In Experiment series 3, for the purpose of side emission, the fibres were modified by three treatment mechanisms: permanent geometry modification of the PMMA POF to impose bending radii along its length, mechanical treatments of the side surface of the fibres and a combination of these two treatment techniques. The geometry of the PMMA POF was modified permanently by heat treatment. The fibres were shaped on an in-house made aluminium tool, which allowed adjusting of the bend radii by means of supporting clips at both ends of the fibres, as shown in the schematic of Figure 5-1. The tool with the fibres wound on it was then placed in an oven (Barlow Whitney) for fifteen minutes at a temperature of 70 °C (in ambient air). The original length of all specimens was 245 mm.
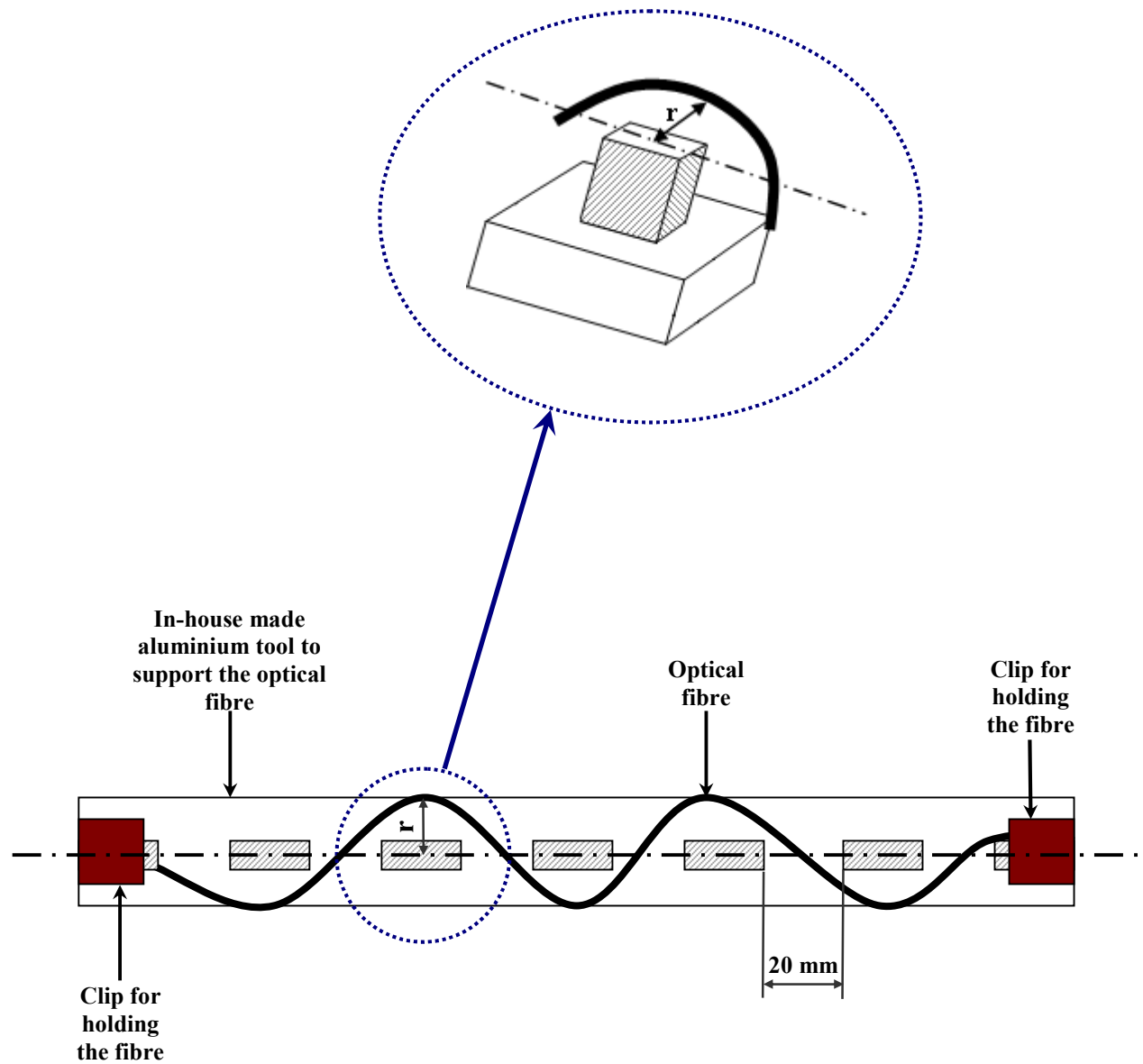
Figure 5-1. Schematic illustration of an in-house designed aluminium tool to hold the PMMA POF in a positioned bend radius using two clips at both ends of the fibres. (Not to scale).

For the second set of experiments in Experiment series 3, silica particles were used for treating the side surface of the PMMA POF. The silica particles were made from rods which were extracted from the silica core fibres 2, 3 and 4 from Table 3-1 and Figure 3-7. The silica rods were crushed using a steel mortar and pestle. The silica particles, as shown in Figure 5-2, exhibited irregular shapes and they were repeatedly crushed until their sizes ranged between ~2 µm to 70 µm.

The silica particle size measurements and the topographical change to the side surface of PMMA POF were investigated using scanning electron microscopy (SEM) (Jeol Winsem, JSM-6400). The fibre samples were coated with carbon using a Polaton SC-7640 sputter coater, prior to examination, to protect the samples from electronic charging and possible degradation. The power transmission through the fibres was measured using a Molectron analogue power meter (PM500A) and the side emission was characterised using an Ocean Optics USB4000 spectrometer, as described in Section 4.3.2 and Section 3.4.1.1, respectively. See Appendix C-1 'C3' for more details on the preparation of the fibre treatments and equipments.
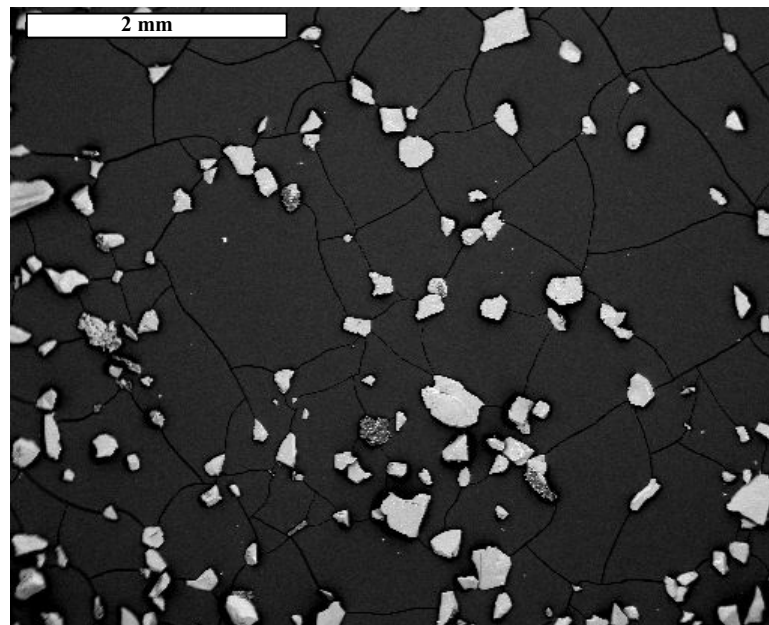
Figure 5-2. SEM secondary electron image of the crushed silica particles.

Curing of 1.5 mm and 5 mm thick components from Epoxy Resin

The optimised epoxy resin system 3 (formulation RS3) from Section 2.3.3.4 (formulated from 100 PHR cycloaliphatic epoxy with 0.6 PHR triarylsulfonium hexafluoroantimonate salt photoinitiator and 2.6 PHR oxetane additive) was used.

The experiments were conducted for curing 1.5 mm and 5 mm thick components made from formulation RS3. For the 1.5 mm thick specimen, the formulation RS3 and the side emitting optical fibre were enclosed between two Melinex polyester films [78]. The two films were sealed and the optical fibre was supported using a strip tape. Melinex polyester films and the strip tape were also used for the preparation of the 5 mm thick specimen. The thickness of the 5 mm thick specimen was maintained by using 5 mm thick aluminium frame which was joined using a commercial permanent epoxy resin. The aluminium frame was drilled with holes to allow centring of the treated fibres. All specimens were covered with aluminium foil from all sides to fulfil the closed mould condition.

Curing of a 1.5 mm thick component from Polyester Resin

A ready formulated polyester resin [141] was also used in the closed mould curing experiments. The preparation of this specimen was similar to that of the epoxy resin (formulation RS3) as described above.

5.4. Results and Discussion

### 5.4.1. Fibre Transmission (*Experiment Series 1*)

For the Experiment series 1, the attenuation of PMMA POF was determined in cut-back tests. The total transmitted power was measured at the fibre end face, starting at a fibre length of 1.1 m, which was then reduced in steps of 10 cm. The fibre was polished to a 1 μm finish to reduce refraction and diffuse scattering at the end face after each cut. This technique allowed the attenuation per 10 cm long fibre segment to be determined and localised defects, which could have caused transmission losses, to be identified. The attenuation *A* was calculated using the following equation [137]:

$$A = 10 \times \log_{10}\left(\frac{I_o}{I}\right)$$

Equation 5-1

where, I_o is input intensity (W) and I is output intensity (W)

The results plotted in Figure 5-3 show that the attenuation of the 10 cm long fibre segments varied randomly along the fibres suggesting that attenuation along the fibres was caused by randomly distributed discrete defects. These randomly distributed discrete defects varied the total transmitted power for short length fibres. For instance, at a length of 1 metre, different specimens of fibre 4 transmitted between 525 mW and 600 mW. However, for longer fibres, the transmission readings are expected to converge.

The untreated PMMA fibres indicated side emission when connected to the Hg lamp, as discussed earlier in Chapter 3. A typical example of the side emission results along an untreated fibre is shown in Figure 5-4. The results in Figure 5-4 and Figure 5-3 for fibre 2 suggest that some of the power loss in transmission due to localised defects along the fibre length were converted to side emission.
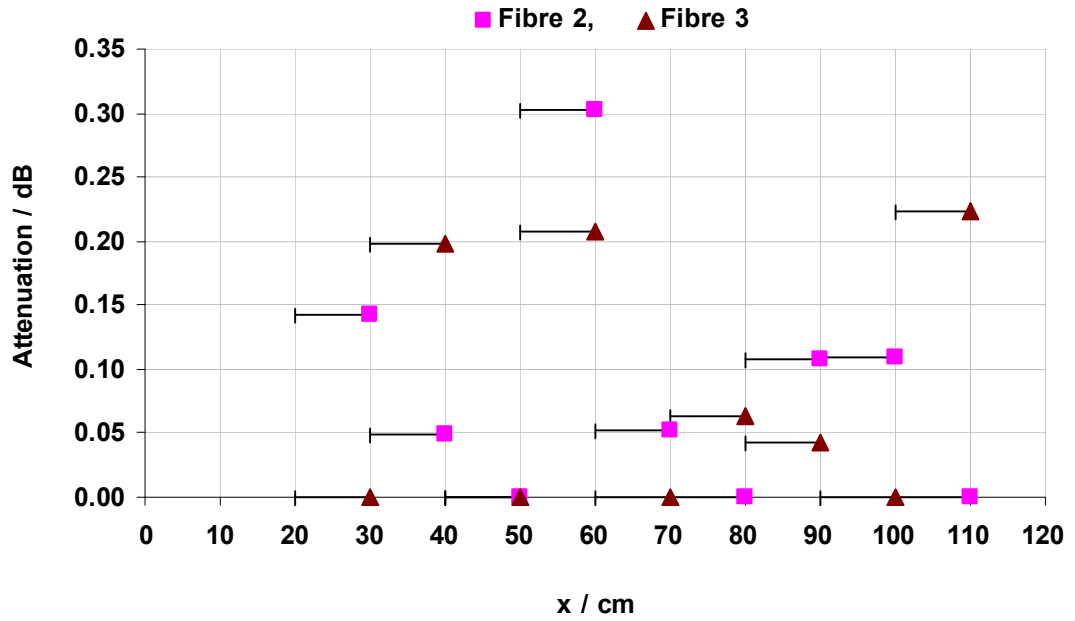
Figure 5-3. Attenuation of 10 cm long fibre segments as a function of the position x along the fibre for the examples of fibre 2 and fibre 3 (see Table 5-1).
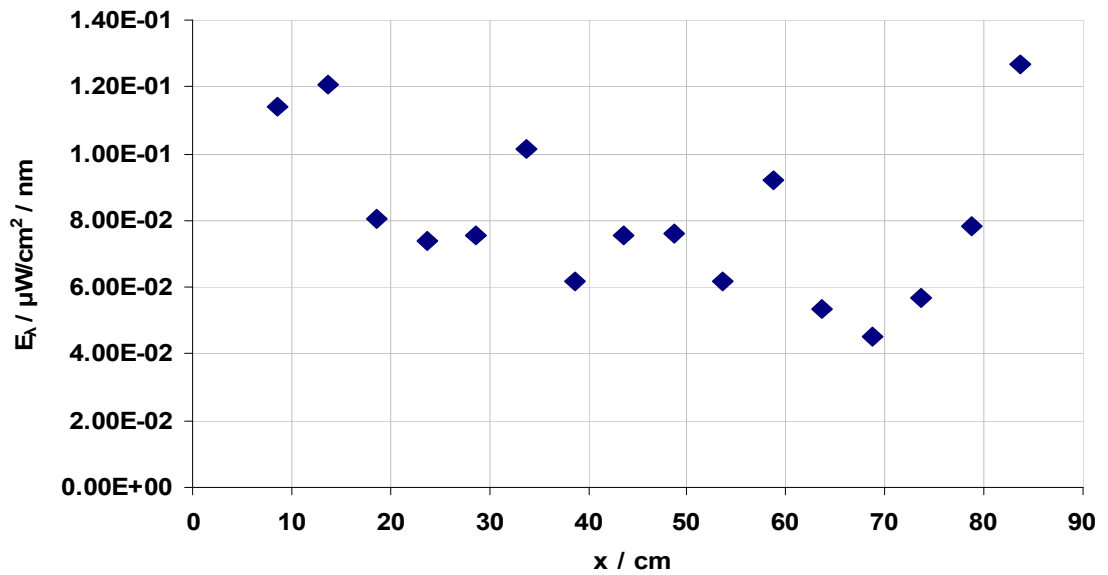

Figure 5-4. Irradiance E_λ at $\lambda = 368$ nm as a function of the position x along fibre 2, measured at radial distance $r = 2$ mm from the fibre axis.

The attenuation per length of the four untreated fibres 1-4 (Table 5-1) also indicated a variation in the attenuation coefficients at wavelength 368 nm as shown in Table 5-2. The resulting coefficients increased as the fibre diameter decreased, Figure 5-5, which is in agreement with the inconsistent attenuation phenomena of different diameters PMMA POFs discussed by Zubia et al. [98].

Table 5-2. Attenuation coefficients k found from power output increase from fibre length cut back, at wavelength 368 nm

Fibre	k / cm^{-1}
1	3.2×10^{-3}
2	2.6×10^{-3}
3	1.5×10^{-3}
4	9.0×10^{-4}
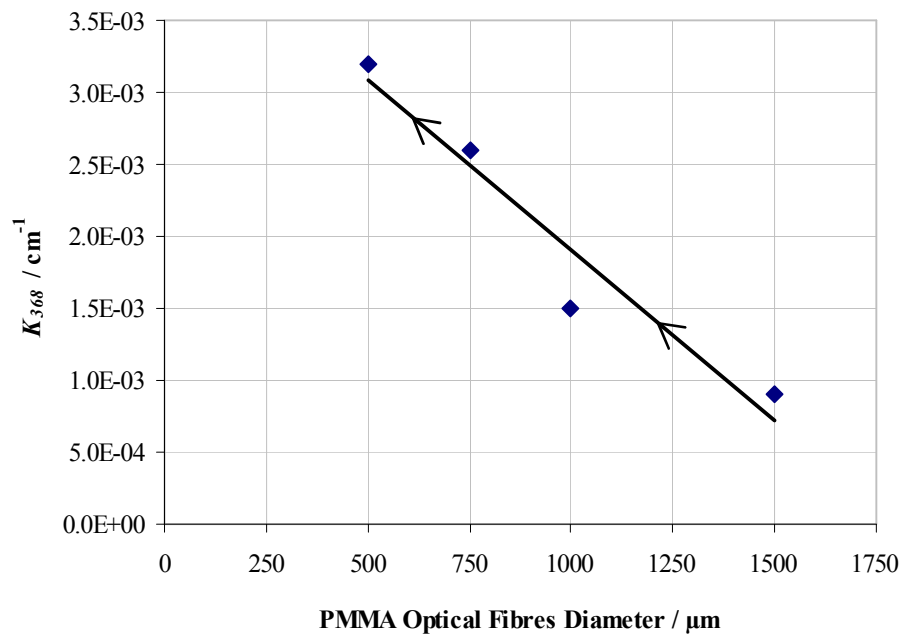
Figure 5-5. A plot of PMMA optical fibres Attenuation coefficients showing a gradual increase in radiation loss as fibre diameter decreases, at wavelength 368 nm.

Manufacturing [98] defects are of the same size regardless of the fibres core/cladding interface diameter. Hence, more attenuation loss occurs as the fibres circumference decreases due to the increase of core/cladding interface per unit area for small diameter fibres. In addition, combining the results found from the spectroscopic experiments, Figure 5-4, with the attenuation measurements, Figure 5-3, it can be concluded that the fluctuation in the results were caused by small number of large discrete defects located at the core/cladding interface. Another factor contributing to the variation in attenuation for different diameters fibres is the variation in core/cladding ratios as demonstrated in Table 5-1. Fibre 1 has the lowest ratio within the group, while fibre 2 has the highest. In side emission applications, different diameter PMMA optical fibres exhibit different attenuation with fibre length, the side emission of treated PMMA optical fibres will not result in a constant linear increase with increased diameters, which limits the effectiveness of such fibres to larger diameters.

5.4.2. Bend Losses (*Experiment Series 2*)

The loss in transmitted power from Experiment series 2, which corresponded to the total power emitted from the side of the fibres at bends, was studied for optical fibres at different fibre diameters, bend radii, and numbers of fibre loops (360° bends). The looped fibres were held in a radial position using a strip tape to avoid losses due to clamping stresses. The total transmission was measured at the fibre end face for bend radii of 25 mm, 12.5 mm and 4 mm. For each bend radius, the experiment was repeated at one, two and three full loops. The attenuation as a function of the number of loops is plotted in Figure 5-6 for fibre 1, fibre 3 and fibre 4. For all fibres, the surrounding medium was air. For an additional experiment, fibre 3 was immersed in a cycloaliphatic epoxy resin. Since the refractive index of air is lower than that of the fibre cladding (n_{cladd} = 1.42 [107]), and the refractive index of the epoxy resin is higher (n_{epoxy} = 1.45 [142]), this change of experimental conditions was expected to affect light guiding in the fibre.

Fibre 1 and fibre 4 showed no change in attenuation at a loop diameter of 50 mm (Figures 5-6A and 5-6C). At a loop diameter of 25 mm, the attenuation of fibre 1 did not vary with increasing number of loops, while the attenuation of fibre 4 increased until it reached 2.2 dB in the third loop. Fibre 3 showed increasing attenuation at loop diameters of 50 mm and 25 mm. All fibres showed a significant increase in attenuation at the smaller loop diameter of 8 mm. These results are in agreement with the observations documented by Durana et al. [138]. Generally, the increase in attenuation with increasing number of loops is the more significant, the greater the fibre diameter. Fibre 3 showed increased power loss, i.e. increased side emission, when immersed in a medium with higher refractive index than the cladding.
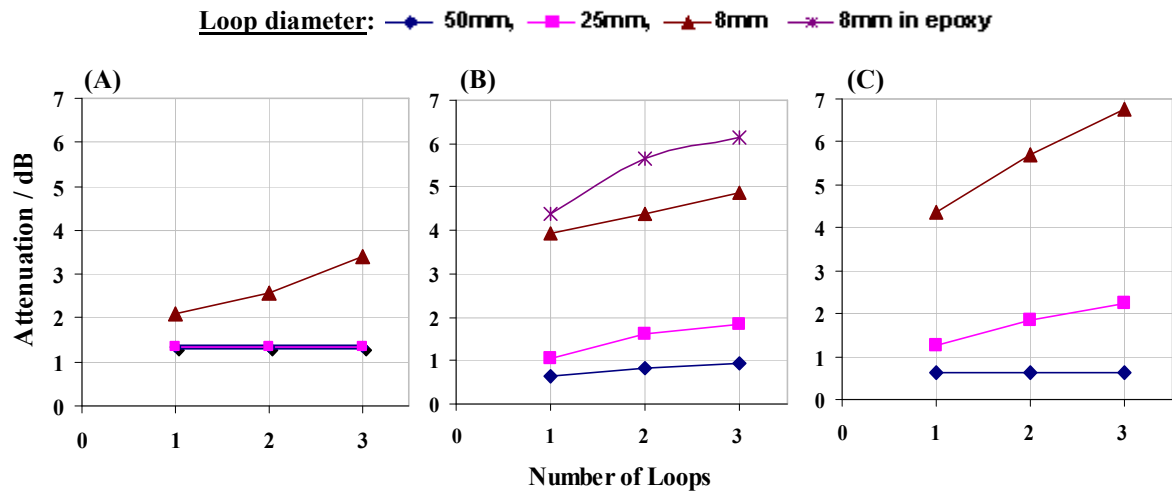
Figure 5-6. Attenuation as a function of the number of full turns of 1 metre long fibres for: (A) fibre 1 (500 μm), (B) fibre 3 (1000 μm), (C) fibre 4 (1551 μm) (Table 5-1); for fibre 3, the effect of immersion in a cycloaliphatic epoxy resin is also illustrated.

5.4.3. Side Emission Enhancements (*Experiment Series 3*)

Geometric Modification

The geometry of different diameter PMMA optical fibres was modified by winding them onto an in-house made tool and then heat treating them, as shown in Figures 5-1. Different geometric modifications, schematically illustrated in Figure 5-7, were tested regarding the total power transmission of the treated fibres. The bending radii were selected based on the results discussed in Section 5.4.2.

The power losses in side emission are compared in Table 5-3 for the different treated fibres. The results indicate that, at a given fibre diameter, the side emission increased with decreasing bend radius. At a given bend radius, the side emission increased with increasing fibre diameter. Due to the process of geometric modification, sharp bends (reduced bend radius) may have occurred near the fibre launch ends (Figure 5-7B and Table 5-3), possibly resulting in increased local emission. These sharp bends should be avoided to achieve more uniform side emission. For fibres modified by bends with identical radii, the side emission decreased significantly along the fibre, as can be observed from the photographic image in Figure 5-8A. However, this behaviour did not occur with fibres with smaller diameter (750 µm), as shown in Figure 5-9, which implies that the effect of bend radii on side emission is linked to fibre diameter. To achieve more uniform emission, fibres were modified with multiple bends of decreasing radii, i.e. increasing side emission, along the fibre (Figure 5-7C).
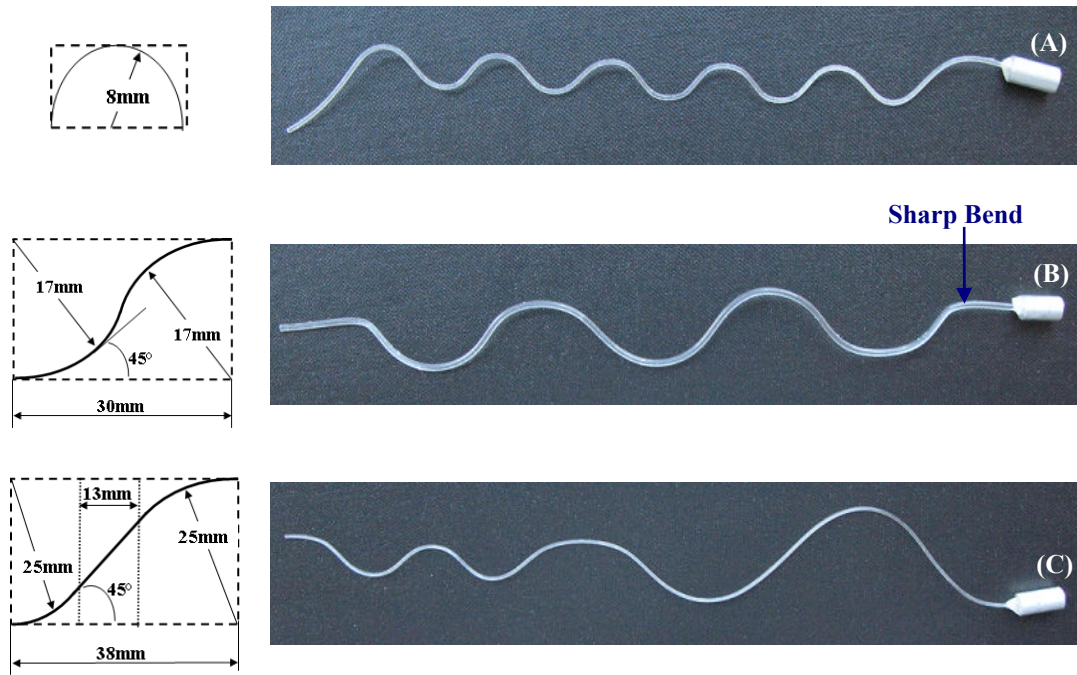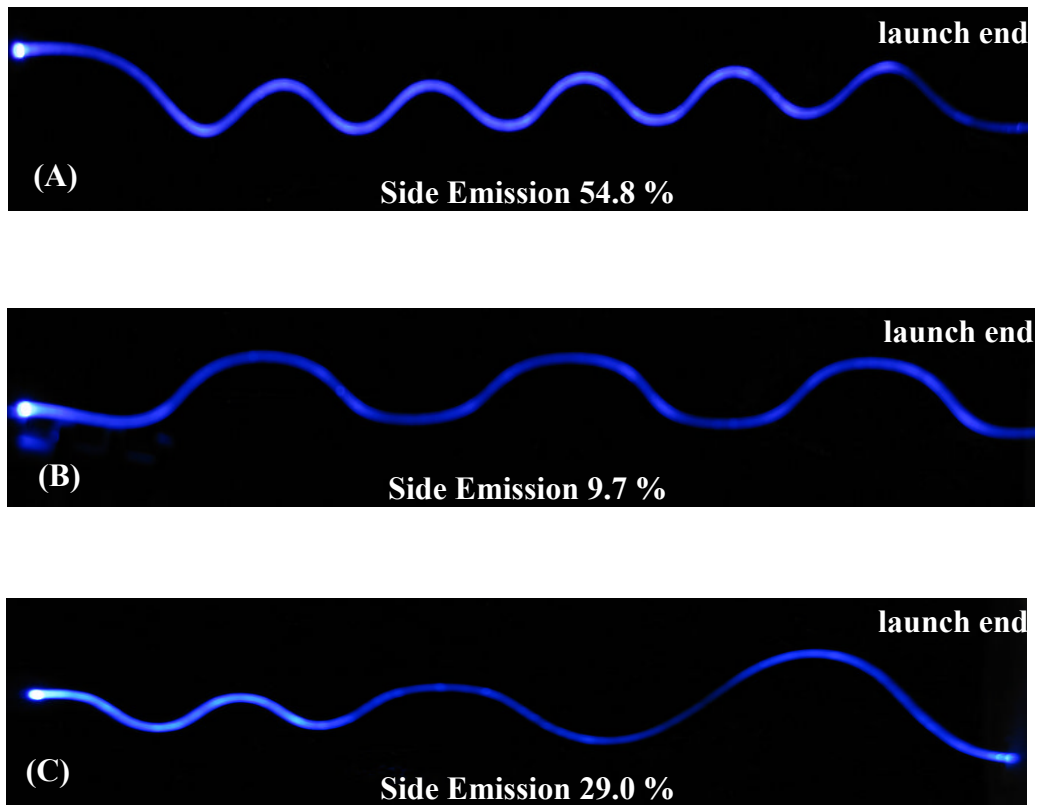
Figure 5-7. Examples of geometric modification of the PMMA optical fibres (details of the bend geometries shown on the left); (A) ten bends, 8 mm radius, (B) twelve bends, 17 mm radius, (C) ten bends, different radii, three bends similar to example A, two bends similar to example B, five bends with dimensions as shown on the left.

Table 5-3. Transmission through PMMA optical fibres exhibiting different geometric modifications. The original length of all fibres before geometric modifications was 245 mm

| Fibre	Fibre modification	Total power transmission of fibre		Loss in transmitted power
		untreated / mW	treated / mW	
2	as in Figure 5-7B (sharp bend)	155	130	16.1 %
	as in Figure 5-7B (no sharp bend)		140	9.7 %
	as in Figure 5-7A		70	54.8 %
	as in Figure 5-7C		110	29.0 %
4	as in Figure 5-7B (sharp bend)	525	120	77.1 %
	as in Figure 5-7B (no sharp bend)		270	48.6 %
	as in Figure 5-7A		15	97.1 %
	as in Figure 5-7C		150	71.4 %
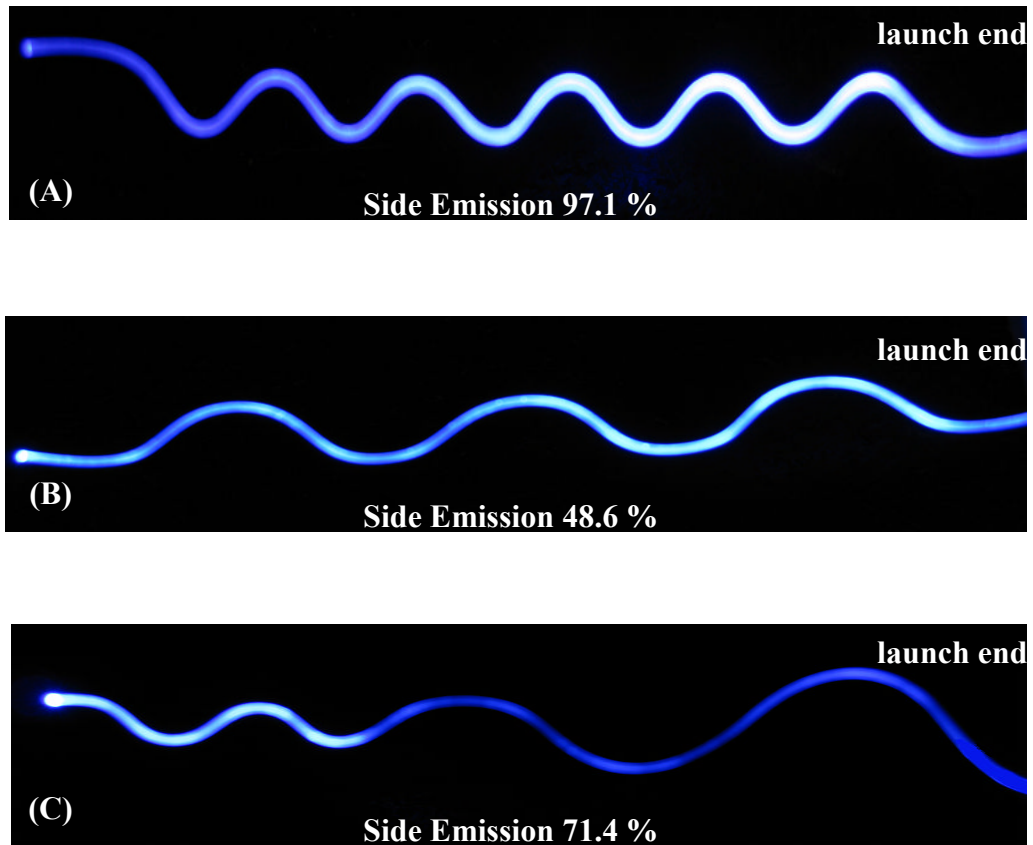
Figure 5-8. Photographic images of geometric modification for PMMA optical fibres (fibre 4, 1551 µm diameter) showing the resulting side emission caused by the shape modification of the fibre when connected to the Hg lamp (40 W/cm^2); (A) ten bends, 8 mm radius, (B) twelve bends, 17 mm radius, (C) ten bends, multiple radii, as shown in Figure 5-7.

Figure 5-9. Photographic images of geometric modification for PMMA optical fibres (fibre 2, 750 µm diameter) showing the resulting side emission caused by the shape modification of the fibre when connected to the Hg lamp (40 W/cm^2); (A) ten bends, 8 mm radius, (B) twelve bends, 17 mm radius, (C) ten bends, multiple radii, as shown in Figure 5-7.

Mechanical Treatment

In the commercial PMMA side emitting optical fibre (fibre 5), side emission was achieved by micro-perforation of the cladding. These micro-holes were found to vary in size and to be distributed non-uniformly (Figure 5-10). This irregularity of the perforation results in strong fluctuations of the side emission, as was discussed earlier in Section 3.4.2.2 of Chapter 3.
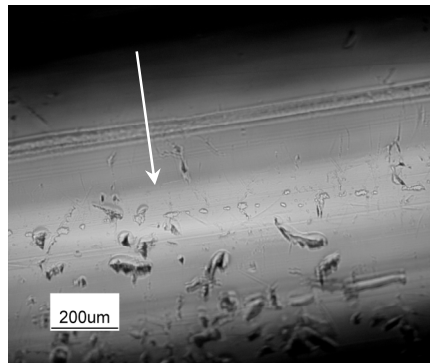
Figure 5-10. Optical reflection microscopic image of fibre 5 (Table 5-1), showing irregular surface perforations.

To achieve more consistent side emission along the fibre, other techniques can be used. Sillyman et al. [3] controlled the side emission by creating notches in the fibre cladding. Varying the distances between the notches along the fibre allowed uniform emission to be obtained. Zarian et al. [4] suggested that uniform high rates of side emission can be achieved by applying micro-cuts on the fibre core. Joseph et al. [5] and Yokogawa et al. [6] demonstrated the possibility of using scattering particles in either the core or the cladding of a fibre. In addition, launching light at both ends of the fibre further improves side emission uniformity as demonstrated by Spigulis et al. [7].

Here, the untreated PMMA optical fibres (Table 5-1) were modified by micro-cutting and embedding of silica particles into the fibres to study the possibility of achieving maximum side emission. Micro-cuts with depths less than 100 µm along the fibre were applied to the poly(vinylidene fluoride) cladding. The micro-cuts were applied to the cladding of the PMMA optical fibre using an in-house made micro-cutting tool. The length of the tip was measured using a micrometer. The micro-cuts were applied at graduated distances to allow uniform emission along the fibre, as shown in Figure 5-11. See Appendix C-1 'C3' for more details about this process.
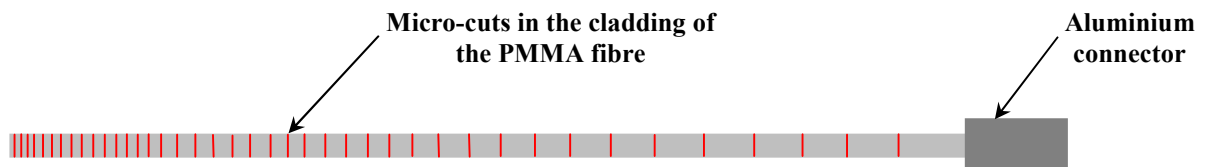
Figure 5-11. Schematic illustration showing micro-cuts applied at graduated distances to allow uniform emission along the fibre.

Silica particles of sizes ranging from ~2 µm to 70 µm were mechanically embedded in the cladding (more details about this process is shown in Appendix C-1 'C3'). Silica was selected because of its high UV transmission [143]. The particles were embedded into the fibres by firmly pressing the fibres onto a layer of evenly spread silica particles on a steel plate by using a wooden block. The process was carried out by turning the fibre three times through 45° so that the silica particles evenly penetrated into the side of the fibres. This process was repeated and the drop in power output at the fibre end was measured after each treatment, until the power was constant.

The depth of micro-cuts and the sizes of the silica particles were selected so that the treatments affected both the cladding and the core of the fibres. The densities of the micro-cuts and of the silica particles were increased progressively to increase side emission. Both

treatments were studied individually and in combination. The micro-cut treatment was quantified by the number of micro-cuts. The quantity of the embedded silica particles in an optical fibre was determined by weighing the fibre before and after the treatment process using the Sartorius HR60 scale (Sartorius HR60).

Measurement of the total power transmission indicated that the side emission efficiency of the fibres increased with increasing number of micro-cuts in the cladding. Relative to the total power transmitted through an untreated fibre, up to 60 % side emission was achieved (85 micro-cuts along the fibre). Further increases of the number of micro-cuts reduced the mechanical integrity of the fibre.

Embedding silica particles in the cladding of the fibre (particles evenly distributed along the fibre, total mass 3×10^{-3} g) resulted in a side emission of 81 % of the total power (Figure 5-12). A combination of micro-cuts and silica particle treatment (Figure 5-13) resulted in a 94.5 % side emission. The micro-cuts were applied before the silica particles were embedded, allowing silica particles to be embedded both in the micro-cuts and the undamaged poly(vinylidene fluoride) cladding (Figure 5-13).

Further enhancement of the side emission efficiency can be achieved by combining mechanical treatment of the fibre with geometric modification. Reshaping fibre 3 (245 mm long) to twelve bends with a 17 mm radius resulted in a side emission of 31 %. The same fibre showed a 96 % side emission when treated by combining silica (mechanical) treatment with geometrical modification. The resulting side emission from silica and geometric modification treatments can also be observed from the photographic images of the top and side views of the fibre in Figure 5-14.

(A)

(B)
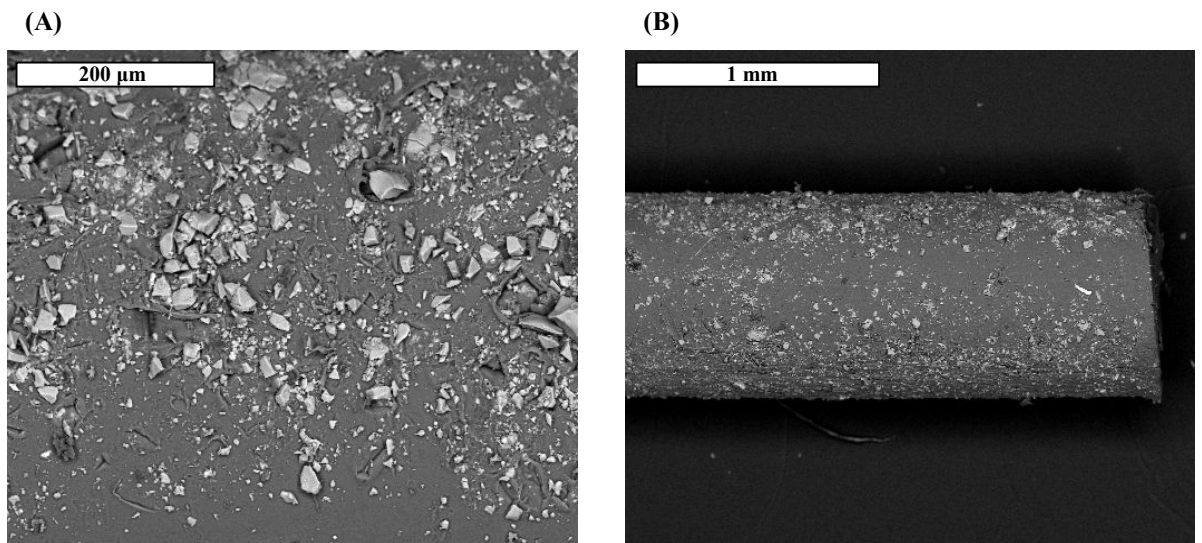
Figure 5-12. SEM secondary electron images of fibre 2 (750 µm diameter) with embedded silica particles; (A) different sizes of silica particles; (B) distribution of silica particles across fibre surface.
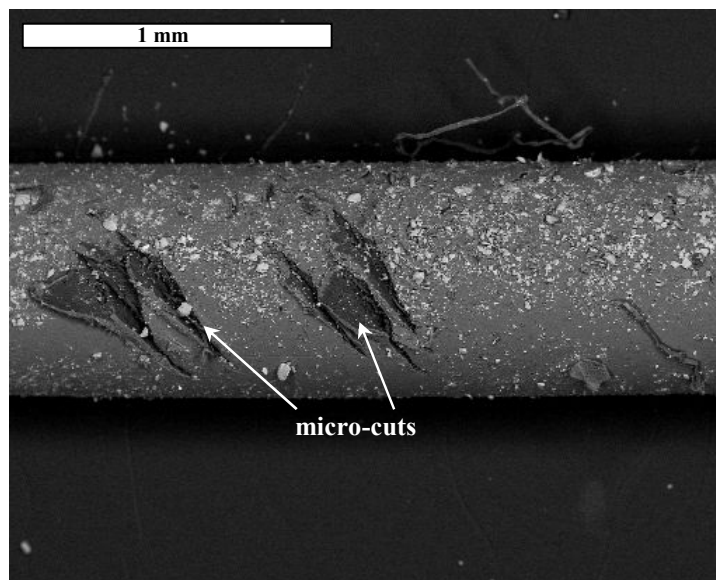
Figure 5-13. SEM secondary electron image of fibre 2, treated with silica particles and micro-cuts.
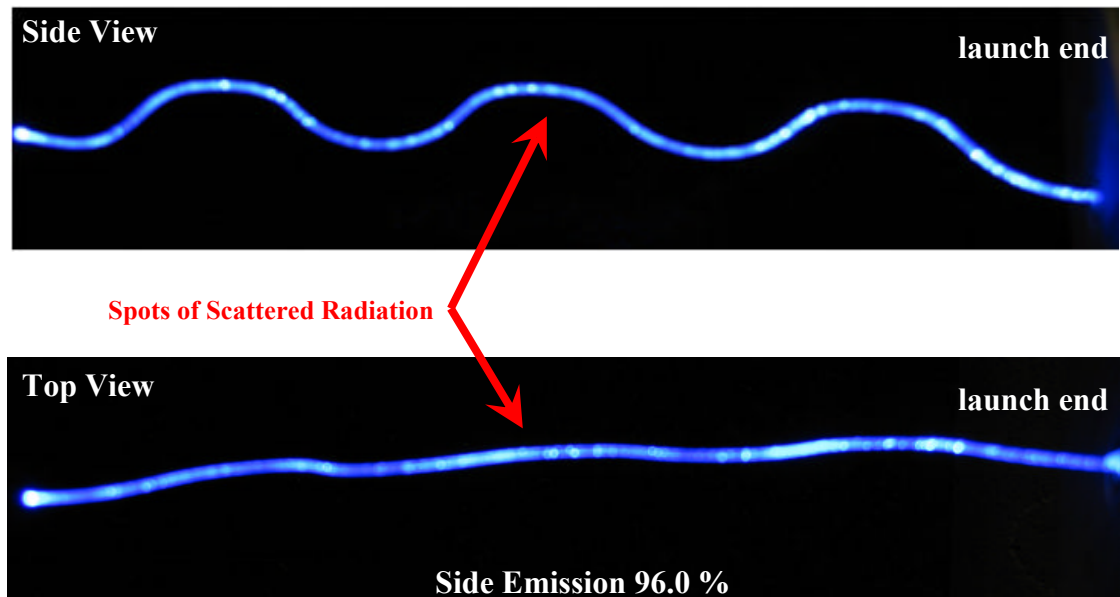
Figure 5-14. Side and top view, photographic images of fibre 3, treated with silica particles and twelve bends with 17 mm radius, connected to the Hg lamp (40 W/cm^2). The bright spots indicate emission at scattering particles.

5.4.4. Photocuring of the Optimised Epoxy Resin System using an Enhanced Side Emitting PMMA Optical Fibre (*Experiment Series 4*)

This section discusses the photocuring behaviour of resin formulations using a closed mould photocuring system, Figure 5-15, comprising:

- The Hg lamp with a nominal flux density of 40 W/cm^2 (Chapter 3, Section 3.4.1.1)

- The cooling device, to prevent the launch face of the optical fibre from degrading (Chapter 4, Section 4.3.2)

- The enhanced side emitting PMMA optical fibre (Section 5.4.3)

- The closed mould setup, to enclose the resin and the embedded PMMA optical fibre (see mould setup in Section 5.3.2)
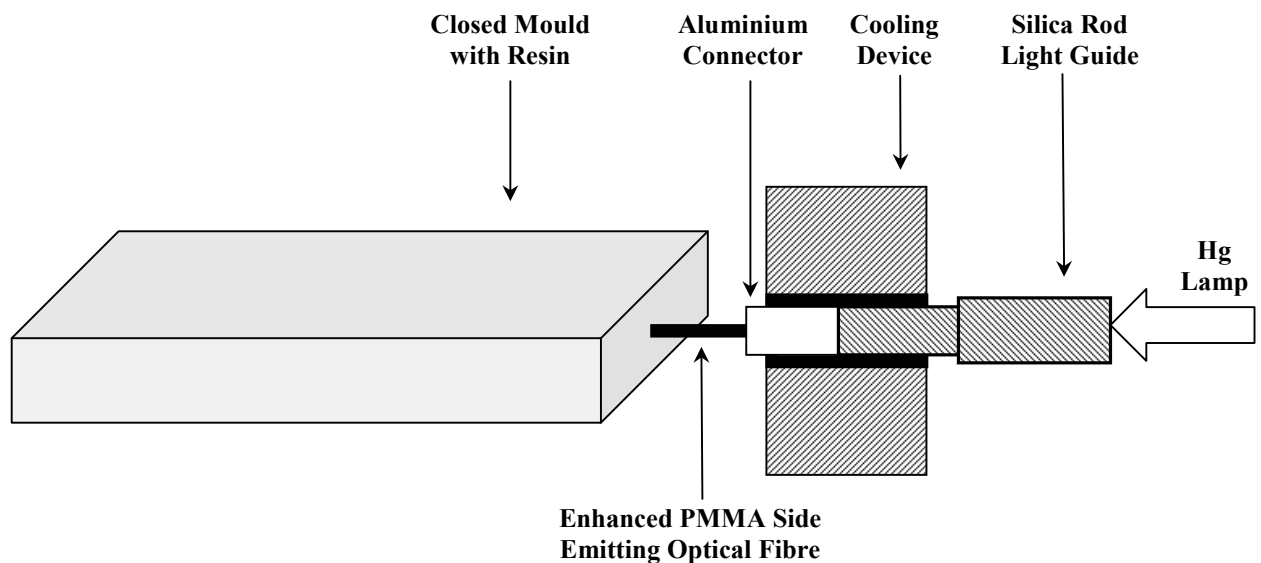
Figure 5-15. Schematic illustration of the closed mould system for photocuring of resins.

This system was used for curing the epoxy formulation RS3 (Chapter 2) into 1.5 mm and 5 mm thick components. The efficiency of the closed mould curing system for epoxy resin was further studied by applying it to component production using a polyester resin (1.5 mm thick). The curing processes for all the samples were conducted at room temperature (25 °C).

Fibre 3 (Table 5-1) was used for the curing processes. All fibres used for the curing process were treated over a length of 245 mm. The fibres were either treated with silica particles or in combination with a geometric modification. The silica treated fibres produced a side emission of ~ 81 % of the total launched radiation. The treated fibres in combination with silica particles and geometric modification of twelve bends with 17 mm radius, as shown earlier in Figure 5-14, produced a side emission of ~ 96 %.

Curing of a Component from Epoxy Resin using a Single Optical Fibre

The objective in curing formulation RS3 using single fibre was to determine the depth of cure for the 1.5 mm thick component away from the side of the fibre. The side emission uniformity along the treated section of the fibre was adopted from the work of Spigulis et al. [7] and was controlled by looping the fibre into one aluminium connector.

The resulting cured component is shown in Figure 5-16. The component fully solidified after 45 minutes of continuous irradiation from the Hg lamp. The distance of cure reached 10 mm from the side of the fibre (Figure 5-16).
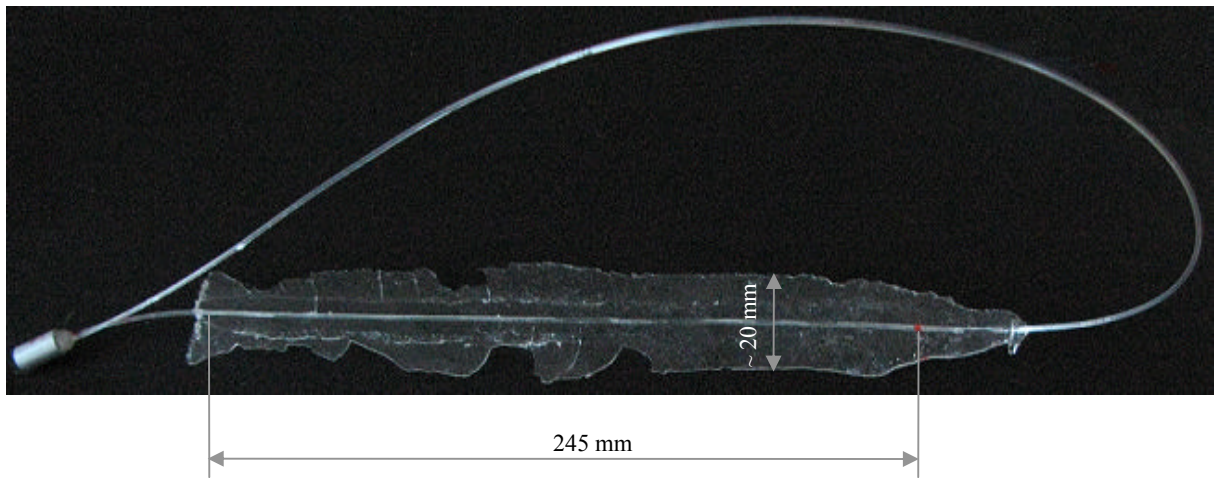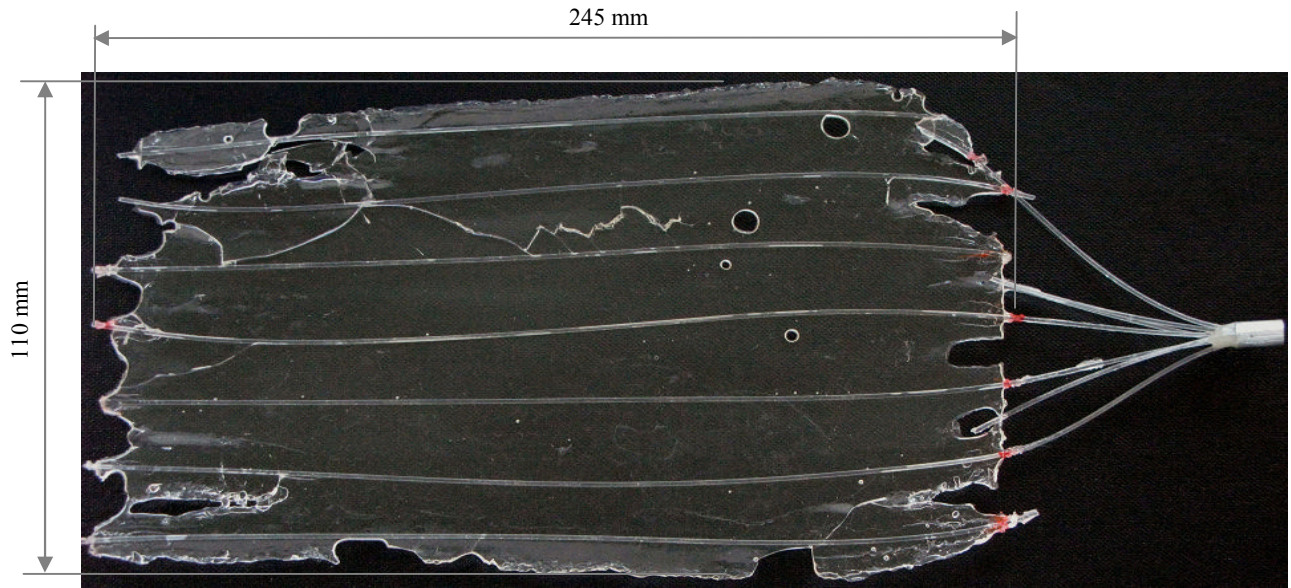
Figure 5-16. 1.5 mm thick component cured from the formulation RS3 (Section 2.3.3.4 of Chapter 2) using a single looped PMMA side emitting optical fibre (fibre 3, 1000 μm diameter) which was treated with silica particles. The sample was cured in 45 mins using the Hg lamp (40 W/cm^2).

Curing of a Components from Epoxy Resin using Multiple Optical Fibres

Large components were produced using multiple side emitting optical fibres. The curing process was conducted for 1.5 mm and 5 mm thick components.

The 1.5 mm thick component was 245 mm long and 110 mm wide. Seven silica treated fibres connected to one aluminium connector were used to cure the specimen. The component fully solidified after 45 minutes of continuous irradiation, as shown in Figure 5-17. The gaps in the component resulted from air bubbles during the curing process. The cracks in the component (Figure 5-17) occurred when it was released from the mould setup (Melinex polyester films and strip tape).
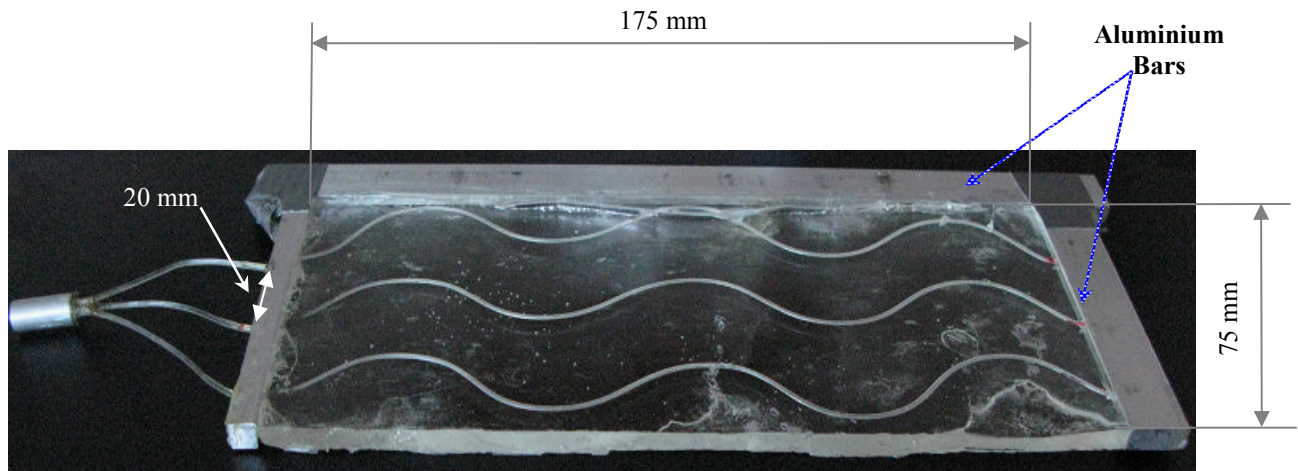
Figure 5-17. 1.5 mm thick component cured from the formulation RS3 (Section 2.3.3.4 of Chapter 2) using seven PMMA side emitting optical fibres (fibre 3, 1000 μm diameter) which were treated with silica particles. The fibres were connected to one aluminium connector. The specimen was cured in 45 mins using the Hg lamp (40 W/cm^2).

The curing of the 5 mm thick component was conducted using three treated fibres (fibre 3) with silica particles and having a geometric modification. The curing process was carried out for 45 minutes of continuous irradiation from Hg lamp. The specimen did not fully cure and remained rubbery. Irradiating the specimen beyond 45 minutes did not improve the curing result.

Thus, the specimen was only irradiated for 45 minutes. The specimen was then stored for 24 hours during which time it fully solidified due to the dark reaction process [1, 30-31], as shown in Figure 5-18. Overall, the long curing period of the specimen suggests that the larger the amount of epoxy resin the longer the polymerisation period will be.

Figure 5-18. 5 mm thick component cured from the formulation RS3 (Section 2.3.3.4 of Chapter 2) using three PMMA side emitting optical fibres (fibre 3, 1000 μm diameter) which were treated with silica particles and with a geometric modification of twelve bends with a 17 mm radius, as shown in Figure 5-14. The fibres were connected to one aluminium connector. The specimen was cured using the Hg lamp (40 W/cm^2). The specimen was connected to the Hg lamp for 45 mins and stored for 24 hours before handling.

Hardness Measurements for the Components Made from Epoxy Resin RS3

A Barcol hardness tester (Figure 2-9 of Chapter 2) was used for measuring the hardness distribution of the components cured using the side emitting optical fibre. The aim of this test was to measure the change in the hardness of the components along the fibre. As this test required a straight fibre, both 1.5 mm and 5 mm thick components were cured using only silica treated fibres. The hardness was measured at eight locations along the components, 10 mm apart, on both the top and bottom surfaces (Figure 5-19).
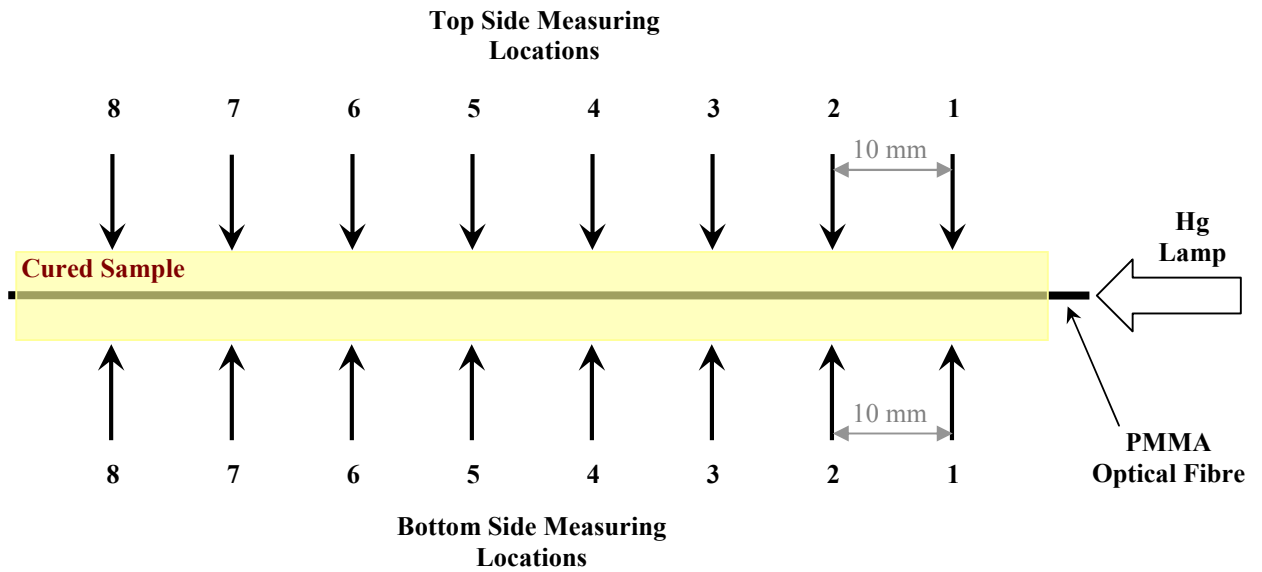
Figure 5-19. Schematic illustration of hardness measurements from both sides of each cured component. The hardness was measured at the numbered locations and distances. The hardness was measured by following standard BS 2782-10 [83]. Not to scale.

The resulting hardness of the 1.5 mm thick component is shown in Figure 5-20 and Table 5-4. The hardness fluctuated along the fibre length. The hardness was slightly less than that of the casting cured using the flood lamp (Figure 2-22 and Table 2-12) which has been discussed earlier in Chapter 2.
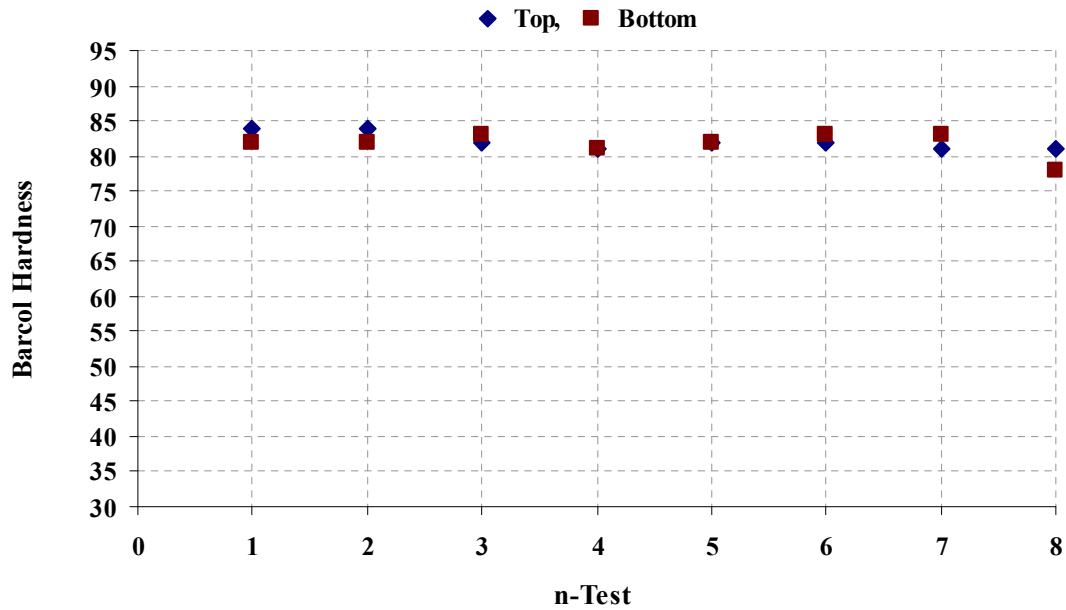
Figure 5-20. Graph of Barcol hardness versus number of test points for the 1.5 mm thick component from the formulation RS3 (Section 2.3.3.4 of Chapter 2) cured using a silica treated PMMA optical fibre (fibre 3, 1000 μm) in 45 mins. The hardness was measured from the top and bottom surfaces of the component.

Table 5-4. Barcol hardness test results of the 1.5 mm thick component from the formulation RS3 (Section 2.3.3.4 of Chapter 2) cured using a silica treated PMMA optical fibre (fibre 3, 1000 μm) in 45 mins.

|	Top Surface	Bottom Surface
Mean	82	82
SD	**1.2**	**1.7**

For the 5 mm thick component, the specimen was cured in a closed mould made from polypropylene copolymer plastic sheet and by using Melinex polyester films [78]. The mould was made for casting a component of dimensions: 5 mm thick, 10 mm wide and 100 mm long.

The 5 mm thick component was irradiated for 45 minutes. Although, the component was physically solid (Figure 5-21), it exhibited very low hardness. Hence, it was stored. The hardness was measured 24 hours and 36 hours after irradiation to study the effect of dark reactions.
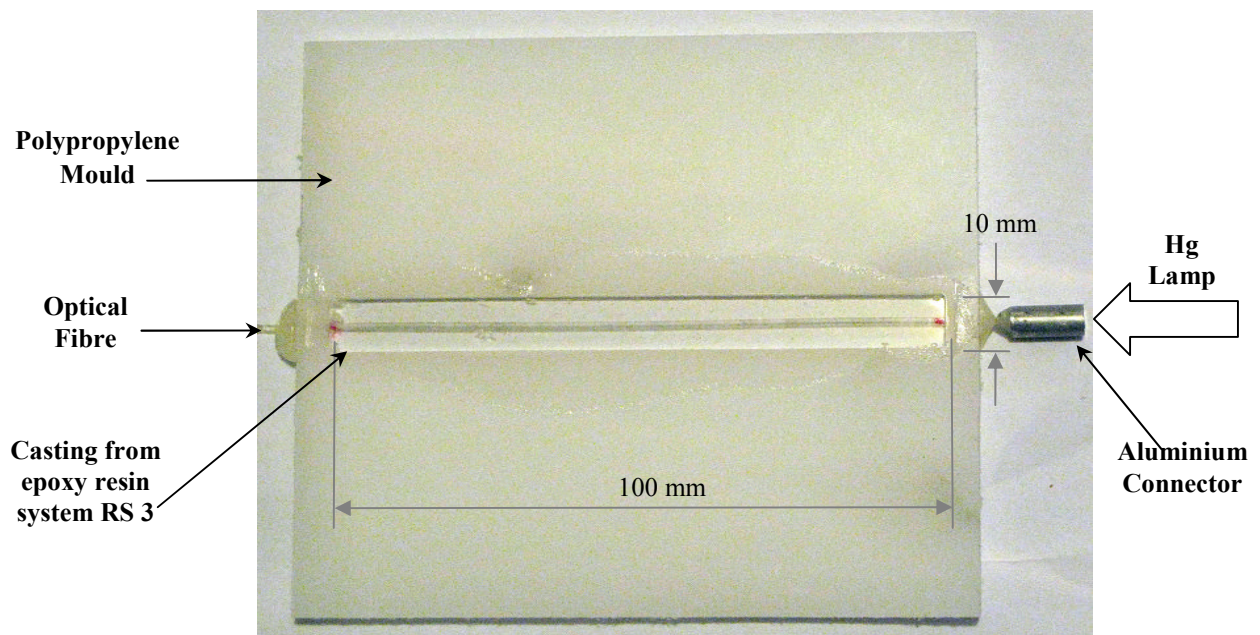
Figure 5-21. 5 mm thick component cured from the formulation RS3 (Section 2.3.3.4 of Chapter 2) and PMMA side emitting optical fibre (1000 μm diameter) which was treated with silica particles. The specimen was cured using the Hg lamp (40 W/cm^2). The specimen was connected to the Hg lamp for 45 mins and handled after 24 hours.

The hardness measurements of the component made after 24 hours showed that the bottom surface was harder than the top surface, as shown in Figure 5-22 and Table 5-5. The hardness of the bottom surface increased gradually from the launch face of the side emitting optical fibre until test point 4 (50 mm away from the fibre connector). The hardness of the bottom surface then slightly reduced.
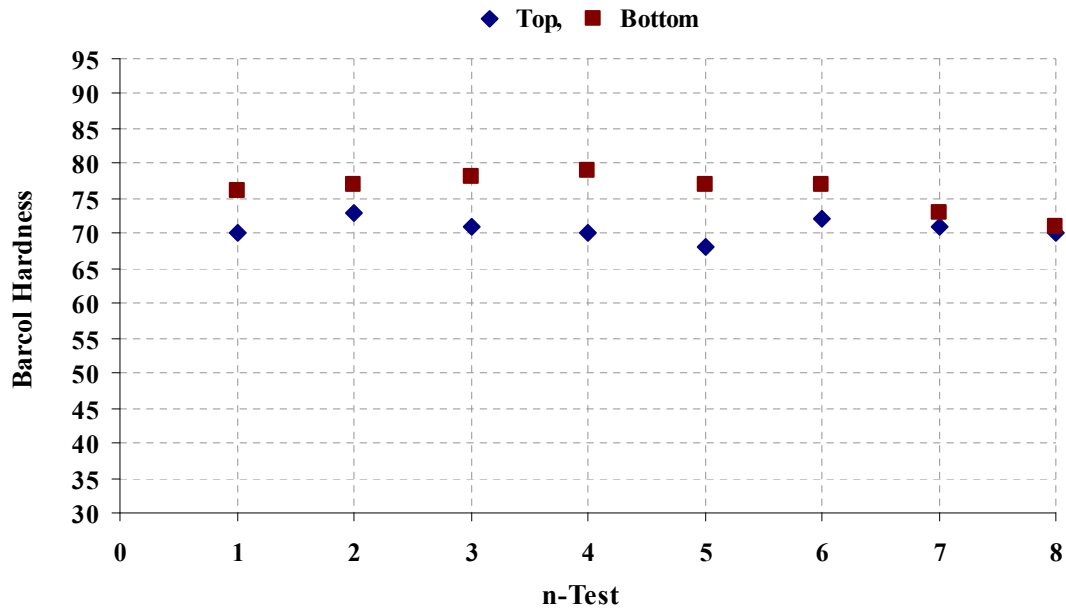
Figure 5-22. Graph of Barcol hardness versus number of test points for the 5 mm thick component from the formulation RS3 (Section 2.3.3.4 of Chapter 2) cured using silica treated PMMA optical fibres (fibre 3, 1000 μm). The hardness was measured from the top and bottom surfaces of the component 24 hours after irradiation.

Table 5-5. Barcol hardness test results of the 5 mm thick component measured 24 hours after irradiation from the formulation RS3 (Section 2.3.3.4 of Chapter 2) cured using silica treated PMMA optical fibres (fibre 3, 1000 μm).

	Top Surface	Bottom Surface
Mean	71	76
SD	**1.5**	**2.7**

The fluctuation in the hardness readings of the 1.5 mm and 5 mm thick components (Figure 5-20 and Figure 5-22) was suspected to have resulted from an inconsistency in the distribution of the embedded silica particles along the fibres. Hence, this was tested by measuring the side emission spectral output of a 40 cm long silica treated optical fibre (fibre 3). The resulting side emission of the fibre (Figure 5-23) indicated small fluctuation in the side emission intensities which explains the fluctuation on the measured hardness after 24 hours. Thus, the harder locations had been irradiated with higher intensity. However, the spectral output of this PMMA optical fibre (in-house treated) showed an improved exponential drop of side emission along the fibre compared to the commercial side emitting PMMA optical fibre which were discussed earlier in Chapter 3 (Figures 3-27 and 3-28). In addition, Figure 5-22 does not show an exponential behaviour in hardness results similar to the fibre spectral output (Figure 5-23). This was due to the continuous irradiation for 45 minutes which more likely was sufficient to give the specimen along the fibre the maximum radiation for the curing process for a definite depth at each location along the fibre and the higher hardness readings (Figure 5-22) were from higher irradiated locations.

The hardness measurements of the component after 36 hours from irradiation indicated an increase in hardness of both top and bottom surfaces (Figure 5-24 and Table 5-6). Although, Figure 5-24 shows small fluctuations in hardness readings, the mean hardness and the standard deviation values were found to be similar. Therefore, the dark reactions within formulation RS3, after being irradiated for 45 minutes, carried on the polymerisation process and the specimen eventually cured evenly.

Figure 5-23. Irradiance E_λ at $\lambda = 368$ nm as a function of the position x along fibre 3 which was treated with silica particles, measured at radial distance $r = 2$ mm from the fibre axis.
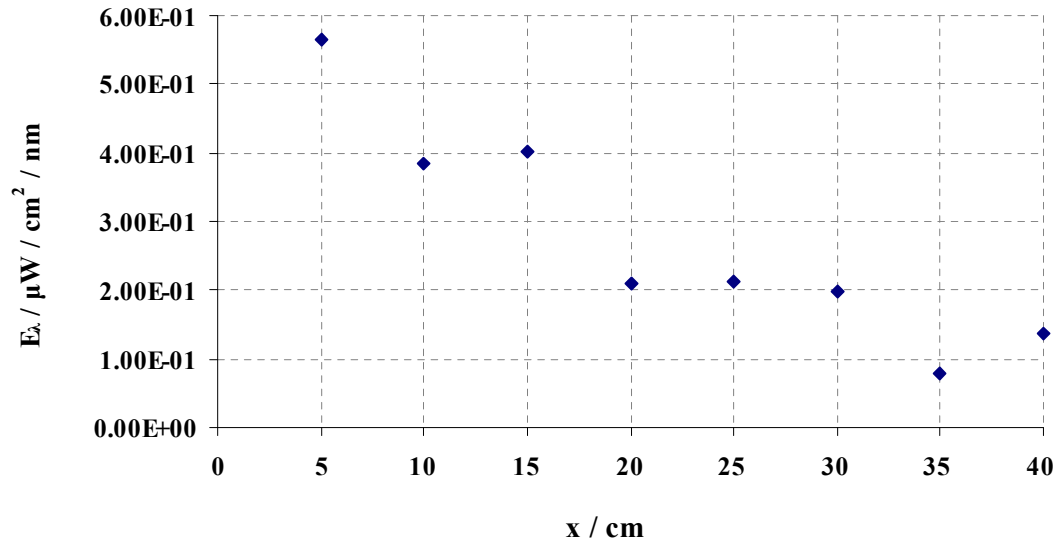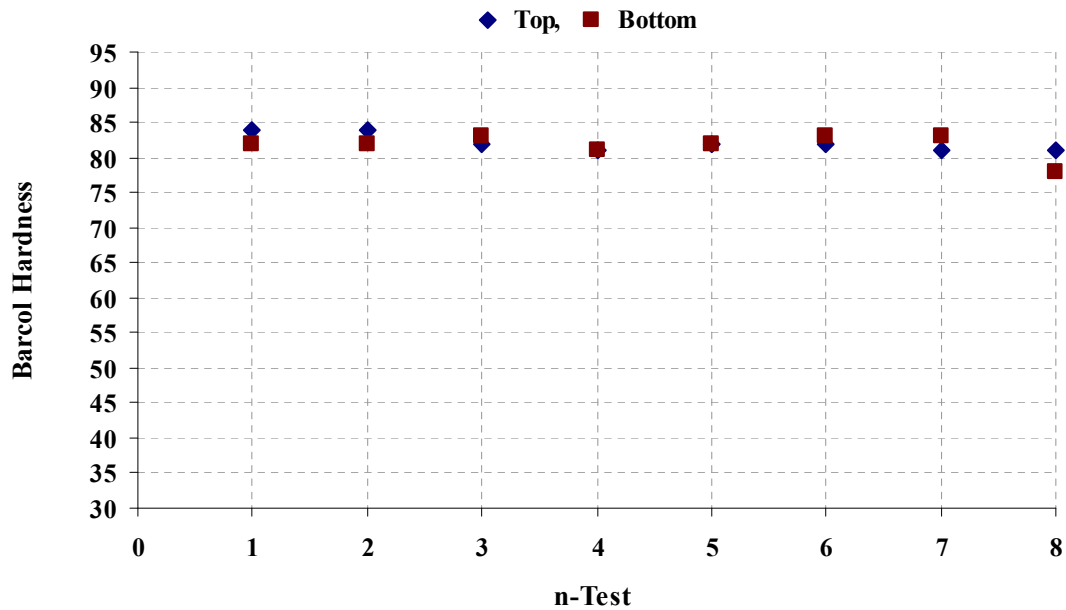

Figure 5-24. Graph of Barcol hardness versus number of test points for the 5 mm thick component from the formulation RS3 (Section 2.3.3.4 of Chapter 2) cured using silica treated PMMA optical fibres (fibre 3, 1000 μm). The hardness was measured from the top and bottom surfaces of the component after 36 hours from irradiation.

Table 5-6. Barcol hardness test results of the 5 mm thick component measured 36 hours after irradiation from the formulation RS3 (Section 2.3.3.4 of Chapter 2) cured using silica treated PMMA optical fibres (fibre 3, 1000 μm).

	Top Surface	Bottom Surface
Mean	85	85
SD	**1.6**	**2.4**

Energy consumed for curing the 1.5 mm thick epoxy component

The energy consumed for the photocuring processes of the 1.5 mm thick components (Figures 5-16 & 5-17) may be calculated using equation 2-4 (Chapter 2). Knowing that the power output of the Hg lamp is 0.2 kW (Section 3.4.1.1), the energy consumed for photocuring the 1.5 mm thick components is 0.15 kWh.

Applying the Closed Mould Curing System for Polyester Resin

The ready formulated polyester resin [141] was also cured using the closed mould setup, as shown earlier in Figure 5-15. For more detail about the photocuring behaviour of polyester resin, see Appendix B-1 'B2'.

The 1.5 mm thick polyester resin specimen was fully cured in seven minutes which is about six times faster than that of the formulation RS3. The component from the polyester resin cured further from the optical fibre than the formulation RS3. The polyester resin cured to a distance of ~ 15 mm from each side of the optical fibre, as shown in Figure 5-25. However, due to the irregular side emission of the fibre the specimen did not cure evenly from the edges (Figure 5-25).

The hardness measurement of the component from polyester resin showed a small variation between the top and bottom surfaces, as shown in Figure 5-26, compared to the hardness of the 1.5 mm thick component from the formulation RS3 (Figure 5-20). This can also be observed from the mean hardness and the standard deviation values from Table 5-4 and Table 5-7. In addition, further irradiation of the polyester specimen did not improve the hardness results. As the polyester resin photocuring process is based on radical reactions, the polymerisation reactions within the resin stops immediately when the radiation source is removed [36]. Thus, the hardness of the specimen from the polyester resin did not change after the irradiation process.

Overall, the closed mould curing behaviour, using the enhanced side emitting PMMA optical fibre, for the polyester resin indicated higher reactivity than that of the optimised epoxy resin system 3 (formulation RS3) and resulted in a faster curing rate. This suggests that the efficiency of the photocuring process is highly dependent upon the reactivity of the resin used and the optical transmission of the required spectrum for the curing process during the curing process.
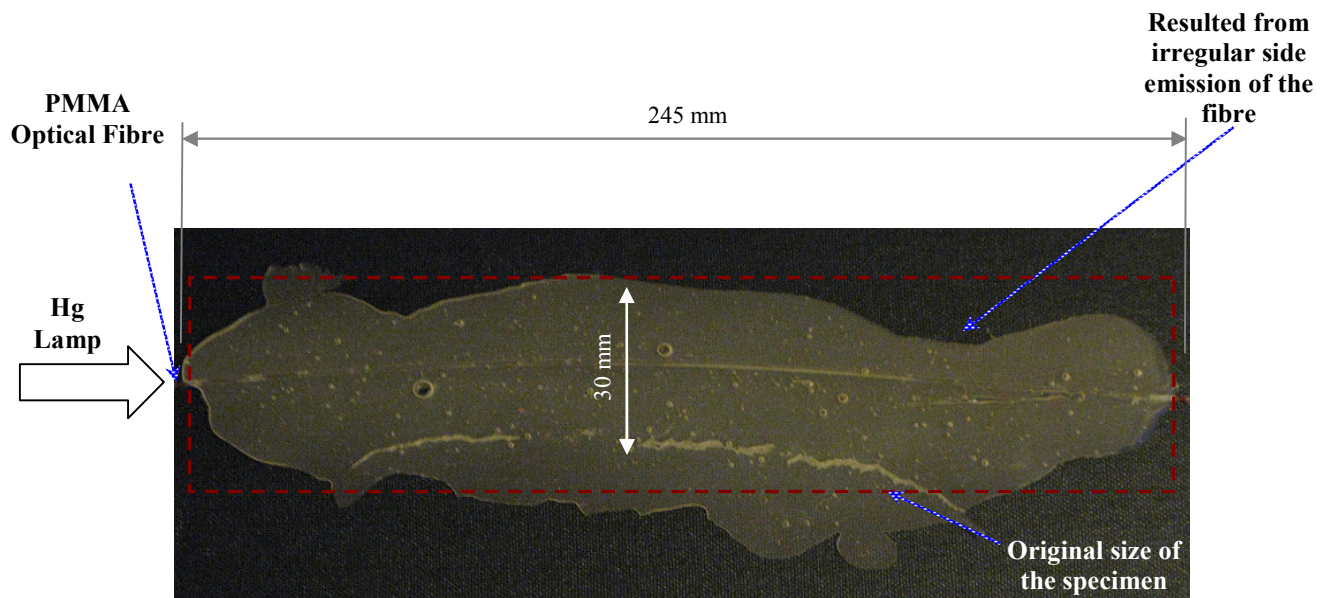
Figure 5-25. 1.5 mm thick component cured from the ready formulated polyester resin using a single PMMA side emitting optical fibre (fibre 3, 1000 μm diameter) which was treated with silica particles. The specimen was cured in 7 minutes using the Hg lamp (40 W/cm^2).
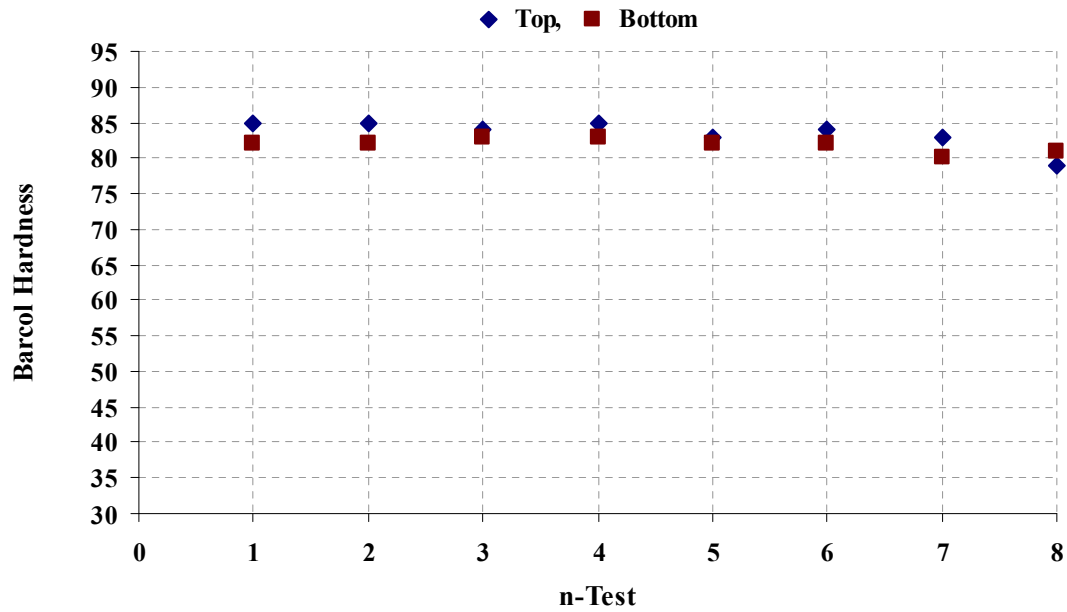
Figure 5-26. Graph of Barcol hardness versus number of test points from each side of the 1.5 mm thick component from the ready formulated polyester resin cured using a silica treated PMMA optical fibre (fibre 3, 1000 μm) in 7 minutes.

Table 5-7. Barcol hardness test results of the 1.5 mm thick component from the ready formulated polyester resin cured using a silica treated PMMA optical fibre (fibre 3, 1000 μm) in 7 minutes.

	Top Surface	Bottom Surface
Mean	84	82
SD	**2.0**	**0.9**

5.5. Chapter Conclusions

For the development of a photocuring process for curing epoxy resin in a closed mould, the attenuation of the PMMA polymer optical fibre (POF) was studied and its side emission efficiency was enhanced. Transmission measurements for PMMA POF at different lengths indicated that, due to discrete defects, the attenuation is non-uniform along the fibres. Due to these effects, even untreated fibres show a certain degree of side emission.

Transmission losses due to side emission at fibre bends increase with increasing bending angle (or number of full loops), increasing fibre diameter and decreasing bend radius. Geometric modification of a fibre (bends with defined radii) allows a defined level of side emission to be achieved.

Mechanical treatment of the 245 mm long fibres by application of 85 micro-cuts and embedding 3×10^{-3} g of scattering silica particles resulted in side emission of most of the power launched into the fibres, 60 % and 81 %, respectively. Fibres treated by embedding silica particles and having a geometry modification gave the best results in terms of side emission intensity. A side emission of 96 % of the total power launched into the fibre was observed. The spectral output of the silica treated PMMA POF emitted side emission with much less fluctuations compared to the commercial side emitting PMMA POF.

The photocuring of an epoxy resin system in a closed mould was achieved by embedding the treated PMMA POF when connected to the Hg lamp (40 W/cm^2). 1.5 mm and 5 mm thick components from the optimised epoxy resin system 3 (formulation RS3) were cured. The 1.5 mm thick components cured in 45 minutes which led to total energy consumption by the Hg lamp of 0.15 kWh. The 5 mm thick component partly cured in 45 minutes. However, due to the cationic photoinitiator within the epoxy, dark reactions continued and the component eventually cured with time (up to 36 hours). The closed mould photocuring system was tested with polyester resin. The 1.5 mm thick component from polyester resin

cured ~ 6 times faster (7 minutes) than that of epoxy resin when the silica treated side emitting PMMA POF was used. Hence, the efficiency of the photocuring process in a closed mould application using the developed system is highly dependent on the resin reactivity as well as on the depth of radiation penetration into the resin.

Chapter 6

Discussion, Conclusions and Recommendations for Future Work

6.1. Discussion

This work was conducted to develop a closed mould photocuring system, such as Resin Transfer Moulding, to cure a photoinitiated cationic epoxy resin. The system was aimed at curing a photoinitiated cationic epoxy resin using an embedded, side emitting optical fibre with radiation exposure ranging from ultraviolet to visible blue (350 nm to 450 nm). The work included characterisation of different types of epoxy resins and commercial side emitting optical fibres to establish an optimised curing system for making thick and thin composite components.

In Chapter 2, characterisation of different types of epoxy resins was conducted using a flood lamp with a nominal flux density of 0.1 W/cm^2. The characterisation process included curing 5 mm thick samples. During this process, the different types of the epoxy resin systems consisted of: two commercial, pre-formulated epoxy resin systems, in-house prepared bisphenol A/F epoxy with triarylsulfonium hexafluorophosphate salts photoinitiator, and in-house prepared cycloaliphatic epoxy with triarylsulfonium hexafluoroantimonate salts photoinitiator. The last two types were further improved using oxetane polyol, and the cycloaliphatic epoxy based formulation was also investigated using two photosensitizers.

Photopolymerisation of the thick resin samples (5 mm) resulted in different curing behaviour for various epoxy resin formulations. The epoxy resin formulation optimisation process resulted in four main resin systems; three of which are based on cycloaliphatic epoxy and one based on bisphenol A/F epoxy. The most efficient formulations of resin systems from both types of epoxides were reached when an oxetane additive was included. The samples cured from the in-house formulated resin systems exhibited more uniformly distributed hardness than the commercial epoxy resin systems. Adding oxetane to the resin system of bisphenol A/F epoxy improved the curing speed and the overall hardness distribution of the casting. Resin systems of cycloaliphatic epoxy were found to be harder with a more uniform hardness distribution than the resin system of bisphenol A/F epoxy.

In-house formulated resin systems from bisphenol A/F and cycloaliphatic epoxides cured faster than the commercially available, pre-formulated epoxy resin systems. The commercial epoxy resin systems cured in 65 minutes, while the optimised resin system from bisphenol A/F and cycloaliphatic epoxides cured in 10 minutes and 2 minutes, respectively. This indicated that curing resin systems derived from cycloaliphatic epoxy consume lower energy than the bisphenol A/F based resin systems. In addition, the effect of viscosity reduction by including an oxetane additive had more influence on cycloaliphatic epoxy than bisphenol A/F.

H-Nu470 and anthracene photosensitizers can be used to improve the curing behaviour of an epoxy based resin system. However, they did not improve the curing speed when added to cycloaliphatic epoxy. The resin system with H-Nu470 photosensitizer did not cure at all, while the resin system with the anthracene photosensitizer cured in a period 6 times longer than the cycloaliphatic epoxy resin formulation with and without the oxetane additive.

The radiation absorption of the optimised resin systems before and during photo-polymerisation was studied by spectroscopic experiments. The absorption behaviour of the optimised resin systems are described by the response spectrum κ_λ, which is derived by using the optical density (OD) and the Beer-Lambert law of absorption. The absorption

spectra determined were compared with the emission spectrum of a high emission Hg lamp (40 W/cm^2) which delivered major emission peaks at wavelengths 368 nm, 406 nm and 440 nm.

The response spectrum κ_λ of the sulfonium photoinitiators were found to overlap the emission peak of the Hg lamp at wavelength 368 nm and covered some of the emission peak at wavelength 408 nm. However, when the photoinitiators were added to either cycloaliphatic or bisphenol A/F epoxy resins the response spectra κ_λ shifted away from the UVA band emission peaks of the Hg lamp leading to lower radiation absorption.

Although the cycloaliphatic epoxy resin formulation with the anthracene photosensitizer showed the highest absorption which overlapped the peak emission at wavelength 368 nm of the Hg lamp, it cured in a period of 6 times longer than the cycloaliphatic epoxy resin formulation with and without the oxetane additive. The resin formulation from bisphenol A/F epoxy resin showed the second highest response κ_λ. The other two resin system formulations using the cycloaliphatic epoxy exhibited the lowest response κ_λ among the others. Oxetane additive decreased the viscosity of cycloaliphatic epoxy resin system and at the same time increased the absorption of the resin system in the UVA band.

The response κ_{368} of the optimised resin systems during the photocuring, at a wavelength of 368 nm, indicated a variation. Resin systems of the bisphenol A/F epoxy resin and the cycloaliphatic epoxy resin formulations with the anthracene photosensitizer cured in a longer period as a result of a continuously increased absorption of the emitted irradiation at wavelength 368 nm. Resin systems from cycloaliphatic epoxy resin with and without oxetane additive had a decreased level of absorption as they cured. None of the optimised resin systems absorption decreased below the absorption measured before the curing process, which almost certainly was caused from the developed optical property of the castings after the curing process. The resin system formulated from cycloaliphatic epoxy and oxetane additive exhibited lower absorption after curing than the resin system

formulation from cycloaliphatic epoxy without the oxetane additive. Hence, adding oxetane to a cycloaliphatic epoxy resin system reduced the absorption after curing. This curing behaviour would allow deeper curing of this resin system comparing to the other resin systems.

Generally, according to the overall characterisation results of different types of epoxy resin systems, the epoxy resin system 3 (formulation RS3) formulated from cycloaliphatic epoxy (100 PHR) with triarylsulfonium hexafluoroantimonate salt photoinitiator (0.6 PHR) and oxetane (2.6 PHR), showed the most efficient curing behaviour. This makes it the appropriate formulation to be used for photocuring applications when an embedded side emitting optical fibre is employed for transmitting the radiation emission from its side to the surrounding resin medium.

Different types of commercial side emitting optical fibres were characterised (Chapter 3). The constituent parts of the fibres, materials and side emission mechanisms were investigated. The fibres were generally of two types. The first type had a silica core with silicone cladding (PDMS) containing particles (either ZnO or Al_2O_3) and diffuser (either PA6 or ETFE). The second type was a polymer optical fibre (POF) with a PMMA core and a PVDF cladding having micro-perforations as a side emission mechanism.

The particles in the claddings of the silica core fibres and the micro-perforations along the claddings of the PMMA core fibres were irregularly distributed. The optical transmission through the side surface of the fibres was studied by coupling each one of them to the high emission Hg lamp (40 W/cm^2) which emits radiation in the UVA and visible (320 nm to 450 nm) bands. The silica core fibre with Al_2O_3 particles and the PMMA core fibres transmitted an emission spectrum identical to the Hg lamp, while fibres with ZnO particles showed high absorption below wavelength 380 nm. However, the measured low intensities at wavelength 368 nm from the side surface of the fibres with ZnO particles showed more uniform exponential decay along the length of the fibres which suggests a more uniform scattering

mechanism compared to both the PMMA core fibres and the silica core fibres with Al_2O_3 particles.

The optical transmission measurements from the side of silica core fibre with Al_2O_3 particles and the PMMA core fibres makes them more suitable for applications requiring irradiation in the UVA band. In addition, even the untreated PMMA core fibres, which are designed to transmit the light from one end to another, produced side emission when connected to the high emission Hg lamp due to the intrinsic and extrinsic losses within the fibres. Overall, even though the side emission from the PMMA core fibres fluctuated, it emitted a higher intensity in the UVA band than the silica core fibre with Al_2O_3 particles. Nevertheless, optimisation of the side emission mechanism of the PMMA core fibre would allow more uniform side emission.

Before implementing the PMMA POF for photocuring epoxy resin in a closed mould and due to the polymeric material of this optical fibre, the optical transmission stability at the launch face of the PMMA POF under continuous irradiation periods from the high emission Hg lamp (40 W/cm^2) was investigated (Chapter 4). The utility of the PMMA POF was studied at peak emissions: 335 nm, 368 nm, 406 nm and 438 nm.

The radiation generated by the Hg lamp caused the launch face of the PMMA POF, at the coupling between the fibre and the Hg lamp, to undergo physical and chemical changes which led to a drop in the radiation launched into and transmitted by the PMMA POF. Hence, a cooling device was made to control the thermal condition at the coupling. Any thermal effect due to radiation absorption using the Hg lamp was better controlled when a cooling device was used. Without the cooling device the photo-degradation effect occurred after 7 minutes. The radiation transmission through the PMMA POF was found to have dropped by an average nominal of 1.2 % per minute to a maximum of 53 % after 13 minutes. But when the cooling device was employed, only 7 % of the radiation transmission was lost after 13 minutes. After 1 h, an overall transmission loss of 45 % was observed.

However, the lower degradation when using the cooling device indicates that the PMMA became more sensitive to UV-A radiation degradation at high temperatures.

The photo-degradation effect was analysed in more detail by monitoring the transmitted spectral intensity. A drop in spectral transmission of the PMMA POF with time was observed in both the UV-A and blue bands. The PMMA POF did not transmit well below the wavelength of 320 nm. The transmission loss increased gradually from longer (450 nm) to shorter (335 nm) wavelengths indicating relatively larger nominal absorption in the UV-A band. By using the Beer-Lambert law, the highest nominal absorption coefficient (α_λ) of the PMMA POF continuously exposed to the Hg lamp was found at 335 nm wavelength, when tested using the cooling device after 30 minutes and 60 minutes, 2.7×10^{-2} cm^{-1} and 6.1×10^{-2} cm^{-1}, respectively. Although, emission from the UV-A band caused photo-degradation, the relative change in the nominal absorption coefficient $\Delta\alpha_\lambda$ during continuous irradiation exposure indicated relatively more loss at a wavelength of 438 nm in the blue band. Furthermore, the irradiated PMMA POF launch face recovered a percentage of the loss in transmission with time. The resulting loss in transmission (44.8 %) after 1 hour of continuous irradiation, with the cooling device in place, was recovered to a maximum of 86 % after 5 weeks.

In Chapter 5, the PMMA POF was further investigated prior to adopting it in a photocuring process for epoxy resin in a closed mould condition. The conducted work determined the transmittance behaviour and side emission efficiency enhancements of the PMMA POF. The transmission measurements for the PMMA POF at different lengths indicated that the attenuation is non-uniform along the fibres due to randomly distributed discrete defects. Hence, even untreated fibres show a certain degree of side emission.

The side emission enhancements of the PMMA POF were carried out by modifying the geometry of the fibre and applying mechanical treatments. Prior to geometry modification (bend radii along the length) of the fibres, the transmission losses were studied by fibre

looping at different bend radii. This study indicated that the side emission at fibre bends increase with increasing bending angle (or number of full loops) and also by increasing fibre diameter and decreasing bend radius. The geometric modification of a fibre (bends with defined radii) allows a defined level of side emission to be achieved locally. A permanent modification of fibre geometry was accomplished by shaping the fibres with bend radii on an in-house made tool and then by conducting a heat treatment (fifteen minutes at a temperature of 70 °C in an oven).

The mechanical treatments of the PMMA POF were applied by micro-cuts (depths less than 100 μm) and embedding silica particles (sizes from ~2 μm to 70 μm). The silica particles were used due to their high transmission in the UVA band. Mechanical treatment of the 245 mm long fibres by application of either 85 micro-cuts or embedding 3×10^{-3} g of scattering silica particles resulted in side emission of most of the power launched into the fibres, 60 % and 81 %, respectively. Fibres treated by embedding silica particles and having geometry modification gave the best results in terms of side emission intensity. A side emission of 96 % of the total power launched into the fibre was observed. In addition, the spectral output of the in-house silica treated PMMA POF produced side emission with much less fluctuations compared to the commercial side emitting PMMA POF.

Hence, after treating the PMMA POF and embedding it in the optimised epoxy formulation RS3 (from Chapter 2), the photocuring process of an epoxy resin system in a closed mould was achieved. The closed mould photocuring process consisted of: Hg lamp (40 W/cm^2), cooling device, silica treated or in combination with bend radii PMMA POF, and a closed mould setup. Thus using this closed mould system, 1.5 mm and 5 mm thick components from the formulation RS3 were cured using an 1000 μm diameter PMMA optical fibre. The polymerisation of the 1.5 mm thick components using single or multiple (up to seven) silica treated PMMA optical fibres cured in 45 minutes, 20 mm wide and 110 wide, respectively. The 5 mm thick component (75 wide and 175 long) was cured with a PMMA optical fibre treated with silica particles and having geometry modification. This component cured to a

certain degree after 45 minutes due to the large volume of resin. The component was found to be soft like rubber. Therefore, time wise, photocuring of 5 mm thick section components from the optimised epoxy formulation RS3 is not recommended. However, since the cationic epoxy resins exhibit dark reaction curing, the polymerisation process continued and the component eventually cured with time (from 24 to 36 hours). The efficiency of the developed closed mould photocuring system was further tested by curing a polyester resin. The 1.5 mm thick component from polyester resin cured ~ 6 times faster (7 minutes) than the optimised epoxy formulation RS3.

For the photocuring processes (Chapter 2), resin systems based on cycloaliphatic epoxy consumed a lower energy (0.013 kWh) than the bisphenol A/F based resin system (0.067 kWh). In addition, a theoretical study was conducted for comparing the consumed energy between the photocuring process (flood lamp) and the conventional thermal curing process (based on a typical cure cycle) for curing parts made from epoxy formulations of similar sizes. Typical values for thermally cured resins, using 24 kW Barlow Whitney oven, were found to be 10.4 kWh (adhesive applications) and 23.4 kWh (thick sections applications). Comparing these values with the consumed energy values for curing of a single casting using the flood lamp, it was found that the flood lamp is ~ 800 times more efficient. But, as the oven (1 m^3) may be used to cure multiple parts during an individual cure cycle, an example was set to study the consumed energy for curing six large parts (70 cm wide, 70 cm long and 0.5 cm thick). This study suggested that the optimised formulations (mostly RS2 and RS3) using the flood lamp still consumed, around ~ 10 times less energy for the curing process. Finally, the cured components (1.5 mm thick) using the enhanced side emitting PMMA POF (single or multiple) and the Hg lamp consumed a total energy of 0.15 kWh (Chapter 5). The cured components using the enhanced side emitting PMMA POF consumed ~ 11 times more energy for the curing process when compared to the cured casting using the flood lamp. However, according to this estimated study, the cured components using the side emitting optical fibres still consumed much less energy (0.15 kWh) than that of the thermally cured process (10.4 kWh for adhesive applications and 23.4

kWh for thick section applications), at least for the geometric dimensions/sizes used during this work.

Thus, the enhanced stability and side emission treatments of the PMMA POF make it a suitable option for curing resins in closed mould applications. However, the efficiency of the developed closed mould photocuring system is highly dependent upon the reactivity as well as the optical properties of the resin system used to the required emission spectrum before and during the curing process.

Wider Applications

Optical fibres could weaken the cured part by effectively acting as a hole and producing a local stress concentration in the structure. However, this curing technique will be suitable for applications where low strength conditions are acceptable. The optical fibre may have a reduced influence on the strength of large components as the diameter of the fibre will be small in relation to the overall structure. In fact, optical fibres are already used for health monitoring applications of large composite parts, such as wind turbines and composite bridge piles [144-145]. For making larger parts, a formulation which is more reactive and more transparent than the optimised RS3 form should be used. The enhanced side emission efficiency of the PMMA POF showed efficient curing results for polyester resin which could be implemented in the Pera Innovation (UK) [141] project regarding the curing of thick components from polyester resin. Furthermore, in the case of low strength applications, this photocuring technique could be adopted for curing epoxy adhesive for bonding (1 mm < x < 2 mm), for sealing or also for making large components using multiple PMMA optical fibres. This technique could also be adopted for applications where heating could damage sensitive components of a part, such as electronic components and decorative work. Finally, the PMMA optical fibre may be used for health monitoring applications after the curing process.

6.2. Conclusions

The objective of this work was to develop a photocuring system for polymerising a photoinitiated cationic epoxy formulation in a closed mould setup where a conventional direct irradiation process is not possible (Chapter 1, Section 1.4). To accomplish this objective, a curing methodology for polymerising 1.5 mm and 5 mm thick components from an epoxy formulation was proposed using an embedded, side emitting optical fibre. The efficiency of the proposed curing process required an investigation into two main areas: optimisation of the epoxy formulations (Chapter 2) and the characterisation of commercially available side emitting optical fibres (Chapter 3). Optimisation of the epoxy formulations was carried out to improve the reactivity of the epoxy formulations for fast and deep curing results as the radiation emitted from the side surface of an optical fibre is relatively small compared to conventional radiation sources. Commercial optical fibres were characterised to establish which optical fibre efficiently transmitted the required radiation at which the photoinitiator within the epoxy formulation was activated and produces the reactive species for the polymerisation process. The resulting optical fibre for the photocuring application was further investigated to improve its stability during the photocuring process (Chapter 4), and its side emission was also enhanced (Chapter 5) for efficient curing results. As a result of this research, the following closed mould photocuring system was established: Hg lamp (40 W/cm^2), cooling device and an embedded side emitting PMMA POF (1000 μm diameter, treated with silica particles in combination with bend radii) in a closed mould setup containing the epoxy resin. Using this system allowed the curing of 1.5 mm thick component (20 mm wide and 245 mm long) after 45 minutes of continuous irradiation. However, the system was not successful in curing the 5 mm thick component (75 mm wide and 175 mm long) immediately after the radiation exposure (45 minutes). The full curing of the 5 mm thick component required a storing time up to 36 hours after being irradiated.

The novel observations identified in this thesis are as follows:

- Silica core fibres using ZnO particles as the scattering mechanism indicated poor side emission in the UVA band due to the high absorption of the ZnO particles (Section 3.4).

- PMMA POFs (polymer optical fibres) were determined to be superior to silica core fibre containing Al_2O_3 particles for side emission (Section 3.4).

- The stability of a PMMA POF from photo-degradation under continuous irradiation from the high emission Hg lamp (40 W/cm^2) can be controlled for longer exposure time by coupling the PMMA POF with a cooling device (Section 4.4).

- The untreated PMMA POF produced side emission due to discrete defects randomly distributed along the fibres when connected to the high emission Hg lamp (40 W/cm^2) (Section 5.4.1).

- The side emission efficiency of the PMMA POF can be improved by mechanical treatments (micro-cuts and silica particles) and by heat treatment (permanent geometric modification producing bend radii along the length) (Section 5.4.3).

- The characterisation process of different types of epoxy resin systems at a given thickness (two commercial pre-formulated epoxy resins, cycloaliphatic and bisphenol A/F epoxies with different sulfonium salts photoinitiators) indicated that the optimised resin system based upon cycloaliphatic epoxy (formulation RS3) were the most efficient formulation in terms of curing rate, hardness and optical transparency during the photocuring process (Sections 2.3 and 2.4).

- 1.5 mm and 5 mm thick components were made from the optimised epoxy formulation RS3. The 1.5 mm thick component was cured in 45 minutes (20 mm wide and 245 long). The 5 mm thick component (75 wide and 175 long) did not fully cure after 45 minutes. Full polymerisation of this casting was completed in 36 hours after irradiation due to dark reaction (Section 5.4.4).

- The efficiency of the closed mould photocuring system is highly dependent upon the resin reactivity as well as on the optical properties of the resin during the curing process (Section 5.4.4).

6.3. Recommendations for Further Work

6.3.1. Side Emitting PMMA POFs

The silica treatment of the PMMA POF could be improved by an alternative technique. Usually, the optical fibres are made by a drawing process. In this case, the silica particles would be mixed with PVDF cladding material. This way would secure the particles within the fibre and improve the handling as well. A further quantification study should be conducted to vary the silica particles density with length to compensate for the exponential decay of the transmitted light and allow more uniform side emission similar to what has been observed from the silica core fibres with either ZnO or Al_2O_3 (Chapter 3). The uniformity of side emission could also be improved using the smallest size range of silica particles as possible.

After the photocuring process, the fibre may also be used as a health monitoring system for optical sensing applications in which the developed strain within a component could be measured [98]. Generally, signals from the electromagnetic (EM) radiation (typically infrared) are used in a strain sensing technique [120, 146-147]. As infrared EM radiation is longer than the UV radiation (Figure 2-1), the silica scattering particles will cause much less attenuation to the transmitted signals for monitoring the change in stresses within a component. Optical fibre materials absorption in the infrared band should be studied prior implementing such methodology for sensing application. Finally, for making longer components using the side emitting PMMA optical fibre, two radiation sources could be used to improve the efficiency of curing, as shown in Figure 6-1.
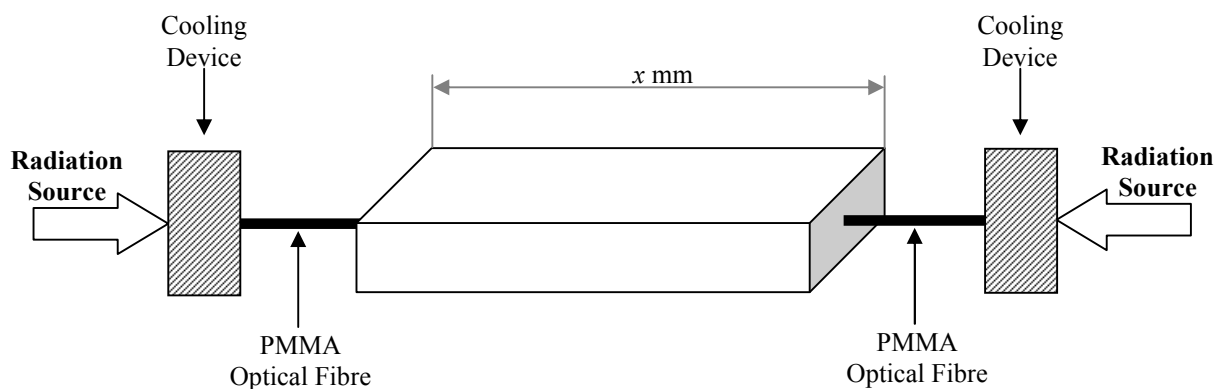
Figure 6-1. Schematic illustration showing a method for curing long (x mm) component by using two radiation sources.

6.3.2. Alternative Resins for Closed Mould Photocuring Application

Due to the long curing periods of the optimised epoxy formulation RS3 when used in the developed closed mould photocuring system, other resins are proposed. Crivello et al. [24, 148-150] suggests a novel class of silicon-containing epoxide monomers (Figure 6-2) and their synthesis as an alternative material to epoxy. The authors reported that these silicon-containing epoxide monomers demonstrate outstanding reactivity in photoinitiated cationic polymerisation, excellent mechanical properties and thermal oxidative resistance.
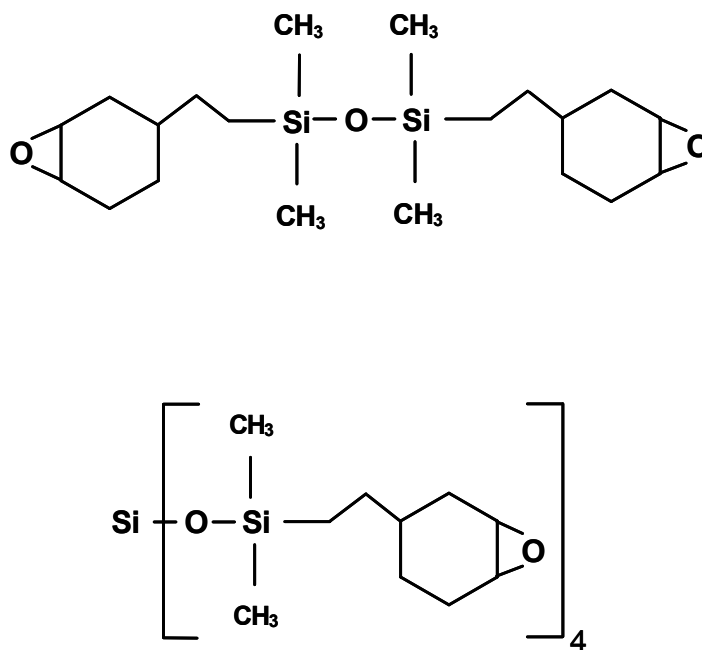
Figure 6-2. Novel class of silicon-containing epoxide monomers.

References:

1. Endruweit A, Johnson M.S, Long A.C. "Curing of Composite Components by Ultraviolet Radiation", Society of Plastics Engineers, 27, 2006, pp.119–128.

2. Narayanan V, Scranton A.B. "Photopolymerization of composites". Trends in Polymer Science, 5, 1997, pp. 415–419.

3. Sillyman S, Kenneth Li K, Inatsugu S. "Source numerical aperture control for efficient light emission from notched, side-lighting fiberoptics". Proceedings of SPIE, Nonimaging Optics and Efficient Illumination Systems. Denver, USA, August 2004, 5529, pp. 70–78.

4. Zarian J.R, Robbins J.A, Sitar D, Holme J.A. "Side lighting optical conduit". United States Patent 5987199, 1999.

5. Joseph E, Smith G. "Side scattering light guide". United States patent. pub. No. US 2006/0140562 A1, 2006.

6. Yokogawa H, Yokoyama M., Sonoda K, Kousaka K. "Side face illuminating optical fiber". United States Patent 6154595, 2000.

7. Spigulis J., Pfafrods D., Stafekis M., Jelinska-platace W. Glowing optical fibre designs and parameters". Proceedings of SPIE, Optical Inorganic Dielectric Material and Devices. Riga, Latvia, August 1996, 2967, pp. 231–236.

8. Zajkowski M. "Emission of flux light in 'side light' fiber optic". Proceedings of SPIE, Photonic Application in Astronomy, Communication, Industry, and High Energy Physics Experiments. 2002, 5125, pp.322–327.

9. Franklin J.B, Smith G.B, Joseph E.K. "Side scattering polymer light guide and method of manufacture". United States patent application publication, 7th Oct. 2004, pub. No. US 2004/0196648 A1.

10. Pfafrods D. "Side emitting optical fibre". Latvijas patents uz izgudrojumu, 20th Oct. 1997, pub. No LV 11644 B.

11. Decker C. "Photoinitiated Crosslinking Polymerization". Progress in Polymer Science, 21, 1996, pp. 593–650.

12. Crivello J.V. "Photoinitiated Cationic Polymerization". Annual Review of Material Science, 13, 1983, pp. 173–190.

13. Fouassier J.P, Ruhlmann D, Graff B, Wieder F. "New insights in photosensitizers-photoinitiators interaction". Progress in Organic Coating, 25, 1995, pp. 169–202.

14. Fawdington K, Tranter P. "Changing the state of a body of material". UK Patent GB2423279, 23 August 2006.

15. Bilanin AJ, Kaufman AE, McCullough R. "Lossy fiber UV curing method and apparatus". United States Patent 6835679, 28 December 2004.

16. Yahathugoda D, Evans N, Endruweit A, Long A.C. "Experimental investigation into UV curing of composites using integrated optical fibres". SAMPE Europe conference and exhibition, Paris, April 2007.

17. Decker C. "Special review: The Use of UV Irradiation in Polymerization". Polymer International, 45, 1998, pp. 133–141.

18. Stowe R.W. "Key factors in the UV curing process-The relationship of exposure conditions and measurement in UV process design and process control: Part I-Introduction". Fusion UV System Inc., Gaithersburg, Md., April 2002, pp. 62–71.

19. Ranby B, Rabek J.F, editor. "Photodegradation, photo-oxidation and photostabilization of polymer". A Wiley-Interscience publication; 1975.

20. Loctite Corporation, "Literature of radiation equipments", www.loctite.com, (21/06/2006).

21. Dow Chemical Company, "UV cure resins, epoxy data sheets", www.dow.com, (19/07/2006).

22. Dymax Corporation, "Radiation curing equipments, radiation spectrum data sheets and pre-formulated epoxy resins data sheets (4-20586 and 6-20353)", www.dymax.com, (19/07/2006).

23. Laserprodukte GmbH, "LED & LD's equipment for adhesive curing", www.lasersystem.de, (10/08/2006).

24. Crivello J.V. "The discovery and development of onium salt cationic photoinitiator". Journal of Polymer Science Part A: Polymer Chemistry, 37, 1999, pp. 4254–4254.

25. Andanur S, Arumugham Y. "Characteristics of ultraviolet cured glass-epoxy textile composites: Part 1: Experimental procedures and testing". Journal of industrial textiles, 32, 2002, pp. 93–118.

26. Martysz D, Antoszczyszyn M, Urbala M, Krompiec S, Fadrycy E. "Synthesis of 1-propenyl ethers and their using as modifiers of UV-cured coating in radical and cationic polymerization". Progress in Organic Coatings, 46, 2003, pp. 302–311.

27. Decker C, Viet T.N.T, Decker D, Weber-Korhl E. "UV-radiation curing of acrylate/epoxide systems". Polymer, 42, 2001, pp. 5531–5541.

28. Crivello J.V. "UV and electron beam-induced cationic polymerization". Nuclear Instruments and Methods in Physics Research B, 151, 1999, pp.8–21.

29. Cho J.D, Kim E.O, Kim H.K, Hong J.W. "An investigation of the surface properties and curing behaviour of photocurable cationic films photosensitized by anthracene". Polymer Testing, 21, 2002, pp. 781–791.

30. Corcione C.E, Greco A, Maffezzoli A. "Time-temperature and time-irradiation intensity superposition for photopolymerization of an epoxy based resin". Polymer, 46, 2005, pp. 8018–8027.

31. Bulut U, Crivello J.V. "Investigation of the reactivity of epoxide Monomers in photoinitiated cationic polymerization". Macromolecules, 38, 2005, pp. 3584–3595.

32. Sipani V, Scranton A.B. "Dark-cure studies of cationic photopolymerization of epoxides: Characterization of the active center lifetime and kinetic rate constants". Journal of Polymer Science: Part A: Polymer Chemistry, 41, 2003, pp. 2064–2072.

33. Hartwig A, Schneider B, Luhring A. "Influence of moisture on the photochemically induced polymerization of epoxy groups in different chemical environment". Polymer, 43, 2002, pp. 4243–4250.

34. Decker C, Viet T.N.T, Thi H.P. "Photoinitiated cationic polymerization of epoxides". Polymer International, 50, 2001, pp. 986–997.

35. Mascioni M, Sands J.M, Palmese G.R. "Real time situ spectroscopic characterization of radiation induced cationic polymerization of glycidyl ethers". Nuclear Instruments and Methods in Physics Research B, 208, 2003, pp. 353–357.

36. Boey F, Rath S.K, Ng A.K, Abadie M.J.M. "Cationic UV cure kinetics for multifunctional epoxies". Journal of Applied Polymer Science, 86, 2002, pp. 518–525.

37. Crivello J.V, Jang M. "Anthracene electron-transfer photosensitizers for onium salt induced cationic polymerizations". Journal of Photochemistry and Photobiology A: Chemistry, 159, 2003, pp. 173–188.

38. Sangermano M, Malucelli G, Priola A, Lengvinaite S, Simokaitiene J, Grazulevicius J.V. "Carbazole derivatives as photosensitizers in cationic photopolymerization of clear and pigmented coating". European Polymer Journal, 41, 2005, pp. 475–480.

39. Sun G.J, Chae K.H. "Properties of 2,3-butanedione and 1-phenyl-1,2-propanedione as new photosensitizers for visible light cure dental resin composites". Polymer, 41, 1999, pp. 6205–6212.

40. Fouassier J.P, Allonas X, Burget D. "Photopolymerization reaction under visible lights: principle, mechanisms and example of applications". Progress in Organic Coating, 47, 2003, pp. 16–36.

41. Smith G.H. "Photopolymerizable composition containing a sensitized aromatic sulfonium compound and a cationacally polymerizable monomer". United States patent application publication, 17th Jan., 1978, Pat. No. 4,069,054.

42. Smith G.H. "Sensitized aromatic iodonium or aromatic sulfonium salt photoinitiator systems". United States patent application publication, 10th Feb., 1981, Pat. No. 4,250,053.

43. Crivello J.V. "Epoxy-functional polymeric microbeads". United States patent application publication, 5th Aug., 2003, Pat. No. 6,602,602 B1.

44. Ram A. "Polymer Engineering", 1997, 1st edition, 233 Spring Street, New York USA, ISBN 0 306 45726 1.

45. ASM. "Engineered materials handbook", Composites, 1993, 4th Edition, Volume 1.

46. Brydson J.A. "Plastic Materials", 1999, 7th edition, Butterworth-Heinemann, Oxford UK, ISBN 0 7506 4132 0.

47. Minford D.J. "Handbook of Aluminum Bonding Technology and Data", 1993, 1st edition, CRC Press LLC, ISBN: 0824788176.

48. Mortimer J. "Adhesive bonding of car body parts". Industrial Robot: An International Journal, 31, 2004, pp. 423–428.

49. Rudd C.D, Long A.C, Kendall K.N, Mangin C.G.E. "Liquid moulding technologies", 1997, first edition, Woodhead publishing limited, Cambridge CB1 6AH, ISBN 1 85573 242 4.

50. Nowers J.R. Narasimhan B. "The effect of interpenetrating polymer network formation on polymerization kinetics in an epoxy-acrylate system". Polymer, 47, 2006, pp. 1108–1118.

51. Varma I.K. Gupta V.B. "Thermosetting resin-properties, Comprehensive composite materials", 2000, Vol.2, ISNB: 0 080437206, pp. 1-56.

52. Chiang T.H, Hsieh T.E. "A study of monomer's effect on adhesion strength of UV-curable resins". International Journal of Adhesion & Adhesives, 26, 2006, pp. 520–531.

53. Nakano S, Endo T. "Thermal cationic curing with benzylammonium salts-2". Progress in Organic Coations, 28, 1996, pp. 143–148.

54. Crivello J.V, Ortiz R.A. "Design and synthesis of highly reactive photopolymerizable epoxy monomers". Journal of Polymer Science: Part A: Polymer Chemistry, 39, 2001, pp. 2385–2395.

55. Yagci Y, Schnabel W. "On the mechanism of photoinitiated cationic polymerization in the presence of polyols". Die Angewandte Makromolekulare Chemie, 270, 1999, pp. 38–41.

56. Crivello J.V, Rajaraman S, Mowers W.A, Liu S. "Free radical accelerated cationic polymerization". Macromolecular Symposia, 157, 2000, pp.109–119.

57. Sangermano M, Malucelli G, Bongiovanni R, Priola A. "Photopolymerization of oxetane based systems". European Polymer Journal, 40, 2004, pp. 353–358.

58. Wang T, Wang Z.H. "Cationic photopolymerization of epoxy systems initiated by cyclopentadien-iron-biphenyl hexafluorophosphate". Polymer Bulletin, 53, 2005, pp. 323–331.

59. Olsson R.T, Bair H.E, Kuck V, Hale A. "Acceleration of the cationic polymerization of an epoxy with hexanediol". Journal of Thermal Analysis and Calorimetry, 76, 2004, pp. 367–377.

60. Spectra group limited, "Supplier of the visible light photoinitiator", www.sglinc.com, (28/7/2006).

61. Crivello J.V, Sangermano M. "Visible and long wavelength photoinitiated cationic polymerization". Journal of polymer science part A: polymer chemistry, 39, 2001, pp. 343–356.

62. Corcione C.E, Greco A, Maffezzoli A. "Photopolymerization kinetics of an epoxy based resin for stereolithography". Journal of Thermal Analysis and Calorimetry, 72, 2003, pp. 687–693.

63. Fernandez-Francos X, Salla J.M, Cadenato A, Morancho J.M, Manteco A, Serra A, Ramis X. "Influence of the initiating mechanism on the cationic photopolymerization of a cycloaliphatic epoxy resin with arylsulfonium salts". Journal of Polymer Science: Part A: Polymer Chemistry, 45, 2007, pp. 16–25.

64. Saniz M.A, Duran A, Fernandez Navarro J.M. "UV highly absorbent coatings with CeO_2 and TiO_2". Journal of Non-Crystalline Solids, 121, 1990, pp. 315–318.

65. Mima T, Masako S. "Relation between blocking property against UV-rays by dyed fabric and its color fastness to light". Proceedings of SPIE - The International Society for Optical Engineering, 4421, 2001, pp. 736–739.

66. Asilturk M, Sayılkan F, Sayılkan H, Icduygu G. "The synthesis and application of Pb-doped GLYMO/Chelated-Zirconium complex coating materials for UV light absorption". Journal of Applied Polymer Science, 99, 2006, pp.1175–1179.

67. DaviesColley R. J, Vant W. N. "Absorption of light by yellow substance in freshwater lakes". American Society of Limnology and Oceanography, 32, 1987, pp. 416–425.

68. Desilles N, Gautrelet C, Lecamp L, Lebaudy P, Bunel C. "Effect of UV light scattering during photopolymerization on UV spectroscopy measurements". European Polymer Journal, 41, 2005, pp.1296–1303.

69. Teramoto N, Shibata M. "Synthesis and photocuring of cinnamoyl trehalose esters". Polymer for Advanced Technologies, 18, 2007, pp. 971–977.

70. Arun A, Reddy B. "Photocurable and thermally stable polymers based on 1,4-Pentadien-3-one-1-*p*-hydroxyphenyl-5-*p*-phenyl methacrylate: copolymerization with ethyl acrylate". Journal of Polymer Science: Part A: Polymer Chemistry, 41, 2003, pp.1632–1640.

71. Crivello J.V, Lam J.H.W. "Photoinitiated cationic polymerization with triarylsulfonium salts". Journal of Polymer Science: Polymer Chemistry Edition, 17, 1979, pp. 977–999.

72. Crivello J.V, Kong S, Jang M. "Cationic polymerization: New development and applications". Macromolecular Symposia, 217, 2004, pp. 47–61.

73. Liu Y. "Sulfonium salt photoinitiators and use thereof". United States patent application publication, 5th May, 2005, Pat. No. US 2005/0095531 A1.

74. Decker C, Bendaikh T. "Interpenetrating polymer networks. II. Sunlight-induced polymerization of multifunctional acrylates". Journal of Polymer Science, 70, 1998, pp.2269–2282.

75. Univar Europe Company, "Supplier of the cycloaliphatic epoxy (UVR-6105)", www.univareurope.com, (08/11/2006).

76. DKSH Market Intelligence Ltd., UK, "Supplier of the oxetane additive", www.dksh.com, (13/09/2008).

77. Sigma-Aldrich Company Ltd., "Supplier of the Anthracene photosensitizer", www.sigmaaldrich.com, (03/09/2007).

78. Polyester Converters (PSG) Group Ltd., "Supplier of the Melinex polyester films" www.psggroup.info/, (28/10/2006).

79. Barber-Colman Company "Supplier of the Barcol Hardness tester for soft materials", www.barber-colman.com, (15/7/2007).

80. Brookfield Engineering Laboratories Inc., "Supplier of the Digital viscometer", www.brookfieldengineering.com. (28/10/2006).

81. Mould release agent PMR-90 supplied by Zyvax Inc. www.zyvax1.com, (05/1/2006).

82. Dwight G. "Physical testing of coating in the field and laboratory". Journal of Protective Coating & Linings, 3, 1986, pp. 30–35.

83. BS-2782-10: Method 1001: 1977 EN 59, Measurement of hardness by means of a Barcol impressor. British standard.

84. Scherzer T, Decker U. "The effect of temperature on the kinetics of diacrylate photopolymerizations studied by Real-time FTIR spectroscopy". Polymer, 41, 2000, pp. 7681–7690.

85. Liang H, Asif A, Shi W. "Photopolymerization and thermal behavior of phosphate diacrylate and triacrylate used as reactive-type flame-retardant monomers in ultraviolet-curable resins". Journal of Applied Polymer Science, 97, 2005, pp. 185–194.

86. Chen Y, Ferracane J.L, Prahl S.A. "A pilot study of a simple photon migration model for predicting depth of cure in dental composite". Dental Materials, 21, 2005, pp. 1075–1086.

87. Gurit Ltd, UK, "Thermally curable ST 70 epoxy resin for thick component applications", www.grurit.com, (28/07/2009).

88. Cassano, A.E., Martin, C.A., Brandi, R.J., Alfano, O.M. "Photoreactor analysis and design: Fundamentals and applications". Industrial & Engineering Chemistry Research, 34, 1995, pp. 21-55.

89. Ocean Optics, Inc., "Supplier of the USB4000 spectrometer", www.oceanoptics.com, (09/06/2007).

90. Weinert A, editor. "Plastic optical fibers: principles, components, installations". Erlangen: Publicis MCD Verlag; 1999.

91. Baumer S, editor. "Handbook of plastic optics". Eindhoven: Wiley-VCH; 2005.

92. Crisp J. "Introduction to fiber optics", 2001, 2ed edition, Butterworth-Heinemann, Oxford OX2 8DP, ISBN: 07506 50303.

93. Hecht J. "Understanding fiber optics", 2006, 5th edition, R.R. Donnelley & Sons, ISNB: 0 13 117429 0.

94. Endruweit A, Alobaidani A, Furniss D, Seddon A, Benson T, Johnson M, Long A. "Spectroscopic experiments regarding the efficiency of side emission optical fibres in the UV-A and visible blue spectrum". Optics and Lasers in Engineering, 46, 2008, pp. 97–105.

95. Spigulis J, Pfafrods D. "Clinical potential of the side-glowing optical fibers". Proceedings of SPIE, Speciality Fiber Optics for Biomedical and Industrial Applications. San Jose, CA, USA, February 1997, 2977, pp. 84–98.

96. Hu Y, Xu JJ, Yuan CW, Lin J, Yin ZD. "A single TiO2-coated sideglowing optical fiber for photocatalytic wastewater treatment". Chin Sci Bull 2005; 50: pp. 1979–1984.

97. Alobaidani A.D, Furniss D, Endruweit A, Johnson M.S, Benson T, Seddon A.B. "Enhancement of the side emission efficiency of commercial PMMA optical fibres in the UV-A and visible blue spectrum for photocuring of epoxy resins". 13th European Conference on Composite Materials (ECCM13). June 2-5, 2008 Stockholm, Sweden.

98. Zubia J, Arrue J. "Plastic Optical Fibers: An Introduction to their technological processes and applications". Optical Fiber Technology, 7, 2001, pp. 101–140.

99. Comyns A.E. "Fluoride glasses", 1989, vol. 27, The society of chemical industry, ISBN: 0 471 92352 4.

100. Takezawa Y, Taketani N, Tanno S, Ohara S. "Empirial estimation method of intrinsic loss spectra in transparent amorphous polymers for plastic optical fibres". Journal of Applied Polymer Science, 46, 1992, pp. 1835–1841.

101. Appajaiah A, Kretzschmar H.J, Daum W. "Aging behavior of polymer optical fibers: Degradation Characterization by FTIR". Journal of Applied Polymer Science, 103, 2007, pp. 860–870.

102. LightTech Inc., "Supplier of the silica core optical fibres", www.lighttech.com, (09/5/2007).

103. Fiber Tech GmbH, "Supplier of the silica core optical fibre", www.fibertech.de, (18/5/2007).

104. Mitsubishi Rayon of Japan "Supplier of the PMMA optical fibres", www.i-fiberoptics.com, (20/7/2007).

105. Barboriak D.P, Padua A.O, York G.E, MacFall J.R. "Creation of DICOM - Aware applications using ImageJ". Journal of Digital Imaging, 18, 2005, pp. 91–99.

106. DeGroot JV, Norris AW, Glover SO, Clapp T. "Highly transparent silicone materials". Proceedings of the SPIE, Linear and Nonlinear Optics of Organic Materials IV. Denver, CO, USA, August 2004, 5517, pp. 116–123.

107. TexLoc Refractive Index of Polymers. Parker-TexLoc, [19/6/2007].

108. Masson F, Decker C ,Andre S , Andrieu X. "UV-curable formulations for UV-transparent optical fiber coatings I. Acrylic resins". Progress in Organic Coatings, 49, 2004, pp. 1–12.

109. Zidan H, Abu-Elnader M. "Structural and optical properties of pure PMMA and metal chloride-doped PMMA films". Physica B, 355, 2005, p 308–317.

110. Hu H, Nair P.K. "Electrical and optical properties of poly(methyl methacrylate) sheets coated with chemically deposited CuS thin films". Surface and Coatings Technology, 81, 1996, pp. 183–189.

111. Yu J.M, Tao X.M, Tam H.Y, Demokan M.S. "Modulation of refractive index and thickness of poly(methyl methacrylate) thin films with UV irradiation and heat treatment". Applied Surface Science, 252, 2005, pp. 1283–1292.

112. Hu X. "Wavelength sensitivity of photo-oxidation of polyamide 6". Polymer Degradation and Stability, 62, 1998, pp. 599–601.

113. Zhenguo J, Kun L, Chengxing Y, Ruixin F, Zhizhen Y. "Structural, optical and electrical properties of ZnO thin films prepared by reactive deposition". Journal of Crystal Growth, 253, 2003, pp. 246–251.

114. Srinivasan G, Kumar J. "Optical and structural characterisation of zinc oxide thin films prepared by sol-gel process". Crystal Research and Technology, 41, 2006, pp. 893 – 896.

115. Hong R, Huang J, He H, Fan Z, Shao J. "Influence of different post-treatments on the structure and optical properties of zinc oxide thin films". Applied Surface Science, 242, 2005, pp. 346–352.

116. Kamalasanan M.N, Chandra S. "Sol-gel synthesis of ZnO thin films". Thin Solid Films, 288, 1996, pp. 112–115.

117. DengPan N, Tao X, Yu Z, XiangJun L. "Synthesis and structure analysis of aluminum doped zinc oxide powders". Science in China Series B: Chemistry, 51, 2008, pp. 823–828.

118. Gluhoi A.C, Bogdanchikova N, Nieuwenhuys B.E. "The effect of different types of additives on the catalytic activity of Au/Al2O3 in propene total oxidation: transition metal oxides and ceria". Journal of Catalysis, 229, 2005, pp. 154–162.

119. Demiryont H, Thompson L.R, Collins G.J. "Optical properties of aluminum oxynitrides deposited by laser-assisted CVD". Applied Optics, 25, 1986, pp. 1311–1318.

120. Bartlett R, Chandy R, Eldridge P, Merchant D, Morgan R, Scully P. "Plastic optical fiber sensors and devices". Transactions of the Institute of Measurement and Control, 22, 2000, pp. 431–457.

121. Wochnowski C, Shams Eldin M.A, Metev S. "UV-laser-assisted degradation of poly(methyl methacrylate)". Polymer Degradation and Stability, 89, 2005, pp. 252–264.

122. Meseguer F. "Piezobirefringence of PMMA: Optical and mechanical relaxations and influence of temperature". Journal of Material Science, 15, 1980, pp. 53–60.

123. Takezawa Y, Tanno S, Taketani N, Ohara S, Asano Hideki. "Analysis of thermal degradation for plastic optical fibers". Journal of Applied Polymer Science, 42, 1991, pp. 2811–2817.

124. Kashiwagi T, Inaba A, Brown J.E. "Effects of Weak Linkages on the Thermal and Oxidative Degradation of Poly(methyl methacrylates)". American Chemical Society, Macromolecules, 19, 1986, pp. 2160–2168.

125. Taguenang J, Kassu A, Ruffin P, Brantley C, Edwards E, Sharma A. "Reversible UV degradation of PMMA plastic optical fibre". Optics Communications, 281, 2008, pp. 2089–2092.

126. Pakhomov P.M, Maryukov M.A, Levin V.M, Chegolya A.S. "Influence of UV radiation on the light transmission of polymer optical fiber". Journal of Applied Spectroscopy, 59, 1993, pp. 528–532.

127. Yao X, Liu D, Yeh H. "Mechanical properties and gradient variations of polymers under ultraviolet radiation". Journal of Applied Polymer Science, 106, 2007, pp. 3253–3258.

128. Harmon J, Noren G, editors. "Optical polymers: fibres and waveguides". ACS symposium series, 795, pp. 2001.

129. Dickens B, Martin W, Waksman D. "Thermal and photolytic degradation of plates of poly(methyl methacrylate) containing monomer". Polymer, 25, 1984, pp.706–715.

130. LasIRvis Optoelectronic Components Ltd, UK, "Supplier of PMMA optical fibres", www.lasirvis.co.uk, (30/08/2007).

131. Torikai A, Ohno M, Fueki K. "Photodegradation of poly(methyl Methacrylate) by monochromatic light: Quantum yield, effect of wavelengths, and light intensity". Journal of Applied Polymer Science, 41, 1990, pp. 1023–1032.

132. Torikai A, Hasegawa H. "Wavelength effect on the accelerated photodegradation of polymethylmethacrylate". Polymer Degradation and Stability, 61, 1998, pp. 361–364.

133. Appajaiah A, Wachtendorf V, Daum W. "Characterization of thermo-oxidative stability of polymer optical fibers using chemiluminescence technique". Polymer Degradation and Stability, 91, 2006, pp. 2605–2613.

134. Sutcliffe E, Srinivasan R. "Dynamics of UV laser ablation of organic polymer surfaces". Journal of Applied Physics, 60, 1986, pp. 3315–3322.

135. Yu J, Tao X, Tam H. "Fabrication of UV sensitive single-mode polymeric optical fiber". Optical Materials, 28, 2006, pp. 181–188.

136. Bormashenko E, Pogreb R, Streltsov V, Socol Y, Itzhaq M, Sutovski S, Sheshnev A, Bormashenko Y. "Polyvinylidene fluoride-piezoelectric polymer for integrated infrared optics application". Optical Materials, 27, 2004, pp. 429–434.

137. Al-Azzawi A, editor. "Fibre optics: principles and practices". Boca Raton: Taylor & Francis Group LLC; 2007.

138. Durana G., Zubia J., Arrue J., Aldabaldetreku G., Javier M. "Dependence of bending losses on cladding thickness in plastic optical fibers". Applied Optics, 42, 2003, pp. 997–1002.

139. Badar A.H., Maclean T.S.M. "Transition and pure bending losses in multimode and single-mode bent optical fibre". IEE Proceedings, 138, 1991, pp. 216–268.

140. Boechat A.P. A., Su D., Hall D.R., Jones J.D.C. "Bend loss in large core multimode optical fiber beam delivery system". Applied Optics, 30, 1991, pp. 321–327.

141. Pera Innovation (UK), "Supplier of the ready formulated polyester resin", www.pera.com, (31/03/09).

142. Yonemura M., Kawasaki A., Kato S., Kagami M. "Polymer waveguide module for visible wavelength division multiplexing plastic optical fiber communication". Optics Letters, 30, 2005, pp. 2206–2208.

143. Zou X., Itoh K., Toratani H. "Transmission loss characteristics of fluorophosphate optical fibers in the ultraviolet to visible wavelength region". Journal of Non-Crystalline Solids, 215, 1997, pp. 11–20.

144. Schroeder K., Ecke W., Apitz J., Lembke E., Lenschow G. "A fibre Bragg grating sensor system monitors operational load in a wind turbine rotor blade". Measurement Science and Technology, 2006, 17, pp. 1167–1172.

145. Poloso T. "Fibre Bragg grating optical sensing technology". Smart Materials Bulletin, 2001. Smart Materials Technology Development Group, Systems Planning and Analysis, Inc.

146. Dobb H., Carroll K., Webb D.J., Kalli K., Komodromos M., Themistos C., Peng, G.D., Argyros A., Large M.C.J.,Eijkelenborg Van M.A., Arresy M., Kukureka, S. "Reliability of fibre Bragg gratings in polymer optical fibre". Proceedings of SPIE - The International Society for Optical Engineering, 2006, 6193 Reliability of Optical Fiber Components, Devices, Systems, and Networks III Strasbourg, France.

147. Lee B. "Review of the present status of optical fiber sensors". Optical Fiber Technology, 2003, 9, pp. 57–79.

148. Crivello J.V., Lee J.L. "The synthesis, characterization, and photoinitiated cationic polymerization of silicon-containing epoxy resins". Journal of Polymer Science Part A, 28, 1990, pp. 479–503.

149. Crivello J.V., Daoshen B.I. "The synthesis and photoinitiated cationic polymerization of multifunctional silicon-containing epoxy monomers and oligomers". Journal of Polymer Science Part A, 32, 1994, pp. 683–697.

150. Crivello J.V., Lee J.L. "The UV cure of epoxy-silicone monomers". Polymeric Material Science and Engineering, Proceeding of the ACS Division, 60, 1989, pp. 217–221.

151. ASM International. "Composites", Engineering materials handbook, Vol. 1, 1995, ISNB: 0 87170 279 7.

152. Takahashi E, Sanda F, Endo T. "Novel pyridinium salt as cationic thermal and photoinitiators and their photosensitization properties". Journal of Polymer Science: Part A: Polymer Chemistry, 40, 2002, pp. 1037–1046.

Appendix A-1:   Published Work

Endruweit A, Alobaidani A.D, Furniss D, Seddon A.B, Benson T, Johnson M.S, Long A.C. "Spectroscopic experiments regarding the efficiency of side emission optical fibres in the UV-A and visible blue spectrum". Optics and Lasers in Engineering, 46, 2008, pp. 97–105.

Alobaidani A.D, Furniss D, Endruweit A, Johnson M.S, Benson T, Seddon A.B. "Enhancement of the side emission efficiency of commercial PMMA optical fibres in the UV-A and visible blue spectrum for photocuring of epoxy resins". 13th European Conference on Composite Materials (ECCM13). June 2-5, 2008 Stockholm, Sweden.

Alobaidani A.D, Furniss D, Johnson M.S. "Optimisation and spectroscopic experiments of cationic epoxy formulations for the application of photocuring of deep resin mediums using side emitting optical fibres". 17th International Conference on Composite Materials (ICCM17). July 27-31, 2009 Edinburgh, UK.

Alobaidani A.D, Furniss D, Johnson M.S, Endruweit A, Seddon A.B. "The effect of polymer degradation on the transmission of PMMA optical fibres exposed to high intensity UV-A and visible blue light". To be submitted to the Journal of Optics and Lasers in Engineering.

Appendix B-1:   Background of Photoinitiated Polymerisation of Resins

B1. Designing a Light Curing System:

Designing a conventional radiation curing application requires consideration of four major factors that lead to successful curing results of a three-dimensional object [17-18, 24]:

- Spectral output of the lamp

- Flux density of the lamp (W/cm^2)

- Resin system properties:

  - Optical properties before and during curing, such as clarity and optical density

  - Monomer reactivity and photosensitivity

- Cure characteristics needed, such as depth of cure, surface cure, speed, overall shrinkage

The main feature for efficient curing rates is the match between the spectral output of the lamp and the absorption spectra of the photoinitiator used in the resin. Mismatching of these two factors will result in a long curing period or the resin system may not cure at all. An effective way of matching these parameters is by getting all applicable photoinitiators that are compatible with the required resin system and obtaining a lamp with spectral output near the absorption spectrum of the photoinitiator. For example, Cyracure sulfonium salts cationic photoinitiators can be activated with standard mercury filled UV bulbs because they can absorb some of the major emission bands at peaks 260 nm, 300 nm and 312 nm, as shown from their overlap in Figure B-1. However, more efficient activation of the photoinitiator can be achieved by using a xenon chloride lamp as shown by a concentration of the emission peak near 300 nm in Figure B-2, which consequently improves the curing

performance [21]. Further improvement in radiation curing can be accomplished by higher flux density as well as by using a photosensitizer that shifts photoinitiators absorption spectrum to the required emission wavelength as discussed in Chapter 2 section 2.2.5.
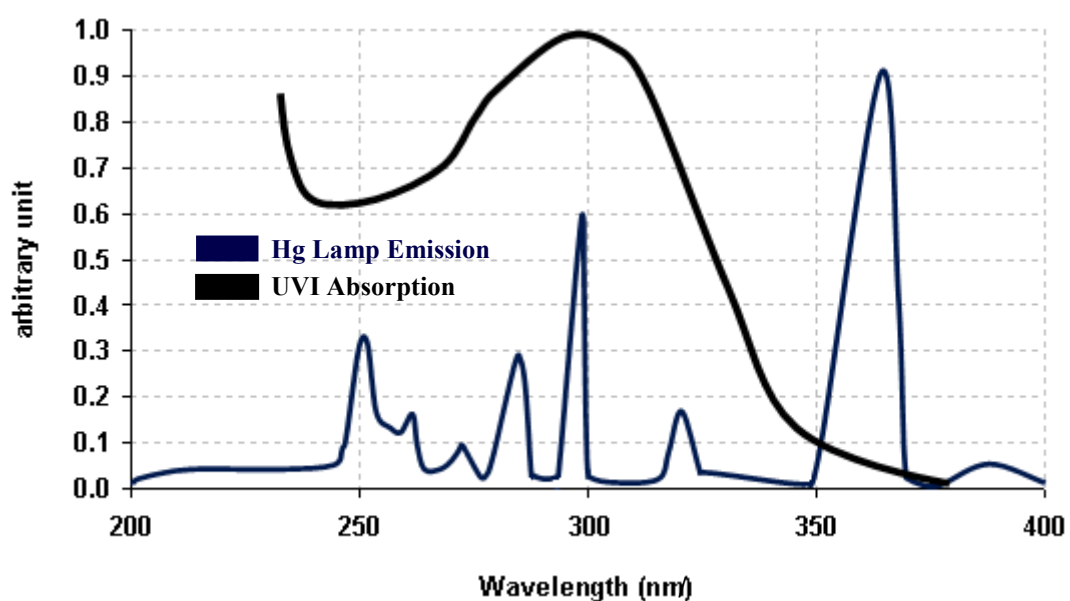
Figure B-1. Cyracure sulfonium salts cationic photoinitiators absorption spectrum and standard mercury UV bulb Emission [21].
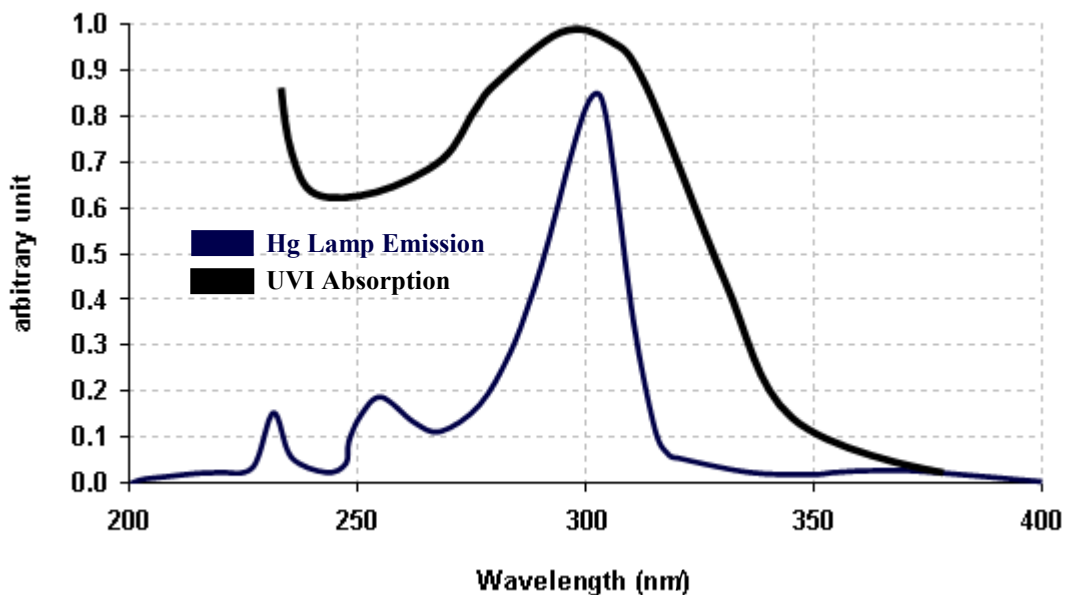
Figure B-2. Cyracure sulfonium salts cationic photoinitiators absorption spectrum and xenon chloride UV bulb emission spectrum [21].

Efficient thick resin curing (greater than 1 mm) requires a photoinitiator that is activated by a long wavelength (greater than 350 nm) and for a large cure depth [21], visible radiation cure systems are recommended. Hence new types photoinitiators have been developed. For example, Spectra Group Ltd [60] developed a number of photoinitiators for different resin systems that absorb long wavelengths ranging from UVA to the visible yellow band, as shown in Figure B-3.
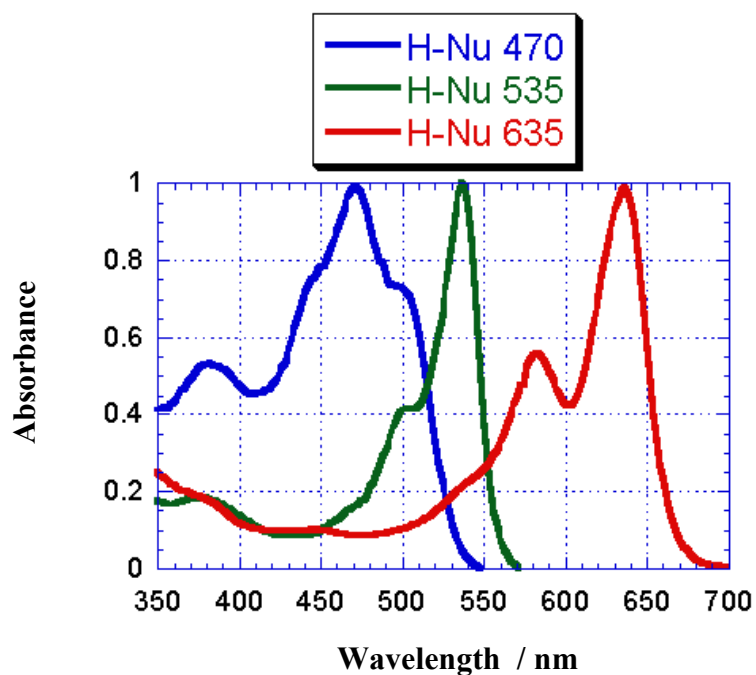
Figure B-3. New visible light photoinitiator [60], the absorbance in OD.

B2. Photoinitiated Free Radical Polymerisation:

Acrylate monomers are the most widely used due to their high reactivity that results in short curing time; e.g., fractions of seconds for thin coatings. The radical mechanism is involved in polymerising three main types of UV-curable resins [11]: unsaturated polyester/styrene, thiol-polyene and acrylate monomers. Initiation, propagation and termination of free radical polymerisation are summarised in the following steps and Figure B-4 [1]:

Curing Mechanism

Step 1: Initiation:

- Decomposition of a photoinitiator to produce free radicals with unpaired electrons

- Radicals bond to monomer molecules

Step 2: Propagation:

- Addition of monomers

- Addition of free radicals to the double bond of a monomer

- Polymer chain grows continuously by an active centre relocated at the end of the growing chain

Step 3: Termination:

- The chain is terminated by deactivating the radicals

- Polymer chain radicals deactivated with another radical

Step 1: Initiation
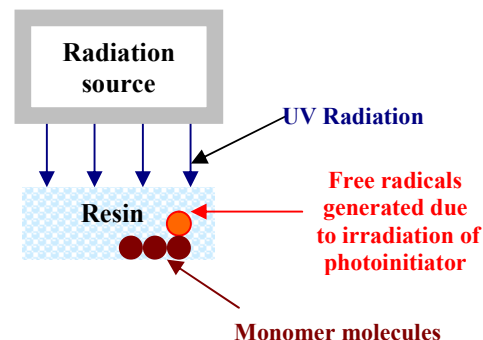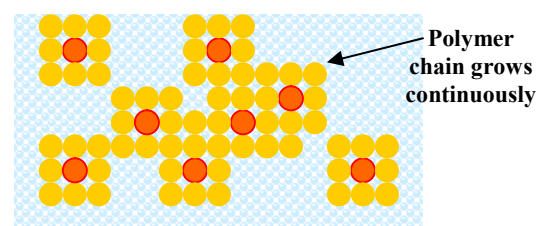
Step 2: Propagation

**Figure B-4.** Schematic of Initiation and propagation steps during photoinitiated free radical polymerisation

Oxygen inhibits photoinitiated radical polymerisation because the free radicals react with oxygen and cause the polymerisation to either slow or stop. To overcome this problem additives are mixed with the resin formulation or also the photocuring process can be carried out in a vacuum or an inert atmosphere [11, 25].

B3. Photoinitiated Cationic Polymerisation

Curing Mechanism

Photoinitiated cationic polymerisation undergoes initiation, propagation, chain transfer, and eventual termination processes. These processes are summarised in the following steps and Figure B-5 [1, 12, 17]:

Step 1: Initiation:

The curing process starts when a resin system is exposed to an irradiant source. The irradiant exposure causes the photoinitiator to ionize by photon absorption. The ionization process generates active centres with fragments R^+ and R^-. Only the positive fragment/charge (R^+) reacts with monomers. The irradiated protonic acids on photolysis of the photoinitiator causes direct protonation of the monomer to form a carbon-, oxygen-, sulfur-, or nitrogen-centred cationic species resulting in the generation of polymer chain.

Step 2: Propagation:

Further polymerisation chain growth takes place be the addition of monomers to the growing cationic chain end.

Step 3: Termination:

The polymerisation chain can be terminated by:

- Uni-molecular rearrangement of both negative ($R^{'-}$) and positive (R^+) charges on the chain

- chain transfer

- Terminating impurities

Step 1: Initiation
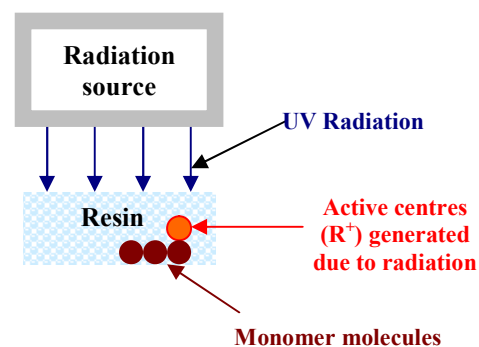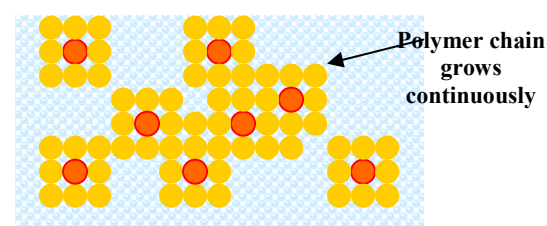
Step 2: Propagation

Figure B-5. Schematic of Initiation and propagation steps during photoinitiated cationic polymerisation

Photocuring Reaction

During the photocuring reaction of epoxy formulations using photoinitiators [11-12, 28, 31-52], such as diaryliodonium or triarylsulfonium salts, both homolytic and heterolytic cleavage mechanisms are involved in the photolysis of the photoinitiator. The photoinitiator results in the generation of a number of reactive species, such as aryl radicals, aryl cationic radicals, aryl cations, and super acid $HSbF_6$.

The initiation of photoinitated cationic polymerisation reaction process is described in the scheme below [52]. Similar reaction was also reported by Bulut et al. [31] and Hartwig et al [33]. In equation B1, the irradiant exposure causes the photoinitiator to produce $HSbF_6$ acid. The $HSbF_6$ is a strong Brønsted acid protonation which causes the epoxide monomers to produce oxiranium ion (right side of equation B1). Hence, the cationic polymerisation of epoxy formulation occurs by the attack of protonated epoxide monomers on other epoxide monomers, as presented in equation B2.

Scheme 1

Equation B-1

Equation B-2

(second part of Equation B2)
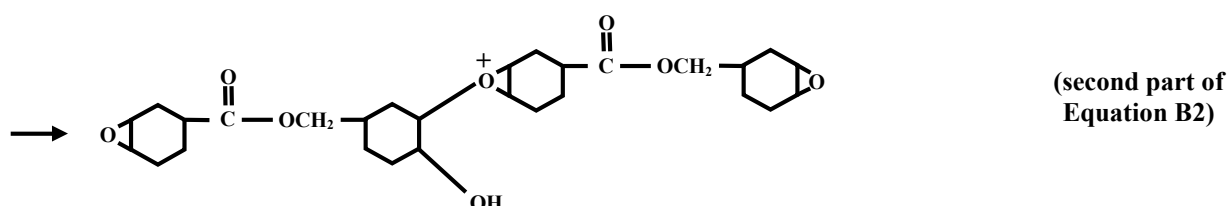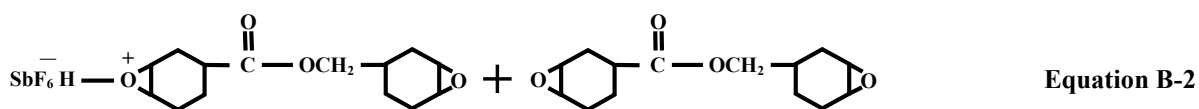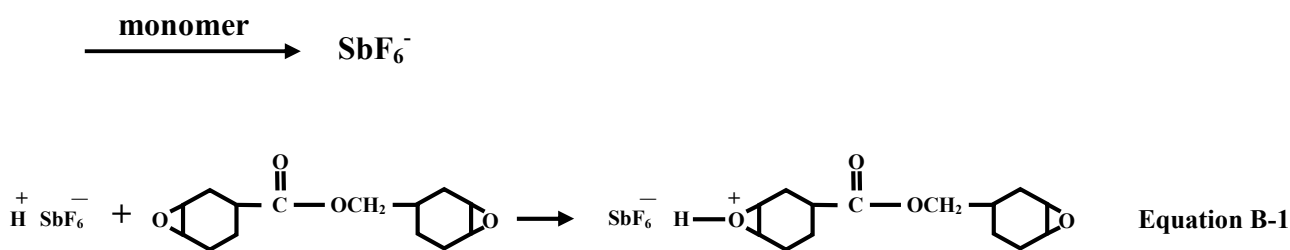
Effects of humidity

Proton donor contaminants such as organic amines, basic pigments or water tend to deactivate the cationic catalyst by neutralizing the protons generated from photolysis of the photoinitiator resulting in a poor curing response [12, 21, 33]. An extensive exposure of a cationic formulation (monomer and photoinitiator) to humid air leads to a deactivation of the initiator by hydrolysis of the organic cation as well as the anion of the supper acid. The presence of water or alcohol molecules within the reaction leads to chain transfer reactions, and hence, reduces or terminates the reactions resulting in poor polymerisation. An example of the effect of water or alcohol molecules on the chemical reaction of the polymerisation process is shown below (scheme 2) [33]:

Scheme 2
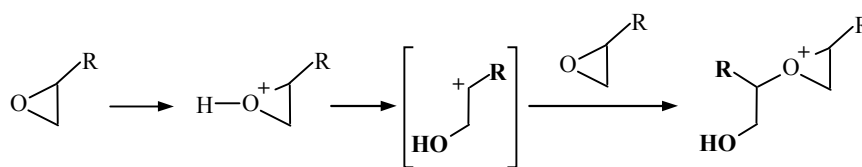
a)   **Initiation and reaction with the next monomer.**
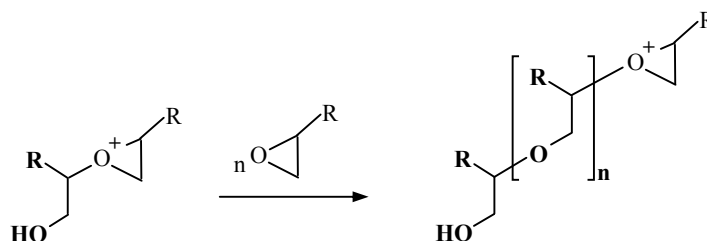
b)   **Chain growth as a result of n monomers.**
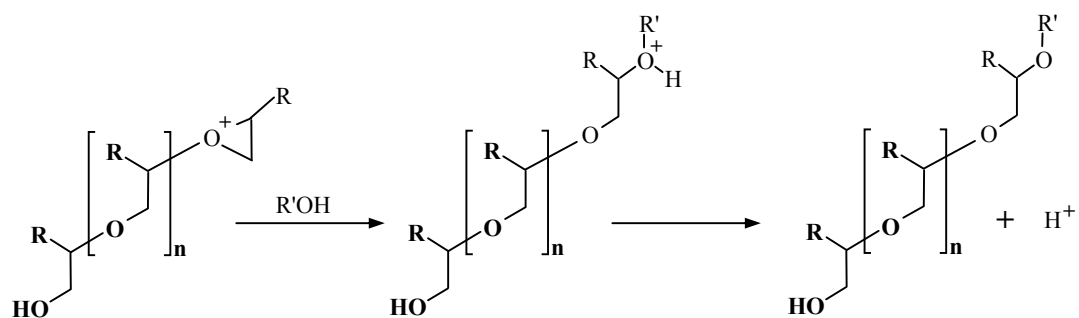
c) **Chain transfer by an alcohol or water (R' =H). Hence, the photochemical reactions are reduced or terminated and so is the polymerization process.**

B4. Types of Epoxy Base Resins Used in Photocuring Applications:

The term 'epoxy resin' describes a range of polymers in which the primary cross-linking occurs through the reaction of an epoxide group. Generally, the chemical structure of an epoxy resin can be represented as a molecule containing a three membered ring, consisting of one oxygen atom and two reactive carbon atoms, Figure B-6. The molecular base to which it is attached can vary widely to different classes of epoxy resins with different viscosities depending on the demand and application of the final product [45].
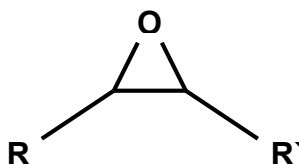
Figure B-6. Basic chemical structure of epoxy group [45].

There are two main types of epoxies used in photoinitiated curing applications:

- Glycidyl compounds:

    o Diglycidyl ether of bisphenol A (DGEBA) or bisphenol F

    o Phenyl glycidyl ether (PGE)

- Cycloaliphatic epoxies

Glycidyl Compounds:

DGEBA and PGE have similar chemical structures as well as low conversion kinetic behaviours [35].

i. Diglycidyl Ether of Bisphenol A (DGEBA) or Bisphenol F:

The bisphenol A, Figure B-7a, is found by reacting acetone with phenol, and the ether is produced when bisphenol A is reacted with epichlorhydrin. Epichlorhydrin is a reaction product of propylene with chlorine. The liquid resin DGEBA is developed by reacting bisphoenol A with 2 mols of epichlorhydrin, and the basic molecule contains two characteristic epoxy groups [46, 49]. The bisphenol F is less viscous than bisphenol A, Figure B-7b. It is usually mixed with bisphenol A to reduce its viscosity as a diluent [151].
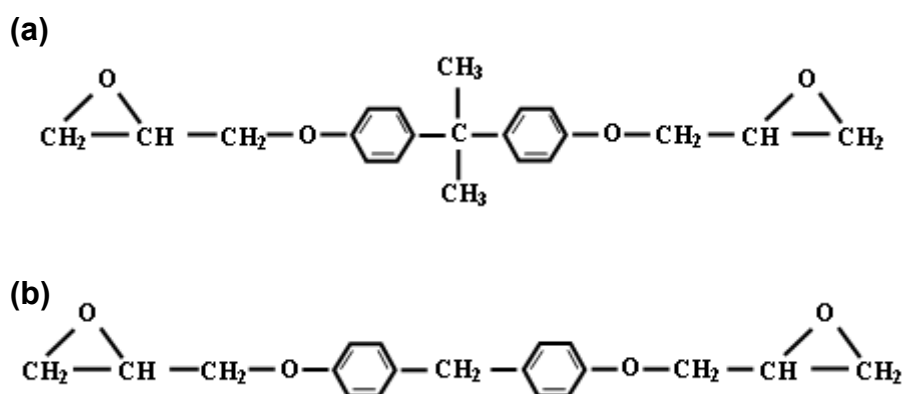
Figure B-7. Chemical structure of commercial: (a) Bisphenol-A and (b) Bisphenol-f [46, 152].

ii. Phenyl Glycidyl Ether (PGE):

PGE is a monofunctional epoxy monomer, Figure B-8. It is used for better elevated temperature performance as well as a diluent for bisphenol A [151]. Adding photoinitiator

to PGE and followed by photocuring, results in a distribution of linear oligomers with a few side reaction products, such as cyclo-ethers which is a form of dark cure [31, 71].
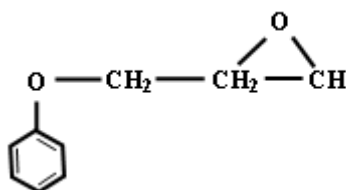
Figure B-8. Chemical structure of Phenyl glycidyl ether (PGE) [45].

Although, glycidyl ether type epoxide monomers can be photocured, they are not considered as useful fast photocurable epoxides as cycloaliphatic epoxy monomers [31, 59]. Bulut et al. [31] studied the curing behaviours of these two classes of epoxy resins using real time infrared technique (RTIR) and found that the cycloaliphatic epoxy monomers cure faster than glycidyl ethers, Figure B-9. The later needed an extended induction period that also relies on dark curing, which is incompatible with many applications that require high speed operation.
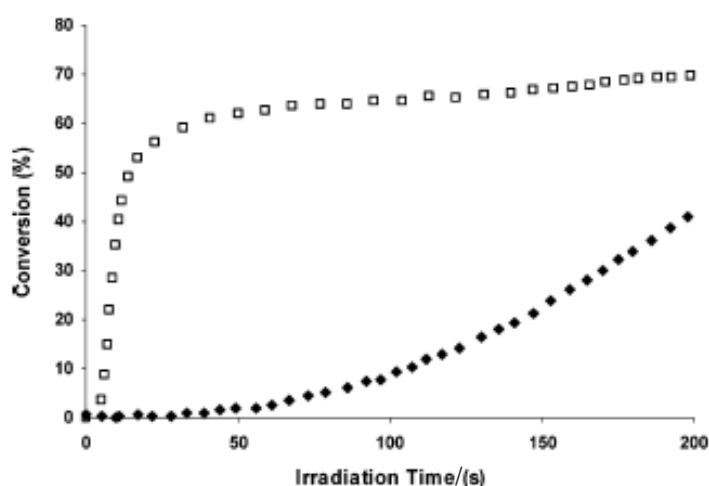
Figure B-9. RTIR comparison of the photopolymerisation of cyclohexene oxide (□) and neopentylglycol diglycidyl ether (♦) [31].

C1. Photographic Images of the Equipments used for the Epoxy Formulations Preparations (Chapter 2)

Figure C-1. Digital Weighing scale: (a) Sartorius HR60, (b) AND EK-1200i.
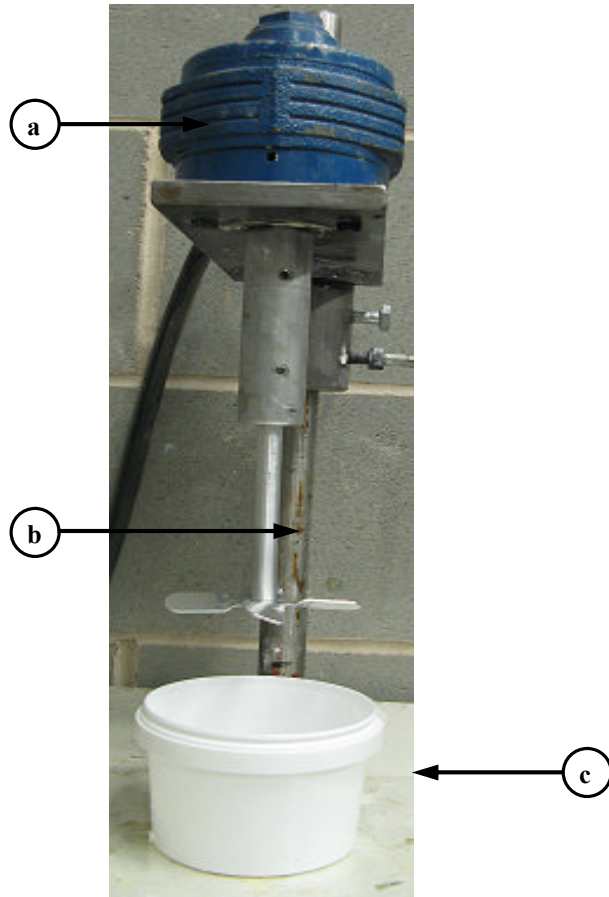
Figure C-2. Epoxy resin formulation mixing equipment: (a) Pneumatic mixing device, and (b) Stirring tool, and (c) Polypropylene cup.

C2. Types of the Commercial Cycloaliphatic Epoxides (Chapter 2)

Various types of Cyracure Cycloaliphatic Epoxides for cationic UV cure applications developed by the Dow Chemical Company [21], as shown in Table-C1.

Table-C1. Types of Cyracure Cycloaliphatic Epoxides

Product	Viscosity at 25 °C (mPa·s)
UVR-6110	350-450
UVR-6107	250-350
UVR-6105	220-250
UVR-6128	550-750

C3. Experimental details and photographic Images of some of the equipments used during the

preparations process of the Side Emitting Optical Fibre (Chapter 5)

Experimental procedures for PMMA optical fibre treatments

All of the side emission enhancement techniques were applied on untreated PMMA optical fibres (Table 5-1 of Chapter 5). These untreated PMMA optical fibres (Table 5-1) were modified by micro-cutting and embedding of silica particles into the fibres to study the possibility of achieving maximum side emission.

The effect of the mechanical treatments on the overall launched power into the optical fibres were continuously measured during the treatment processes using a power-meter located at the other free end of the fibre using Molectron PM500A analogue power-meter (see Section 4.3.2 of Chapter 4 for more details about the power-meter).

The depth of micro-cuts and the sizes of the silica particles were selected so that the treatments affected both the cladding and the core of the fibres. The densities of the micro-cuts and of the silica particles were increased progressively to increase side emission. Both treatments were studied individually and in combination. The micro-cut treatment was quantified by the number of micro-cuts. The quantity of the embedded silica particles in an optical fibre was determined by weighing the fibre before and after the treatment process using the Sartorius HR60 scale (Sartorius HR60, Figure C-1).

Micro-cuts Treatment

The micro-cuts were applied to the cladding of the PMMA optical fibres using in-house made micro-cutting tool. Stanley heavy duty blades (part number 2-11-921 from RS Components Ltd.) were used for the micro-cutting tool. Micro-cuts with depths less than 100 μm along the fibre were applied to the poly(vinylidene fluoride) cladding. The depth of the micro-cuts was controlled by positioning the blade in a wooden body (40 mm thick, 80 mm long and 50 mm wide) so that only the sharp tip pointed out, as shown in Figure C-3. The process for making the micro-cutting tool was as follows:

- **Step 1:** creating a ~ 39 mm deep, ~ 30 mm wide and ~ 1 mm thick groove using a drilling process (1 mm diameter drill bit) at the top side of the wooden body. The groove was centered and made 5 mm away from the front side of the wooden body

- **Step 2:** inserting the Stanley heavy duty blade in the groove of the wooden body and pressing it firmly so that the tip of the blade penetrate the remaining ~ 1 mm thick wooden body

- **Step 3:** measuring the exposed length of the tip of the blade (100 μm) out of the lower side of the wooden body using a micrometer.

- **Step 4:** applying permanent epoxy adhesive to bond the blade in the wooden body

- **Step 5:** covering the exposed end of the blade at the top side of the wooden body with wooden cover (15 mm thick, 30 mm long and 50 mm wide) and using permanent epoxy adhesive

The micro-cuts were applied at graduated distances (spaced from the launch face of the PMMA fibre:15 mm, 14 mm, 13 mm, 12 mm…2mm) to allow uniform emission along the fibre, as shown in Figure 5-11 of Chapter 5.
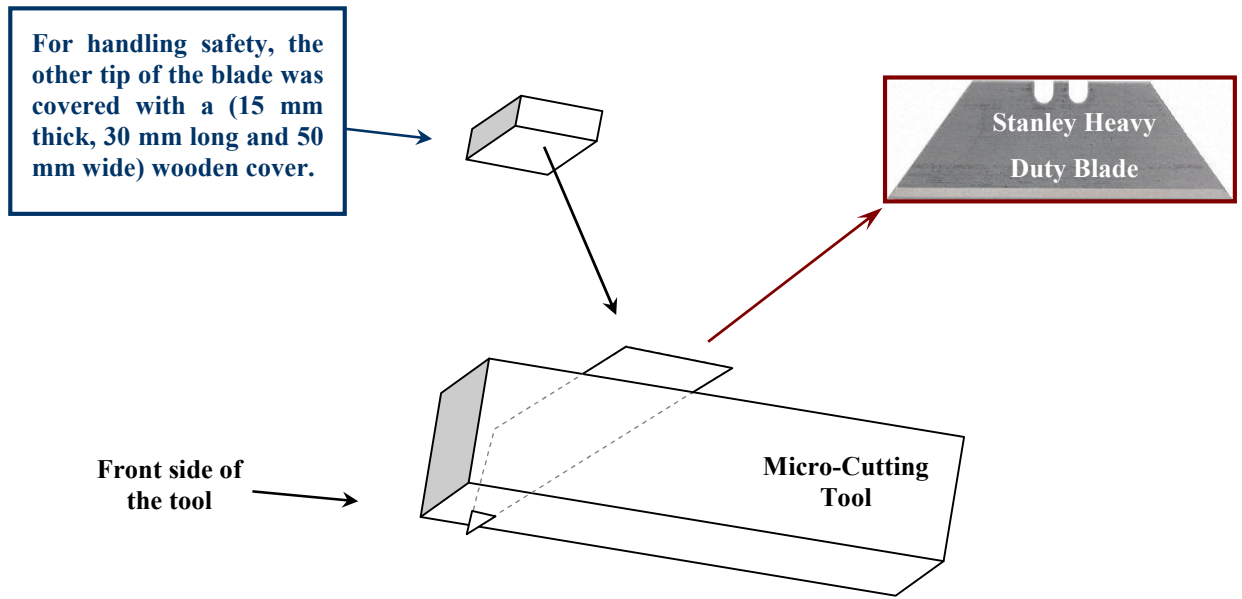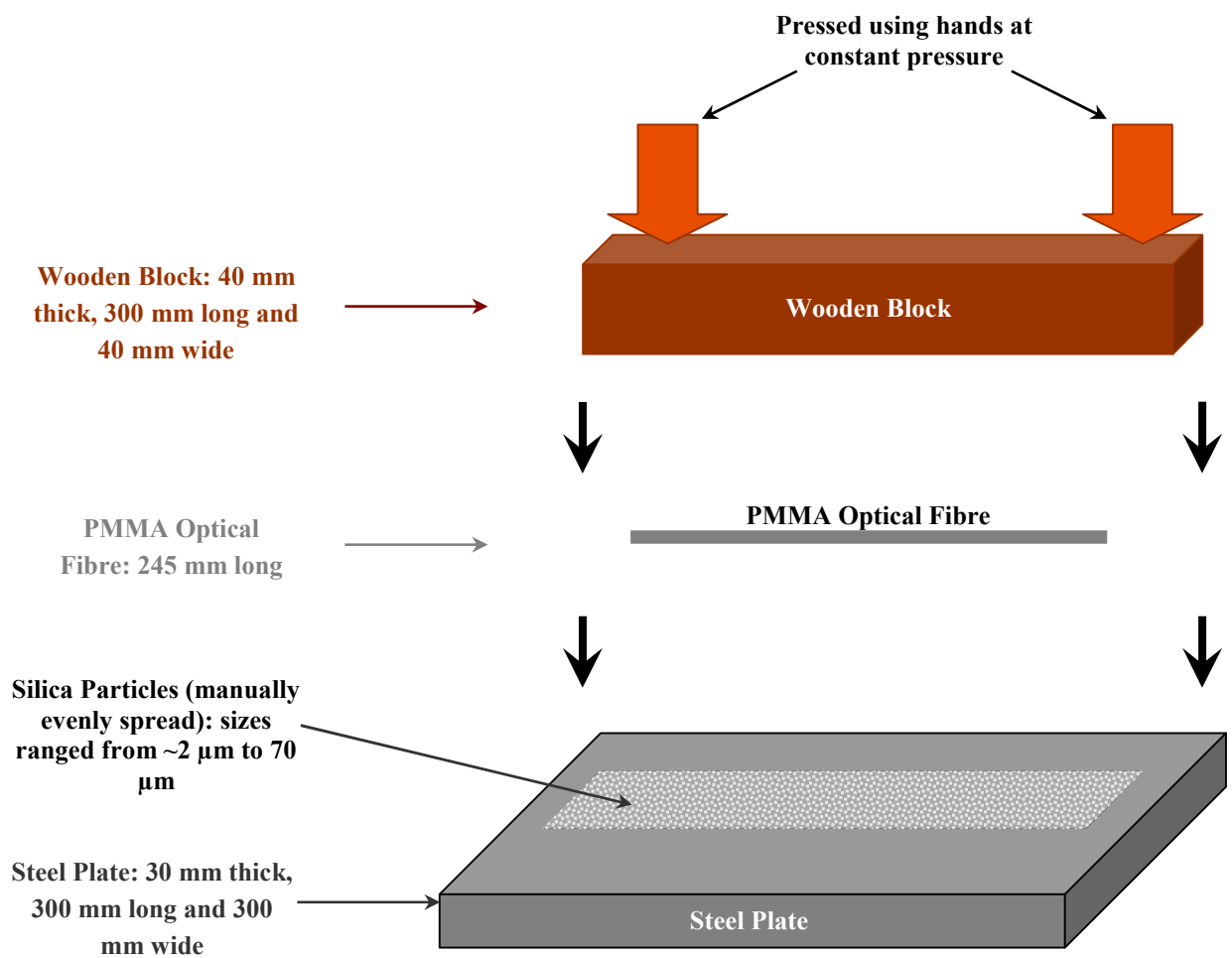
Figure C-3. Schematic illustration of the in-house made tool (40 mm thick, 80 mm long and 50 mm wide) for applying micro-cuts. The body of the tool is made of wood. The tip of the blade was measured using a micrometer. The free end tip of the blade was protected using wooden body. (Not to scale)

Silica Particles Treatment

For the silica particles mechanical treatment, silica was selected because of its high UV transmission [143]. During the preparation process, silica rods were first extracted from the fibres used in Chapter 3 (Table 3-1) and then were repeatedly crushed using steel mortar and pestle (Figure C-6) until the particles sizes ranged from ~ 2 μm to 70 μm. The sizes of the particles were measured via scanning electron microscopy (SEM) (Jeol Winsem, JSM-6400); example is shown in Figure 5-2 of Chapter 5.

After that, the silica particles were mechanically embedded in the claddings of the PMMA fibres. The process was carried out by spreading a layer of evenly distributed silica particles on a steel plate, as shown in Figure C-4. A 245 mm long PMMA fibre was then positioned

on top of the silica particles layer. The particles were embedded into the fibres by firmly pressing the positioned fibres on the particle layer using a wooden block. This process was conducted manually (by hand) with constant pressure. The process was continued by turning the fibre three times through 45° so that the silica particles evenly penetrated into the side of the fibres. This process was repeated and the drop in power output at the fibre end was measured after each treatment, until the power was constant.

Figure C-4. Schematic illustration of the in-house made process for mechanically embedding silica particles in the claddings of the PMMA optical fibres. (Not to scale)

Photographic Images of some of the equipments used during the preparations process of the Side Emitting Optical Fibre

Figure C-5. Barlow Whitney oven used for heat treatment of the fibre samples wound on the aluminum tool (Figure 5-1 of Chapter 5).

Figure C-6. Steel mortar and pestle used for crushing silica rods.

Appendix D-1:   Derivation of the Response Spectrum κ_λ

The absorbed electromagnetic radiation in a material is described by the optical density (OD):

$$OD = -\log_{10}\left(\frac{I}{I_0}\right)$$

Equation 2-5

where I_0 is the input intensity on a material and I is the transmitted intensity through a material.

The absorption of a material in terms of the properties of the material through which the electromagnetic radiation is travelling from the Beer-Lambert law:

$$I = I_0 e^{-\varepsilon_\lambda cl}$$

Equation D-1

where, λ is the wavelength, I_0 is the input intensity, I is the transmitted intensity, l is path length, c is the concentration of absorbing species, ε_λ is the extinction coefficient of the absorbing species.

The response spectrum κ_λ represents both the extinction coefficient of the absorbing species (ε_λ) and the concentration of absorbing species (c) of a material:

$$k_\lambda = \varepsilon_\lambda \cdot c$$

Equation 2-7

The fraction of radiation absorption in length l (depth of resin) is described by:

$$\frac{I_0 - I}{I_0} = 1 - e^{-k_\lambda l}$$

Equation D-2

Hence, the total rate of energy absorption [88] by the photoinitiator to produce reactive species for a depth of resin l is given by:

$$e = \int_0^\infty E_\lambda \left(1 - e^{-k_\lambda l}\right) d\lambda$$

Equation 2-6

where κ_λ is the response spectrum of the resin system and E_λ is the emission spectrum of the irradiating light source.

The response spectrum κ_λ can be found using equations 2-5, D-1 and 2-7, as shown from the following steps:

substituting equation 2-7 in equation D-1,

$$\frac{I}{I_0} = e^{-k_\lambda l}$$

Equation D-3

taking the $\log_{10}$ of both sides of equation D-3 and by multiplying by -1, results in,

$$-\log_{10}\left(\frac{I}{I_0}\right) = -\log_{10}\left(e^{-k_\lambda l}\right)$$

Equation D-4

knowing that from equation 2-5 $OD = -\log_{10}\left(I/I_0\right)$, *hence equation D-4 can be rewritten as,*

$$OD = -\log_{10}\left(e^{-k_\lambda l}\right)$$

Equation D-5

now by multiplying both sides of equation D-5 by -1 and taking the inverse log$_{10}$ of the following is found,

$$10^{(-OD)} = e^{-k_\lambda l}$$

Equation D-6

Finally, by taking the ln of both sides of equation D-6, k_λ can be determined,

$$k_\lambda = \frac{-\ln\left[10^{-OD}\right]}{l}$$

Equation 2-7

Appendix E-1: Sample Preparations for Optical Fibres

E1. Scanning Electron Microscopy (SEM) and Energy Dispersive X-ray spectroscopy (EDX)

The perpetrations of the fibre samples for the SEM and EDX tests were carried out by attaching the fibre samples to a tab mount. The attached fibre samples were then coated with carbon using a Polaton SC-7640 sputter coater, prior to examination, to protect the samples from electronic charging and possible degradation. Note that all fibres samples were just cut and attached to the tab mount without any further modification, such as polishing, to avoid any misleading information that can cause an error in the final results. Figure E-1a, E-1b, E-1c and E-1d show an example of the prepared fibres.
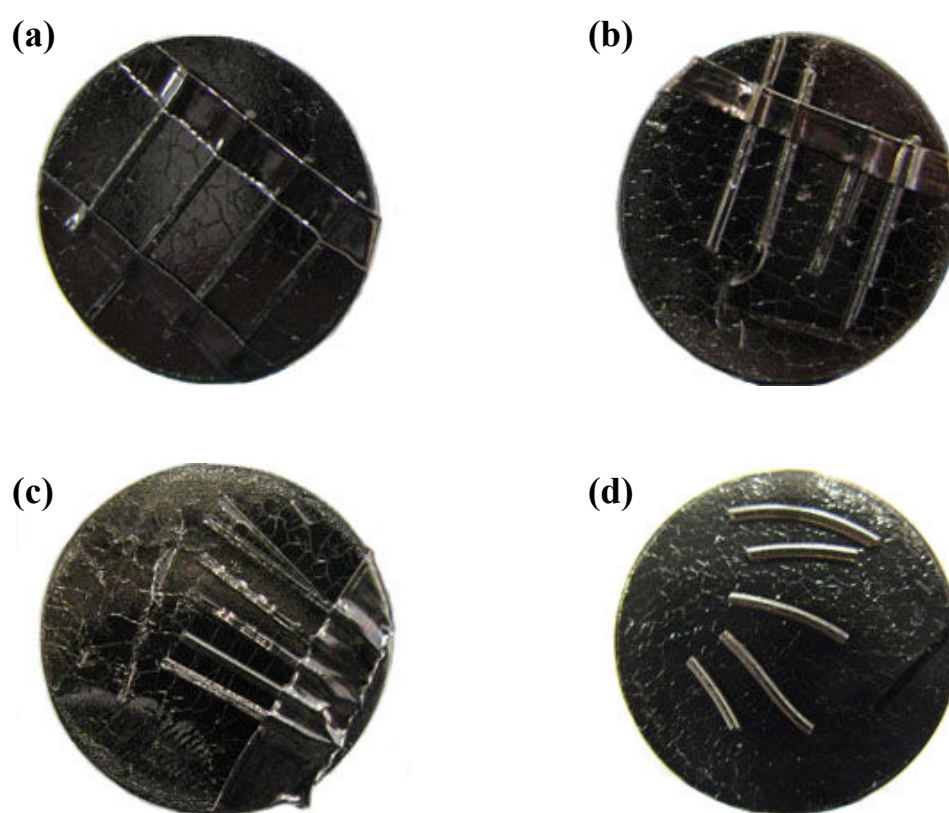
**Figure E-1.** (a) Silica core fibre 937 µm, (b) Silica core fibre 1083 µm, (c) Silica core fibre 1540 µm and (d) PMMA core fibre 1501 µm.

E2. Fourier Transform Infrared Spectroscopy (FTIR) (Bruker, Tensor 27):

The fourier transform infrared spectroscopy (FTIR) was used as a chemical analysis investigation technique for determining of polymer materials using a data base library provided with the device. This device requires a small size sample ($\approx$ 1 mm^2). The polymeric material of the fibres were removed from the fibres using a sharp blade and placed in the device.

E3. Transmission Light Microscope

The optical fibre testing under transmission light microscope were carried out for mounted and loose samples. The optical fibres were mounted using an epoxy mount, as shown in Figure E-2. The samples were then was polished to a 1 μm finish. This process was only done for the PMMA optical fibres.
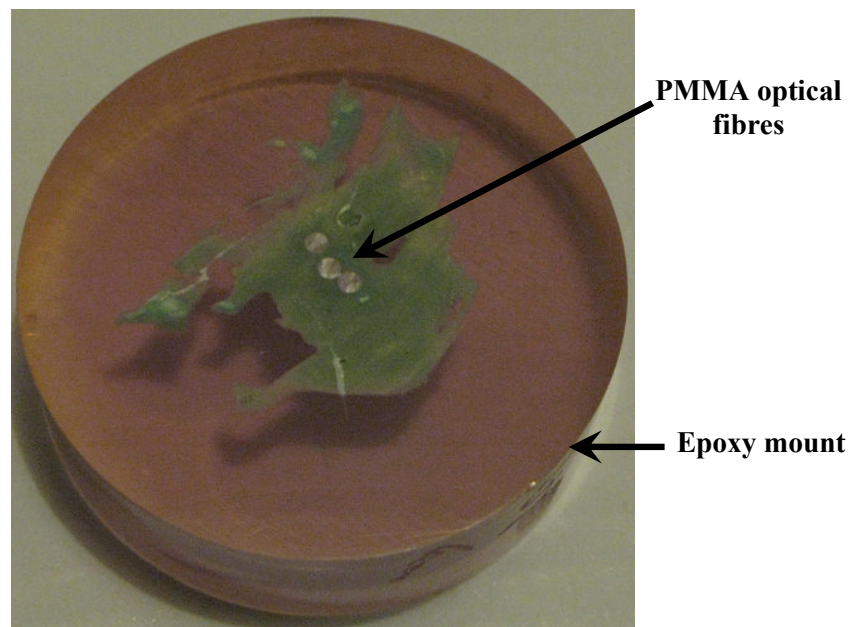

Figure E-2. Mount of 1000 μm diameter PMMA optical fibre for transmission light microscope test.

Appendix F-1: Determination of the Radiation Launching Conditions into PMMA Optical Fibre

F1. BlueWave 200 [22] radiation source (mercury (Hg) lamp) divergent angle:

The silica rod light guide of the Hg lamp divergent angle was calculated from experimental measurements and then by using trigonometric equations, as shown below:
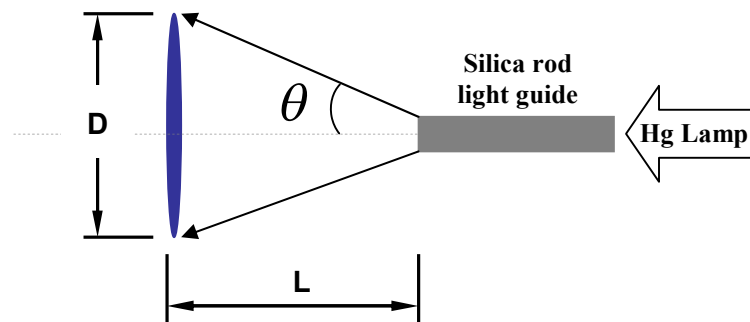
Figure F-1. Schematic illustration of the experimental measurements for calculation of the spot lamp divergent angle

The dimensions were experimentally measured as illustrated in Figure F-1, and found to be:

D = 165mm, L = 170mm

The divergent angle of the radiation can be determined using the following trigonometric function:

$$\tan\theta = \frac{\frac{1}{2}D}{L}$$

Equation F-1

θ is calculated from the inverse tangent function of equation F-1, and the spot lamp divergent angle is $\theta \approx \mathbf{26°.}$

F2. PMMA Optical Fibre Cone of Acceptance and Critical Angles:

The cone of acceptance is the maximum angle at which the ray of radiation can be received into the core of the optical fibre and then is able to travel along the fibre [92-93]. It is expressed as follows:

$$acceptance\ angle = sin^{-1}\ NA$$

Equation F-2

where NA is the numerical aperture and expressed by the following equation [92-93]:

$$NA = \sqrt{n^2{}_{core} - n^2{}_{clading}} \quad \text{(no units)}$$

Equation F-3

where, n is the refractive index.

The critical angle is so-called because any radiation rays entering the core at a greater angle than the critical angle will not be guided in the fibre core. The radiation rays with angles of incidence less than the critical angle cause total internal reflection [92-93]. The critical angle of an optical fibre can found by using the following equation (from Chapter 2):

$$\psi_{critical} = \arcsin\left(\frac{n_{cladding}}{n_{core}}\right)$$

Equation 3-2

where, n is the refractive index.

Therefore, by substituting the refractive index values of the PMMA optical fibre components from Table 3-2 of Chapter 3 into equations F-3 and F-4, the numerical aperture (NA) equals to **0.4498** and the critical angle $(\phi_{critical})$ is **72°**, and from equation F-2 the PMMA optical fibres *acceptance angle is* ≈ **27°**, Figure F-2.
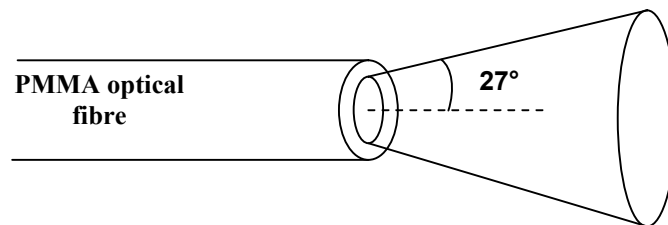

Figure F-2. Acceptance angle of PMMA optical fibre.

The cone of acceptance of PMMA optical fibre is greater than the divergent angle of the silica rod light guide of the Hg lamp which concludes that the emission angle of the radiation source matches the cone of acceptance of the optical fibres and all of the radiated rays launched into the PMMA optical fibre end face will undergo total internal reflection in the fibre core.

F3. Emission Window of the Side Emitting Optical Fibres

Mathematically, the geometry of an optical fibre is a cylinder, as shown below,

Cylinder area $(CA) = 2(\pi\, r^2) + (2\pi r)\, l$ **(Equation F-5)**
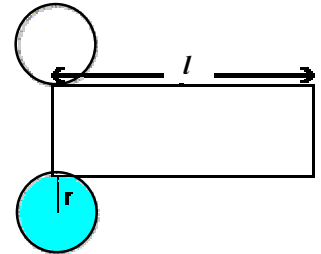
where, r is the radius of circle, and l is the length.

Hence, the side emission window (SE) is the side surface area of an optical fibre and can be expresses by

$$SE = (2\pi r)\, l \qquad \text{(Equation F-6)}$$

where, l is the length (mm) of the optical fibre, and r is its radius (mm).

Thus, for the earlier treated PMMA optical fibres with length 245 mm and 1000 μm (1 mm) diameter, the emission window (SE) is 770 mm^2, as also shown in Figure 5-16. In addition, larger fibre diameter allows more radiation transmission and also results in an increased emission window (SE).
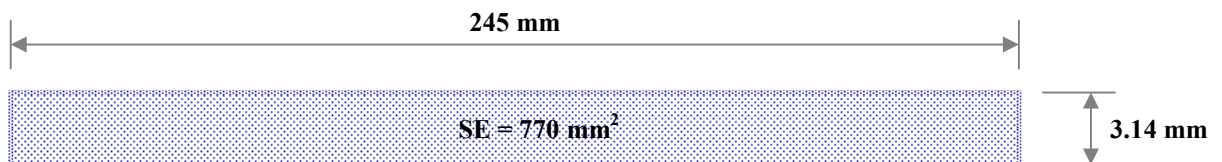
Figure F-3. Emission window (SE) of a 245mm long and 1000μm diameter PMMA optical fibre (fibre 3 from Table 5-1 of Chapter 5).